

Signatures of Majorana fermions and ground state degeneracies in topological superconductors

Von der Fakultät für Physik und Geowissenschaften

der Universität Leipzig

genehmigte

D I S S E R T A T I O N

zur Erlangung des akademischen Grades

Doctor rerum naturalium

Dr. rer. nat.

vorgelegt

von Diplom-Physiker Björn Zocher

geboren am 05.12.1987 in Borna

Gutachter: Prof. Dr. Bernd Rosenow, Universität Leipzig
Prof. Felix von Oppen, Ph.D., Freie Universität Berlin

Tag der Verleihung: 16.12.2013

Bibliographische Beschreibung:

Zocher, Björn

Signatures of Majorana fermions and ground state degeneracies in topological superconductors

Universität Leipzig, Dissertation

202 S., 162 Lit., 56 Abb.

Referat:

Motivated by the recent experimental progress in the search for Majorana fermions, we identify signatures of topological superconductivity and propose realistic experiments to observe these signatures. In the first part of this thesis, we study charge transport through a topological superconductor with a pair of Majorana end states, coupled to leads via quantum dots with resonant levels. The nonlocality of the Majorana bound states opens the possibility of Cooper pair splitting with nonlocal shot noise. In the space of quantum dot energy levels, we find a characteristic four-peaked cloverlike pattern for the strength of noise due to Cooper pair splitting, distinct from the single ellipsoidal peak found in the absence of Majorana end states.

Semiconductor-superconductor hybrid systems are promising candidates for the realization of Majorana fermions and topological order in solid state devices. In the second part, we show that the topological order is mirrored in the excitation spectra and can be observed in nonlinear Coulomb blockade transport through a ring-shaped nanowire. Especially, the excitation spectrum is almost independent of magnetic flux in the topologically trivial phase but acquires a characteristic h/e magnetic flux periodicity in the nontrivial phase. The transition between the trivial and nontrivial phase is reflected in the closing and reopening of an excitation gap.

In the third part, we investigate characteristic features in the spin response of doped three-dimensional topological insulators with odd-parity unequal-spin superconducting pairing, which are predicted to have gapless Majorana surface modes. These Majorana modes contribute to the spin response, giving rise to a characteristic temperature behavior of the Knight shift and the spin-lattice relaxation time in magnetic resonance experiments.

Contents

1. Introduction	1
1.1. Topological superconductivity and Majorana fermions	3
1.2. Proposed realization of Majorana fermions	6
1.3. Experimental situation	7
1.4. This thesis	9
1.4.1. Transport signatures of Majorana bound states coupled to quantum dots	9
1.4.2. Signatures of topological order in Coulomb blockade transport through semiconductor – superconductor nanowire rings	11
1.4.3. Spin response in three-dimensional topological superconductors . .	12
2. Introduction to topological superconductivity	15
2.1. Topological invariant for bilinear Hamiltonians	15
2.2. One-dimensional lattice model of spinless fermions	20
2.3. Two-dimensional topological superconductor	25
2.4. Ground-state degeneracy on nontrivial manifolds	27
2.5. Semiconductor-superconductor hybrid systems	31
3. Transport signatures of Majorana bound states coupled to quantum dots	37
3.1. Model system and theoretical methods	39
3.1.1. Model system	39
3.1.2. Generalized scattering formalism	41
3.1.3. Microscopic model	46
3.2. Normal-state–Majorana bound state–normal-state device	47
3.3. Coupling one quantum dot to a Majorana bound state	52
3.4. Coupling two quantum dots to a pair of Majorana bound states	55
3.4.1. Weak quantum dot–lead coupling	57
3.4.2. Strong quantum dot–lead coupling	59
3.4.3. Effect of finite temperatures	61

3.4.4.	Amplitude of the current cross-correlations	62
3.4.5.	Spinless p -wave superconductor	63
3.4.6.	Realistic semiconductor-superconductor hybrid system	65
3.4.7.	Relation to previous work	71
3.5.	Spinful quantum dots with finite Coulomb repulsion	72
3.5.1.	One spinful quantum dot coupled to a Majorana bound state	74
3.5.2.	Two spinful quantum dots coupled to a pair of Majorana bound states	78
3.6.	Summary	79
4.	Signatures of topological order in Coulomb blockade transport through semiconductor–superconductor nanowire rings	81
4.1.	Model system	82
4.1.1.	Setup and Coulomb Hamiltonian	82
4.1.2.	Hamiltonian for the semiconductor-superconductor hybrid system	85
4.1.3.	Material parameters	88
4.2.	Idealized one-dimensional ring-shaped nanowire	89
4.2.1.	Wave functions: Spinless p -wave superconductor	93
4.2.2.	Wave functions: Semiconductor-superconductor hybrid system	95
4.2.3.	Numerical results	96
4.3.	General single-band Hamiltonian	99
4.3.1.	Dependence on geometry details	100
4.3.2.	Nonmagnetic disorder	102
4.3.3.	Non-superconducting segments	105
4.4.	Multi-band Hamiltonian	107
4.5.	Cotunneling of Cooper pairs	110
4.6.	Connection to possible experiments	114
4.7.	Summary	116
5.	Spin response in three-dimensional topological superconductors	117
5.1.	Model system	119
5.1.1.	Hamiltonian for the doped topological insulator	119
5.1.2.	Superconducting pairing Hamiltonians	122
5.1.3.	Doped topological insulator with odd-parity interorbital pairing	124
5.1.4.	Competing pairing symmetries	131
5.2.	Density of states and linear magnetic response	132
5.2.1.	Odd parity, interorbital unequal-spin pairing	134

5.2.2. Competing pairing symmetries	137
5.3. Experimental detection scheme	142
5.4. Summary	144
6. Summary and conclusions	147
A. Lattice model for the semiconductor-superconductor hybrid system	151
A.1. Lattice model for the semiconductor-superconductor hybrid system	151
A.2. Lattice model for the quantum dot-topological superconductor nanowire- quantum dot system	153
B. Majorana bound states coupled to quantum dots	155
B.1. Bogoliubov-de Gennes Hamiltonian for the coupled quantum dot-Majorana bound state system	155
B.2. Majorana energy splitting	156
B.3. Proximity induced superconducting pairing between two quantum dots	158
B.4. Zero-voltage conductance for the quantum dot-Majorana bound state-quan- tum dot device	160
B.5. Transport properties of a double-quantum dot system coupled via the su- perconducting proximity effect	161
C. Three-dimensional topological superconductors and spin response	163
C.1. Lattice Hamiltonian for the three-dimensional topological superconductor .	163
C.2. Projection of the pairing Hamiltonians for the doped three-dimensional topological insulator	165
C.3. Density of states and spin susceptibilities for superconductors	169
C.3.1. Density of states	169
C.3.2. Spin susceptibilities	170
C.4. Nuclear magnetic resonance	172
C.4.1. Knight shift	173
C.4.2. Spin-lattice relaxation rate	174
Bibliography	177

1. Introduction

The search for new states of quantum matter is one of the central pursuits in modern physics. In condensed matter physics we know in principle the Hamiltonian exactly, at least in the simplification which is relevant for the vast majority of applications. The fundamental constituents of any condensed matter system are nuclei and electrons which are bound together by the Coulomb interaction. As a consequence, the underlying theory is quantum electrodynamics with a trivial extension for several species of charged particles (electrons and nuclei). However, we also know that at low temperature many systems exhibit quantum phases which behave dramatically different compared to their fundamental constituents. This phenomenon is called emergence [1,2], and the list of examples is long and ranges from crystallization and magnetism to high-temperature superconductivity and quantum Hall effects.

The traditional paradigms to characterize such emergent quantum phases are Landau's Fermi liquid theory [3] and the Ginzburg-Landau theory of symmetry breaking [4]. In Fermi liquid theory, the interacting many-body problem is significantly simplified by identifying the interacting fermions with effectively noninteracting quasiparticles with renormalized parameters such as mass, velocity, and other dynamical properties. This theory was particularly successful in describing the normal-state properties of liquid ^3He and metals. However, at low temperatures some systems provide instabilities towards phases which are characterized by a local order parameter and in these cases the paradigm of the noninteracting electron picture fails. The phase transitions are usually well described by the Ginzburg-Landau theory where an effective field theory for the order parameter of the interacting fermion system is investigated. This field theory is determined by general properties such as the symmetry of the order parameter and dimensionality, and gives a universal description of the broken-symmetry phase. The classification of phases with broken symmetries is well described by the mathematical concept of group theory which describes the physical system in terms of symmetry groups. Together, Fermi liquid theory and the theory of symmetry breaking were successful in the explanation of a series of interacting many-body problems. Examples are crystalline solids, where translational symmetry is broken, magnets, where spin rotation symmetry is broken, and superconduc-

tors, where the global gauge symmetry is broken leading to exotic phenomena such as Josephson effects and flux quantization.

Over the last thirty years, there were several experimental and theoretical discoveries which did not fit into this simple traditional picture. Until the discovery of the quantum Hall effect in a two-dimensional electron gas subjected to a strong perpendicular magnetic field [5], it was conjectured that most states of matter can be classified in terms of the Ginzburg-Landau theory of symmetry-breaking, i.e., by local order parameters. However, for the quantum Hall states there is no local order parameter, instead, each state is characterized by a global topological invariant [6]. Topology is a mathematical concept to characterize different geometrical objects and to classify them into broad classes. Topological classification and in particular homotopy theory discards small details and focuses on the fundamental distinction of shapes. In the quantum Hall effect, the topological invariant n is given by a Brillouin zone integral over the Berry curvature and determines the precisely quantized transverse conductance $\sigma_{xy} = ne^2/h$ [6]. This topological invariant cannot change unless the energy gap between electronic bands closes and reopens. In particular, it remains unchanged by small perturbations in the physical system. Similarly to order parameters in systems with broken symmetry, the topological invariants act as topological order parameters in systems without symmetry breaking. The transition between two phases, which can be distinguished by a topological invariant, is called topological phase transition.

With the theoretical prediction and the experimental confirmation of the two-dimensional quantum spin Hall effect in HgTe/CdTe quantum wells [7,8] and its three-dimensional counterpart in bismuth chalcogenides [9,10], the search for topological phases attracted much interest [11,12]. While the quantum Hall states belong to a class of topological states which explicitly breaks time-reversal symmetry, these new quantum states called topological insulators belong to a class which is invariant under time reversal and in which spin-orbit coupling plays a key role. The topological insulator can be distinguished from the trivial band insulator by a \mathbb{Z}_2 topological invariant which is determined by the electronic band structure. It is well-known that the electronic band structure of trivial insulators is characterized by a band gap and hence has vanishing longitudinal conductivity for sufficiently small voltages and temperatures. In contrast, the topological insulator has a band gap in the bulk, but has gapless surface states consisting of an odd number of Dirac fermion modes which give rise to quantized electronic transport. With surface we here mean any interface between the topological and the trivial insulator (including vacuum). The existence of the surface states is deeply related to the \mathbb{Z}_2 topological invariant because the topological invariant can only change when the excitation gap closes. As a consequence,

there is a region between the topological and the trivial insulator where the excitation gap closes giving rise to low-energy electronic states [11].

Shortly after the prediction and the experimental confirmation of topological insulators, theorists generalized this concept to superconductors where we distinguish between topologically trivial and nontrivial superconductors [12–15]. The situation in superconductors is analogous to insulators because the Bogoliubov-de Gennes Hamiltonian for the quasiparticles of a superconductor is equivalent to the Hamiltonian for an insulator, with the band gap replaced by the superconducting gap and the electrons replaced by quasiparticles. However, despite the recent efforts on topological phases of matter, a complete classification of topological phases which also captures interacting systems is still missing.

1.1. Topological superconductivity and Majorana fermions

Topological superconductors are one type of topologically nontrivial states of quantum matter. They are particularly interesting because they host Majorana fermions as low-energy quasiparticle excitations. Majorana fermions [16] are particles which are their own antiparticles. In the notation of second quantization, this yields the simple relation

$$\gamma = \gamma^\dagger, \quad (1.1.1)$$

where γ denotes the quasiparticle operator for the Majorana fermion. The anti-commutation relation for Majorana fermion operators has the unusual form

$$\gamma_m \gamma_n + \gamma_n \gamma_m = 2\delta_{mn}. \quad (1.1.2)$$

This relation is strikingly different from the usual fermion anti-commutation relations $c_m c_n + c_n c_m = 0$ and $c_m^\dagger c_n + c_n c_m^\dagger = \delta_{mn}$ for fermion operators c_m . Majorana fermions were originally proposed as real-valued solutions of the Dirac equation describing charge neutral fermionic fields in the context of high-energy physics [16]. However, it is still unclear if there are elementary particles which are Majorana fermions. Ettore Majorana suggested that neutrinos could be described by Majorana fermions, but the experimental verification (as well as the falsification) of this hypothesis is still elusive.

More than five decades later, it was proposed that Majorana fermions might emerge as exotic quasiparticle excitations in certain condensed matter systems [17–19]. Being its own antiparticle implies that the Majorana fermion can be represented as equal superposition of electron and hole components. Therefore, Majorana fermions are likely to exist as quasiparticle excitations in superconductors where particle-hole symmetry relates states

with positive energy and states with negative energy. More precisely, in superconductors creating a quasiparticle with energy E is equivalent to annihilating a quasiparticle with energy $-E$,

$$\gamma(E) = \gamma^\dagger(-E). \quad (1.1.3)$$

As a consequence, the states with zero-energy are special as they are by default charge neutral superpositions of electrons and holes. The most common type of superconductors is characterized by pairing between electrons with opposite spin directions forming a singlet. In second quantization, the Bogoliubov quasiparticles describing singlet pairing read $\gamma_\uparrow = uc_\uparrow^\dagger + vc_\downarrow$, where c_σ^\dagger creates an electron with spin $\sigma = \uparrow, \downarrow$. For $u = v^*$, the operator γ_\uparrow describes a neutral fermion at zero energy, but it is not a Majorana fermion due to the spin degree of freedom. A Bogoliubov quasiparticle, which satisfies for $E = 0$ the Majorana criterion by construction, is $\gamma = uc_\sigma^\dagger + vc_\sigma$ where fermions with the same spin direction are paired into Cooper pairs with triplet symmetry. This type of pairing does not occur in conventional superconductors and was first predicted to be realized in the fractional quantum Hall state at filling fraction $\nu = 5/2$ [19, 20]. Before we discuss the details of the experimental realization of Majorana fermions, we will concentrate on their exotic properties.

Recently, Majorana fermions have attracted much interest, mainly because of their special exchange statistics [21–23]. It is well known that the many-body wave function for bosons is invariant under exchange of two bosons and the many-body wave function for fermions acquires a minus sign under exchange of two fermions. In three spatial dimensions, the statistics of bosons and fermions are the only possible statistics of particle exchange since the fermion and boson statistics are the only one-dimensional representations of the permutation group of indistinguishable particles. In contrast, in two dimensions, exchange of two identical particles is not only described by the change of the order of the particles, i.e., the permutation group, but it is also necessary to specify the paths along which the particles are exchanged. As a consequence, in two dimensions particle exchange is no longer described by the permutation group but by the braid group. The braid group is much richer than the permutation group and in addition to bosons and fermions, there are more general types of wave functions called anyons. We distinguish between abelian [24, 25] and non-abelian anyons [20]. Abelian anyons acquire a complex phase $\exp(i\theta)$, which is described by the statistical angle θ , under particle exchange and therefore interpolate between $\theta = 0$ for bosons and $\theta = \pi$ for fermions. It was shown that certain fractional quantum Hall states have anyonic quasiparticles with abelian statistics, e.g. the $\nu = 1/3$ state with $\theta = \pi/3$ [26]. In addition, there are non-abelian anyons which necessarily have a degenerate space of ground states and whose many-body wave functions are more generally

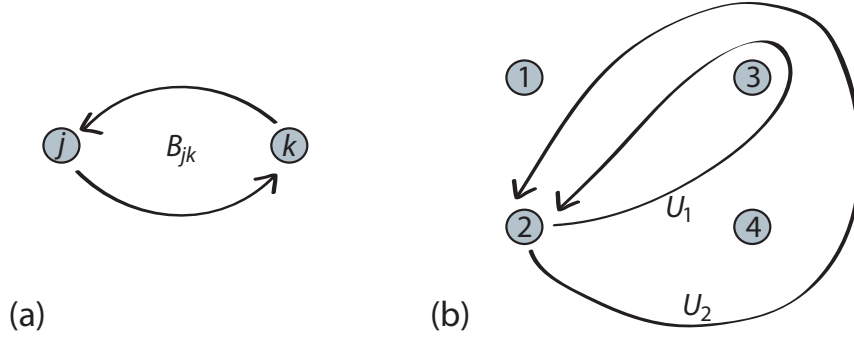


Figure 1.1.1.: Sketch of a two-dimensional topological superconductor with well-separated vortices binding Majorana fermions. (a) Under the counter-clockwise exchange of two Majorana fermions j and k , the many-body wave function is transformed by the unitary operator B_{jk} . (b) Two exchange paths of Majorana fermions with identical initial and final Majorana configuration. The two paths are described by the unitary operators U_1 and U_2 which do not commute $U_1U_2 \neq U_2U_1$.

transformed by matrices within the ground-state space. Since matrix multiplication is in general non-commutative, the outcome of the exchange of non-abelian anyons depends on the order of how the particles are exchanged.

Majorana fermions are one particularly simple type of non-abelian anyons. In the following, we consider the exchange statistics of Majorana fermions which are bound to defects in a two-dimensional system as illustrated in figure 1.1.1(a). The adiabatic counter-clockwise exchange of two Majorana fermions γ_j and γ_k is described by the unitary operator

$$B_{jk} = \exp\left(-\frac{\pi}{4}\gamma_j\gamma_k\right). \quad (1.1.4)$$

Thus, two consecutive exchanges return both Majorana fermions to their initial positions, but the final state is $|f\rangle = B_{jk}^2|i\rangle = -\gamma_j\gamma_k|i\rangle$, which is in general not identical to the initial state $|i\rangle$. A transformation of the form Eq. (1.1.4) is fully determined by the topology of the exchange paths and does not depend on details of the paths [27].

In the following, we consider an example which illustrates the non-abelian character of the Majorana exchange statistics. We consider four Majorana fermions which are bound to some defects and which are not coupled to each other. As illustrated in figure 1.1.1(b), we consider two exchange paths with the same initial and final configuration of Majorana fermions. For exchange U_1 , we directly move Majorana 2 counter-clockwise around Majorana 3. For exchange U_2 , we first move Majorana 2 counter-clockwise around Majorana 4 and then we move Majorana 2 counter-clockwise around Majorana 3. These two

interchanges are described by the unitary operators

$$U_1 = B_{23}^2 = -\gamma_2\gamma_3, \quad (1.1.5a)$$

$$U_2 = B_{24}^2 B_{23}^2 = (-\gamma_2\gamma_4)(-\gamma_2\gamma_3) = -\gamma_4\gamma_3 \quad (1.1.5b)$$

and $[U_1, U_2] = -2\gamma_2\gamma_4 \neq 0$, i.e., the transformations U_1 and U_2 do not commute. We note that the operator U_2 is identical to the operator B_{43}^2 which describes the counter-clockwise exchange of Majoranas 4 and 3 despite the fact that both Majoranas have not been moved physically according to the exchange trajectories in figure 1.1.1(b). Realizing this unconventional exchange statistics stimulated huge research efforts in the condensed matter community [21–23].

1.2. Proposed realization of Majorana fermions

The first system, which was proposed to realize Majorana fermions, is the fractional quantum Hall state at filling fraction $\nu = 5/2$ [20]. The insight of Moore and Read was to identify the many-body wave function of the $\nu = 5/2$ state with chiral correlators (conformal blocks) in a two-dimensional conformal field theory and quasiparticle excitations with Ising anyons (Majorana fermions bound to vortices). Greiter *et al.* [28] and Read *et al.* [19] more generally suggested that Majorana fermions appear as vortex excitations in spin polarized superconductors with $p + ip$ pairing and that the $\nu = 5/2$ state can be described by a condensate of composite fermions with $p + ip$ pairing symmetry. Later, it was proposed that this unconventional pairing symmetry and hence Majorana fermions also appear in other systems such as the A-phase of ^3He films [18], in Sr_2RuO_4 [29], and in cold atoms in optical traps [30]. However, despite the intense research efforts over the last years clear signatures of Majorana fermions and the topological superconducting state in these systems are still missing.

In 2007, Fu and Kane proposed in a pioneering work [31] that the $p + ip$ superconducting pairing can be induced on the surface of a strong topological insulator which is strongly coupled to a conventional s -wave superconductor. The surface of a topological insulator is described by a single Dirac cone with a helical band structure. Because of the single electronic band, the system is effectively spinless and because of the helical spin structure, there is a finite antiparallel spin component between states with opposite momenta. The underlying ingredient for induction of $p + ip$ pairing is the strong spin-orbit coupling of the topological insulator which gives rise to momentum dependent spin directions. Later, it was realized that the same mechanism can be used to induce $p + ip$ pairing symmetry in

more conventional semiconductor nanowires with strong Rashba spin-orbit coupling such as InSb and InAs in proximity to an s -wave superconductor [32–37]. There, the system becomes effectively spinless by applying a strong magnetic field which opens a Zeeman gap. The large spin-orbit coupling guarantees that there is a finite antiparallel spin component between opposite momenta within each electronic band and the superconducting pairing opens a quasiparticle excitation gap. Based on these proposals, a large number of possible systems was suggested including vortices in topological insulators [38], cold atomic gases [39], carbon nanotubes [40], chains of quantum dots [41], and domain walls in topological insulator nanowires [42].

Currently, it was proposed that Majorana fermions might also occur as surface states on three-dimensional topological superconductors with intrinsic odd-parity pairing symmetry [43, 44]. Fu and Berg [45] showed that the strong spin-orbit-coupled bands of a doped topological insulator indeed favor an odd-parity pairing symmetry which gives rise to the existence of surface Majorana modes. The advantage of this system is the intrinsic superconductivity which does not require the superconducting proximity effect. On the other hand, the Majorana fermions in this system are delocalized on the entire surface and thus magnetic films are necessary to bound the Majorana fermions to some defect.

1.3. Experimental situation

Before coming to the recent experimental findings, we briefly recap the characteristic signatures of Majorana fermions and what needs to be shown experimentally to verify the existence of Majorana fermions. The defining properties of Majorana fermions are, for system sizes much larger than the superconducting coherence length, zero excitation energy and non-abelian braiding statistics. The ultimate proof for the existence of Majorana fermions would be the demonstration of non-abelian statistics by using them to build a quantum computer [27, 46]. However, experimentally this has not yet been realized and the high level of difficulty makes it challenging that the non-abelian statistics (and the Majorana quantum computer) will be realized in the near future. Therefore, a legitimate goal is to study other consequences of Majorana fermions and to show that these consequences can be clearly distinguished from the situation without Majorana fermions [47–54]. Recently, a series of experimental works presented first evidence for Majorana fermions in semiconductor-superconductor hybrid devices. We divide the experiments into two classes studying the local density of states via tunneling experiments and studying supercurrents via Josephson effects. A detailed analysis of the experiments goes beyond the scope of this introduction, but we still want to discuss some questions and potential difficulties with the

interpretation of these experiments in terms of Majoranas fermions.

Mourik *et al.* [55] investigated the differential conductance for tunneling into an InSb nanowire proximity coupled to a NbTi superconductor. They showed evidence for the zero-energy nature of Majorana fermions in the form of a zero-bias anomaly in the differential conductance above a certain critical value of the Zeeman field. The behavior of this zero-bias feature under rotations of the magnetic field and against local variations of gate voltages is consistent with the theoretical predictions. Later, these findings have been confirmed by other experimental groups in similar systems [56–58]. However, there are several features in the experimental data which shed doubt on the interpretation in terms of Majorana fermions, in particular since these features appear in all published experimental data. These features include: (i) the absence of a clear signature associated with the closing of the quasiparticle excitation gap at the topological phase transition separating the topologically nontrivial from the trivial phase; (ii) the measured zero-bias conductance is more than an order of magnitude smaller than the expected quantized value $2e^2/h$; (iii) the observation of a soft superconducting gap instead of a hard gap with suppressed differential conductance for voltages smaller than the gap and sharp coherence peak. In addition to these unexpected experimental observations, theorists proposed a number of alternative scenarios which explain the appearance of the zero-bias anomaly based on more conventional physical phenomena. These scenarios involve pair-breaking effects by strong nonmagnetic disorder [59], smooth confinement potentials [60], weak antilocalization [61], Kondo physics [62], or the 0.7 anomaly in nanowires [58]. Therefore, we conclude that tunneling experiments alone are not sufficient to verify the existence of Majorana fermions and that complementary experiments are desirable.

So far, one experiment reported evidence of unconventional Josephson effects in semiconductor-superconductor nanowires [63]. In conventional superconductivity, the only low-energy charge carriers which can tunnel across the junction between two superconductors are Cooper pairs with charge $2e$ which give rise to a 2π periodic Josephson current $I \propto \sin(\phi)$, where ϕ denotes the superconducting phase difference across the junction. In contrast, the presence of Majorana fermions enables the tunneling of single electrons with charge e across the junction between two topological superconductors. This halving of the transferred charge from $2e$ to e yields a doubling of the Aharonov-Bohm phase for constructive interference. Therefore, the periodicity of the Josephson current $I \propto \sin(\phi/2)$ is 4π and hence doubled as compared to conventional superconductors. However, this effect cannot be seen in dc Josephson experiments where fluctuations between the two degenerate ground states screen the 4π periodicity. In contrast, in the ac Josephson effect the 4π periodicity is not screened and gives rise to unconventional Shapiro steps [64]. It was shown

experimentally that above some critical value of the Zeeman field, the height of the first Shapiro step is doubled which is a signature of the topological phase transition. However, in a recent theoretical work it was shown that fractional Josephson effects can also appear in high-transparency conventional superconductor–normal-state–superconductor junctions as a result of Landau-Zener processes associated with the Andreev bound states of the junction [65].

We conclude that despite the recent experimental progress clear experimental signatures of Majorana fermions and the topological superconducting state are still absent. We believe that additional theoretical work is necessary in order to identify complementary experimental signatures and to clearly distinguish the case with Majorana fermions from the case without Majorana fermions.

1.4. This thesis

In the following, we give a brief description of the content of this thesis. In chapter 2, we begin with an introduction to the basic physics and concepts of topological superconductivity. There, we provide the basic theoretical methods to distinguish between trivial and nontrivial superconducting states and we show how to obtain ground-state properties of the superconductor. In particular, we note that the following main chapters of this thesis build on the concept introduced in chapter 2. In the three main chapters, we study physical consequences of topological superconductivity and their experimental signatures. In the following, we briefly present the content of the main chapters.

1.4.1. Transport signatures of Majorana bound states coupled to quantum dots

In chapter 3, we consider transport through a three-terminal normal-state–topological superconductor nanowire–normal-state device. The topological superconductor nanowire is characterized by a pair of Majorana fermions which are bound to the two ends of the nanowire. Because of the finite length of the nanowire, the Majorana bound states are tunnel coupled to each other and have a finite energy splitting $\epsilon_M \sim \Delta \exp(-L/\xi_{SM}) \sin(k_F L)$, where ξ_{SM} is the superconducting coherence length and k_F the Fermi momentum in the semiconductor. A possible probe for the nonlocal nature of Majorana bound states is Cooper pair splitting [66–68]. The electrons in superconductors form Cooper pairs and the process of converting a Cooper pair into two electrons in spatially separated normal metal contacts is called Cooper pair splitting. To realize Cooper pair splitting, a tunneling ma-

trix element is required, which allows a pair of electrons to leave the superconductor into two separate contacts. One particular realization of such a matrix element is the Majorana energy splitting ϵ_M . It has been shown theoretically that at sufficiently low voltages and small level broadening, Cooper pair splitting by the pair of Majorana bound states is the dominating transport process and gives rise to positive current cross-correlations [69, 70]. For voltages larger than the Majorana energy splitting ϵ_M , resonant tunneling of electrons and holes gives rise to negative current cross-correlations, and the total current cross-correlations vanish.

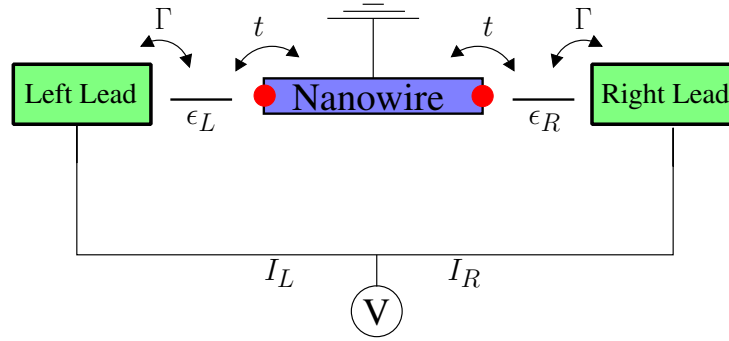


Figure 1.4.1.: Illustration of a system with a pair of Majorana bound states coupled to quantum dots which themselves are coupled to lead electrodes. Cooper pair splitting can be detected by correlating the currents I_L and I_R that flow via Majorana bound states into the superconductor nanowire.

In this chapter, we study the effect of quantum dots on the transport signatures of Majorana bound states. In particular, we focus on the physics of coupling a pair of Majorana bound states at the ends of a quasi one-dimensional topological superconductor nanowire to lead electrodes via quantum dots in the Coulomb blockade regime. The proposed experimental setup is illustrated in figure 1.4.1. As demonstrated in recent experiments with similar systems [71–73], the quantum dots suppress local Andreev reflection and thus provide a suitable tool to probe current cross-correlations. Building on this observation, we investigate the effect of quantum dots on the differential conductance and on the current cross-correlations in topological superconductors. We underline our findings for an effective low-energy model with numerical results for a microscopic model of a spinless p -wave superconductor [19] and the more realistic semiconductor-superconductor hybrid system discussed above.

1.4.2. Signatures of topological order in Coulomb blockade transport through semiconductor – superconductor nanowire rings

In chapter 4, we investigate signatures of topological order and the topological phase transition in quasi one-dimensional ring shaped superconductor nanowires in nonlinear Coulomb blockade transport. Here, we associate topological order with the existence of ground-state degeneracies which depend on the manifold on which the system is defined. We focus on a regime in which the quasiparticle gap Δ is larger than the single-particle level spacing d . In the Coulomb blockade regime, the total particle number and hence the parity of the superconductor nanowire are fixed by the charging energy $E_c > \Delta$, and the degeneracy of grand canonical ground states is reflected in the excitation energies, which can be observed in nonlinear Coulomb blockade transport [74, 75]. The lowest excited states above the ground state of a trivial superconductor with even parity involve two quasiparticles and thus breaks a Cooper pair, incurring an excitation energy $\delta E \approx 2\Delta$, which is essentially independent of magnetic flux. In contrast, the ground state for odd parity always has one quasiparticle, and hence the lowest excited state involves both annihilating and creating a quasiparticle which costs the excitation energy $\delta E \approx d^2/\Delta \ll 2\Delta$.

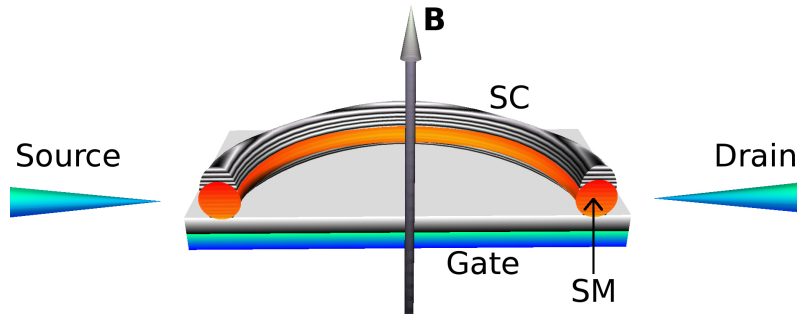


Figure 1.4.2.: Cross section of the experimental setup for a ring shaped semiconductor-superconductor hybrid system. We consider a quasi one-dimensional semiconductor (SM) nanowire with strong spin-orbit coupling and a magnetic field B perpendicular to the plane of the semiconductor ring. The superconductor (SC) is sputtered on top of the semiconductor which itself is deposited on a gate electrode. The semiconductor is weakly tunnel coupled to source and drain electrodes.

For nontrivial topological superconductors, the situation is very different. Here, ground states without unpaired particles at the Fermi energy have odd parity for periodic boundary condition, and even parity for antiperiodic boundary condition. Therefore, the excitation energy δE oscillates between d^2/Δ and 2Δ as function of magnetic flux with period h/e which is doubled as compared to trivial superconductors. This connection between the ground-state degeneracy on manifolds with nonzero genus and the h/e flux periodicity of

ring structures demonstrates that these properties are a general consequence of topological order and that nonlinear Coulomb blockade transport is a suitable tool to investigate this order.

We propose an experiment which directly investigates consequences of topological order on a nontrivial manifold. For this purpose, we use the Coulomb energy as a tool to fix the parity of the hybrid system and thus, to observe the above discussed ground-state degeneracy. Our analysis is based on the identification of the pfaffian \mathbb{Z}_2 invariant for Hamiltonians in class D, i.e., Hamiltonians whose only symmetry is particle-hole symmetry [76], with the parity \mathcal{Q} of the grand canonical ground state. Thus, we use this key piece of information about the grand canonical ground state to construct two classes of states with parity \mathcal{Q} and $-\mathcal{Q}$, where the class of states with parity \mathcal{Q} ($-\mathcal{Q}$) contains all eigenstates with an even (odd) number of quasiparticle excitations. We find two types of excitation spectra which display trivial or nontrivial superconductivity depending on parameter values. The transition between the different topological phases is characterized by the closing and reopening of an excitation gap. As these findings only rely on the existence of a superconducting gap $\Delta > d$ and the S^1 topology of the system, the excitation spectra are robust against nonmagnetic disorder, spatial variations of the superconducting pairing potential, geometry details, and the existence of additional transverse subbands.

1.4.3. Spin response in three-dimensional topological superconductors

Recent experiments showed first evidence for unconventional superconductivity with a critical temperature $T_c \approx 4$ K in the electron doped topological insulator $\text{Cu}_x\text{Bi}_2\text{Se}_3$ [43]. Based on specific heat measurements, it was proposed that this system possibly shows a fully-gapped, time-reversal invariant p -wave superconducting state [77]. By now, the existence of surface states in $\text{Cu}_x\text{Bi}_2\text{Se}_3$ has been probed by photoemission [78] and point contact spectroscopy [79–83]. Currently, the experimental situation for the superconducting state of $\text{Cu}_x\text{Bi}_2\text{Se}_3$ is rather controversial [84]. While recent point contact spectroscopy experiments [79–81] showed signatures of subgap surface states, no such signatures were found in references [82, 83]. As a consequence, at the moment the superconducting pairing symmetry of $\text{Cu}_x\text{Bi}_2\text{Se}_3$ cannot be unambiguously determined from tunneling spectroscopy, and data obtained by complementary experimental techniques are desirable.

Nuclear magnetic resonance and quadrupole resonance, as well as the electron and muon spin resonance are another class of powerful techniques to investigate the electronic properties locally. The Knight shift for example is determined by the static spin susceptibility, which is directly connected to the spin structure of the superconducting pairing. In conven-

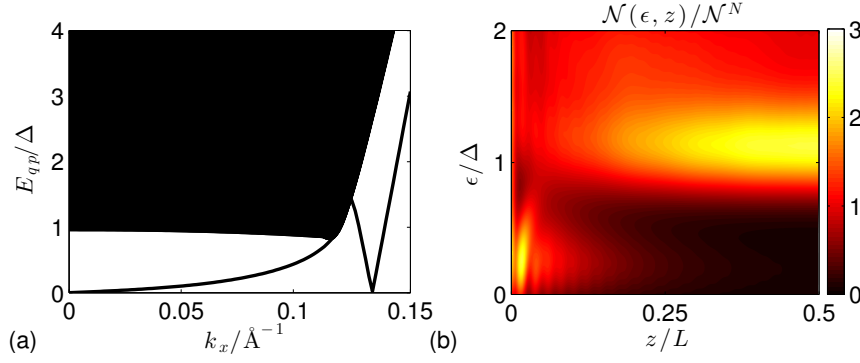


Figure 1.4.3.: (a) Cut through the quasiparticle excitation spectrum for a topological insulator with odd-parity interorbital pairing. The energy band within the superconducting gap reflects the surface states. (b) Local density of states as function of distance from the surface and energy. Note the subgap states near $z = 0$ which decay exponentially into the bulk.

tional s -wave superconductors with spin-singlet pairing, the Knight shift is significantly reduced and vanishes for zero temperature because spins pair up and longitudinal spin excitations cost the pair-breaking energy 2Δ . However, in superconductors with strong spin-orbit coupling the spin susceptibility is suppressed as compared to the normal state, but does not vanish for zero temperature due to coupling between up and down spins. In chapter 5, we study characteristic features in the spin response of odd-parity pairing in doped topological insulators and predict clear signatures for the above resonance techniques.

Fu and Berg [45] showed that strong spin-orbit-coupled bands indeed favor an odd-parity interorbital unequal-spin pairing [85, 86]. To gain insight into its topologically nontrivial nature, we map this pairing Hamiltonian onto the conduction band, which yields an effective time-reversal invariant $p \pm ip$ pairing in three dimensions. Because of this topology, there is a pair of Majorana zero-energy modes located at each surface and protected by time-reversal symmetry. Additionally, there are unconventional surface Andreev bound states originating from the band inversion as shown in figure 1.4.3(a). In addition to terms linear in momentum, we here consider quadratic momentum terms, which determine the energy range of coexistence between Dirac modes and unconventional surface Andreev bound states, and which may give rise to other species of zero-energy surface Andreev bound states. The main motivation for introducing the quadratic terms is the possibility to investigate the competition between the different surface states and the bulk.

The coexistence of the Majorana zero-energy modes and the surface Andreev bound states originating from the band inversion [87] gives rise to two characteristic length scales. The Dirac modes decay on the nanometer scale ξ_0 whereas the decay length ξ_1 for the Ma-

Majorana zero-energy modes is hundreds of nanometer as shown in figure 1.4.3(b). Hence, the local spin susceptibility shows different characteristic behavior in the bulk, at the surface, and within ξ_1 into the bulk. Conventional bulk nuclear magnetic resonance can distinguish between competing pairing symmetries by the characteristic temperature dependence of the Knight shift and the spin-lattice relaxation rate. We propose that nuclear magnetic resonance in thin films of several hundred nanometer thickness, or depth controlled probes [88,89] allow to clearly determine the pairing symmetry and investigate the Majorana zero-energy modes.

2. Introduction to topological superconductivity

In this chapter, we give an elementary introduction to topological superconductivity with the focus on the most important aspects for understanding the basic physics. Our goal is to provide basic concepts and tools which are useful to describe superconductors in general and to discriminate between topologically distinct superconducting phases in special. In section 2.1, we begin with an introduction to general superconducting Hamiltonians and discuss how to obtain various ground-state properties of superconductors, such as the energy, mean particle number, and parity. In particular, we show that the parity of the many-body wave function determines the topology of the superconducting state, and we formulate a criterion for topological superconductivity. Then, in section 2.2 we discuss in some detail a toy model for a one-dimensional superconductor and show that this model is characterized by two classes of ground-state wave functions with distinct topology. In section 2.3, we generalize this toy model by extending the model to two dimensions, and we discuss the topological order of this system in section 2.4. We conclude this chapter in section 2.5 with the introduction of an experimentally promising system in which topological superconductivity can be engineered using a semiconductor nanowire with strong spin-orbit coupling, exposed to a magnetic field, and proximity coupled to a conventional s -wave superconductor.

2.1. Topological invariant for bilinear Hamiltonians

We begin our discussion with an abstract introduction to the zero-temperature formalism of how to calculate ground-state properties and excited states of a general superconducting system described by a bilinear Hamiltonian. In the mean-field approximation, superconductors are characterized by nonvanishing anomalous expectation values of operators which annihilate or create pairs of electrons. These anomalous expectation values result from the decoupling of an attractive electron-electron interaction and give rise to the superconducting order parameter. The consequence of the anomalous expectation values is the violation

of particle-number conservation in the mean-field ground-state wave function which is a coherent superposition of states with different particle numbers. Instead of a certain particle number, the mean-field wave function is characterized by particle-number parity, i.e., particle number modulo two. In this section we will discuss a connection between the parity of the wave function and the topological properties of the superconducting state.

In the following, we consider a superconducting system which is described by a bilinear Hamiltonian in the mean-field approximation. In second quantization, we write the general Hamiltonian as

$$H = C^\dagger T C + \frac{1}{2} C^\dagger \Delta (C^\dagger)^T + \frac{1}{2} C^T \Delta^\dagger C, \quad (2.1.1)$$

where $C = (c_1, c_2, \dots, c_N)^T$ is an N -component column vector of fermion annihilation operators c_i , and C^\dagger is the corresponding N -component row vector of fermion creation operators. Here, we do not specify the number N , however, for electrons the c operators are typically labeled by momentum and spin, and then N is two times the number of momenta. The Hermitian $N \times N$ matrix T contains the kinetic and potential energy terms, which describe the normal-state properties, and the $N \times N$ matrix Δ contains the superconducting pairing potential. In addition, the pairing matrix is skew-symmetric $\Delta^T = -\Delta$ which is a direct consequence of the anti-commutation relations of fermions.

It is standard practice to consider the so-called Nambu space representation of the Hamiltonian in Eq. (2.1.1) by including fermion creation and annihilation operators into a single $2N$ -component vector. Hence, we rewrite the Hamiltonian in matrix form as

$$H = \frac{1}{2} \begin{pmatrix} C^\dagger & C^T \end{pmatrix} \mathcal{H}_{\text{BdG}} \begin{pmatrix} C \\ (C^\dagger)^T \end{pmatrix} + \frac{1}{2} \text{Tr}(T), \quad (2.1.2)$$

where \mathcal{H}_{BdG} is the Hermitian $2N \times 2N$ matrix denoting the single-particle Hamiltonian,

$$\mathcal{H}_{\text{BdG}} = \begin{pmatrix} T & \Delta \\ -\Delta^* & -T^* \end{pmatrix}, \quad (2.1.3)$$

and $\text{Tr}(T)$ denotes the trace of the matrix T . Here, the trace term is a real number and appears because to obtain Eq. (2.1.2) we split the kinetic energy into two parts. Then, we used the fermionic anti-commutation relations to interchange the order of creation and annihilation operators in one of the parts. This interchange gives rise to a minus sign in the second line of Eq. (2.1.3) and in addition, it yields a constant rest term when interchanging creation and annihilation operators which describe the same fermion.

The entries in the basis vector $(C^\dagger \ C^T)$ are not independent of each other and can be transformed into each other by applying a particle-hole transformation $C \rightarrow (C^\dagger)^T$ and

$C^\dagger \rightarrow (C)^T$. In matrix notation, the particle-hole operator is given by

$$\mathcal{P} = \tau_x \mathcal{K} \equiv \begin{pmatrix} \mathbf{0} & \mathbf{1} \\ \mathbf{1} & \mathbf{0} \end{pmatrix} \mathcal{K}, \quad (2.1.4)$$

where \mathcal{K} denotes an operator which applies complex conjugation to all elements on the right and $\mathbf{1}$ ($\mathbf{0}$) denotes the $N \times N$ identity matrix (zero matrix). Applying the transformation \mathcal{P} to the Hamilton matrix, we find $\mathcal{P} \mathcal{H}_{\text{BdG}} \mathcal{P}^{-1} = -\mathcal{H}_{\text{BdG}}$. From this relation, we conclude that for all positive eigenvalues E_i of \mathcal{H}_{BdG} , there is a negative counterpart $-E_i$ which is also an eigenvalue of \mathcal{H}_{BdG} . In addition, the corresponding eigenvectors $|\psi_E\rangle$ and $|\psi_{-E}\rangle$ can be transformed into each other by applying the operator $\mathcal{P}|\psi_E\rangle = |\psi_{-E}\rangle$.

The Hamiltonian Eq. (2.1.1) can be diagonalized by a unitary transformation described by $N \times N$ matrices U and V which transform the fermion operators C and C^\dagger into new fermion operators A and A^\dagger by

$$C = UA + V(A^\dagger)^T. \quad (2.1.5)$$

This transformation is called Bogoliubov transformation and the operators A are called Bogoliubov quasiparticle operators. The conditions for the unitarity of transformation Eq. (2.1.5) are

$$UU^\dagger + VV^\dagger = \mathbf{1}, \quad (2.1.6a)$$

$$UV^T + VU^T = \mathbf{0}. \quad (2.1.6b)$$

With this transformation, we write

$$\begin{pmatrix} C \\ (C^\dagger)^T \end{pmatrix} = \begin{pmatrix} U & V \\ V^* & U^* \end{pmatrix} \begin{pmatrix} A \\ (A^\dagger)^T \end{pmatrix} \quad (2.1.7)$$

and hence,

$$H = \frac{1}{2} \begin{pmatrix} A^\dagger & A^T \end{pmatrix} \begin{pmatrix} U^\dagger & V^\dagger \\ V^T & U^T \end{pmatrix} \mathcal{H}_{\text{BdG}} \begin{pmatrix} U & V \\ V^* & U^* \end{pmatrix} \begin{pmatrix} A \\ (A^\dagger)^T \end{pmatrix} + \frac{1}{2} \text{Tr}(T). \quad (2.1.8)$$

In the following, we demand that the Hamiltonian is diagonal in the new operators,

$$H = A^\dagger D A + E_0 \quad (2.1.9)$$

with the diagonal matrix $D = \text{diag}(E_1, \dots, E_N)$, which has nonnegative entries only, and

with the ground-state energy E_0 . This demand yields the eigenvalue equation

$$\mathcal{H}_{\text{BdG}} \begin{pmatrix} U & V \\ V^* & U^* \end{pmatrix} = \begin{pmatrix} U & V \\ V^* & U^* \end{pmatrix} \begin{pmatrix} D & 0 \\ 0 & -D \end{pmatrix} \quad (2.1.10)$$

and the ground-state energy is given by

$$E_0 = \frac{1}{2} \text{Tr}(T) - \frac{1}{2} \text{Tr}(D). \quad (2.1.11)$$

The eigenvalue equation (2.1.10) is called Bogoliubov-de Gennes equation. The ground-state many-body wave function $|\psi\rangle$ of Hamiltonian Eq. (2.1.1) is given by the state for which all quasiparticle states A_i with quasiparticle energy $E_i > 0$ are empty, i.e., $A_i|\psi\rangle = 0$. According to Eq. (2.1.9), the Hamiltonian is the sum over occupied quasiparticles with nonnegative energy plus the residual energy E_0 . Since the ground state is characterized by zero quasiparticles, the terminology *ground-state energy* is justified for E_0 .

To further investigate the ground-state properties, we distinguish two generic cases:

- (i) All quasiparticle energies are positive, $E_i > 0$, and the superconductor is fully gapped with the energy gap $E_G = \min(E_i)$. As a consequence, the many-body ground-state wave function is uniquely defined by the state without quasiparticles A_i . This situation is for instance realized in conventional *s*-wave superconductors where electrons form spin singlet Cooper pairs and where the superconducting gap is protected against nonmagnetic perturbations according to Anderson's theorem [90].
- (ii) Some excitation energies vanish, i.e., $E_i = 0$ for i in some set S of indices. In this case, the ground state is not uniquely defined and there is a 2^n -dimensional space of ground states where n denotes the number of elements in S . To further discuss this situation, we specify the set S and assume that the energies $E_i = 0$ for $i = 1, \dots, n$. By definition of the operators A_i , there is one ground state $|\psi(\mathbf{0})\rangle$ for which $A_i|\psi(\mathbf{0})\rangle = 0$ for all i . Starting from this specific state, we construct new states

$$|\psi(\mathbf{s})\rangle = (A_1^\dagger)^{s_1} \dots (A_n^\dagger)^{s_n} |\psi(\mathbf{0})\rangle \quad (2.1.12)$$

with $\mathbf{s} = \{s_1, \dots, s_n\}$ and $s_i \in \{0, 1\}$. On the first view, this space of degenerate ground states looks rather artificial for superconducting systems. However, in the following sections we will show that this situation is for instance realized in topological superconductors where zero-energy states exist in defects.

For the rest of this section, we consider systems which fall into class (i) where all energies $E_i > 0$ and where the ground state is unique. In most problems, the ground-state wave

function is highly complicated and usually we are not interested in the explicit form of the wave function itself. Instead, we are interested in some specific properties of the ground state such as its energy E_0 which is determined by diagonalizing the matrix \mathcal{H}_{BdG} . In addition, we are interested in the mean particle number and the parity of the ground state. Similarly, we are not interested in the explicit form of the wave functions for the excited states. Again, we are only interested in the excitation energies E_i and in the operators A_i which describe the quasiparticle excitations. In the following, we show how all these quantities can be derived from the Bogoliubov-de Gennes matrix \mathcal{H}_{BdG} without knowing the explicit form of the ground-state wave function.

The ground-state electron number is given by the expectation value of the particle-number operator $\hat{N} = C^\dagger C$ in the state where all quasiparticle levels are empty. Rewriting the particle-number operator in terms of quasiparticle operators and taking the expectation value with respect to the ground state ($\langle A_i^\dagger A_i \rangle = 0$), we find

$$N_0 = \text{Tr}(V^\dagger V). \quad (2.1.13)$$

For superconductors, the particle number operator \hat{N} does not commute with the Hamiltonian and as a consequence, there are states which do not have a definite mean-field particle number. In contrast, the parity operator $\hat{P} = (-1)^{\hat{N}}$ commutes with the Hamiltonian because all terms in the Hamiltonian contain two fermion operators and each fermion operator changes the parity. Hence, two fermion operators change the parity twice which is equivalent to no change of the parity. As a consequence, the eigenstates of H can be divided into two classes ψ_e and ψ_o with even ($\langle \psi_e | \hat{P} | \psi_e \rangle = +1$) and odd parity ($\langle \psi_o | \hat{P} | \psi_o \rangle = -1$).

The parity of the unique ground-state wave function is determined by the number

$$\mathcal{Q} = \frac{\text{Pf}(\mathcal{H}_{\text{BdG}} i \tau^x)}{\sqrt{\det(\mathcal{H}_{\text{BdG}} i \tau^x)}}, \quad (2.1.14)$$

where τ^x denotes the Pauli matrix acting on the particle-hole space introduced above. Pf denotes the so-called pfaffian which is defined for $2N \times 2N$ skew-symmetric matrices as

$$\text{Pf}(A) = \frac{1}{2^N N!} \sum_{\sigma \in S_{2N}} \text{sign}(\sigma) \prod_{i=1}^N a_{\sigma(2i-1), \sigma(2i)}. \quad (2.1.15)$$

Here, S_{2N} denotes the permutation group and $\text{sign}(\sigma)$ is the signature of the permutation σ . One special property of the pfaffian is $\text{Pf}(A)^2 = \det(A)$ which is a crucial relation to see that \mathcal{Q} is dimensionless and in particular, $\mathcal{Q} = \pm 1$. As noted above, for systems with gapped quasiparticle excitation spectrum the number $\mathcal{Q} = +1(-1)$ corresponds to

the even (odd) parity of the ground state. For a proof of Eq. (2.1.14), we refer the reader to reference [91].

For superconducting systems without time-reversal symmetry, i.e., systems in class D of the Altland-Zirnbauer classification of Hamiltonians [13, 92], the parity \mathcal{Q} becomes particularly interesting. It was proposed that \mathcal{Q} is a topological invariant which is intricately related to the topology of the superconductor. This topological invariant is robust against weak perturbations of the system, where weak is defined in comparison to the superconducting gap E_G , and cannot be changed in a continuous way without closing the excitation gap of the superconductor.

If we apply Eq. (2.1.14) to an ordinary s -wave superconductor (without or very weak magnetic perturbations) described within the BCS framework, we always find $\mathcal{Q} = +1$, i.e., an s -wave superconductor has always even parity independent of the microscopic details. The origin of the even parity is that all electrons near the Fermi surface form Cooper pairs and pairs have by definition an even parity. However, below we will show that theoretically, there are also more exotic superconductors with $\mathcal{Q} = -1$ and that these systems behave very different as compared to conventional s -wave superconductors.

2.2. One-dimensional lattice model of spinless fermions

In this section we introduce a simple toy model for a one-dimensional superconductor and we apply the concepts discussed above in section (2.1) to this model. We consider a one-dimensional chain of N spinless fermions as illustrated in figure 2.2.1(a). The fermions can hop between nearest-neighbor lattice sites and exhibit long-range-ordered p -wave superconductivity. We write the Hamiltonian as

$$H_K = - \sum_{x=1}^{N-1} \left(t_0 c_x^\dagger c_{x+1} + t_0 c_{x+1}^\dagger c_x + \Delta_0 c_x^\dagger c_{x+1}^\dagger + \Delta_0^* c_{x+1} c_x \right) - \mu_0 \sum_{x=1}^N c_x^\dagger c_x, \quad (2.2.1)$$

where μ_0 denotes the chemical potential, t_0 the hopping amplitude between nearest neighbors, and Δ_0 the superconducting pairing potential between nearest neighbors. The operator c_x (c_x^\dagger) denotes the annihilation (creation) operator for a spinless fermion on site x . We stress that for spinless fermions onsite pairing is not possible since Pauli's exclusion principle forbids doubly occupied sites. Hence, pairing between nearest neighbors is the simplest possible pairing term for spinless systems. We note that the Hamiltonian Eq. (2.2.1) is sometimes dubbed *Kitaev model* since Kitaev introduced this model to describe Majorana bound states in quantum wires [76].

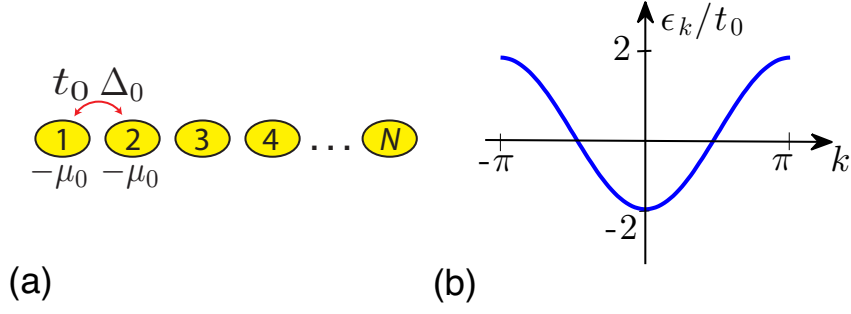


Figure 2.2.1.: (a) Illustration of the one-dimensional chain of spinless fermions Eq. (2.2.1) with nearest-neighbor hopping potential t_0 , nearest-neighbor superconducting pairing potential Δ_0 , and chemical potential μ_0 . (b) Bare dispersion relation $\epsilon_k = -2t_0 \cos(k)$ for a half filled one-dimensional tight-binding model with band width $4t_0$.

At first, we consider the limit that the chain forms a closed loop with periodic boundary conditions. This limit allows us to study the properties of the superconducting bulk without perturbations from the ends of the chain. Therefore, it is appropriate to consider Hamiltonian Eq. (2.2.1) in momentum space by Fourier transformation of the fermion operators

$$c_x = \frac{1}{\sqrt{2\pi N}} \sum_k e^{-ikx} c_k. \quad (2.2.2)$$

In the following, we assume that the number of lattice sites N is even which yields the allowed momenta $k = 2\pi n/N$ with $n \in \{-N/2 + 1, -N/2 + 2, \dots, N/2\}$. The analysis of the chain with an odd number of lattice sites is analogous and therefore we neglect this case here. We rewrite the Hamiltonian as

$$H_K = \sum_k \left\{ \epsilon_k c_k^\dagger c_k + \Delta_0 \sin(k) c_k^\dagger c_{-k}^\dagger + \Delta_0^* \sin(k) c_{-k} c_k \right\} \quad (2.2.3)$$

with the kinetic energy $\epsilon_k = -2t_0 \cos(k) - \mu_0$. From the pairing term, we see that there are two special momenta $k = 0$ and $k = \pi$, which do not contribute in the pairing since $\sin(0) = \sin(\pi) = 0$. All other fermions are paired with their time-reversed partners, i.e., pairing is between momenta k and $-k$. According to Eq. (2.1.8), we rewrite the Hamiltonian as

$$H_K = \frac{1}{2} \sum_{0 < k < \pi} C_k^\dagger \mathcal{H}_k C_k + \frac{1}{2} \sum_{l=0, \pi} \begin{pmatrix} c_l^\dagger & c_l \end{pmatrix} \begin{pmatrix} \epsilon_l & 0 \\ 0 & -\epsilon_l \end{pmatrix} \begin{pmatrix} c_l \\ c_l^\dagger \end{pmatrix} + \frac{1}{2} \sum_{-\pi < k \leq \pi} \epsilon_k \quad (2.2.4)$$

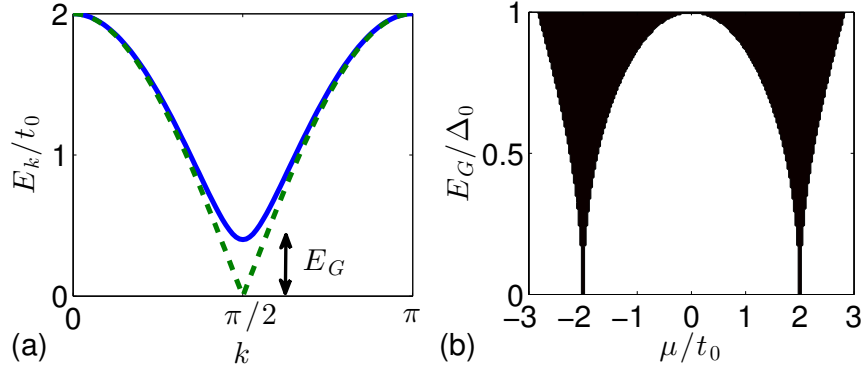


Figure 2.2.2.: (a) Quasiparticle excitation spectrum E_k as function of momentum k for the one-dimensional Kitaev model Hamiltonian Eq. (2.2.3) with $\mu_0 = 0$. The solid line is the spectrum for $\Delta_0 = t_0/4$ and the dashed line is the spectrum for $\Delta_0 = 0$. (b) Quasiparticle excitation spectrum as function of chemical potential. The black area is characterized by a continuum of quasiparticle states bounded from below by a quasiparticle gap for $|\mu_0| \neq 2t_0$. For $|\mu_0| = 2t_0$, the quasiparticle gap closes.

with the Bogoliubov-de Gennes matrix

$$\mathcal{H}_k = \begin{pmatrix} \epsilon_k & 0 & 0 & \Delta_0 \sin(k) \\ 0 & \epsilon_{-k} & -\Delta_0 \sin(k) & 0 \\ 0 & -\Delta_0^* \sin(k) & -\epsilon_k & 0 \\ \Delta_0^* \sin(k) & 0 & 0 & -\epsilon_{-k} \end{pmatrix} \quad (2.2.5)$$

and the vector

$$C_k^\dagger = \begin{pmatrix} c_k^\dagger & c_{-k}^\dagger & c_k & c_{-k} \end{pmatrix}. \quad (2.2.6)$$

By diagonalizing the matrix \mathcal{H}_k , we find the quasiparticle energies

$$E_k = \sqrt{(-2t_0 \cos(k) - \mu_0)^2 + |\Delta_0|^2 \sin^2(k)}. \quad (2.2.7)$$

As shown in figure 2.2.2, for $|\Delta_0| \ll t_0$ the quasiparticle spectrum has a superconducting gap of magnitude $E_G = |\Delta_0| \sqrt{1 - \mu_0^2/4t_0^2}$ which is finite for all $|\mu_0| \neq 2t_0$.

Since for $|\mu_0| \neq 2t_0$ all quasiparticle energies are nonzero and the spectrum is fully gapped, we can calculate the topological number \mathcal{Q} introduced above in Eq. (2.1.14),

$$\mathcal{Q} = \frac{\epsilon_0}{|\epsilon_0|} \underbrace{\left(\prod_{0 < k < \pi} \frac{E_k^2}{E_k^2} \right)}_{\equiv 1} \frac{\epsilon_\pi}{|\epsilon_\pi|} = \text{sign}(\epsilon_0 \epsilon_\pi). \quad (2.2.8)$$

If we insert the expression for the single-particle energies $\epsilon_0 = -\mu_0 - 2t_0$ and $\epsilon_\pi = -\mu_0 + 2t_0$, we find $\mathcal{Q} = \text{sign}(\mu_0^2 - 4t_0^2)$ which yields $\mathcal{Q} = +1$ for $|\mu_0| > 2t_0$ and $\mathcal{Q} = -1$ for $|\mu_0| < 2t_0$. Thus, we find that the one-dimensional spinless p -wave superconductor has two topologically distinct phases which are both characterized by the same superconducting order parameter Δ_0 . For $|\mu_0| > 2t_0$, the superconductor is in the trivial phase which is topologically equivalent to the vacuum. This equivalence becomes immediately clear when considering the limit $\mu_0 \rightarrow -\infty$, in which the system becomes fully depleted, and in the limit $\mu_0 \rightarrow +\infty$, in which the system becomes fully occupied. However, for $|\mu_0| < 2t_0$ the situation is different. Here, we find a topological number $\mathcal{Q} = -1$ and therefore, the superconducting state cannot be continuously transformed into the vacuum state without closing the energy gap. Equivalently, we could argue that in this case, the Hamiltonian Eq. (2.2.3) cannot be continuously transformed into the vacuum Hamiltonian $|\mu_0| \sum c_x^\dagger c_x$ without closing the energy gap.

So far, we have shown that the spinless superconductor with periodic boundary conditions shows two phases which can be distinguished by the topological number \mathcal{Q} . Except for the topological number, both systems show a superconducting gap characterized by Δ_0 , and so far, we have not seen a way to experimentally distinguish between the two phases. For that purpose, we now consider a finite chain with open boundary conditions. It will be instructive to consider two special limits. As illustrated in figure 2.2.3(a), for $\Delta_0 = t_0 = 0$ the Hamiltonian is just a sum over local chemical potentials and the ground state is the completely empty (filled) wave function for $\mu_0 < 0$ ($\mu_0 > 0$). Obviously, this describes the trivial phase which was characterized by the topological invariant $\mathcal{Q} = +1$ in the last paragraph.

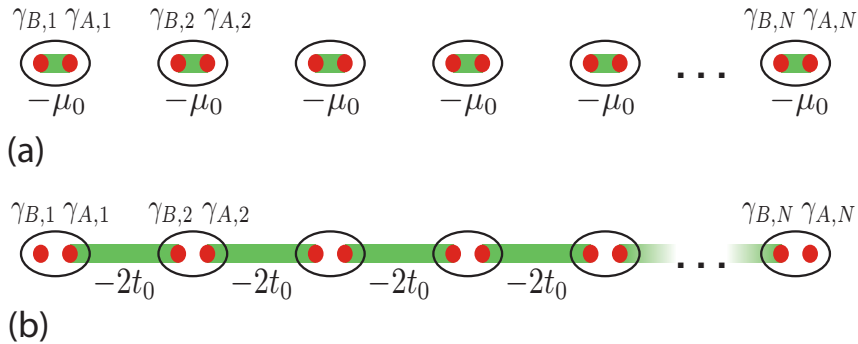


Figure 2.2.3.: Illustration of the Hamiltonian Eq. (2.2.1) and the ground state (a) for $\mu_0 \neq 0$ and $\Delta_0 = t_0 = 0$, and (b) for $\mu_0 = 0$ and $\Delta_0 = t_0$. The green bonds describe pairs of Majorana fermions which form a finite energy quasiparticle. Note that in (b), there are two uncoupled Majorana operators $\gamma_{B,1}$ and $\gamma_{A,N}$ which give rise to a zero-energy quasiparticle state.

To understand the physics of the topologically nontrivial phase more easily, we consider the special limit $\Delta_0 = t_0 > 0$ and $\mu_0 = 0$. To diagonalize Hamiltonian Eq. (2.2.1), we decompose the fermion operators into a sum of Majorana operators [76],

$$c_x^\dagger = \frac{1}{2}(\gamma_{A,x} + i\gamma_{B,x}), \quad (2.2.9a)$$

$$c_x = \frac{1}{2}(\gamma_{A,x} - i\gamma_{B,x}). \quad (2.2.9b)$$

This decomposition can be understood as decomposition of a complex Dirac fermion into real and imaginary parts which correspond to Majorana fermions. The Majorana operators can be obtained by inverting the transformation, i.e.,

$$\gamma_{A,x} = c_x^\dagger + c_x, \quad \gamma_{B,x} = \frac{c_x^\dagger - c_x}{i}. \quad (2.2.10)$$

Hence, it can be easily seen that the γ operators are Hermitian and satisfy the Majorana anti-commutation relations $\{\gamma_i, \gamma_j\} = 2\delta_{ij}$ for $i, j \in \{(Ax), (Bx)|x \in \{1, \dots, N\}\}$. Using the definitions Eqs. (2.2.9), we rewrite Hamiltonian H_K as

$$H_K = it_0 \sum_{x=1}^{N-1} \gamma_{A,x} \gamma_{B,x+1}, \quad (2.2.11)$$

where only Majorana operators on adjacent lattice sites are coupled and form bonds between (A, x) and $(B, x+1)$ as sketched in figure 2.2.3(b). However, we note that the operators $\gamma_{B,1}$ and $\gamma_{A,N}$ are not coupled to any Majorana operator and thus commute with the Hamiltonian.

In the next step, it is useful to define new fermion operators d_x and d_x^\dagger by

$$\gamma_{A,x} = d_x + d_x^\dagger, \quad (2.2.12a)$$

$$\gamma_{B,x+1} = \frac{d_x - d_x^\dagger}{i} \quad (2.2.12b)$$

for $1 \leq i \leq N-1$. The fermion operators d_x are defined on the bond between two adjacent lattice sites and satisfy fermionic anti-commutation relations. In addition, we define another fermion operator $f = (\gamma_{A,N} + i\gamma_{B,1})/2$ which yields

$$\gamma_{A,N} = f + f^\dagger, \quad (2.2.13a)$$

$$\gamma_{B,1} = \frac{f - f^\dagger}{i}. \quad (2.2.13b)$$

This fermion operator describes a highly nonlocal state since $\gamma_{B,1}$ and $\gamma_{A,N}$ are localized at opposite ends of the chain. With these definitions, we finally rewrite the Hamiltonian

$$H_K = 2t_0 \sum_{x=1}^{N-1} d_x^\dagger d_x - t_0(N-1), \quad (2.2.14)$$

with the ground-state energy $E_0 = -t_0(N-1)$. Hence, it is obvious that the ground state $|\psi_{GS}\rangle$ is characterized by the empty single-particle states $d_x|\psi_{GS}\rangle = 0$ and the d_x correspond to the Bogoliubov quasiparticle annihilation operators. However, since the fermion operator f is absent from Hamiltonian Eq. (2.2.14) occupying the corresponding quasiparticle state requires zero excitation energy. As a consequence, the ground state is two-fold degenerate and the corresponding wave functions can be distinguished by the occupancy of the f -fermion. As discussed above in Eq. (2.1.12), the two ground states are given by $|\psi_1\rangle$ and $|\psi_2\rangle = f^\dagger|\psi_1\rangle$ with $\langle\psi_1|f^\dagger f|\psi_1\rangle = 0$ and $\langle\psi_2|f^\dagger f|\psi_2\rangle = 1$. This behavior is very different from conventional gapped superconductors, where there exists a unique ground state with even parity such that all electrons form Cooper pairs.

In the more general case $|\mu_0| < 2t_0$ and Δ_0 arbitrary, the Majorana bound states are no longer simply given by $\gamma_{A,N}$ and $\gamma_{B,1}$ but decay exponentially into the bulk of the chain. The physically relevant parameter regime $|\Delta_0| \ll t_0$ is characterized by a superconducting gap which is typically much smaller than the width $4t_0$ of the electronic bands. In this limit, the Majorana wave functions decay exponentially on the length scale of the superconducting coherence length ξ . Here, ξ is given by the ratio of Fermi velocity $v_F = \partial\epsilon_k/\partial k(\epsilon_k = 0)$ and quasiparticle gap E_G . Consequently, this yields for the Kitaev model $\xi = v_F/\Delta = 2t_0/\Delta_0$ in units of the lattice distance. The overlap of the Majorana wave functions results in an exponentially small energy splitting ϵ_M between the states $|\psi_1\rangle$ and $|\psi_2\rangle$. However, if the nanowire becomes much longer than the superconducting coherence length, the splitting becomes so small that the states $|\psi_1\rangle$ and $|\psi_2\rangle$ are quasi-degenerate for all temperatures which are relevant for experiments and possible applications.

2.3. Two-dimensional topological superconductor

Aside from the special choice of parameters $t_0 = \Delta_0$ and $\mu_0 = 0$, it is difficult to investigate the Kitaev model Eq. (2.2.1) analytically. For arbitrary parameters, the decomposition of the Hamiltonian into a sum over bonds between adjacent lattice sites is not possible and diagonalizing the Hamiltonian requires the diagonalization of the $N \times N$ matrix \mathcal{H}_{BdG} . However, in many cases it is easier to study differential equations instead of large systems

of algebraic equations.

In this section we consider the continuum limit of the model introduced in the last section and in addition, we extend the system into two spatial dimensions. To derive the continuum model from the tight-binding Hamiltonian H_K , we consider the case that the wave functions change slightly on the length scale of the lattice constant a . For realistic semiconductor systems this assumption is justified since the lattice constant is the distance between atoms, and the Fermi wavelength λ_F is typically at least one order of magnitude larger than the distance between the atoms. For the tight-binding dispersion relation $\epsilon_k = -2t_0 \cos(ka) - \mu_0$, this condition is satisfied if $\mu_0 \approx -2t_0$, i.e., if the number of electrons in the system is small compared to the number of lattice sites.

In this low-density limit, we approximate the lattice fermion operators c_x by electron field operators $\psi(x)$ with the continuous space-variable x . Henceforth, we replace the fermion anti-commutation relations for the lattice operators by the anti-commutation relations for the field operators

$$\{\psi(x), \psi^\dagger(x')\} = \delta(x - x') \quad (2.3.1)$$

and

$$\{\psi(x), \psi(x')\} = 0, \quad (2.3.2)$$

and we approximate the sum over lattice sites by an integral $\sum_x \approx \int dx/a$. Moreover, we expand all nearest-neighbor terms in powers of $a \ll \lambda_F$ and keep the lowest nonvanishing powers only,

$$\begin{aligned} c_x^\dagger c_{x+a} &\approx a\psi^\dagger(x)\psi(x+a) \\ &\approx a\psi^\dagger(x)\left(\psi(x) + a\frac{\partial}{\partial x}\psi(x) + \frac{a^2}{2}\frac{\partial^2}{\partial x^2}\psi(x)\right), \end{aligned} \quad (2.3.3a)$$

$$c_x^\dagger c_{x+a}^\dagger \approx a\psi^\dagger(x)\psi^\dagger(x+a) \approx a\psi^\dagger(x)\left(\psi^\dagger(x) + \frac{\partial}{\partial x}\psi^\dagger(x)\right). \quad (2.3.3b)$$

Here, the appearance of the lattice distance a as prefactor is necessary for dimensional reasons, since the field operators have units $1/\sqrt{a}$ and the operators in the lattice model are dimensionless. Applying these replacements to the individual terms in the lattice Hamiltonian Eq. (2.2.1), we find

$$c_x^\dagger c_x \approx a\psi^\dagger(x)\psi(x), \quad (2.3.4a)$$

$$c_x^\dagger c_{x+a} + c_x^\dagger c_{x-a} \approx a^3\psi^\dagger(x)\frac{\partial^2}{\partial x^2}\psi(x) + 2a\psi^\dagger(x)\psi(x), \quad (2.3.4b)$$

$$c_x^\dagger c_{x+a}^\dagger \approx a^2\psi^\dagger(x)\frac{\partial}{\partial x}\psi^\dagger(x). \quad (2.3.4c)$$

This yields the one-dimensional continuum Hamilton operator for spinless fermions with p -wave superconducting pairing,

$$H_{1D} = \int dx \psi^\dagger(x) \left(-\frac{\hbar^2}{2m^*} \frac{\partial^2}{\partial x^2} - \mu \right) \psi(x) + \int dx \left\{ \Delta \psi^\dagger(x) \frac{\partial}{\partial x} \psi(x) + \Delta^* \left(\frac{\partial}{\partial x} \psi(x) \right) \psi(x) \right\}, \quad (2.3.5)$$

where $m^* = \hbar^2/2a^2t_0$, $\Delta = a\Delta_0$, and $\mu = \mu_0 + 2t_0$. The first line in Eq. (2.3.5) is the usual Hamiltonian for a one-dimensional spinless electron gas with effective mass m^* and Fermi energy μ . The second line describes the p -wave pairing with superconducting order parameter Δ . The p -wave symmetry can be easily seen if one Fourier transforms the Hamiltonian and therefore replaces the first derivative terms by linear momentum terms which are odd under $k \rightarrow -k$.

In the following, we extend this model by adding the y direction to the Hamiltonian. We assume that the kinetic energy of the electrons in the x - y plane is isotropic, i.e., the effective mass m^* is the same for x and y directions, and we assume that the pairing potential also has p -wave symmetry in y direction with the same order parameter Δ as for the x direction but with a phase shift of $\pi/2$. With these assumptions, we write the Hamiltonian for spinless fermions with $p_x + ip_y$ pairing symmetry in the convenient form

$$H_{2D} = \int d^2r \psi^\dagger(\mathbf{r}) \left(-\frac{\hbar^2}{2m^*} \frac{\partial^2}{\partial \mathbf{r}^2} - \mu \right) \psi(\mathbf{r}) + \int d^2r \left\{ \Delta \psi^\dagger(\mathbf{r}) \left(\frac{\partial}{\partial x} + i \frac{\partial}{\partial y} \right) \psi(\mathbf{r}) + \Delta^* \left[\left(\frac{\partial}{\partial x} - i \frac{\partial}{\partial y} \right) \psi(\mathbf{r}) \right] \psi(\mathbf{r}) \right\}. \quad (2.3.6)$$

The topological number \mathcal{Q} for the infinitely large one-dimensional (two-dimensional) system described by Eq. (2.3.5) (Eq. (2.3.6)) can again be determined by Fourier transforming the Hamiltonian and applying Eq. (2.1.14). Simplifying the expression for \mathcal{Q} consequently, we find that the parity is entirely determined by the quasiparticle energy at zero momentum. This yields the final result $\mathcal{Q} = -\text{sign}(\mu)$. In the context of the continuum model, the topologically nontrivial phase for $\mu > 0$ is usually called *weak pairing phase* and the topologically trivial phase for $\mu < 0$ is called *strong pairing phase* [19].

2.4. Ground-state degeneracy on nontrivial manifolds

Topological phases are quantum phases which cannot be described by the Ginzburg-Landau theory with a local order parameter. Instead, the defining order of topological phases is a

pattern of long-range quantum entanglement which is called topological order [93–95]. One characteristic property of a topologically ordered state is the dependence of the ground-state degeneracy on the topology of the manifold on which the system is defined [96]. This degeneracy on manifolds might also serve as a starting point for a general classification of topological phases of strongly correlated quantum matter, in contrast to the topological band theory which is only applicable to noninteracting systems [11, 31, 98, 99]. In this section we investigate the degeneracy of the two-dimensional spinless $p_x + ip_y$ superconductor Eq. (2.3.6) on the torus and discuss differences to the findings for conventional s -wave superconductors [19, 96].

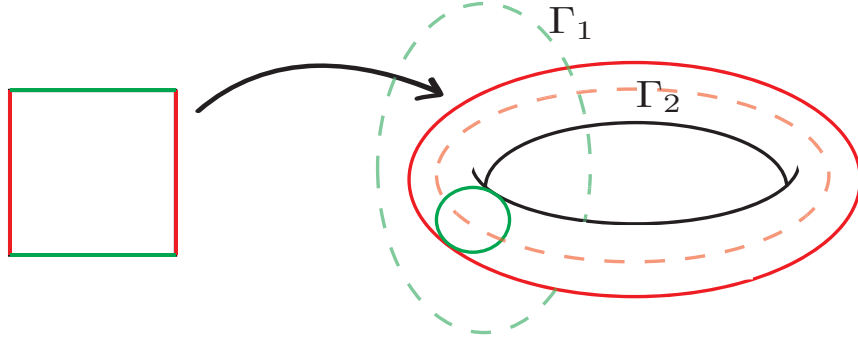


Figure 2.4.1.: Illustration of the bijective mapping from a square with periodic boundary conditions onto the torus. Under this mapping, both green (red) lines are mapped onto one of the fundamental circles on the torus. The loops Γ_1 and Γ_2 describe the two holes piercing the torus and are identified with magnetic flux lines 0 or $\Phi_{1/2} = h/2e$.

Before discussing superconducting systems on the torus, we briefly discuss some properties of the torus and its relation to squares. It can be shown that a torus is topologically equivalent to a unit-square with periodic boundary conditions in both x and y direction. The bijective map from the unit square to the torus embedded into a three-dimensional space can be easily written down as

$$\begin{pmatrix} x \\ y \end{pmatrix} \mapsto \begin{pmatrix} (R + r \cos(2\pi x)) \cos(2\pi y) \\ (R + r \cos(2\pi x)) \sin(2\pi y) \\ r \sin(2\pi y) \end{pmatrix}, \quad (2.4.1)$$

where R denotes the major radius and $r \ll R$ denotes the minor radius of the torus as depicted in figure 2.4.1. Hence, instead of considering Hamiltonian H_{2D} on the torus, it is sufficient to consider the system on a square with periodic boundary conditions. In addition, we may imagine that either zero magnetic flux or half of a magnetic flux quantum $\Phi_{1/2} = h/2e$ threads either of the two fundamental cycles Γ_1 or Γ_2 in the torus. The effect of

the magnetic flux $\Phi_{1/2}$ is the multiplication of the wave function by $\exp(2\pi i e \Phi_{1/2}/h) = -1$ if a particle of charge e encircles the magnetic flux once. Hence, we can represent the magnetic flux $\Phi_{1/2}$ through one of the fundamental cycles either by a vector potential and periodic boundary conditions, or by no vector potential and an antiperiodic boundary condition. These two choices are related by a gauge transformation and thus are fully equivalent. In our analysis, we choose to incorporate the magnetic flux via changing the boundary conditions along the two fundamental cycles. Hence, we identify the four magnetic flux configurations on the torus with boundary conditions on the square,

$$\{(0, 0), (0, \Phi_{1/2}), (\Phi_{1/2}, 0), (\Phi_{1/2}, \Phi_{1/2})\} \equiv \{(++), (+-), (-+), (--)\}, \quad (2.4.2)$$

where the $+$ ($-$) refers to (anti-) periodic boundary conditions along the respective direction on the square. For each of the four boundary conditions, the allowed values for the momenta $\mathbf{k} = (k_x, k_y)$ run over the usual sets, $k_i = 2\pi n_i$ for $+$ and $k_i = 2\pi(n_i + 1/2)$ for $-$, where $n_i \in \mathbb{Z}$ and $i = x, y$. In particular, the special momentum $\mathbf{k} = (0, 0)$ is a member of the set of allowed momenta only in the case $++$.

In the following, we consider a superconducting system on the torus with a nonvanishing quasiparticle excitation gap above the ground state. As elementary low-energy excitations, the superconductor has Bogoliubov quasiparticles and vortices with magnetic flux $\Phi_{1/2}$. We introduce the process \mathcal{B}_i ($i = x, y$) which creates a vortex-antivortex pair, followed by the vortex encircling the torus in i direction and finally the pair annihilation. We may imagine the vortex and the antivortex as the two points where a closed $h/2e$ magnetic flux tube pierces the torus. Under the process \mathcal{B}_i , we create such a closed flux tube, move one of the punctures around the torus, and thereby deform the flux tube. Finally, the vortex-antivortex pair is annihilated which can be understood by smoothly fusing the punctures. However, this leaves a closed flux tube through one of the holes of the torus which cannot be smoothly contracted to a point without crossing the torus and thereby creating new vortices. Therefore, the process \mathcal{B}_i introduces a magnetic flux $\Phi_{1/2}$ into the hole of the torus which is not encircled by the vortex. Consequently, we may identify \mathcal{B}_i with an operator which changes the boundary condition $+\leftrightarrow-$ for the other cycle \bar{i} .

Before discussing the spinless $p_x + ip_y$ superconductor, we consider the conventional s -wave superconductor which has two electronic bands, one for each spin direction and the pairing is between electrons with (\mathbf{k}, \uparrow) and $(-\mathbf{k}, \downarrow)$. In particular, for $++$ boundary conditions the electrons with $(\mathbf{0}, \uparrow)$ and $(\mathbf{0}, \downarrow)$ pair. As a consequence of the two spin bands, the ground-state wave function is a product over all pairs (\mathbf{k}, \uparrow) and $(-\mathbf{k}, \downarrow)$, and in particular, for the parity of the ground state it is irrelevant whether the $\mathbf{k} = \mathbf{0}$ state is one

of the allowed momenta or not. Thus, all four combinations of boundary conditions are characterized by a wave function with even parity corresponding to $\mathcal{Q} = +1$. In addition, the above introduced operators \mathcal{B}_x and \mathcal{B}_y allow to change the boundary conditions and thus, they transform the different ground states into each other. We conclude that the ordinary s -wave superconductor shows a four-fold degeneracy of the ground state on the torus [97].

In contrast, for the $p_x + ip_y$ superconductor the situation is richer. Depending on the chemical potential, the ground state of the $p_x + ip_y$ superconductor is realized by the weak or the strong pairing phase. Here, aside from the unpaired state $\mathbf{k} = \mathbf{0}$ all states \mathbf{k} and $-\mathbf{k}$ are paired. In the strong pairing phase $\mu < 0$, the single-particle state corresponding to the momentum $\mathbf{k} = \mathbf{0}$ is unoccupied and hence, all four combinations of boundary conditions are characterized by a wave function, which contains only pairs \mathbf{k} and $-\mathbf{k}$, with even parity similarly to the conventional s -wave superconductor. As a consequence, the strong pairing phase possesses the same four-fold degeneracy as the ordinary s -wave superconductor and the operators \mathcal{B}_i transform between the different ground states.

In contrast, the ground state of the weak pairing phase on the torus depends on boundary conditions for each of the two primitive directions. Here, the ground state with only periodic boundary conditions is special and shows an odd parity since all momenta \mathbf{k} and $-\mathbf{k}$ are paired except for $\mathbf{k} = \mathbf{0}$ where a single electron resides. In contrast, the three ground states with at least one antiperiodic boundary condition are described by an even parity since there, the momentum $\mathbf{k} = \mathbf{0}$ does not correspond to a single-particle eigenstate. The operators \mathcal{B}_i now behave very different as compared to the trivial superconductor. If we apply the operators to the ground state $|- - \rangle$ for antiperiodic boundary conditions in both directions, we find a new ground state

$$\mathcal{B}_x |- - \rangle = |- + \rangle, \quad (2.4.3a)$$

$$\mathcal{B}_y |- - \rangle = |+ - \rangle. \quad (2.4.3b)$$

However, the consecutive application of both operators $\mathcal{B}_y \mathcal{B}_x |- - \rangle$ is *blocked* because applying \mathcal{B}_x changes the boundary condition in y direction and then \mathcal{B}_y would no longer give a new ground state since $\mathcal{Q}(++) \neq \mathcal{Q}(-+)$. Instead, the final state would be an excited state which contains a Bogoliubov quasiparticle above the superconducting gap. As a consequence the vortex/antivortex pair is blocked from the pair annihilation and hence the consecutive operation $\mathcal{B}_y \mathcal{B}_x$ is not a mapping from the ground-state space into itself [96].

We conclude that there are in total four ground states, three for boundary conditions

$+-$, $-+$, $--$ which are linear combinations of states with even values of the fermion number in both phases, and for $++$ boundary conditions the ground state has odd (even) fermion number for $\mu > 0$ ($\mu < 0$).

2.5. Semiconductor-superconductor hybrid systems

While superconductors with $p_x + ip_y$ pairing symmetry have been investigated theoretically for a long time, so far, it is not clear whether there is a realization in nature. Candidate materials for systems with $p_x + ip_y$ pairing symmetry are the Pfaffian quantum Hall state at filling fraction $\nu = 5/2$ [19], superfluid $^3\text{He A}$ [18], and Sr_2RuO_4 [29]. However, experiments on the systems are all highly complicated and despite intensive experimental work, direct signatures of topological superconductivity and of Majorana fermions remain elusive. In recent years, a series of theoretical works established that one can engineer the topological superconductor in more conventional materials. The common ingredient in these proposals is the use of semiconducting materials with strong spin-orbit coupling and proximity coupling to an ordinary s -wave superconductor. These proposals are based on two material classes: (i) topological insulator materials with protected surface Dirac fermion states [31, 38] and (ii) semiconducting quantum wires with strong Rashba spin-orbit coupling and induced magnetization [32–36]. In the following, we only discuss the second type of proposals of a semiconducting quantum wire, however, the physics is very similar for the Dirac surface states of topological insulators.

In figure 2.5.1(a), we illustrate the basic setup required to engineer a spinless $p_x + ip_y$ Hamiltonian [32–36]. We consider a one-dimensional semiconductor nanowire aligned along the x direction with strong Rashba spin-orbit coupling with spin in the y direction. We assume that this nanowire is deposited on an s -wave superconductor and that a magnetic field is pointing in z direction. We model this system by the Hamiltonian $H = H_{\text{SM}} + H_{\text{SC}}$ with the normal state Hamiltonian

$$H_{\text{SM}} = \int dx \sum_{\sigma, \sigma'} \psi_{\sigma}^{\dagger}(x) \left(-\frac{\hbar^2}{2m^*} \frac{\partial^2}{\partial x^2} \sigma_0 - \mu \sigma_0 - i\alpha \hbar \frac{\partial}{\partial x} \sigma_y + E_Z \sigma_z \right) \psi_{\sigma'}(x) \quad (2.5.1)$$

and the superconducting proximity Hamiltonian

$$H_{\text{SC}} = \int dx \left(\Delta \psi_{\uparrow}(x) \psi_{\downarrow}(x) + \Delta^* \psi_{\downarrow}^{\dagger}(x) \psi_{\uparrow}^{\dagger}(x) \right). \quad (2.5.2)$$

Here, Hamiltonian H_{SM} contains four terms: the kinetic energy of free electrons with effective mass m^* , the chemical potential μ , which determines the filling of the nanowire,

the Rashba spin-orbit velocity α , and the Zeeman energy $E_Z = g\mu_B B/2$. The matrices σ_y and σ_z denote the 2×2 Pauli spin matrices and σ_0 the corresponding identity matrix. The operator $\psi_\sigma^\dagger(x)$ ($\psi_\sigma(x)$) creates (annihilates) a fermion with spin σ at position x . The Hamiltonian H_{SC} describes the spin-singlet pairing between electrons in the nanowire with proximity induced pairing potential Δ . If the interface between the nanowire and the superconductor is good enough Cooper pairs tunnel between these two systems with the effect that electrons in the nanowire feel an effective pairing potential.

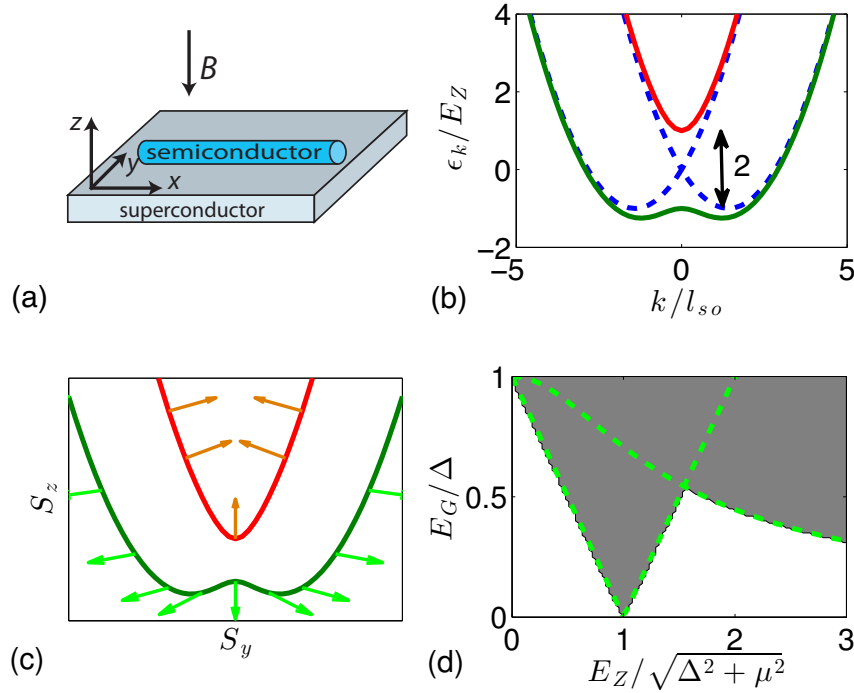


Figure 2.5.1.: (a) Schematic sketch of the semiconductor-superconductor heterostructure. A semiconductor nanowire with strong spin-orbit coupling is proximity coupled to an s -wave superconductor which itself is located in the x - y plane. A magnetic field is applied in z direction. (b) Dispersion relation of Hamiltonian H_{SM} for finite Zeeman energy (solid lines) and vanishing Zeeman energy (dashed lines). The Zeeman energy E_Z opens a spin gap $2E_Z$ at zero momentum. (c) Expectation value of the spin operator for the two energy bands for $E_Z > 0$ and $\alpha < 0$. (d) Quasi-particle excitation spectrum as function of Zeeman energy. The grey area is the continuum of quasiparticle states bounded from below by the quasiparticle gap. The dashed lines denote the energy gap at zero momentum and at the finite Fermi momentum k_F .

Let us first consider the case $\Delta = 0$ and investigate the Hamiltonian H_{SM} which describes the normal state of the nanowire. As above, we consider a translationally invariant system

and Fourier transform the fermionic field operators $\psi_\sigma(x)$ which yields

$$H_{\text{SM}} = \int \frac{dk}{2\pi} \sum_{\sigma, \sigma'} \psi_{k\sigma}^\dagger \left(\frac{\hbar^2 k^2}{2m^*} \sigma_0 - \mu \sigma_0 + \alpha \hbar k \sigma_y + E_Z \sigma_z \right)_{\sigma\sigma'} \psi_{k\sigma'}. \quad (2.5.3)$$

Hence, we find two electronic bands with the dispersion relations

$$\epsilon_\pm(k) = \frac{\hbar^2 k^2}{2m^*} - \mu \pm \sqrt{E_Z^2 + (\alpha \hbar k)^2}, \quad (2.5.4)$$

which are shown in figure 2.5.1(b). The effect of spin-orbit coupling on the parabolic dispersion of the electron gas is a shift with respect to the origin by the momenta $\delta k_\pm = \pm m^* \alpha / \hbar$ and by the energy $\delta E = m^* \alpha^2 / 2$. This creates two electronic bands which cross at $k = 0$ [see figure 2.5.1(b)] and the spin of the two electronic bands is aligned along $\pm y$. Switching on a magnetic field now tilts the spins into z direction and thereby opens a spin gap $2E_Z$ at $k = 0$ which separates the two bands. For $|\mu| > E_Z$, there are four Fermi points which gives rise to a topologically trivial superconducting state. In contrast, when the Fermi level resides within the spin gap at zero momentum, i.e., $|\mu| < E_Z$, the number of Fermi points is two and the nanowire appears to be *spinless* in the sense that just a single electronic band is partially occupied.

In order to understand the effect of the superconducting proximity effect, we first consider the spin structure of the lower electronic band. In figure 2.5.1(c), we sketch the spin orientation of the electron wave function as function of momentum for $\alpha < 0$. The situation for $\alpha > 0$ is equivalent with inverted y direction of the spin operator, i.e., $S_y \rightarrow -S_y$. For positive momenta, the spins of the lower band are pointing in y direction since for large momenta the spin-orbit term, which is linear in k , dominates over the Zeeman energy. This connection between the spin and the momentum direction is called helicity. In the limit $k \rightarrow 0$, the spin direction rotates in $-z$ direction and for $k = 0$, the spins of the lower band are perfectly aligned in $-z$ direction. For negative momenta, the situation is now complementary as for positive momenta but with $y \rightarrow -y$ spin direction. As a consequence, despite the existence of an applied magnetic field, the states within the same electronic band and with finite momentum k and $-k$ have a nonvanishing antiparallel component which allows for s -wave pairing between the states of the lower electronic band. Similarly, we find a nonvanishing antiparallel spin component for the upper helical band.

In the following, we consider the situation of a nonzero pairing amplitude $\Delta \neq 0$. Diagonalizing the Hamiltonian using a Bogoliubov transformation, we find the quasiparticle energies [35] by solving the corresponding 4×4 Bogoliubov-de Gennes equations. We find

the energies

$$E_{k,\pm} = \sqrt{(\alpha\hbar k)^2 + \xi_k^2 + E_Z^2 + \Delta^2 \pm 2\sqrt{\xi_k^2(\alpha\hbar k)^2 + \xi_k^2 E_Z^2 + E_Z^2 \Delta^2}} \quad (2.5.5)$$

with $\xi_k = \hbar^2 k^2 / 2m^* - \mu$. The superconducting pairing modifies the energy spectrum in a crucial way. In figure 2.5.1(d), we display the quasiparticle energies for fixed chemical potential and fixed pairing amplitude as function of E_Z . Evaluating Eq. (2.5.5) at $k = 0$ we find

$$E_{0,-} = |E_Z - \sqrt{\Delta^2 + \mu^2}| \quad (2.5.6)$$

which vanishes for $E_Z^2 = \Delta^2 + \mu^2$. For $E_Z = 0$, the system is an ordinary s -wave superconductor with spin-orbit coupling and the superconducting gap at all four Fermi points $(\pm 0, \pm 2m^*\alpha/\hbar)$. Switching on the Zeeman field and considering the limit $E_Z \rightarrow \sqrt{\Delta^2 + \mu^2}$, we find the closing of the excitation gap at $k = 0$ while the gap at the finite-momentum Fermi points does not change qualitatively. For $E_Z > \sqrt{\Delta^2 + \mu^2}$, the quasiparticle gap at $k = 0$ opens again. With further increasing Zeeman field, the quasiparticle gap is determined by the finite momentum Fermi points and decreases like $\Delta\alpha\hbar k_F/E_Z$ due to the alignment of the spins in the lower helical band and the reduction of the antiparallel spin components. The closing of the excitation gap for $E_Z^2 = \Delta^2 + \mu^2$ is crucial for the topological properties of the semiconductor nanowire. If we determine the topological number \mathcal{Q} using Eq. (2.1.14), we find

$$\mathcal{Q} = \text{sign}(\mu^2 + \Delta^2 - E_Z^2). \quad (2.5.7)$$

Hence, we conclude that the closing and reopening of the excitation gap is intricately related to a change of the ground-state parity and therefore to a topological phase transition between a trivial and a nontrivial superconducting phase similarly to the situation in section 2.2. Therefore, we find that Eq. (2.5.7) yields the necessary condition

$$E_Z^2 > \Delta^2 + \mu^2 \quad (2.5.8)$$

for the existence of the topological phase in spin-orbit coupled systems.

In the following, we show that in the topological phase the semiconductor nanowire can be mapped isomorphically onto the one-dimensional spinless superconductor Hamiltonian Eq. (2.3.5) by projecting H_{SC} onto the lower helical band $\epsilon_{-,k}$ [33, 34]. We consider this mapping in the limit $|\mu|, |\Delta| \ll E_Z$ far away from the topological phase transition. We approximate the spinful electron operators by the fermion operators χ_k for the lower helical

band,

$$\begin{pmatrix} \psi_{k\uparrow} \\ \psi_{k\downarrow} \end{pmatrix} \approx \frac{1}{\sqrt{2}} \begin{pmatrix} \frac{k}{|k|} \sqrt{1 - \frac{E_Z}{\sqrt{E_Z^2 + (\alpha\hbar k)^2}}} \\ \sqrt{1 + \frac{E_Z}{\sqrt{E_Z^2 + (\alpha\hbar k)^2}}} \end{pmatrix} \chi_k. \quad (2.5.9)$$

In the next step, we rewrite the superconducting pairing H_{SC} in terms of the fermion operators χ_k for the lower helical band

$$H_{\text{SC}} \approx \sum_k \left\{ \Delta \frac{\alpha\hbar k}{2\sqrt{E_Z^2 + (\alpha\hbar k)^2}} \chi_{-k} \chi_k + \Delta^* \frac{\alpha\hbar k}{2\sqrt{E_Z^2 + (\alpha\hbar k)^2}} \chi_k^\dagger \chi_{-k}^\dagger \right\}, \quad (2.5.10)$$

which is nonzero for finite spin-orbit coupling. Hence, in the limit $|\mu|, |\Delta| \ll E_Z$, the semiconductor nanowire is described by a one-dimensional spinless superconductor with the effective electronic band structure

$$\epsilon_p(k) = \frac{\hbar^2 k^2}{2m^*} - \mu - \sqrt{(\alpha\hbar k)^2 + E_Z^2} \quad (2.5.11)$$

and with the effective p -wave superconducting potential

$$\Delta_p(k) = \Delta \frac{\alpha}{2\sqrt{E_Z^2 + (\alpha\hbar k)^2}}. \quad (2.5.12)$$

If we further assume that $m^* \alpha^2 \ll E_Z$, we approximate the denominator in Eq. (2.5.12) by $2E_Z$. As a consequence, we find the effective parameters for the spinless superconductor $m_p = m^*$, $\mu_p = -E_Z$, and $\Delta_p = \Delta\alpha/2E_Z$ [36].

3. Transport signatures of Majorana bound states coupled to quantum dots

In the introductory chapter we have argued that the defining properties of Majorana bound states are zero excitation energy and non-abelian braiding statistics. Obviously, the ultimate proof for the existence of Majorana bound states would be the demonstration of non-abelian statistics by using them to build a topological quantum computer. However, experimentally this has not yet been realized and the high level of difficulty makes it unlikely that the topological quantum computer will be realized in the near future. Therefore, a legitimate goal is to study other consequences of Majorana bound states and to show that these interesting and relevant consequences can be clearly distinguished from the situation without Majoranas. While recent experiments show evidence for the zero-energy nature of Majorana bound states in the form of a zero-voltage anomaly in the differential conductance in semiconductor-superconductor heterostructures [55–58], it has been demonstrated in a series of theoretical works [59–62] that such a feature is not an unambiguous proof for Majorana bound states and might also result from more conventional mechanisms.

In this chapter we identify signatures in nonlocal charge transport which we believe are more specific of the Majorana nature than the zero-voltage conductance studied in recent tunneling experiments. Due to the finite length of the topological superconductor nanowire, the Majorana bound states at the ends are tunnel coupled to each other and have an energy splitting $\epsilon_M \sim \Delta_{\text{eff}} \exp(-L/\xi) \sin(k_F L)$ [100, 101]. Here, ξ is the coherence length and Δ_{eff} the quasiparticle energy gap of the topological superconductor nanowire. The Majorana energy splitting depends in an oscillatory manner on the distance between the Majorana bound states with oscillation period $2\pi/k_F$. Since the Fermi momentum k_F depends on both chemical potential and magnetic field strength, the nonlocal transport, i.e. transport involving quantum mechanical tunneling between the two localized Majorana states, is expected to depend in an oscillatory manner on these parameters as well. This characteristic aspect of Majorana physics is absent in samples where the splitting is

suppressed due to the large distance between the Majorana bound states.

For a normal-state–Majorana bound state–normal-state device, it was shown theoretically that at sufficiently low voltages $eV < \epsilon_M$ and small level broadening $\Gamma \ll \epsilon_M$, crossed Andreev reflection by the pair of Majorana bound states is the dominating transport channel and gives rise to positive current cross-correlations and a crossed Fano factor of two [69, 70, 102–106]. Crossed Andreev reflection denotes the nonlocal conversion of an incoming electron into a hole excitation in a separate lead [107–109], in contrast to local Andreev reflection where electron and hole reside in the same lead. Crossed Andreev reflection is equivalent to Cooper pair splitting where a Cooper pair is converted into two electrons in spatially separated leads. Similarly, we can identify local Andreev reflection with the injection a Cooper pair in a single lead. The current cross-correlations mediated by crossed Andreev reflection are positive since the charge of the incoming and the charge of the outgoing particles are opposite. For $eV > \epsilon_M$, the current is dominated by local Andreev reflection and resonant tunneling of electrons and holes gives rise to negative current cross-correlations which exactly cancel the positive contributions from $eV < \epsilon_M$. As a consequence, the total current cross-correlations vanish in the limit $eV \gg \epsilon_M$.

Despite the theoretical prediction of positive current cross-correlations for $eV < \epsilon_M$, this setup is of limited use to experimentally probe cross-correlations. As shown in recent tunneling experiments [55–58], the differential conductance of semiconductor-superconductor heterostructures is characterized by a soft superconducting gap with a smooth subgap conductance whose origin is not yet fully understood but most likely related to interface effects between the superconductor and the normal-conducting lead [110]. As a consequence, the current fluctuations are also determined by these interface effects which makes it experimentally very difficult to detect current cross-correlations. In addition, we note that the positive cross-correlations and especially the crossed Fano factor of two are difficult to detect experimentally because for $eV < \epsilon_M$, the current mediated by the Majorana bound states is nonresonant and thus suppressed. However, when approaching the resonance for $eV \rightarrow \epsilon_M$, the negative cross-correlations due to fermionic statistics become important and thus the crossed Fano factor vanishes.

In this chapter we study the effect of quantum dots on the transport signatures of Majorana bound states. In particular, we focus on the physics of coupling a pair of Majorana bound states at the ends of a quasi one-dimensional topological superconductor nanowire to leads via quantum dots in the Coulomb blockade regime. Recent experiments on similar three-terminal systems with ordinary s -wave superconductors [71–73] have shown that quantum dots are suitable tools to generate Cooper pair splitting. In particular, quantum dots suppress local Andreev reflection and allow for Cooper pair splitting with large ef-

efficiency approaching 100% [73, 111]. In addition, coincidence measurements have shown positive current cross-correlation as expected for crossed Andreev processes [73]. Building on these observations, we investigate the effect of quantum dots on the differential conductance and on the current cross-correlations in topological superconductors. Here, the key role of the quantum dots is to stimulate an imbalance between the competing transport processes with the goal to perturb the fine-tuning between positive and negative current cross-correlations and thus to produce finite cross-correlations even for $eV \gg \epsilon_M$.

This chapter is organized as follows: In section 3.1, we introduce the proposed model system and the theoretical method. We continue in section 3.2 with the study of the differential conductance and current correlations in a simple normal-state–Majorana bound state–normal-state structure. In section 3.3, we investigate the energy spectrum and the charge transport in the two-terminal normal-state–quantum dot–Majorana bound state device. Then, we continue in section 3.4 by considering two quantum dots coupled to the Majorana bound states and compare the results to the simpler setup without quantum dots and with one quantum dot. In our numerical analysis, we concentrate on the semiconductor–superconductor heterostructure which we was introduced in chapter 2.5, however, our main results are more general and can also be applied to other (quasi) one-dimensional topological superconductor systems. Finally, we consider the case of interacting spinful quantum dots in section 3.5 and discuss the differences which originate from the spin degree of freedom. We summarize our results in section 3.6.

3.1. Model system and theoretical methods

3.1.1. Model system

As illustrated in figure 3.5.1, we investigate a three-terminal normal-state–quantum dot–nanowire–quantum dot–normal-state device. In this section, we introduce the model for the closed quantum dot–nanowire–quantum dot system without the coupling to the electron reservoirs. We consider the Hamiltonians

$$H_M = \frac{\epsilon_M}{2} i\gamma_L \gamma_R, \quad (3.1.1a)$$

$$H_D = \sum_{i=L,R} \left\{ \epsilon_i d_i^\dagger d_i + t_i^* d_i^\dagger \gamma_i + t_i \gamma_i d_i \right\}, \quad (3.1.1b)$$

$$H_S = \Delta^* d_L^\dagger d_R^\dagger + \Delta d_R d_L. \quad (3.1.1c)$$

Here, H_M describes two Majorana bound states with an energy splitting (tunnel coupling) ϵ_M . The Majorana bound states are described by Hermitian operators $\gamma_i = \gamma_i^\dagger$ which satisfy the anti-commutation relations $\{\gamma_i, \gamma_j\} = 2\delta_{ij}$. The Majorana operators can be combined into a single fermion state described by the fermion operators $f^\dagger = (\gamma_L + i\gamma_R)/2$ and $f = (\gamma_L - i\gamma_R)/2$. The chemical potential of the superconductor nanowire hosting the Majorana bound state is zero. For the derivation of the Majorana energy splitting starting from a microscopic model of superconducting spinless fermions, we refer to Appendix B.2.

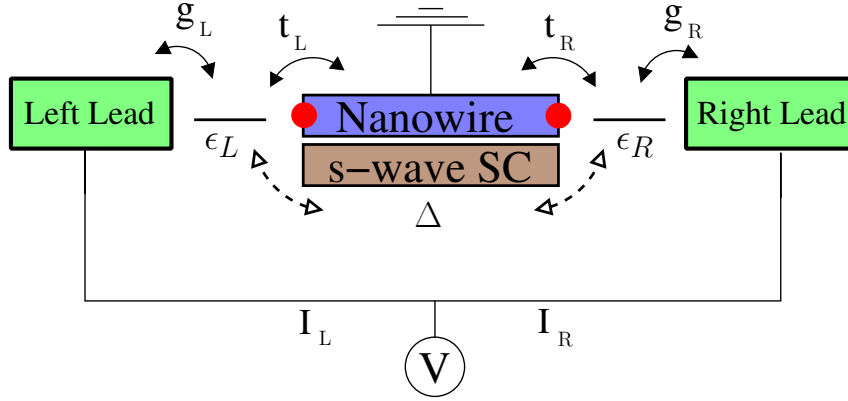


Figure 3.1.1.: Schematic setup for a system with a pair of Majorana bound states (red dots) coupled to quantum dots which themselves are coupled to lead electrodes. The leads are biased with the positive chemical potential eV . Crossed Andreev reflection can be detected by correlating the currents I_L and I_R that flow into the superconductor nanowire via Majorana bound states. The nearby s -wave superconductor also induces a proximity pairing Δ between the quantum dots.

Hamiltonian H_D describes two quantum dots and their coupling to the Majorana bound states, where d_i (d_i^\dagger) annihilates (creates) an electron with energy ϵ_i on quantum dot i . We consider the regime where the quantum dot single-particle level spacing $\delta\epsilon$ satisfies $\delta\epsilon > eV > k_B T$. We assume that the spin degeneracy is lifted by the Zeeman energy splitting, and that the ground state of the quantum dot has an even number of electrons. Then, Kondo physics is absent, and in the Coulomb blockade regime, it is justified to consider only a single quantum dot level in H_D . The quantum dot i is coupled to the Majorana bound state i with coupling strength t_i . As long as $\Delta \rightarrow 0$, we choose the tunneling matrix elements t_i to be real and positive. This choice is justified, since a complex phase $|t_i|e^{i\phi_i}$ can be removed by the local gauge transformation $d_i \rightarrow d_i e^{i\phi_i}$.

Hamiltonian H_S describes an additional proximity induced pairing between the quantum dots with an amplitude $\Delta \sim \rho_S \exp(-L/\xi_{SC}) \sin(k_F L)/(k_F L)$ [108], where ρ_S is the normal-state quantum dot level broadening due to the coupling between superconductor and quantum dot, k_F the Fermi momentum, L the length, and ξ_{SC} the coherence length

of the superconductor. We have in mind that the superconducting pairing term may mainly be due to a coupling between the quantum dots and the s -wave superconductor in a semiconductor-superconductor heterostructure. For the derivation of the induced pairing amplitude in a realistic system, we refer to Appendix B.3.

We diagonalize the Hamiltonian for the coupled Majorana bound state–quantum dot system by the Bogoliubov transformation

$$\alpha_\epsilon = \sum_{i=L,R} \left(\frac{u_i}{2} \gamma_i + v_i d_i + w_i d_i^\dagger \right). \quad (3.1.2)$$

With the demand $[H_D + H_M + H_S, \alpha_\epsilon] = -\epsilon \alpha_\epsilon$, we find the corresponding Bogoliubov-de Gennes equation

$$h\Psi = \epsilon(\mathbb{I}_D + \frac{1}{2}\mathbb{I}_M)\Psi \quad (3.1.3)$$

with

$$h = \left(\begin{array}{cc|cccc} 0 & i\frac{\epsilon_M}{2} & t_L & 0 & -t_L^* & 0 \\ -i\frac{\epsilon_M}{2} & 0 & 0 & t_R & 0 & -t_R^* \\ \hline t_L^* & 0 & \epsilon_L & 0 & 0 & \Delta^* \\ 0 & t_R^* & 0 & \epsilon_R & -\Delta^* & 0 \\ -t_L & 0 & 0 & -\Delta & -\epsilon_L & 0 \\ 0 & -t_R & \Delta & 0 & 0 & -\epsilon_R \end{array} \right) \quad (3.1.4)$$

in the basis $\{\gamma_L, \gamma_R, d_L^\dagger, d_R^\dagger, d_L, d_R\}$. Here, the 6×6 matrices $\mathbb{I}_D = \text{diag}(0, 0, 1, 1, 1, 1)$ and $\mathbb{I}_M = \text{diag}(1, 1, 0, 0, 0, 0)$ denote the identity matrices in the dot and Majorana space. The factor of $1/2$ in the Majorana sector of the Bogoliubov-de Gennes equation originates from the algebra $\{\gamma_i, \gamma_j\} = 2\delta_{ij}$ of Majorana fermions which differs from the algebra of ordinary fermions. Since the two Majorana operators γ_L and γ_R can be combined into a fermion f , it is also possible to express the Bogoliubov-de Gennes equations in terms of this fermion without the factor of $1/2$. For details about the alternative representation of the Hamilton matrix Eq. (3.1.4), we refer to Appendix B.1.

3.1.2. Generalized scattering formalism

As shown in figure 3.1.1, we assume that the mesoscopic device introduced above is connected to two electron reservoirs by means of two leads which are considered to be ideal Fermi liquids. The reservoirs are held at the same chemical potential $eV \geq 0$. We model the semi-infinite ideal leads $i = L, R$ by the energy independent density of states ρ_i and assume that the lead i is coupled to the quantum dot i via the coupling strength g_i . This coupling strength has two effects, (i) it provides a matrix element for tunneling of an elec-

tron/hole from the lead to the dot and (ii) in addition, it gives rise to the level broadening $\Gamma_i = 2\pi\rho_i|g_i|^2$ in the quantum dots. We assume that the size L of the region between the two electron reservoirs is much smaller than the phase breaking length l_ϕ and the energy relaxation length l_{rel} such that the electron motion can be regarded to be quantum mechanically coherent.

In our analysis, we concentrate on the average current $I_i = \langle \hat{I}_i \rangle$ in lead i , and on the zero-frequency shot noise

$$S_{ij} = 2 \int_{\mathbb{R}} dt \langle \delta \hat{I}_i(0) \delta \hat{I}_j(t) \rangle, \quad (3.1.5)$$

which measures the correlation of the current fluctuations in leads i and j , where the current fluctuation operator $\delta \hat{I}_i = \hat{I}_i - I_i$ measures the deviation of the current from the average current. To compute the average current I_i in lead i and the zero-frequency noise S_{ij} through the normal–superconductor–normal device, we use a generalized scattering matrix approach which also allows for Andreev reflection processes.

In the following, we derive the expressions for the average current and the shot noise starting from the multi-terminal Landauer–Büttiker single-particle approach for purely normal systems [113–115],

$$I_i = \frac{e}{h} \int_{\mathbb{R}} d\epsilon \sum_k A_{k,k}^i n_k, \quad (3.1.6a)$$

$$S_{ij} = \frac{2e^2}{h} \int_{\mathbb{R}} d\epsilon \sum_{k,l} A_{k,l}^i A_{l,k}^j n_k (1 - n_l), \quad (3.1.6b)$$

where the roman indices denote the lead electrodes, $A_{k,l}^i = \delta_{ik}\delta_{il} - s_{i,k}^* s_{i,l}$ contains the scattering matrix elements, and where n_k is the Fermi function for electrons in lead k . To extend this formalism to superconductors which explicitly mix electron and hole degrees of freedom, Anantram and Datta [116] rewrote Eq. (3.1.6) by taking electron and hole degrees of freedom explicitly into account. Thus, we decompose the current I_i into the electron current I_i^e and the hole current I_i^h . The same holds for the current fluctuations and the noise correlator. Thus, we find

$$I_i^\alpha = \frac{q_\alpha}{h} \int_0^\infty d\epsilon \sum_{k;\gamma} A_{k,k;\gamma,\gamma}^{(i\alpha)} n_{k,\gamma}, \quad (3.1.7a)$$

$$S_{ij}^{\alpha\beta} = \frac{2q_\alpha q_\beta}{h} \int_0^\infty d\epsilon \sum_{k,l;\gamma,\delta} A_{k,l;\gamma,\delta}^{(i\alpha)} A_{l,k;\delta,\gamma}^{(j\beta)} n_{k,\gamma} (1 - n_{l,\delta}), \quad (3.1.7b)$$

where the greek indices denote electron (e) and hole (h) degrees of freedom, q_α is the charge of particle type α , and with the matrix $A_{k,l;\beta,\gamma}^{(i\alpha)} = \delta_{ik}\delta_{il}\delta_{\alpha\beta}\delta_{\alpha\gamma} - s_{i,k}^{\alpha\beta*} s_{i,l}^{\alpha\gamma}$. We note that in

Eq. (3.1.7) we integrate over positive energies since the negative energies are associated with holes and therefore implicitly included via the hole index. For purely normal systems, the expressions Eq. (3.1.6) and Eq. (3.1.7) are fully equivalent since $s_{i,k}^{\alpha\beta} = \delta_{\alpha\beta} s_{i,k}^{\alpha\alpha}$. However, in principle the matrix A in Eq. (3.1.7) also allows for scattering of electrons to holes and vice versa via the matrix elements $s_{i,k}^{eh}$ and $s_{i,k}^{he}$. As a consequence, Eqs. (3.1.7) is also suitable to describe superconducting systems. Superconductors are characterized by four different types of transport processes. The matrix element $s_{i,i}^{\alpha\alpha}$ is the reflection amplitude of a particle α in lead i . The matrix element $s_{i,k}^{\alpha\alpha}$ with $i \neq k$ is the transmission amplitude of an α particle from lead k to lead i . For $\alpha \neq \beta$, the matrix element $s_{i,k}^{\alpha\beta}$ describes the conversion of an incoming α particle in lead k into an outgoing β -particle in lead i . For $i = k$ this conversion process is called local Andreev reflection and for $i \neq k$ it is called crossed Andreev reflection.

Using the relations $q_e = e$ and $q_h = -e$ for the charge of electrons and holes, and summing up the contributions of electrons and holes to the total current in lead i , we find the final expressions for the average current in lead i and the correlations between the current fluctuations in leads i and j ,

$$I_i = \frac{e}{h} \int_0^\infty d\epsilon \sum_\alpha \text{sign}(\alpha) \sum_{k;\gamma} A_{k,k;\gamma,\gamma}^{(i\alpha)} n_{k,\gamma}, \quad (3.1.8a)$$

$$S_{ij} = \frac{2e^2}{h} \int_0^\infty d\epsilon \sum_{\alpha,\beta} \text{sign}(\alpha\beta) \sum_{k,l;\gamma,\delta} A_{k,l;\gamma,\delta}^{(i\alpha)} A_{l,k;\delta,\gamma}^{(j\beta)} n_{k,\gamma} (1 - n_{l,\delta}). \quad (3.1.8b)$$

Here, the sign functions originate from the opposite charge of electrons and holes. As before, roman indices denote the left (L) and right (R) lead, greek indices denote electron (e) and hole (h) channels, $\text{sign}(e) = +1$ and $\text{sign}(h) = -1$, and

$$A_{k,l;\beta,\gamma}^{(i\alpha)} = \delta_{ik} \delta_{il} \delta_{\alpha\beta} \delta_{\alpha\gamma} - s_{i,k}^{\alpha\beta*} s_{i,l}^{\alpha\gamma}. \quad (3.1.9)$$

The reservoir distribution functions $n_{k,\gamma}$ are Fermi functions with different chemical potentials for the electron and hole bands

$$n_{k,\gamma} = \frac{1}{1 + e^{\beta(\epsilon - \text{sign}(\gamma)eV_k)}}. \quad (3.1.10)$$

For the setup in figure 3.1.1, we assume that $V_L = V_R \equiv V$. The coefficients $s_{i,j}^{\alpha\beta}$ are the elements of the scattering matrix

$$S(\epsilon) = 1 - 2\pi i W^\dagger \left[\mathcal{G}^{-1}(\epsilon) + i\pi W W^\dagger \right]^{-1} W, \quad (3.1.11)$$

where W describes the coupling between the states of the system without leads and the scattering states in the leads. The matrix

$$\mathcal{G}^{-1}(\epsilon) = \epsilon \mathbb{I}_D + \frac{\epsilon}{2} \mathbb{I}_M - h \quad (3.1.12)$$

is the inverse of the retarded electron Green function for the closed system Eq. (3.1.4), and $i\pi WW^\dagger$ is the self energy due to the level broadening on the quantum dots. The factor of $1/2$ in front of the unit matrix for the Majorana sector originates from the unconventional form of the anti-commutation relations for the Majorana fermions as compared to the ordinary fermion algebra. The coupling matrix W in the lead basis $\{\psi_L^\dagger, \psi_R^\dagger, \psi_L, \psi_R\}$ is given by

$$W_{i_l \alpha_{i_l}, i_d \alpha_{i_d}} = \text{sign}(\alpha_{i_d}) g_{i_l} \sqrt{\rho_{i_l}} \delta_{i_l, i_d} \delta_{\alpha_{i_l}, \alpha_{i_d}}, \quad (3.1.13)$$

where α_{i_d} (α_{i_l}) denotes the particle species of quantum dot i_d (lead i_l). The coupling strengths g_i give rise to the level broadening $\Gamma_i = 2\pi\rho_i|g_i|^2$ in the dots. In the following, we concentrate on the special case $\Gamma_L = \Gamma_R \equiv \Gamma$, $t_L = t_R \equiv t$, and take the limit of zero temperature. We note that, unlike the rate equation formalism, the scattering approach does not assume weak coupling between the leads and the mesoscopic system and can also be applied even to ballistic conductors [115].

In the following, we analyze the zero-temperature limits of Eqs. (3.1.8). For that purpose, we define the matrix

$$\mathcal{R}_{ij}^{\alpha\beta} = \sum_k s_{ik}^{\alpha e*} s_{jk}^{\beta e}, \quad (3.1.14)$$

which only depends on the matrix elements describing the scattering of an incoming electron. With this definition and with $n_{k,h} = 0$, $n_{k,e} = \Theta(eV - \epsilon)$, we write for the average current in lead i ,

$$I_i = \frac{e}{h} \int_0^{eV} d\epsilon (1 - \mathcal{R}_{ii}^{ee} + \mathcal{R}_{ii}^{hh}). \quad (3.1.15)$$

Similarly, we find for the current correlations

$$S_{ij} = \frac{2e^2}{h} \int_0^{eV} d\epsilon \left\{ \mathcal{R}_{ij}^{ee} (\delta_{ij} - \mathcal{R}_{ji}^{ee}) + \mathcal{R}_{ij}^{hh} (\delta_{ij} - \mathcal{R}_{ji}^{hh}) + |\mathcal{R}_{ij}^{eh}|^2 + |\mathcal{R}_{ij}^{he}|^2 \right\}, \quad (3.1.16)$$

where we used the unitarity of the scattering matrix to obtain the linear \mathcal{R} terms. For $i = j$, we express Eq. (3.1.16) in terms of the scattering matrix elements and find the local noise correlators

$$S_{ii} = \frac{2e^2}{h} \int_0^{eV} d\epsilon \sum_{k,l} |s_{ik}^{he*} s_{il}^{hh} - s_{ik}^{ee*} s_{il}^{eh}|^2, \quad (3.1.17)$$

which is always nonnegative independent of the details of the mesoscopic system. In contrast, the cross-correlations

$$S_{LR} \equiv S_{RL} = \frac{2e^2}{h} \int_0^{eV} d\epsilon \left\{ -|\mathcal{R}_{LR}^{ee}|^2 - |\mathcal{R}_{LR}^{hh}|^2 + |\mathcal{R}_{LR}^{eh}|^2 + |\mathcal{R}_{LR}^{he}|^2 \right\} \quad (3.1.18)$$

contain both positive and negative contributions. Therefore, the cross-correlations can either be positive or negative [116] depending on the relative size of the positive and negative terms in Eq. (3.1.18). This is in stark contrast to purely normal-conducting systems where cross-correlations are always negative due to the presence of a single charge carrier species [114].

In the following, we analyze the nature of the negative cross-correlation terms. We write the negative contributions as

$$|\mathcal{R}_{LR}^{ee}|^2 = |s_{LL}^{ee*} s_{RL}^{ee} + s_{LR}^{ee*} s_{RR}^{ee}|^2, \quad (3.1.19a)$$

$$|\mathcal{R}_{LR}^{hh}|^2 = |s_{LL}^{he*} s_{RL}^{he} + s_{LR}^{he*} s_{RR}^{he}|^2 \stackrel{SS^\dagger=1}{=} |s_{LL}^{hh*} s_{RL}^{hh} + s_{LR}^{hh*} s_{RR}^{hh}|^2, \quad (3.1.19b)$$

which are nonzero for $s_{LL}^{\alpha\alpha} s_{LR}^{\alpha\alpha} \neq 0$ or $s_{RR}^{\alpha\alpha} s_{RL}^{\alpha\alpha} \neq 0$. Therefore, we conclude that resonant tunneling of electrons and holes gives rise to negative current cross-correlations. In contrast, the existence of positive cross-correlations demands the existence of a nonzero matrix element s^{eh} describing Andreev processes,

$$|\mathcal{R}_{LR}^{eh}|^2 = |s_{LL}^{ee*} s_{RL}^{eh} + s_{LR}^{ee*} s_{RR}^{eh}|^2. \quad (3.1.20)$$

The Fano factor F relates the actual shot noise S to the Poisson noise that would be measured if the system produced noise S_P due to single independent electrons [114]. The Poissonian statistics of charge transmission requires the Poissonian noise $S_P = 2eI$ [117], which yields the Fano factor

$$F = \frac{S}{2eI}. \quad (3.1.21)$$

For purely normal systems, the Fano factor assumes values between zero (all channels are transparent) and one (Poissonian noise). For superconducting systems, the Fano factor assumes values between zero and two, where the $F = 2$ corresponds to the charge $2e$ of Cooper pairs. In our analysis, we define a more general Fano factor

$$F_{ij}^k = \frac{S_{ij}}{2eI_k}, \quad (3.1.22)$$

which relates the current correlations between leads i and j with the current in lead k . In

most calculations we assume symmetric lead contacts and hence $I_L = I_R$. In these cases, we use the simplified notation $F_{ij}^L = F_{ij}^R \equiv F_{ij}$.

3.1.3. Microscopic model

To make contact with possible experiments and to study the robustness of the results for the effective Majorana model introduced above, we consider the Hamiltonian describing a narrow semiconductor nanowire with strong spin-orbit coupling which is predicted to host Majorana end states [32–35]. We describe the low-energy physics of the nanowire by the tight-binding lattice Hamiltonian

$$H = H_{\text{SM}} + H_{\text{SC}} \quad (3.1.23)$$

with the normal-state Hamiltonian

$$H_{\text{SM}} = - \sum_{\mathbf{r}, \mathbf{r}', \sigma} t_{\mathbf{r}\mathbf{r}'} c_{\mathbf{r}\sigma}^\dagger c_{\mathbf{r}'\sigma} + \sum_{\mathbf{r}, \sigma} \left(E_Z \hat{\sigma}_{\sigma\sigma}^z - \mu + V_{\mathbf{r}} \right) c_{\mathbf{r}\sigma}^\dagger c_{\mathbf{r}\sigma} \\ + \frac{i\hbar\alpha}{2a} \sum_{\mathbf{r}, \sigma} \left(c_{\mathbf{r}\sigma}^\dagger \hat{\sigma}_{\sigma\bar{\sigma}}^y c_{\mathbf{r}+\boldsymbol{\delta}_x\bar{\sigma}} - c_{\mathbf{r}\sigma}^\dagger \hat{\sigma}_{\sigma\bar{\sigma}}^y c_{\mathbf{r}-\boldsymbol{\delta}_x\bar{\sigma}} - c_{\mathbf{r}\sigma}^\dagger \hat{\sigma}_{\sigma\bar{\sigma}}^x c_{\mathbf{r}+\boldsymbol{\delta}_y\bar{\sigma}} + c_{\mathbf{r}\sigma}^\dagger \hat{\sigma}_{\sigma\bar{\sigma}}^x c_{\mathbf{r}-\boldsymbol{\delta}_y\bar{\sigma}} \right), \quad (3.1.24)$$

where the operator $c_{\mathbf{r}\sigma}^\dagger$ ($c_{\mathbf{r}\sigma}$) creates (annihilates) an electron at site \mathbf{r} with spin σ and mass m . The first term in H_{SM} describes hopping on a simple square lattice with lattice parameter a , $t_{\mathbf{r}, \mathbf{r}+\boldsymbol{\delta}} = t_0 \equiv \hbar^2/2m^2a^2$ for the nearest-neighbor lattice vectors $\boldsymbol{\delta}_x = (a, 0)$ and $\boldsymbol{\delta}_y = (0, a)$, and $t_{\mathbf{r}, \mathbf{r}} = -2t_0$. The second term in Eq. (3.1.24) contains the Zeeman splitting $E_Z = g\mu_B B/2$ due to a magnetic field in z direction, the chemical potential μ , and the electrostatic potential $V_{\mathbf{r}}$ which describes nonmagnetic disorder. The second line in Eq. (3.1.24) represents the Rashba spin-orbit coupling with spin-orbit velocity α , and $\hat{\sigma}^s$ are the Pauli spin matrices with $s = x, y, z$. The proximity coupling between the s -wave superconductor and the nanowire is described by the effective s -wave pairing Hamiltonian

$$H_{\text{SC}} = \Delta_{\text{SC}} \sum_{\mathbf{r}} \left(c_{\mathbf{r}\uparrow}^\dagger c_{\mathbf{r}\downarrow}^\dagger + c_{\mathbf{r}\downarrow} c_{\mathbf{r}\uparrow} \right) \quad (3.1.25)$$

with the superconducting pairing potential Δ_{SC} .

In our numerics, we use the lattice constant $a = 10$ nm and the realistic material parameters $\hbar^2/2m = 500$ meV \cdot nm², $E_Z = 1$ meV, $\hbar\alpha = 10$ meV \cdot nm, and $\Delta_{\text{SC}} = 0.5$ meV. We consider a nanowire of length $L = 520$ nm and width 70 nm. For the above parameters and $\mu = 0$, the superconducting coherence length is $\xi = v_F/\Delta_{\text{eff}} = 150$ nm where v_F denotes

the Fermi velocity and Δ_{eff} the superconducting gap. For details about the numerical calculations, we refer to Appendices A.1 and A.2.

3.2. Normal-state–Majorana bound state–normal-state device

Before discussing the full model, we consider simpler systems for zero temperature without quantum dots and with one quantum dot only. We begin our discussion with the limit where the Majorana bound states are directly coupled to the leads as sketched in figure 3.2.1 and where no quantum dots are present, i.e., we consider $t_L = t_R = 0$. This situation was studied for $\epsilon_M = 0$ in reference [69] using the Keldysh Green function approach and for arbitrary ϵ_M in reference [70] using a scattering matrix approach.

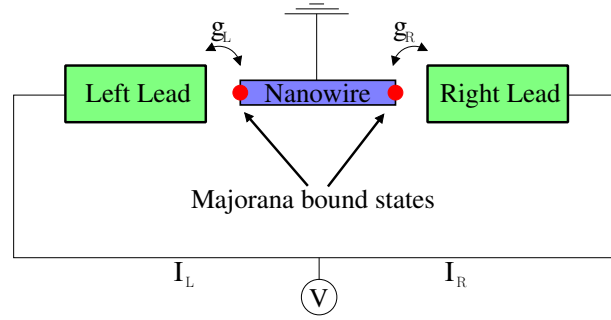


Figure 3.2.1.: Schematic setup of a topological superconductor nanowire with a pair of Majorana bound states (red dots) coupled to lead electrodes. The leads are biased with the positive chemical potential eV with respect to the grounded superconductor nanowire.

In this limit, the Hamiltonian simplifies significantly to $H = H_M$ and the inverse Green function matrix is given by

$$\mathcal{G}^{-1}(\epsilon) = \frac{1}{2} \begin{pmatrix} \epsilon & -i\epsilon_M \\ i\epsilon_M & \epsilon \end{pmatrix} \quad (3.2.1)$$

in the basis $\{\gamma_L, \gamma_R\}$ for the Majorana bound states. This Green function describes a two-level system where the tunnel coupling ϵ_M splits the two zero-energy levels into a doublet at $\pm\epsilon_M$. We describe the coupling between the leads and the Majorana bound states by the matrix

$$W = \frac{1}{\sqrt{2}} \begin{pmatrix} \sqrt{\frac{\Gamma_L}{2\pi}} & 0 & -\sqrt{\frac{\Gamma_L}{2\pi}} & 0 \\ 0 & \sqrt{\frac{\Gamma_R}{2\pi}} & 0 & -\sqrt{\frac{\Gamma_R}{2\pi}} \end{pmatrix} \quad (3.2.2)$$

in the basis $\{\psi_L^\dagger, \psi_R^\dagger, \psi_L, \psi_R\}$ for the leads and $\{\gamma_L, \gamma_R\}$ for the Majorana bound states,

and with $\Gamma_i = 4\pi\rho_i|g_i|^2$. By inserting these expressions for W and \mathcal{G} into Eq. (3.1.11), we find the 4×4 scattering matrix

$$S(\epsilon) = \begin{pmatrix} 1 + A & A \\ A & 1 + A \end{pmatrix} \quad (3.2.3)$$

with

$$A = \frac{1}{\epsilon_M^2 - (i\Gamma_L + \epsilon)(i\Gamma_R + \epsilon)} \begin{pmatrix} i\Gamma_L(i\Gamma_R + \epsilon) & -\epsilon_M\sqrt{\Gamma_L\Gamma_R} \\ \epsilon_M\sqrt{\Gamma_L\Gamma_R} & i\Gamma_R(i\Gamma_L + \epsilon) \end{pmatrix}. \quad (3.2.4)$$

We note that this expression for the scattering matrix is different from the one in reference [70]. The differences originate from different definitions of ϵ_M and the Γ_i , and have no physical consequences.

Using Eq. (3.1.15) for the total average current $I = I_L + I_R$ that flows via the superconductor into the ground, we find the total zero-temperature differential conductance,

$$G(eV = \epsilon) \equiv \frac{\partial I}{\partial V} = \frac{2e^2}{h} \frac{(\Gamma_L^2 + \Gamma_R^2)\epsilon^2 + 2\Gamma_L^2\Gamma_R^2 + 2\epsilon_M^2\Gamma_R\Gamma_L}{(\epsilon_M^2 - \epsilon^2 + \Gamma_L\Gamma_R)^2 + \epsilon^2(\Gamma_L + \Gamma_R)^2}. \quad (3.2.5)$$

Here, the first two terms originate from the scattering matrix element describing local Andreev reflection and the last term originates from the matrix element describing crossed Andreev reflection. In particular, we find that the crossed Andreev contribution is proportional to ϵ_M^2 and hence is nonzero only for a finite coupling between the Majorana bound states. In the limit where only one lead is coupled to one Majorana bound state, say $\Gamma_L = \Gamma$ and $\Gamma_R = 0$, the differential conductance is determined by local Andreev reflection only and acquires the form

$$G(eV = \epsilon) = \frac{2e^2}{h} \frac{\epsilon^2\Gamma^2}{(\epsilon_M^2 - \epsilon^2)^2 + \epsilon^2\Gamma^2}. \quad (3.2.6)$$

We note that for $\epsilon_M = 0$, we recover the quantized zero-bias conductance $2e^2/h$ which was predicted to be a signature of Majorana bound states [21, 22] as discussed in the introductory chapter 1.3.

In figure 3.2.2(a), we plot the differential conductance for extremely asymmetric coupling, where only one of the Majorana bound states is coupled to the corresponding lead, and for symmetric coupling, where each Majorana bound state is coupled to the corresponding lead with the same coupling strength. For $\Gamma_R = 0$, the differential conductance Eq. (3.2.6) has a peak at $eV = \epsilon_M$ of quantized height $G(\epsilon_M) = 2e^2/h$ whereas in the

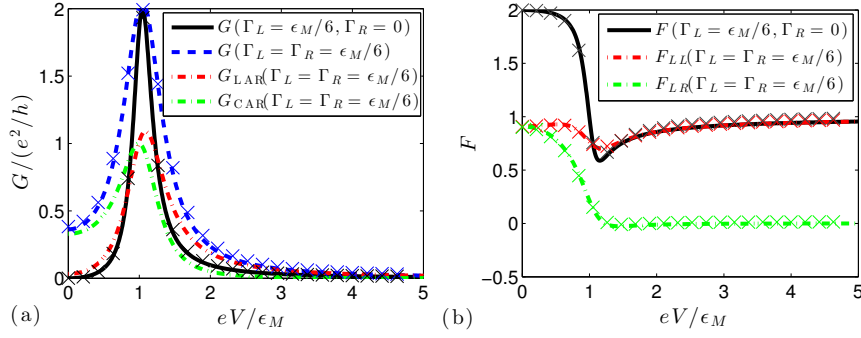


Figure 3.2.2.: (a) Total differential conductance as function of voltage for tunneling into a pair of Majorana bound states. G_{LAR} (G_{CAR}) denote the differential conductance due to local (crossed) Andreev reflection. (b) Fano factor as function of voltage. The \times markers denote the results for the microscopic model of the semiconductor-superconductor nanowire.

symmetric case the peak is not quantized and located at $e^2V^2 = 2\epsilon_M\sqrt{\epsilon_M^2 + \Gamma^2} - \epsilon_M^2 - \Gamma^2$ for $\Gamma < \sqrt{3}\epsilon_M$ and at $V = 0$ for $\Gamma > \sqrt{3}\epsilon_M$. In addition, we find that the differential conductance for symmetric coupling is dominated by crossed (local) Andreev processes for $e^2V^2 < \epsilon_M^2 - \Gamma^2$ ($e^2V^2 > \epsilon_M^2 - \Gamma^2$).

Similarly, we determine the zero-temperature current correlations $S_{ij} = \int_0^{eV} d\epsilon P_{ij}(\epsilon)$ using Eq. (3.1.16). We find

$$P_{ii}(\epsilon) = \frac{4e^2}{h} \frac{2\Gamma_i^2\epsilon^2(\epsilon^2 - \epsilon_M^2 + \Gamma_i^2)^2 + \Gamma_L\Gamma_R\epsilon_M^2[(\epsilon_M^2 - \epsilon^2 + \Gamma_L\Gamma_R)^2 + \epsilon^2(\Gamma_L + \Gamma_R)^2]}{[(\epsilon_M^2 - \epsilon^2 + \Gamma_L\Gamma_R)^2 + \epsilon^2(\Gamma_L + \Gamma_R)^2]^2}, \quad (3.2.7a)$$

$$P_{i\bar{i}}(\epsilon) = \frac{4e^2}{h} \frac{\Gamma_L\Gamma_R\epsilon_M^2[(\epsilon_M^2 - \epsilon^2 + \Gamma_L\Gamma_R)^2 - \epsilon^2(\Gamma_L + \Gamma_R)^2]}{[(\epsilon_M^2 - \epsilon^2 + \Gamma_L\Gamma_R)^2 + \epsilon^2(\Gamma_L + \Gamma_R)^2]^2}, \quad (3.2.7b)$$

where $\bar{i} = L(R)$ for $i = R(L)$. In the limit $\epsilon_M = 0$, the current correlations become particularly simple, $P_{ij}(\epsilon) = \delta_{ij}(8e^2/h)\Gamma_i^2\epsilon^2/(\Gamma_i^2 + \epsilon^2)^2$. Thus, the cross-correlations vanish exactly and the only nonzero Fano factors are

$$F_{ii}^i(eV = x\Gamma_i) = \frac{S_{ii}}{2eI_i} = 1 - \frac{x}{(1+x^2)\arctan(x)} \quad (3.2.8)$$

with the limits $F_{ii}^i = 0$ for $eV \ll \Gamma_i$ and $F_{ii}^i = 1$ for $eV \gg \Gamma_i$. Here, the Fano factor is bounded by one because after the resonance at $eV = 0$ the Fano factor for superconducting systems typically assumes its normal-state value $F = 1$ [118].

For $\epsilon_M > 0$, we distinguish between symmetric coupling to the leads and the extremely

asymmetric limit when only one lead is coupled to one of the Majoranas. In figure 3.2.2(b), we compare the crossed and the local Fano factors. For $\Gamma_L = \Gamma$ and $\Gamma_R = 0$, we find that the local Fano factor is two for $eV \ll \epsilon_M$ and decreases when approaching the resonance at ϵ_M . In the limit $eV \gg \epsilon_M$, the Fano factor converges to one in analogy to the situation for vanishing Majorana energy splitting in Eq. (3.2.8). In contrast, for symmetric coupling strengths $\Gamma_L = \Gamma_R = \Gamma$, the situation is much richer since there the cross-correlations S_{LR} and as a consequence, the crossed Fano factor F_{LR} , are nonzero. For $eV \ll \epsilon_M$, we find positive cross-correlations $F_{LR} \approx F_{ii} \approx 1$, where $F_{LR} = S_{LR}/2eI_L$. This yields a total Fano factor $F_{\text{tot}} = (S_{LL} + S_{RR} + S_{LR} + S_{RL})/2e(I_L + I_R) = 2$ describing the transfer of Cooper pairs with charge $2e$ into the grounded superconductor. The crossed Fano factor $F_{LR} + F_{RL} = 2$ directly measures the transferred charge $2e$ of the crossed Andreev process. As shown in figure 3.2.2(b), with increasing voltage F_{LR} significantly decreases and is suppressed for $eV \approx \epsilon_M$ in contrast to F_{ii} which is approximately independent of voltage with a small valley at $eV = \epsilon_M$. The origin of the suppression of cross-correlations is resonant tunneling of electrons and holes which gives rise to negative cross-correlations as discussed in Eq. (3.1.19b). Since each Majorana bound state is an equal superposition of electron and hole components, the negative contribution cancel the positive contribution exactly.

In figure 3.2.3, we show the differential conductance and the Fano factor for the microscopic model of the semiconductor-superconductor hybrid system with symmetric tunneling strengths $\Gamma_L = \Gamma_R$. As discussed in chapter 2.5, the nanowire is in the topologically trivial phase for $E_Z^2 < \Delta_{\text{SC}}^2 + \mu^2$. There, the transport for $eV < E_G \equiv |E_Z - \sqrt{\Delta_{\text{SC}}^2 + \mu^2}|$ is nonresonant and thus suppressed, $G \propto \rho_{\text{SM}}$ where ρ_{SM} denotes the normal-state density of states of the semiconductor nanowire [118]. The local Fano factor F_{ii} is two and the crossed Fano factor vanishes signaling that the transport is fully determined by nonresonant local Andreev reflection. For $eV > E_G$, the current is carried by resonant Andreev processes and as a consequence, the local Fano factor drops to one which gives rise to the sharp yellow-red transition in figure 3.2.3(c).

In contrast, for $E_Z^2 > \Delta_{\text{SC}}^2 + \mu^2$ the nanowire is in the topologically nontrivial phase with a pair of split Majorana bound states at $\epsilon_M \sim \Delta_{\text{eff}} \exp(-L/\xi) \sin(k_F L)$ [see Appendix B.2 for details] which oscillates as function of magnetic field (chemical potential) [101]. In full agreement with our results for the low-energy model discussed above, we find that the differential conductance is peaked for $eV \approx \epsilon_M$ and that the crossed Fano factor is two (zero) for $eV < \epsilon_M$ ($eV > \epsilon_M$) as shown in figure 3.2.2(d).

In addition, we find that the topological phase transition at $E_Z^2 = \Delta_{\text{SC}}^2 + \mu^2$ clearly shows up in the local and the crossed Fano factors. In particular, the crossed Fano factor

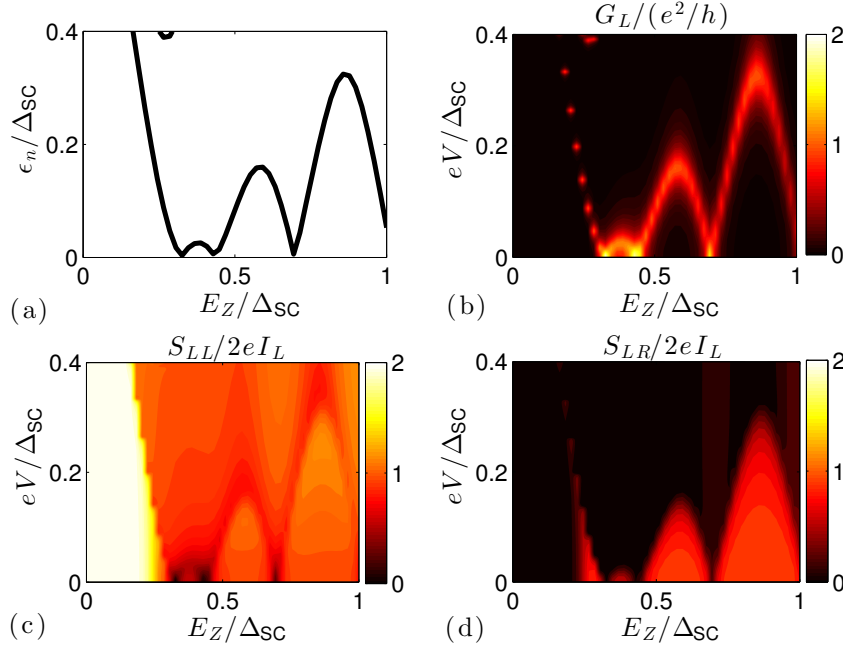


Figure 3.2.3.: Transport properties of the microscopic model for the semiconductor-superconductor nanowire in the three-terminal geometry illustrated in figure 3.2.1 with symmetric coupling $\Gamma_L = \Gamma_R$. (a) Lowest excitation energy, (b) differential conductance in the left lead, (c) Fano factor in the left lead, and (d) crossed Fano factor as function of voltage and Zeeman energy.

increases if E_Z approaches the topological phase transition from below due to the closing of the excitation gap in the nanowire which gives rise to a divergence of the superconducting coherence length and thereby allows for crossed Andreev reflection processes via the bulk superconducting state. Hence, we propose that the appearance of cross-correlations F_{LR} with increasing magnetic field signals the closing of the bulk excitation gap which is intricately related to the bulk topological phase transition.

Despite the clear theoretical prediction of the crossed Fano factor of two for $eV \ll \epsilon_M$, we argue that this setup is of limited use for an experimental verification of Majorana bound states. The major drawback in this proposal is that for $eV \ll \epsilon_M$, the current is nonresonant and hence very small. On the other hand, when approaching the resonance $eV = \epsilon_M$, the crossed Fano factor is almost completely suppressed. In order to observe finite cross-correlations for $eV \gg \epsilon_M$, we suggest to perturb the fine-tuning between the different transport channels. Quantum dots are natural candidates to favor some transport processes and suppress competing processes. In the following sections, we investigate the effect of quantum dots on the differential conductance and on the current cross-correlations.

3.3. Coupling one quantum dot to a Majorana bound state

In this section, we consider the situation that one quantum dot is coupled to one of the Majorana bound states. Especially, we consider $t_R = 0$ and $\Gamma_R = 0$. Throughout this section, we set $\epsilon_L \equiv \epsilon_d$, $d_L \equiv d$, and $t_L \equiv t$. The excitation spectrum for the quantum dot–Majorana bound state system can be calculated exactly by solving the 4×4 Bogoliubov-de Gennes equation for the Hamilton matrix Eq. (3.1.4). This yields the two quasiparticle energies

$$E_{\pm} = \frac{1}{\sqrt{2}} \sqrt{\epsilon_M^2 + 4|t|^2 + \epsilon_d^2 \pm \sqrt{(\epsilon_M^2 + 4|t|^2 + \epsilon_d^2)^2 - 4\epsilon_M^2\epsilon_d^2}}. \quad (3.3.1)$$

For fixed $|\epsilon_M| \gg |t|$, the quasiparticle energy spectrum has levels at $|\epsilon_M|$ and $|\epsilon_d|$, with avoided crossings where these two levels intersect each other. The energy splitting due to the avoided crossing is $\pm 2|t|$. However, for $\epsilon_M = 0$ or $\epsilon_d = 0$, there is one special Bogoliubov quasiparticle at exactly zero energy which is described by a pair of Majorana operators.

In the following, we concentrate on the situation $\epsilon_M > 0$ and $\epsilon_d = 0$, where we find the zero-energy Majorana operators

$$\gamma_1 = \frac{t^*d^\dagger + td}{|t|}, \quad (3.3.2a)$$

$$\gamma_2 = \frac{\sqrt{8}|t|^2\gamma_R - i\epsilon_M(t^*d^\dagger - td)}{|t|\sqrt{\epsilon_M^2 + 8|t|^2}}. \quad (3.3.2b)$$

Here, γ_1 is completely localized on the quantum dot, while γ_2 is partially delocalized, and the weight of γ_2 on the quantum dot is determined by the Majorana energy splitting. The existence of these zero-energy Majorana operators depends on the fine-tuning of the quantum dot energy level and thus, they are not topologically protected. In particular, we note that for finite ϵ_d , the Majorana operators are tunnel-coupled with coupling energy $\delta E \approx |\epsilon_d\epsilon_M|/\sqrt{\epsilon_M^2 + 4|t|^2}$. We note that throughout this chapter, the name *Majorana bound state* is used for the topological Majoranas γ_L and γ_R which should not be confused with the induced Majorana operators Eq. (3.3.2).

Pictorially, we can understand the formation of the zero-energy Majorana states by considering a mechanism similar to the one in the introductory chapter 2.2 when studying the one-dimensional Kitaev chain. As illustrated in figure 3.3.1, we can decompose the quantum dot fermion operators d and d^\dagger into a pair of Majorana operators. There exists

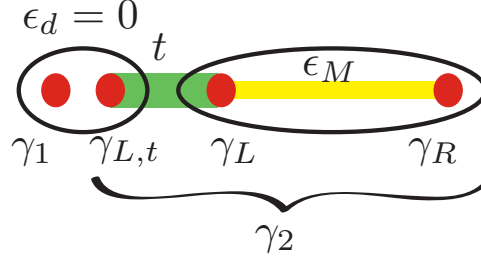


Figure 3.3.1.: Formation of the zero-energy Majorana operators for $\epsilon_d = 0$. The quantum dot fermion operators d and d^\dagger are decomposed into two Majorana operators γ_1 and $\gamma_{L,t}$. Due to the coupling $(t^*d^\dagger - td)\gamma_L$, only $\gamma_{L,t}$ is coupled to γ_L while γ_1 commutes with the Hamiltonian indicating zero energy. Since two Majorana operators are necessary to describe a physical fermion, there exists another zero-energy Majorana operator γ_2 which is a nontrivial combination of $\gamma_{L,t}$, γ_L , and γ_R .

a special decomposition for which only one of the dot Majoranas couples to γ_L . In the limit $\epsilon_d = 0$, the two Majoranas in the dot are not coupled to each other, such that an uncoupled Majorana γ_1 resides on the quantum dot. Since the three other Majorana operators cannot form a single physical fermion, there necessarily exists another zero-energy Majorana operator γ_2 which is in general not localized, as can be seen from Eq. (3.3.2).

In the following, we study the transport properties through the quantum dot–Majorana bound state junction. By inserting the Bogoliubov-de Gennes Hamiltonian into Eq. (3.1.12) and neglecting the uncoupled quantum dot, we obtain the inverse Green function matrix

$$\mathcal{G}^{-1}(\epsilon) = \begin{pmatrix} \frac{\epsilon}{2} & i\frac{\epsilon_M}{2} & -t^* & t \\ -i\frac{\epsilon_M}{2} & \frac{\epsilon}{2} & 0 & 0 \\ -t & 0 & \epsilon - \epsilon_d & 0 \\ t^* & 0 & 0 & \epsilon + \epsilon_d \end{pmatrix} \quad (3.3.3)$$

in the basis $\{\gamma_L, \gamma_R, d^\dagger, d\}$. The coupling of the quantum dot to the left lead is given by the coupling matrix

$$W = \begin{pmatrix} 0 & 0 \\ 0 & 0 \\ \sqrt{\frac{\Gamma}{2\pi}} & 0 \\ 0 & -\sqrt{\frac{\Gamma}{2\pi}} \end{pmatrix} \quad (3.3.4)$$

in the basis $\{\psi_L^\dagger, \psi_L\}$ for the lead. Inserting the expressions Eqs. (3.3.3) and (3.3.4) into

Eq. (3.1.11) for the scattering matrix, we find the 2×2 scattering matrix

$$S(\epsilon) = \frac{1}{Z} \begin{pmatrix} [\epsilon^2 - \epsilon_M^2][4\epsilon^2 - (2\epsilon_d + i\Gamma)^2] - 16|t|^2\epsilon^2 & -8i|t|^2\Gamma\epsilon \\ -8i|t|^2\Gamma\epsilon & [\epsilon^2 - \epsilon_M^2][4\epsilon^2 - (2\epsilon_d - i\Gamma)^2] - 16|t|^2\epsilon^2 \end{pmatrix} \quad (3.3.5)$$

with

$$Z = (\epsilon_M^2 - \epsilon^2)(4\epsilon_d^2 - (2\epsilon + i\Gamma)^2) - 8\epsilon|t|^2(i\Gamma + 2\epsilon). \quad (3.3.6)$$

Using Eqs. (3.1.15) and (3.1.16) for the zero-temperature average current I , which flows via the superconductor into the ground, and the shot noise, we find the total differential conductance and the current correlations

$$G_L = \frac{2e^2}{h} T_A|_{\epsilon=eV}, \quad (3.3.7a)$$

$$P_{LL} = \frac{8e^2}{h} T_A(1 - T_A)|_{\epsilon=eV}, \quad (3.3.7b)$$

where

$$T_A(\epsilon) = \frac{64|t|^4\Gamma^2\epsilon^2}{\left[(\epsilon_M^2 - \epsilon^2)(\Gamma^2 - 4\epsilon^2 + 4\epsilon_d^2) - 16\epsilon^2|t|^2\right]^2 + 16\epsilon^2\Gamma^2[\epsilon_M^2 - \epsilon^2 + 2|t|^2]^2} \quad (3.3.8)$$

is the probability that an incoming electron with energy ϵ is Andreev reflected as a hole. We note that the numerator of the Andreev probability is proportional to the square of the voltage and thus vanishes for zero voltage despite the existence of a pair of zero-energy Majorana operators γ_1 and γ_2 .

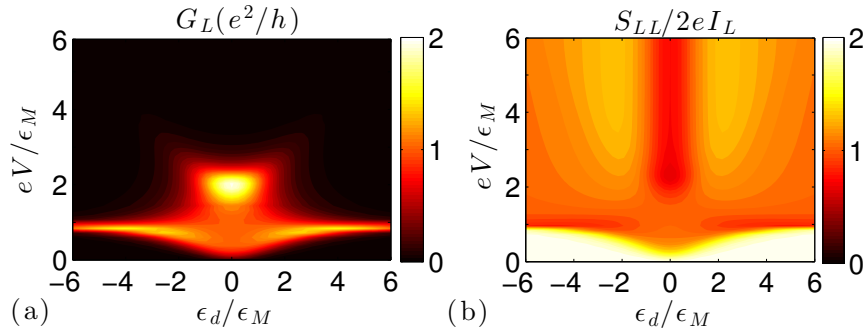


Figure 3.3.2.: (a) Differential conductance and (b) local Fano factor as function of voltage and quantum dot level for the normal-state-quantum dot-Majorana bound state device with $t = \epsilon_M$ and $\Gamma = 2\epsilon_M$.

In figure 3.3.2, we show the differential conductance and the local Fano factor for the normal-state-quantum dot-Majorana bound state device. In the ϵ_d - V plane, the differen-

tial conductance shows peaks whenever $eV \approx E_{\pm}$ and hence displays the two electronic bands of the quasiparticle spectrum. We find two different characteristic regimes. For $|\epsilon_d| \gg \epsilon_M, |t|$, the differential conductance is determined by virtual processes via the quantum dot. As a consequence, the differential conductance has one sharp peak at $eV \approx \epsilon_M$ of height $\approx 2e^2/h$ and renormalized width $\Gamma(|t|/\epsilon_d)^2$ and another peak at $eV \approx |\epsilon_d|$ of suppressed height $(16e^2/h)(|t|/\epsilon_d)^4$ and width Γ .

In the opposite limit $|\epsilon_d| \lesssim \epsilon_M, |t|$, the quantum dot is characterized by the formation of the zero-energy Majorana states γ_1 and γ_2 . However, in contrast to a topological zero-energy Majorana bound state, the Majorana states γ_1 and γ_2 do not show a zero-bias conductance peak because they are partially localized on the same dot which gives rise to destructive interference between the Andreev reflection due to γ_1 and γ_2 . Instead, the differential conductance is characterized by nonuniversal behavior for $eV \ll \epsilon_M$ with a plateau-like feature of height $\lesssim e^2/h$ and a wide peak of height $\approx 2e^2/h$ and width $\Gamma|t|/\epsilon_M$ at $eV \approx E_+ = \sqrt{\epsilon_M^2 + 4|t|^2}$.

In figure 3.3.2(b), we display the local Fano factor $F_{LL} = 2$ for $eV \lesssim E_-$ which can be directly seen from Eqs. (3.3.7) for $T_A \ll 1$. With increasing voltage, the quadratic term in Eq. (3.3.7b) becomes important and gives rise to $F_{LL} \approx 1$ for $eV > E_-$. At $eV \approx E_-$, we find a sharp crossover between the two behaviors. Therefore, the local Fano factor is mainly determined by the lowest excitation energy as it is usually the case for tunneling into a superconductor [118].

3.4. Coupling two quantum dots to a pair of Majorana bound states

In this section, we consider the full system containing two quantum dots and the pair of Majorana bound states. In the case $\Delta = 0$, the quasiparticle energy spectrum has levels at ϵ_M , $|\epsilon_R|$, and $|\epsilon_L|$, with avoided crossings where these levels intersect each other as shown in figure 3.4.1. If at least one of the quantum dot levels resides at the chemical potential of the superconductor, e.g. $\epsilon_L = 0$, we always find one zero-energy state described by the Majorana operators

$$\gamma_1 = \frac{t_L^* d_L^\dagger + t_L d_L}{|t_L|}, \quad (3.4.1a)$$

$$\gamma_2 = \frac{\sqrt{8}|t_L|(t_R^* d_R^\dagger + t_R d_R - \epsilon_R \gamma_R) + i \frac{\epsilon_M \epsilon_R}{|t_L|} (t_L^* d_L^\dagger - t_L d_L)}{\sqrt{\epsilon_R^2 \epsilon_M^2 + 8|t_L|^2(\epsilon_R^2 + 8|t_R|^2)}}. \quad (3.4.1b)$$

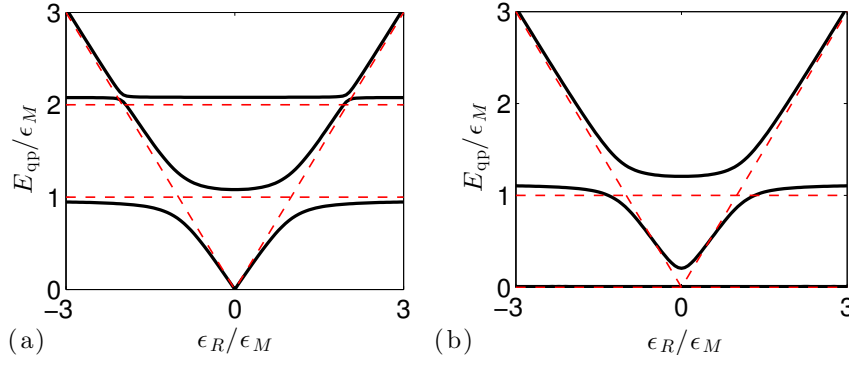


Figure 3.4.1.: Quasiparticle energy spectrum for the quantum dot–Majorana bound state–quantum dot system with $t_L = t_R = \epsilon_M/4$ as function of ϵ_R . (a) $\epsilon_L = 2\epsilon_M$ and (b) $\epsilon_L = 0$. The red dashed lines denote the uncoupled case $t_L = t_R = 0$. Note the existence of a zero-energy quasiparticle in panel (b) for all values of ϵ_R .

Here, γ_1 is localized on the resonant dot, while γ_2 is partially delocalized, and the weight of γ_2 on the resonant dot is determined by the energy ϵ_R of the nonresonant dot. In the limit $\epsilon_L = \epsilon_R = 0$ and $t_L = t_R = t \in \mathbb{R}$, the Majorana operators acquire a particularly simple form and we find

$$\gamma_1 = \frac{1}{\sqrt{2}}(d_L^\dagger + d_L), \quad \gamma_2 = \frac{1}{\sqrt{2}}(d_R^\dagger + d_R). \quad (3.4.2)$$

In this limit, both zero-energy Majorana operators are fully localized on the two separate quantum dots and thus form a nonlocal fermion state. Pictorially, we can understand the formation of the zero-energy Majorana states by considering a mechanism similar to the one in section 3.3. As sketched in figure 3.4.2, we can decompose the quantum dot fermion operators into a pair of Majorana operators each. In the limit $\epsilon_L = \epsilon_R = 0$, the two Majoranas in each dot are not coupled to each other, such that an uncoupled Majorana resides on the respective dot.

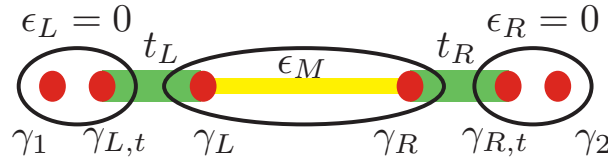


Figure 3.4.2.: Formation of the zero-energy Majorana operators for $\epsilon_L = \epsilon_R = 0$. The quantum dot fermion operators d_i and d_i^\dagger are decomposed into two Majorana operators each. Due to the peculiar coupling $(t_i^* d_i^\dagger - t_i d_i) \gamma_i$, only $\gamma_{i,t}$ is coupled to γ_i ($i = L, R$) while γ_1 and γ_2 commute with the Hamiltonian indicating zero energy.

The superconducting pairing potential Δ gives rise to the formation of quasiparticles which are superpositions of electron and hole components from different quantum dots. Thus, it couples the quantum dots if they are close to the chemical potential of the superconductor, i.e., for $|\epsilon_L|, |\epsilon_R| < |\Delta|$, or if they are anti-symmetrically aligned, i.e. for $\epsilon_L = -\epsilon_R$. As a consequence, for $\epsilon_L = \epsilon_R = 0$, the pairing term competes with the formation of the zero-energy Majorana states and therefore gives rise to an effective Majorana energy splitting Δ which couples the zero-energy Majorana operators in Eq. (3.4.2).

3.4.1. Weak quantum dot–lead coupling

We begin our analysis of charge transport through the quantum dot–Majorana bound state–quantum dot system in the regime $\Delta = 0$ and $\Gamma \ll t < \epsilon_M$. In figure 3.4.3, both differential conductance and cross-correlations S_{LR} are displayed as a function of bias voltage for several characteristic points in the ϵ_L – ϵ_R plane. The differential conductance is peaked at the eigenenergies of the Bogoliubov-de Gennes Hamiltonian in Eq. (3.1.4). The peak width is determined by the level broadening Γ and the quantum dot–Majorana coupling t . If one of the dot levels is aligned with the chemical potential of the superconductor, say $\epsilon_L = 0$, we always find a zero-bias peak with height

$$G_0 = \frac{4e^2}{h} \frac{1}{1 + \frac{\epsilon_M^2}{|8t_L t_R|^2} \left(\epsilon_R^2 + \frac{\Gamma^2}{4} \right)} \quad (3.4.3)$$

because of the existence of the induced Majorana states Eq. (3.4.2). For details about the derivation of Eq. (3.4.3), we refer to Appendix B.4.

In the special limit $\epsilon_L = \epsilon_R = 0$, the zero-voltage differential conductance is approximately quantized with value $4e^2/h$ which is identical to the zero-energy limit of Eq. (3.2.5) for two uncoupled Majoranas and hence describes two zero-energy Majorana states, one at each end of the nanowire. For $\epsilon_R \neq 0$, we find that the differential conductance is suppressed since in this limit both Majorana zero-energy states have finite weight on the left quantum dot and thus, destructive interference reduces the differential conductance, similar to the situation in section 3.3 for a single quantum dot coupled to one of the Majorana bound states. Since the existence of zero-energy Majorana states implies a strongly reduced coupling between the ends of the nanowire, we find that these resonances yield only a small contribution to the cross-correlations despite their large conductance.

In contrast, we do not find a zero-bias conductance peak if both quantum dots are non-resonant. In this regime, there is a striking difference between symmetric ($\epsilon_L = \epsilon_R$) and

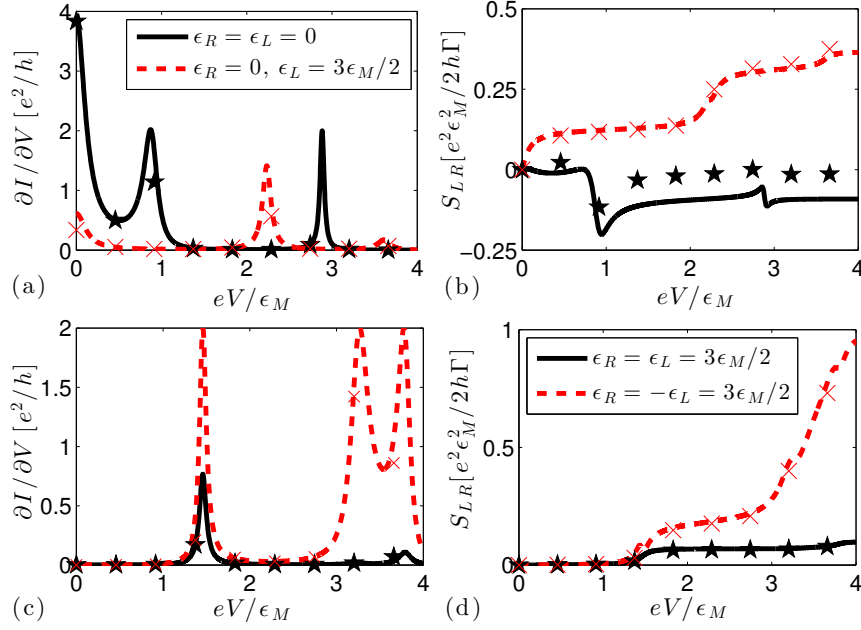


Figure 3.4.3.: Current cross-correlations S_{LR} in the weak quantum dot-lead coupling regime with $\Gamma = \epsilon_M/8$, $t = 2\epsilon_M/5$, and $\Delta = 0$. The lines for panel (b) are defined in (a), those for panel (c) in (d). The \times and \star markers denote the results for the spinless superconductor model with $\epsilon_M = 0.01$ meV and $\Gamma = \epsilon_M/5$.

antisymmetric ($\epsilon_L = -\epsilon_R$) positions of the dot levels. In both cases, we find contributions to the differential conductance and S_{LR} due to the hybridization between the quantum dots and the Majorana bound state. However, in the antisymmetric case both the differential conductance and S_{LR} are much larger than in the symmetric case, and additional resonances close to the quantum dot energies contribute to cross-correlations. This is due to the fact that Cooper pairs have zero energy, which leads to a suppression of transmission through two quantum dot levels which have both the same energy in the symmetric case, but allows passage through quantum dots with opposite level energies in the antisymmetric case.

As shown in figure 3.4.3, these findings agree very well with results for the microscopic model of a spinless p -wave superconductor defined in Eq. (3.4.6). The only small deviation in S_{LR} can be seen if both quantum dots are tuned to the chemical potential of the superconductor, where the effective model has a small negative S_{LR} for large bias voltage, while it approaches zero for the microscopic model. This deviation has its origin in the presence of an additional transport channel due to a proximity coupling Δ in the microscopic model, which in principle could be described by the Hamiltonian H_S in Eq. (3.1.1c), but which is not included in the effective model $H = H_M + H_D$ considered in this section.

3.4.2. Strong quantum dot–lead coupling

In this section, we consider the case $t < \epsilon_M \ll \Gamma$ and begin with the situation $\Delta = 0$. In figure 3.4.4(a), we show the current cross-correlations S_{LR} for $\epsilon_M \ll eV = \Gamma/2$ in the ϵ_L - ϵ_R plane. We find a characteristic four-leaf clover feature with a suppression of cross-correlations along lines with either $\epsilon_L = 0$ or $\epsilon_R = 0$, and peaks at $|\epsilon_L| = |\epsilon_R| \approx \Gamma/2$. The height of the peaks scales like ϵ_M^2/Γ and therefore directly reflects the Majorana energy splitting. The width of the clover feature is determined by the broadening Γ and hence much larger than the Majorana energy splitting. Similarly to the situation in the last section, we find a suppression of the cross-correlations along $\epsilon_L = 0$ and $\epsilon_R = 0$ which is mediated by the formation of zero-energy Majorana states by virtue of the quantum dot–Majorana bound state coupling.

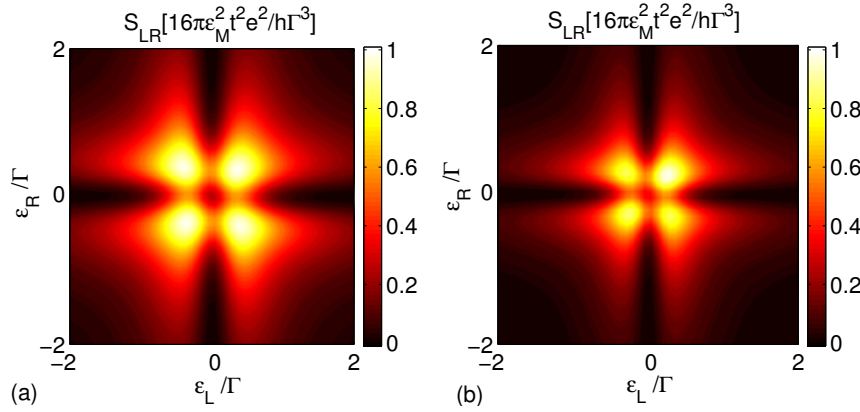


Figure 3.4.4.: Current cross-correlations S_{LR} for strong quantum dot–lead coupling. (a) Effective model with $eV = \Gamma/2$, $t = \Gamma/20$, $\epsilon_M = \Gamma/5$, and $\Delta = 0$. (b) Spinless superconductor with $\epsilon_M = 0.01$ meV and $\Gamma = 3\epsilon_M$. For both (a) and (b), the pattern changes little for larger bias voltages.

We find an approximate symmetry between symmetric and antisymmetric positions of the quantum dot levels. This symmetry was absent in the weak-coupling limit $\Gamma \ll t$ and can be understood as follows. For $\Gamma \gg t$, the quantum dots are strongly coupled to the lead electrodes and effectively become part of them. As a consequence, there are no separate resonances at the positions of the quantum dot levels anymore, and only a single resonance due to the Majorana bound states in the topological superconductor nanowire survives. The broadening of this resonance is renormalized by the quantum dot–lead coupling and becomes t^2/Γ , which is much smaller than Γ . As the quantum dot levels can neither resolve this small broadening of the resonance, nor resolve the location of the resonance, the distinction between symmetric and antisymmetric quantum dot levels becomes blurred, and the approximate symmetry arises. On the other hand, the emergence of the Majorana

zero-energy state Eq. (3.4.1), which appears for $\epsilon_L = 0$ or $\epsilon_R = 0$ and resides on the respective quantum dot, is not qualitatively affected by the large broadening Γ , and the current cross-correlations are still suppressed in this case, giving rise to the four-leaf clover pattern in figure 3.4.4(a).

In figure 3.4.4(b), we complement these findings for the low-energy model with results for the microscopic model Eq. (3.4.6) for a spinless p -wave superconductor, for which a similar four-leaf clover structure emerges. However, similarly to the weak quantum dot–lead coupling regime, there are small deviations with respect to the effective model near $\epsilon_L = \epsilon_R = 0$, mediated by the superconducting proximity effect.

To gain insight into the effect of an additional proximity term H_S , we first discuss the situation without Majorana bound state, $H = H_D + H_S$. In figure 3.4.5(a), we show the cross-correlations for the superconducting proximity case. Here, S_{LR} has a single peak of height $\propto \Delta^2/\Gamma$ near $\epsilon_L = \epsilon_R = 0$, with broadening Γ along the direction $\epsilon_L = \epsilon_R$, and width eV along the direction $\epsilon_L = -\epsilon_R$. In contrast to the Majorana bound state case, there is no additional structure in this peak. For details about the transport properties of mediated by the superconducting proximity effect, we refer to Appendix B.5.

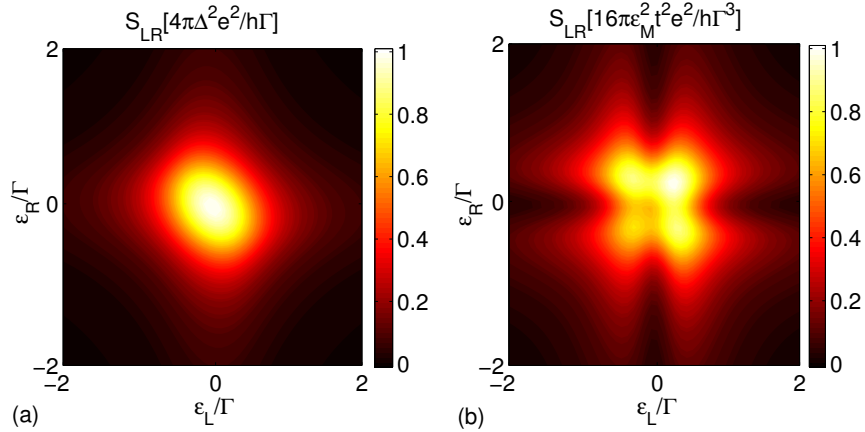


Figure 3.4.5.: Current cross-correlations S_{LR} for $eV = \Gamma/2$. The quantum dots are coupled (a) via the superconducting proximity effect with $\Delta = \Gamma/10$ and (b) via superconducting proximity effect and with coupling to a pair of Majorana bound state with $t = \Gamma/20$, $\Delta = \Gamma/20$, and $\epsilon_M = \Gamma/5$.

In figure 3.4.5(b), we consider the combined Hamiltonian $H = H_M + H_D + H_S$ which allows for crossed Andreev reflection via the Majorana bound states and additionally via the superconducting proximity effect. As function of quantum dot energy levels, we also find a four-leaf clover feature similar to the case $\Delta = 0$ studied above. However, here we find that the center of this feature acquires a peak of height Δ^2/Γ due to the proximity term in H_S . From this, we conclude that the contributions from the superconducting proximity

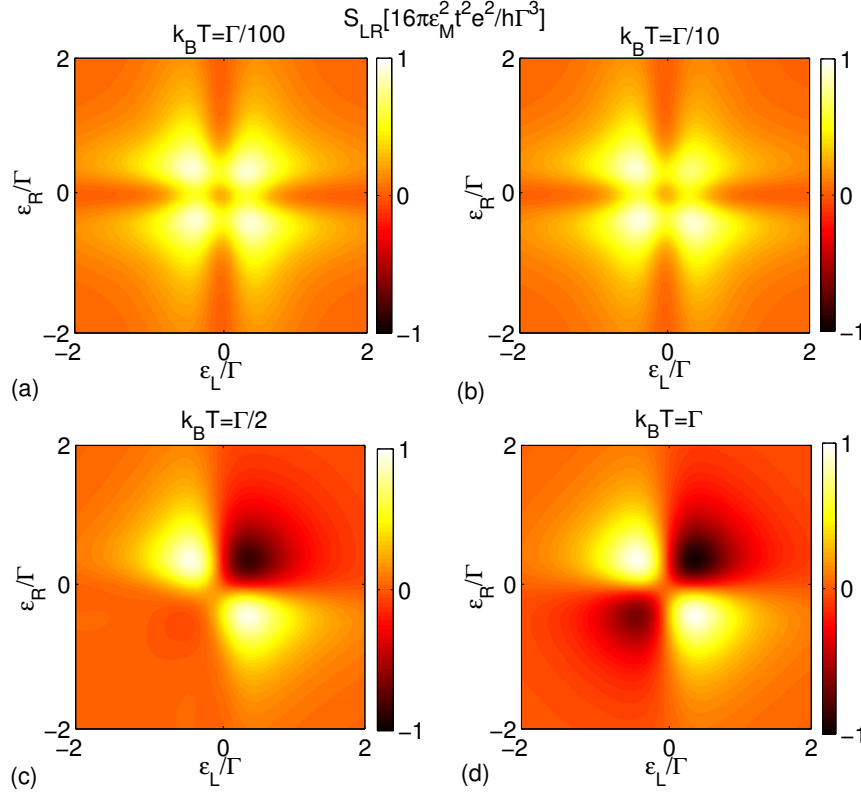


Figure 3.4.6.: Finite temperature current cross-correlations S_{LR} for strong dot-lead coupling with $eV = \Gamma/2$, $t = \Gamma/20$, $\epsilon_M = \Gamma/5$, and $\Delta = 0$. (a) $k_B T = 0$, (b) $k_B T = \Gamma/10$, (c) $k_B T = \Gamma/2$, and (d) $k_B T = \Gamma$. In our numerical calculations, we used an energy cutoff $\epsilon_c = 5eV$ in the energy integrals of Eq. (3.1.8).

effect and the Majorana bound state mediated crossed Andreev reflection approximately add up. The relative peak heights in the cross-correlations reflect the ratio of Δ^2 and ϵ_M^2 .

3.4.3. Effect of finite temperatures

In this section, we study the current cross-correlations through the quantum dot–Majorana bound states–quantum dot device for finite temperatures T . We determine the current and the current correlations for finite T using the finite temperature expressions in Eq. (3.1.8). As shown in figure 3.4.6(a), for $k_B T \ll eV$ the cross-correlations show the characteristic four-leaf clover feature with equal peak heights. With increasing temperature [Figures 3.4.6(b) and (c)] the amplitude of the symmetrically arranged peaks in the cloverlike pattern decreases and becomes negative while the height of the anti-symmetrically arranged peaks remains constant. Here, we observe that finite temperatures break the 90° rotation symmetry of the cross-noise pattern. For $k_B T \geq eV$, the cross-correlations also

show a cloverlike pattern, but now with negative height for symmetric and positive height for antisymmetric dot levels. We attribute the negative cross-correlations for symmetric dot levels $\epsilon_L \approx \epsilon_R$ to resonant tunneling of electrons and holes. For antisymmetric dot levels $\epsilon_L \approx -\epsilon_R$, this resonant tunneling is suppressed and crossed Andreev reflection with zero total Cooper pair energy is enhanced, giving rise to positive cross-correlations. Hence, we conclude that for $k_B T > \Gamma$ the pattern from figure 3.4.4(a) is modulated in such a way that the peaks for symmetric dot levels become negative of same height.

Above, we have found that for $T = 0$ the cross-correlations are significantly reduced when at least one of the dot levels lies at the chemical potential of the superconductor. For $k_B T \geq \Gamma$, this suppression becomes complete with vanishing cross-correlations along the lines $\epsilon_L = 0$ and $\epsilon_R = 0$.

3.4.4. Amplitude of the current cross-correlations

For zero temperature, we find the maxima of the cloverlike pattern at $|\epsilon_L| = |\epsilon_R| = \Gamma/2$ with amplitude

$$S_{LR,\max}^M = 8\pi \frac{2e^2}{h} \frac{\epsilon_M^2 t_M^2}{\Gamma^3} \quad (3.4.4)$$

for $\epsilon_M, t_M \ll \Gamma$. This analytical result is exact for zero temperature. However, for finite temperatures the cross-correlations are still proportional to the Majorana energy splitting ϵ_M^2 which is also confirmed by the numerics in figure 3.4.7 where we plot the Majorana bound state mediated cross noise as function of ϵ_M . In particular, we find that the cross-correlations vanish for vanishing Majorana energy splitting independent of temperature.

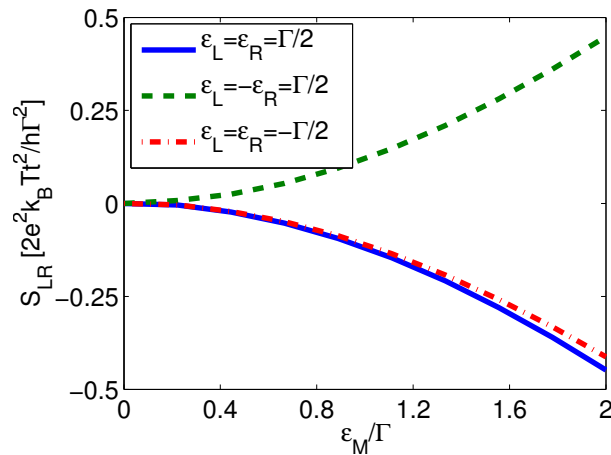


Figure 3.4.7.: Current cross-correlations S_{LR} for strong quantum dot-lead coupling with $eV = \Gamma/2$, $t = \Gamma/20$, $\epsilon_M = \Gamma/10$, $\Delta = 0$, and $k_B T = \Gamma$ as function of the Majorana energy splitting ϵ_M .

For cross-correlations induced by the standard superconducting proximity effect, we find for the case $eV/\Gamma \rightarrow \infty$ a maximum along $\epsilon_L + \epsilon_R = 0$ with amplitude

$$S_{LR,\max}^S = 2\pi \frac{2e^2}{h} \frac{\Delta^2}{\Gamma} \quad (3.4.5)$$

for $\Delta \ll \Gamma$. Thus, the current cross-correlations vanish for $\Delta = 0$ similarly to the Majorana bound state case. For details about the system in which the topologically nontrivial nanowire is replaced by an ordinary superconductor and the derivation of Eq. (3.4.5), we refer to Appendix B.5.

3.4.5. Spinless p -wave superconductor

We complement our calculations for the effective low-energy Majorana model by the analysis of a microscopic lattice model for a spinless p -wave superconductor with Hamiltonian [76],

$$H_K = - \sum_{j=1}^{N-1} \left(t_K c_{j+1}^\dagger c_j + \Delta_K c_j c_{j+1} + \text{H.c.} \right) - \mu_K \sum_j^N c_j^\dagger c_j, \quad (3.4.6)$$

where the c_j annihilate a spinless fermion on site j with nearest-neighbor hopping t_K and nearest-neighbor pairing amplitude Δ_K . This model describes the low-energy physics of a nanowire in the topologically nontrivial phase. In the numerical analysis, we use the parameters $L = 1000$ nm for the nanowire length, $N = 200$ sites, $t_K = 20$ meV, $\Delta_K = 0.8$ meV, and $\mu_K = 39.4$ meV. These parameter values yield the superconducting gap $\Delta_{\text{SC}} = 0.3$ meV and the Majorana energy splitting $\epsilon_M = 0.01$ meV. For the coupling of the operators c_1 and c_N to the dots, we use $t_{D,K} = 0.025$ meV. The results for this model agree very well with those for the effective model Eq. (3.1.1) as can be seen from figures 3.4.3 and 3.4.4.

In addition, we study the effect of additional transverse channels N_\perp in the nanowire and estimate a critical channel number for which the cross-correlations induced by the proximity effect and the Majorana bound state are equal. The coupling Hamiltonian between a multichannel nanowire and a quantum dot can be written as

$$H_T = T_{SD} \left(d^\dagger \psi(\mathbf{r} = \mathbf{0}) + \psi^\dagger(\mathbf{r} = \mathbf{0}) d \right), \quad (3.4.7)$$

where d ($\psi(\mathbf{r} = \mathbf{0})$) denotes the annihilation operator for the dot (nanowire at site $\mathbf{r} = \mathbf{0}$) and T_{SD} the coupling matrix element. We decompose the operator $\psi(\mathbf{r} = \mathbf{0})$ into Majorana

bound state and delocalized states,

$$\psi(\mathbf{r} = \mathbf{0}) = \frac{\gamma_L}{\sqrt{2\xi}} + \frac{1}{\sqrt{L}} \sum_{k,n; E_k > 0} \psi_{k,n} \quad (3.4.8)$$

where $\psi_{k,n}$ denotes the operator for an electron with transverse channel index n and longitudinal momentum k . If the energy difference between the subbands is larger than the superconducting gap, we write the coupling Hamiltonian Eq. (3.4.7) as sum of the coupling between the dot and the Majorana bound state and the coupling between the dot and the Bogoliubov quasiparticles,

$$H_T = \frac{T_{SD}}{\sqrt{2\xi}} (d^\dagger - d) \gamma_L + \frac{T_{SD}}{\sqrt{L}} \sum_{n,k; E_k \geq \Delta_{SC}} \left(\psi_{n,k}^\dagger d + d^\dagger \psi_{n,k} \right). \quad (3.4.9)$$

Hence, we find the quantum dot–Majorana bound state coupling strength $t_M = T_{SD}/\sqrt{2\xi}$ and the quantum dot–quasiparticle coupling strength $t_S = T_{SD}/\sqrt{L}$.

In the previous section, we have determined the amplitude of the current cross-correlations mediated by Majorana bound state and the superconducting proximity effect. Using this result, we find that the relative strength of the Majorana and the proximity induced cross noise is determined by the ratio of Eqs. (3.4.4) and (3.4.5). There, the Majorana energy splitting is

$$\epsilon_M \approx \Delta_{SC} \sin(k_F L) e^{-L/\xi} \quad (3.4.10)$$

and the proximity induced pairing potential is

$$\Delta \approx \rho_S t_S^2 \cos(k_F L) e^{-L/\xi}, \quad (3.4.11)$$

where Δ_{SC} denotes the quasiparticle gap, k_F the Fermi momentum, and $\rho_S = L N_\perp / 2\pi v_F$ the normal-state density of states of the nanowire [108]. For details about the analytical derivation of the expressions for the Majorana energy splitting ϵ_M in Eq. (3.4.10) and the proximity induced superconducting pairing Δ between the quantum dots in Eq. (3.4.11), we refer to Appendices B.2 and B.3.

In the following, we approximate the sin and the cos term by one and only compare the maxima of Δ and ϵ_M . With v_F denoting the Fermi velocity and N_\perp denoting the number of partially occupied transverse channels, this yields

$$\frac{S_{LR}^M}{S_{LR}^S} = \left(\frac{4\pi v_F \Delta_{SC}}{N_\perp T_{SD} \sqrt{\xi} \Gamma} \right)^2. \quad (3.4.12)$$

For the observation of the clover like pattern in the current cross-correlations, we demand that the Majorana bound state mediated cross noise is larger than the one mediated by the superconducting proximity effect, i.e., $S_{LR}^M > S_{LR}^S$. In this way, we obtain the condition that

$$N_{\perp} < 4\pi \frac{v_F \Delta_{SC}}{\sqrt{\xi} T_{SD} \Gamma}. \quad (3.4.13)$$

For the parameters used in figure 3.4.4(b), this yields the condition $N_{\perp} \leq 7$.

3.4.6. Realistic semiconductor-superconductor hybrid system

In the following, we study the current cross-correlations for the realistic semiconductor model introduced in section 3.1.3. In particular, we investigate the effect of small changes of the chemical potential or the external magnetic energy, different numbers of transverse channels, and nonmagnetic disorder on the cloverlike cross-correlation pattern. For details about the numerical diagonalization of the Hamiltonian, we refer to Appendices A.1 and A.2.

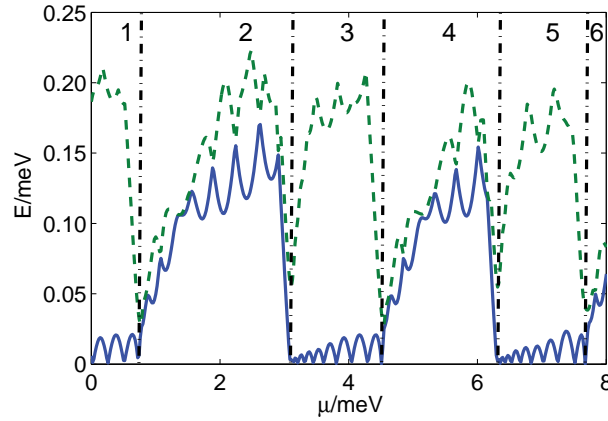


Figure 3.4.8.: Lowest quasiparticle energies of the semiconductor model as function of chemical potential μ . The numbers denote the number of partially occupied subbands. Even numbers correspond to the trivial superconducting phase with a quasiparticle gap $\sim \Delta_{\text{eff}}$. Odd numbers correspond to the nontrivial phase with an oscillating subgap state at ϵ_M . The transitions between odd and even numbers are characterized by a topological phase transition which shows up as closing and reopening of the quasiparticle excitation gap.

Variation of the chemical potential

In this section, we consider the influence of small changes of the chemical potential on the current cross-correlations. In figure 3.4.8, we plot the two lowest quasiparticle energies for

Hamiltonian Eq. (3.1.23). Here, a topologically nontrivial phase exists in sectors with a subgap state of energy $\epsilon_M \ll \Delta_{\text{eff}}$. This low-energy state corresponds to two coupled Majorana bound states with energy splitting ϵ_M . Such a state always exists if an odd number of subbands is partially occupied. As function of the chemical potential the Majorana energy splitting oscillates with period $2\pi v_F/L$ and with energy minima of $\epsilon_M = 0$.

In figure 3.4.9, we plot the current cross-correlations for two values of the chemical potential for which the Majorana energy splitting has a local maximum and a local minimum. We find that the patterns in the current cross-correlations are very different in the two cases, with a cloverlike pattern for $\epsilon_M \neq 0$ and an ellipsoidal pattern for $\epsilon_M = 0$. This is in full agreement with our findings that the Majorana induced current cross-correlations are proportional to ϵ_M^2 . Thus, we conclude that small variations of the chemical potential can be used as a tool to switch between different patterns of current cross-correlations. Such a switching mechanism does not exist in the topologically trivial phase and is thus a signature for Majorana bound states with oscillating Majorana energy splitting. The change of the chemical potential can be realized by applying a global gate voltage. An alternative route to demonstrate the oscillations is a change of the magnetic field which gives rise to oscillation of periodicity $\omega_B = 4\pi v_F/g\mu_B L$.

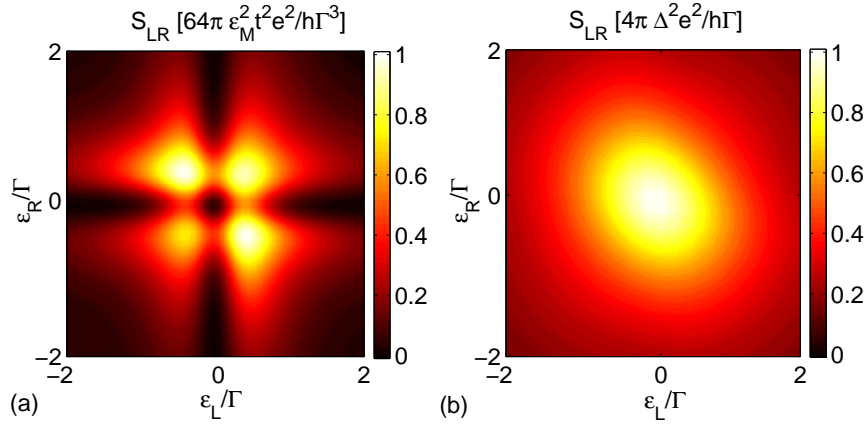


Figure 3.4.9.: Current cross-correlations S_{LR} for $T_{SD} = 0.12 \text{ meV} \cdot \text{nm}^{1/2}$ and $\Gamma = 0.04 \text{ meV}$. (a) Cloverlike pattern for $\mu = 0.1 \text{ meV}$ with $\epsilon_M = 0.01 \text{ meV}$ and (b) elliptic pattern for $\mu = 0$ with $\epsilon_M = 0.001 \text{ meV}$.

Above we have discussed that the proximity induced pairing oscillates as function of $k_F L$ which changes when changing the chemical potential. However, for the standard proximity coupling in semiconductor nanowires we do not find a unique Fermi momentum because of the spin-orbit coupling. Thus, the oscillation of the proximity induced pairing potential is smeared out and we always find a nonzero contribution of the superconducting proximity effect to the cross-correlations.

Multiband systems

Due to the finite extension of the nanowire in y direction, we expect to find a multiband system where the bands have a separation of several meV. For an even number of occupied transverse channels, the nanowire is in the topologically trivial phase, i.e., the Majorana bound states are absent and thus, we find a single ellipsoidal cross-noise pattern similar to the one in figure 3.4.5(a) where we studied the current cross-correlations through a pair of quantum dots with superconducting pairing. For an odd number of occupied transverse channels, the nanowire is in the topologically nontrivial phase with Majorana end states. In figure 3.4.10, current cross-correlations are shown for $\mu = 4.1$ meV and width 70 nm which corresponds to the three-band case and for $\mu = 6.1$ meV and width 90 nm which corresponds to the five-band case. In both case, we still find the characteristic four-leaf clover pattern in current cross-correlations, similar to the single-band case. However, the amount of noise for $\epsilon_L = \epsilon_R = 0$ is increased by a factor of ≈ 9 in the three-band system as compared to the single-band case, as expected from the estimate Eq. (3.4.12). This numerical finding confirms our analytical result Eq. (3.4.12) that the cloverlike pattern is not restricted to the single-band nanowire and can also be found in multiband nanowires.

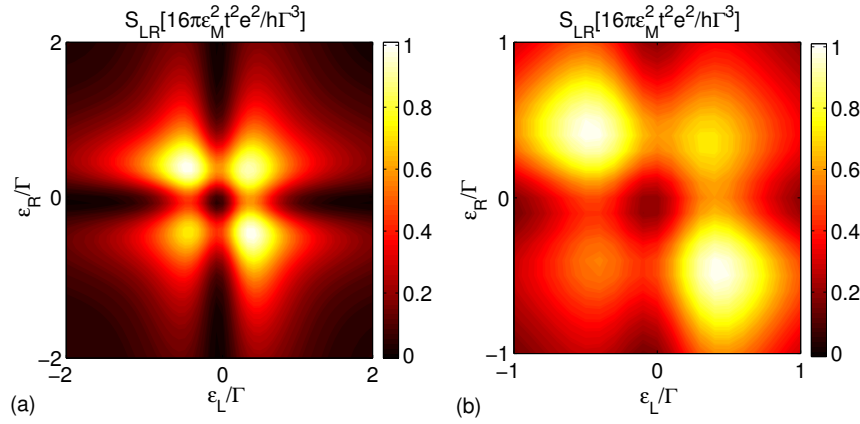


Figure 3.4.10.: Current cross-correlations S_{LR} for $T_{SD} = 4\sqrt{10}\epsilon_M \text{ nm}^{1/2}$ and $\Gamma = 4\epsilon_M$. (a) Three-band semiconductor of width 70 nm with $\mu = 4.1$ meV and (b) five-band semiconductor of width 90 nm with $\mu = 6.1$ meV.

Nonmagnetic disorder

In this section, we address the question of how robust the cross-correlation pattern is against nonmagnetic disorder. We consider a spatially fluctuating disorder potential with

mean value $\langle V(\mathbf{r}) \rangle = 0$ and random variations with

$$\langle V(\mathbf{r}')V(\mathbf{r}) \rangle = U^2\delta(\mathbf{r} - \mathbf{r}'). \quad (3.4.14)$$

We here consider the regime of disorder strengths $U \lesssim U_m$ with $U_m = \sqrt{\alpha\hbar\Delta_{\text{SC}}}$, since strong disorder $U \gg U_m$ breaks the nanowire into topological and nontopological domain walls and thereby gives rise to additional localized subgap states. For a detailed discussion of the physical interpretation of U_m , we refer to section 4.3.2. In figures 3.4.11(a) and (b), we display the disorder averaged current cross-correlations for disorder strengths $\Delta_{\text{SC}}\sqrt{a}/4$ and $\Delta_{\text{SC}}\sqrt{a}/2$. We here averaged over 50 random disorder configurations, and find that the cloverlike pattern is robust with respect to moderate nonmagnetic disorder.

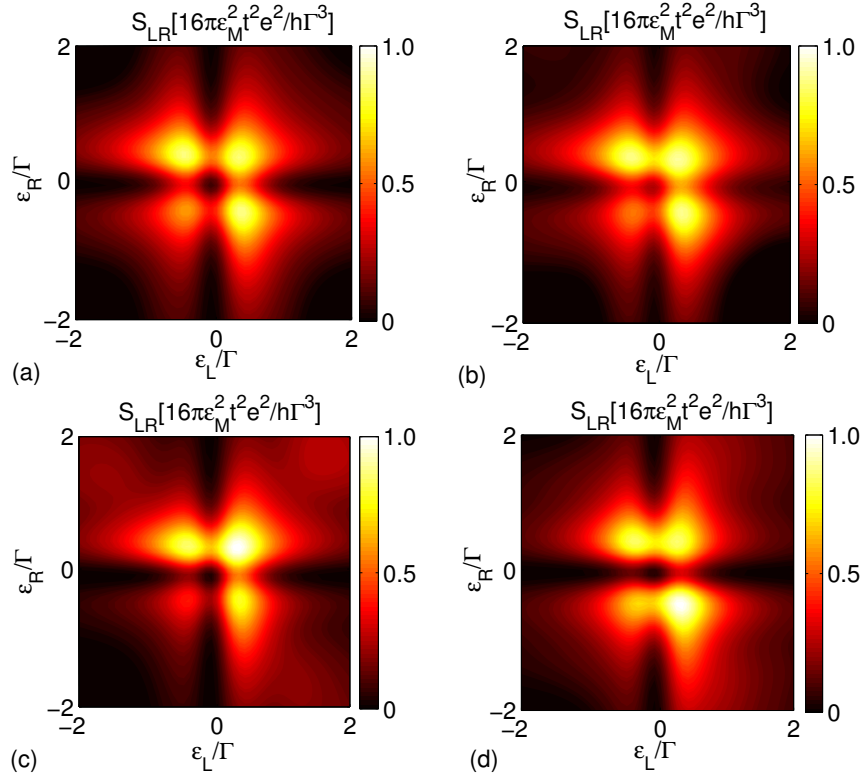


Figure 3.4.11.: Current cross-correlations S_{LR} of the single-band semiconductor model with $\mu = 0$ for various disorder strengths. Ensemble averaged cross-correlations for disorder strengths (a) $U = \Delta_{\text{SC}}\sqrt{a}/4$ and (b) $U = \Delta_{\text{SC}}\sqrt{a}/2$. Cross-correlations for a characteristic disorder realization with (c) $U = \Delta_{\text{SC}}\sqrt{a}/4$ and (d) $U = \Delta_{\text{SC}}\sqrt{a}/2$.

In figures 3.4.11(c) and (d), we display the current cross-correlations for single characteristic disorder configurations of strengths $U = \Delta_{\text{SC}}\sqrt{a}/4$ and $U = \Delta_{\text{SC}}\sqrt{a}/2$, respectively. When comparing the cross-correlations for a random configuration with the clean case, we find that nonmagnetic disorder distorts the cloverlike pattern and disorder averaging

averages over distortions which restores the cloverlike pattern as shown in figures 3.4.11(a) and (b).

Variation of the Zeeman field

In figure 3.4.12, we display the local and nonlocal current correlations and the corresponding Fano factors for the microscopic model of the semiconductor nanowire as function of Zeeman energy and voltage for $\epsilon_L = -\epsilon_R = \Delta_{\text{SC}}/10$. As discussed in chapter 2.5, the nanowire is in the topologically trivial phase for $E_Z^2 < \Delta_{\text{SC}}^2 + \mu^2$ and in the nontrivial phase for $E_Z^2 > \Delta_{\text{SC}}^2 + \mu^2$. We find different characteristic behavior of the current correlations in the topologically trivial and nontrivial superconducting phases.

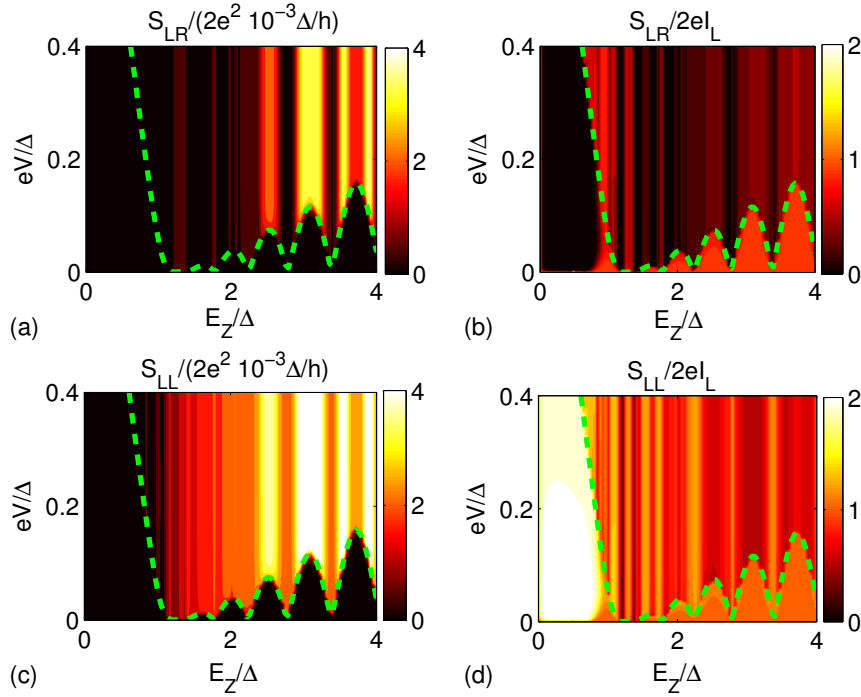


Figure 3.4.12.: (a) Current cross-correlations, (b) crossed Fano factor, (c) local current correlations in the left lead, and (d) Fano factor in the left lead for the microscopic model for $\epsilon_L = -\epsilon_R = \Delta_{\text{SC}}/10$ as function of magnetic field and voltage.

In the trivial phase for $E_Z^2 < \Delta_{\text{SC}}^2 + \mu^2$, the current correlations and the corresponding Fano factors are qualitatively similar to our findings in section 3.2 where the nanowire was directly coupled to the normal-conducting lead electrodes. In particular, we find that the cross-correlations as well as the crossed Fano factor vanishes and that the local Fano factor is two (one) for $eV \lesseqgtr \sqrt{\Delta_{\text{SC}}^2 + \mu^2} - E_Z$ and drops to one above this threshold. In addition, we also find that the topological phase transition at $E_Z^2 = \Delta_{\text{SC}}^2 + \mu^2$ clearly shows up in the

local and the crossed Fano factors. In particular, the crossed Fano factor increases when $E_Z^2 \rightarrow \Delta_{\text{SC}}^2 + \mu^2$ due to the closing of the excitation gap in the nanowire, which gives rise to a divergence of the superconducting coherence length and thereby allows for crossed Andreev reflection processes via the bulk superconducting state.

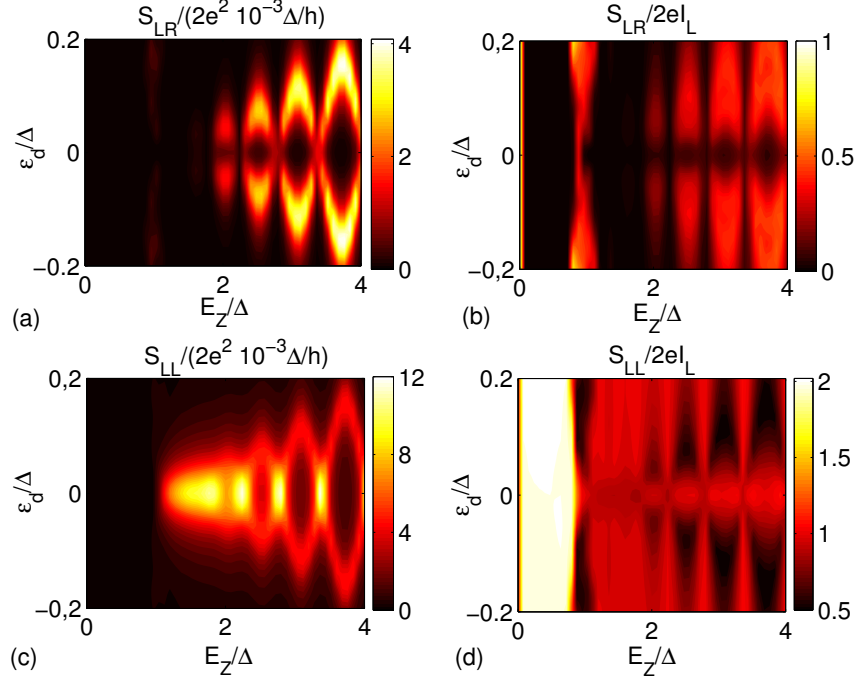


Figure 3.4.13.: (a) Current cross-correlations, (b) crossed Fano factor, (c) local current correlations in the left lead, and (d) Fano factor in the left lead for the microscopic model for $eV = \Delta_{\text{SC}}/5$ as function of magnetic field and quantum dot energy level $\epsilon_L = -\epsilon_R$.

In contrast, for $E_Z^2 > \Delta_{\text{SC}}^2 + \mu^2$ the nanowire is in the topologically nontrivial phase with a pair of split Majorana bound states at $\epsilon_M \sim \Delta_{\text{eff}} \exp(-L/\xi) \sin(k_F L)$ [see Appendix B.2 for details] which oscillates as function of magnetic field. In this phase, we find that the quantum dots qualitatively affect the cross-correlations as compared to the case without quantum dots. Our main observation is the existence of oscillating cross-correlations $S_{LR} \propto \epsilon_M^2$ for $eV \gg \epsilon_M$ which directly reflects the Majorana character of the subgap state.

In figure 3.4.13, we show the current correlations and the Fano factors for $eV = \Delta_{\text{SC}}/5$ as function of Zeeman energy and antisymmetric quantum dot energy $\epsilon_L = -\epsilon_R$. We find that both the cross-correlations and the crossed Fano factor show finite contributions for $eV > \epsilon_M$ and clearly display the oscillating Majorana energy splitting. In particular, we find that the cross-correlations are suppressed for $\epsilon_d \rightarrow 0$ and show a peak of height $\propto \epsilon_M^2$ for $|\epsilon_d| \approx \epsilon_M$. Similarly, we also find that the auto-correlations S_{LL} reflect the oscillating Majorana energy splitting.

3.4.7. Relation to previous work

In the recent work [119] (short LLS in the following), current cross-correlations in a setup similar to ours were studied by using the diagonalized master equation approach in the sequential tunneling regime. In particular, for $\epsilon_M = 0$ finite current cross-correlations were found, in disagreement with our result that current cross-correlations are proportional to ϵ_M^2 and should thus vanish in the limit $\epsilon_M \rightarrow 0$. In the following, we discuss possible reasons for this discrepancy.

The physical conditions under which the diagonalized master equation approach is justified are (i) that the bath correlation time is small compared to the relaxation time of the quantum dot–Majorana bound states–quantum dot device, i.e., weak coupling between the leads and the dot–Majorana bound state–dot system $\Gamma \ll k_B T$, and (ii) that the excitation energies ΔE within each parity sector are large compared to Γ [120]. For $\epsilon_M = 0$, the states with different parity are always degenerate, which should be unproblematic since the coherent superposition between these states is unimportant for electronic transport. However, for energies $\epsilon_M = \epsilon_L = \epsilon_R = 0$, LLS find in their Eq. (16) an additional degeneracy of the two lowest lying states in each sector, which is problematic since it violates condition (ii). Thus, we conclude that for the energy spectrum used by LLS the diagonalized rate equation approach is not appropriate in the vicinity of this point.

Nonetheless, if one forgoes the question of whether the diagonalized master equation approach is applicable, we can compare the single-particle energy spectrum we find by solving the Bogoliubov-de Gennes equations with the many-particle energy spectrum discussed by LLS when diagonalizing the Hamiltonian in the eight-dimensional many-body Fock space. Since parity is a good quantum number for the isolated dot–Majorana bound state–dot system, it is possible to decompose the Fock space into two four-dimensional subspaces with even and odd parity, and to diagonalize the Hamiltonian in each subspace separately. Then, the ground state is given by the vector with lowest energy, and the parity changing excitations are described by many-body wave functions with a parity different from that of the ground state. In particular, for $\epsilon_M = \epsilon_L = \epsilon_R = 0$ and $|t_L| = |t_R| = t$, LLS find in their Eq. (16) that the states for even and odd parity are degenerate, and that each sector has energies $\{-\sqrt{2}t, -\sqrt{2}t, \sqrt{2}t, \sqrt{2}t\}$. Thus, the excitation energies for parity changing excitations of the ground state are $\{0, 0, 2\sqrt{2}t, 2\sqrt{2}t\}$.

In contrast, in this thesis we use the Bogoliubov-de Gennes formalism to diagonalize the Hamiltonian. The Bogoliubov-de Gennes formalism is a single-particle formalism based on the single-particle Schrödinger equation and describes quasiparticle excitations above the ground state. Since the Bogoliubov-de Gennes formalism doubles the physical Hilbert space, only three out of the six eigenvalues obtained by diagonalizing the Hamiltonian

Eq. (3.1.4) are independent solutions. Excited states can be constructed by adding one quasiparticle (three possible states), two quasiparticles (three possible states), or three quasiparticles (one state). Thus, together with the ground state, these states span an eight-dimensional Fock space, in agreement with LLS. Using the Bogoliubov-de Gennes formalism, we find for parameters $\epsilon_M = \epsilon_L = \epsilon_R = 0$ the single-particle excitation energies $\{0, 2t, 2t\}$, and as a consequence the three-particle excitation energy $4t$. Thus, the energy difference between the many-body ground state and parity changing excited states should be $\{0, 2t, 2t, 4t\}$, different from the excitation spectrum obtained above by using the energies of LLS. This discrepancy in the energy spectrum casts additional doubt on the results of LLS and their interpretation. In addition, even when using the correct energy spectrum, there exist degeneracies between excited states within each parity sector for the choice of parameters $|\epsilon_R| = |\epsilon_L|$, where the current cross-correlations are strongest. Therefore, it seems that the applicability of the diagonalized rate equation approach to the three-terminal quantum dot–Majorana bound states–quantum dot device is limited.

3.5. Spinful quantum dots with finite Coulomb repulsion

Above, we have investigated the effect of coupling quantum dots to Majorana bound states with a nonzero Majorana energy splitting ϵ_M in sections 3.3 and 3.4. There, we have assumed that the quantum dots are fully spin polarized and that the Coulomb charging energy of the quantum dots is infinitely large. We have shown that, when aligning the quantum dots with the chemical potential of the superconductor, a pair of exactly zero-energy Majorana states is induced on the quantum dots. In addition, we have shown that the induced pair of Majorana operators significantly affects the nonlocal transport properties of the three-terminal normal-state–quantum dot–Majorana bound states–quantum dot–normal-state device.

In this section, we study the effect of finite Coulomb repulsion on the induced Majorana states. For that purpose, we modify the Hamiltonian for the quantum dots by considering spinful quantum dots with finite Coulomb repulsion. Hence, we replace the Hamiltonian H_D from Eq. (3.1.1b) by

$$H_D = \sum_{i=L,R} \left(H_{D,i} + H_{T,i} \right) \quad (3.5.1)$$

with

$$H_{D,i} = \sum_{\sigma=\uparrow,\downarrow} \epsilon_{i\sigma} d_{i\sigma}^\dagger d_{i\sigma} + U_i d_{i\uparrow}^\dagger d_{i\uparrow} d_{i\downarrow}^\dagger d_{i\downarrow}, \quad (3.5.2a)$$

$$H_{T,i} = \sum_{\sigma=\uparrow,\downarrow} \left(t_{i\sigma} d_{i\sigma}^\dagger \gamma_i + t_{i\sigma}^* \gamma_i d_{L\sigma} \right). \quad (3.5.2b)$$

The operator $H_{D,i}$ denotes the Hamiltonian for the quantum dot i with the fermion annihilation (creation) operators $d_{i\sigma}$ ($d_{i\sigma}^\dagger$) with spin σ . The quantum dots are characterized by the single-particle energy levels $\epsilon_{i\sigma}$ and the Coulomb energy $U_i > 0$ which penalizes double occupancy. The operator $H_{T,i}$ denotes the coupling Hamiltonian with coupling strength $t_{i\sigma}$ between the quantum dot i and the corresponding Majorana bound state γ_i . In figure 3.5.1, we show a schematic illustration of the system.

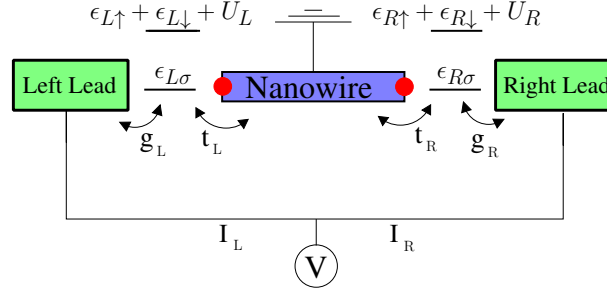


Figure 3.5.1.: Schematic setup of a topological superconductor nanowire with a pair of Majorana end states (red dots) coupled to quantum dots. The quantum dots are characterized by single-particle levels $\epsilon_{i\sigma}$ and by the Coulomb energy U_i for $i = L, R$. The parameter t_i is the coupling between the quantum dot i and Majorana i .

In total, the system now contains the four fermions describing the two quantum dots and one fermion describing the Majorana bound states. Each of these five fermions is defined on a two-dimensional Hilbert space \mathcal{F}_λ which is spanned by the basis vectors for zero and single occupancy. Hence, Hamiltonian $H = H_M + H_D$ itself is defined on a 2^5 -dimensional Hilbert space $\mathcal{F} = \bigotimes \mathcal{F}_\lambda$ where \bigotimes denotes the direct product. The Hamiltonian does not conserve particle number since Majorana bound states are an equal superposition of electron and hole degrees of freedom. However, the Hamiltonian commutes with the parity operator

$$\mathcal{P} = (1 - 2f^\dagger f) \prod_{i,\sigma} (1 - 2d_{i\sigma}^\dagger d_{i\sigma}), \quad (3.5.3)$$

and hence conserves particle number modulo two. The reason for the vanishing of the commutator of H and \mathcal{P} is that all individual terms in the Hamiltonian contain two fermion

operators. Since each fermion operator changes the parity, two fermion operators change the parity twice which is equivalent to no change of the parity. Because of this commutation relation, the Hilbert space can be decomposed into two 2^4 -dimensional subspaces \mathcal{F}_e and \mathcal{F}_o with even and odd parity, i.e., $\mathcal{F} = \mathcal{F}_e \oplus \mathcal{F}_o$ where \oplus denotes the direct sum of two vector spaces. Here, even parity corresponds to $\mathcal{P}\psi_e = +\psi_e$ for $\psi_e \in \mathcal{F}_e$ and odd parity corresponds to $\mathcal{P}\psi_o = -\psi_o$ for $\psi_o \in \mathcal{F}_o$.

To diagonalize the Hamiltonian for arbitrary parameters, we use an unbiased exact diagonalization technique. For that purpose, we construct two classes of ansatz wave functions with even and odd parity,

$$|\psi^e\rangle = \left[u^{(e)} + \sum_{a<b} v_{ab}^{(e)} a^\dagger b^\dagger + \sum_{a<b<c<d} w_{abcd}^{(e)} a^\dagger b^\dagger c^\dagger d^\dagger \right] |0\rangle, \quad (3.5.4a)$$

$$|\psi^o\rangle = \left[\sum_a u_a^{(o)} a^\dagger + \sum_{a<b<c} v_{abc}^{(o)} a^\dagger b^\dagger c^\dagger + w^{(o)} d_{L\uparrow}^\dagger d_{L\downarrow}^\dagger f^\dagger d_{R\uparrow}^\dagger d_{R\downarrow}^\dagger \right] |0\rangle. \quad (3.5.4b)$$

Here, the summation indices correspond to the fermion operators $\{d_{L\uparrow}^\dagger, d_{L\downarrow}^\dagger, f^\dagger, d_{R\uparrow}^\dagger, d_{R\downarrow}^\dagger\}$ and we formally introduce an order of fermion operators, $d_{L\uparrow}^\dagger < d_{L\downarrow}^\dagger < f^\dagger < d_{R\uparrow}^\dagger < d_{R\downarrow}^\dagger$. The ket vector $|0\rangle$ denotes the vacuum which is defined by $d_{L\sigma}|0\rangle = f|0\rangle = d_{R\sigma}|0\rangle = 0$ for $\sigma = \uparrow (\downarrow)$. In total, each wave function for odd and for even parity is characterized by 16 coefficients (u_i, v_j, w_k) . We then derive the many-body Schrödinger equation by minimizing the energy expectation values $\langle\psi^e|H|\psi^e\rangle$ and $\langle\psi^o|H|\psi^o\rangle$ with respect to the coefficients (u_i, v_j, w_k) . By solving both resulting matrix equations, we find the ground state and all excited states. This is an exact diagonalization method in the many-particle Hilbert space which yields the full energy spectrum and the corresponding wave functions. We note that by applying this method to the bilinear Hamiltonians in Eq. (3.1.1) studied above and simplifying the matrices consequently, we obtain exactly the Bogoliubov-de Gennes equations in Eq. (3.1.4).

3.5.1. One spinful quantum dot coupled to a Majorana bound state

In the following, we consider the situation where one Majorana bound state is coupled to a quantum dot, i.e., $H_{T,R} = 0$. The Hilbert space for this system is eight-dimensional containing four states with even and four states with odd parity, respectively. For this system, the ansatz wave functions $|\psi^e\rangle$ and $|\psi^o\rangle$ for the even and odd parity states become

particularly simple,

$$|\psi^e\rangle = \left[u^{(e)} + v_{\uparrow\downarrow}^{(e)} d_{L\uparrow}^\dagger d_{L\downarrow}^\dagger + v_{\uparrow f}^{(e)} d_{L\uparrow}^\dagger f^\dagger + v_{\downarrow f}^{(e)} d_{L\downarrow}^\dagger f^\dagger \right] |0\rangle, \quad (3.5.5a)$$

$$|\psi^o\rangle = \left[u_{\uparrow}^{(o)} d_{L\uparrow}^\dagger + u_{\downarrow}^{(o)} d_{L\downarrow}^\dagger + u_f^{(o)} f^\dagger + v_{\uparrow\downarrow f}^{(o)} d_{L\uparrow}^\dagger d_{L\downarrow}^\dagger f^\dagger \right] |0\rangle. \quad (3.5.5b)$$

For $\epsilon_{L\uparrow} = \epsilon_{L\downarrow} \equiv \epsilon_d$ and $t_{L\downarrow}^2 = t_{L\uparrow}^2 \equiv t^2$, we solve the many-body Schrödinger equation and we find the energies

$$E_{1,\pm,p} = \frac{1}{2} \left[\epsilon_M + \epsilon_d \pm \sqrt{8t^2 + (\epsilon_d + p\epsilon_M)^2} \right], \quad (3.5.6a)$$

$$E_{2,\pm,p} = \frac{1}{2} \left[\epsilon_M + U + 3\epsilon_d \pm \sqrt{(U + \epsilon_d - p\epsilon_M)^2 + 8t^2} \right], \quad (3.5.6b)$$

where even (odd) parity corresponds to $p = +1$ ($p = -1$). The energies are mainly determined by the energies of the left quantum dot $\{0, \epsilon_d, 2\epsilon_d + U\}$ and the energies of the Majorana level $\{0, \epsilon_M\}$. When these energies cross, the coupling t splits some of them and gives rise to avoided level crossings in the energy spectrum. In figure 3.5.2, we show the eigenenergies and the energies of the parity changing excitations as function of the quantum dot level ϵ_d . We here concentrate on parity changing excitations since they are the relevant excitations in transport processes. While the energy spectrum itself does not look very symmetric, the spectrum for parity changing excitations is mirror-symmetric around $\epsilon_d = -U/2$. The origin for the mirror symmetry is the particle-hole symmetry ($d_{L\sigma} \leftrightarrow d_{L\sigma}^\dagger$) of Hamiltonian Eq. (3.5.1) with the replacements $U \rightarrow -U$ and $\epsilon_d \rightarrow \epsilon_d + U$.

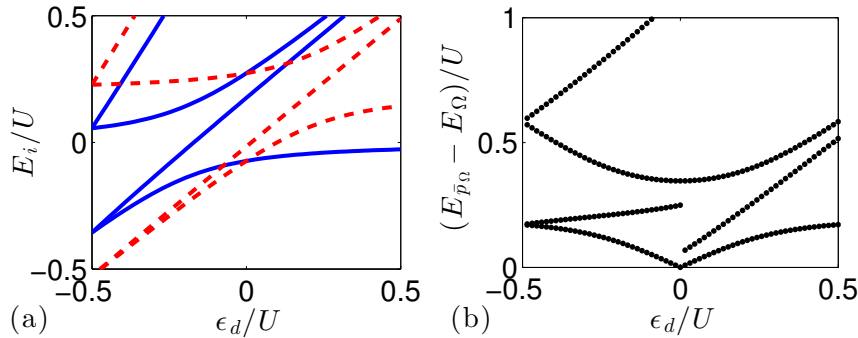


Figure 3.5.2.: (a) Energies $E_{i,\pm,\pm}$ of the quantum dot-Majorana bound state system for even parity (solid lines) and odd parity (dashed lines). (b) Excitation energies for parity changing excitations between the ground state and the lowest excited states. The excitation spectrum is mirror symmetric around $\epsilon_d = -U/2$. The system parameters are $\epsilon_M = t_{L\sigma} = U/10$ and $\epsilon_{L\uparrow} = \epsilon_{L\downarrow} \equiv \epsilon_d$.

The ground state shows different characteristic behavior in the three regimes (i) $\epsilon_d < -U$,

(ii) $-U < \epsilon_d < 0$, and (iii) $\epsilon_d > 0$. In our discussion of the energy spectrum, we focus on the limit $0 < t \ll \epsilon_M \ll U$, in which we can identify the eigenstates with the occupation of the bare fermion states. The regime (i) $\epsilon_d < -U$ is characterized by a unique ground state with even parity. For weak coupling t , this ground state corresponds to the doubly occupied quantum dot and empty Majorana level with ground-state energy $E_{2,-,e}$, and the lowest excited state corresponds to occupying the Majorana level and thus, costs the excitation energy $E_{2,-,o} - E_{2,-,e}$. At the special point $\epsilon_d = -U$, this excitation energy vanishes and the ground state is two-fold degenerate with one even and one odd parity ground state. In the regime (ii) with $-U < \epsilon_d < 0$, the ground state and the first excited state have odd parity corresponding to one fermion which is mainly localized on the quantum dot. For $\epsilon_d < -U/2$ ($\epsilon_d > -U/2$), the ground state is the antisymmetric (symmetric) superposition of spin up and down quantum dot electron, and the first excited state is then the opposite superposition. The second excited state has even parity and in the weak t limit, it corresponds to occupying the Majorana level. At the second special point $\epsilon_d = 0$, the energy $E_{1,-,e} - E_{1,-,o}$ for the lowest parity changing excitation vanishes and the ground state is again two-fold degenerate with one odd and one even parity ground state. In the regime (iii) with $\epsilon_d > 0$, the parity of the ground-state wave function is again even corresponding to a completely empty system. Here, the lowest excited state with odd parity has excitation energy $E_{1,-,o} - E_{1,-,e}$ and describes occupying the Majorana level.

In the following, we further investigate the special points $\epsilon_{i\sigma} = 0$ and $\epsilon_{i\sigma} = -U$ where the ground state is two-fold degenerate. For $\epsilon_{i\sigma} = 0$, we find the odd and the even parity ground-state wave functions

$$|\psi^o(\epsilon_d = 0)\rangle = \left[\frac{A_+}{\sqrt{2}}(d_{L\uparrow}^\dagger + d_{L\downarrow}^\dagger) - A_- f^\dagger \right] |0\rangle, \quad (3.5.7a)$$

$$|\psi^e(\epsilon_d = 0)\rangle = \left[A_+ - \frac{A_-}{\sqrt{2}}(d_{L\uparrow}^\dagger + d_{L\downarrow}^\dagger) f^\dagger \right] |0\rangle, \quad (3.5.7b)$$

where $A_\pm = \sqrt{1 \pm \epsilon_M / \sqrt{\epsilon_M^2 + 8t^2}} / \sqrt{2}$. Both wave functions have only contributions from the empty and the single-occupied quantum dot in order to minimize the Coulomb energy. The unitary operator γ_1 , which describes rotations $\gamma_1 |\psi^o(\epsilon_d = 0)\rangle = |\psi^e(\epsilon_d = 0)\rangle$ and $\gamma_1 |\psi^e(\epsilon_d = 0)\rangle = |\psi^o(\epsilon_d = 0)\rangle$ in the two-dimensional space of ground-state wave functions is given by

$$\gamma_1 = \frac{1}{\sqrt{2}}(d_{L\uparrow}^\dagger + d_{L\downarrow}^\dagger + d_{L\uparrow} + d_{L\downarrow}). \quad (3.5.8)$$

This operator satisfies the Majorana criteria $\gamma_1^\dagger = \gamma_1$ and $\gamma_1^2 = 1$. Similarly, we define another unitary operator γ_2 by the rotations $\gamma_2 |\psi^o(\epsilon_d = 0)\rangle = -i |\psi^e(\epsilon_d = 0)\rangle$ and

$\gamma_2|\psi^e(\epsilon_d = 0)\rangle = i|\psi^o(\epsilon_d = 0)\rangle$ in the two-dimensional space of ground-state wave functions. We find

$$\gamma_2 = -\frac{i}{\sqrt{2}} \frac{\epsilon_M(d_{L\uparrow}^\dagger + d_{L\downarrow}^\dagger - d_{L\uparrow} - d_{L\downarrow}) - \sqrt{8}t(f^\dagger - f)}{\sqrt{\epsilon_M^2 + 8t^2}}, \quad (3.5.9)$$

which is also a Majorana operator. However, in contrast to γ_1 , this operator also has weight from the Majorana bound state $\gamma_R = (f^\dagger - f)/i$. The origin for the formation of this pair of Majorana operators is the peculiar coupling between the quantum dot and the Majorana bound state. For $\epsilon_d = 0$, the Coulomb charging energy blocks the quantum dot from being doubly occupied and therefore the three quantum dot states $|0\rangle$, $|\uparrow\rangle = d_{L\uparrow}^\dagger|0\rangle$, and $|\downarrow\rangle = d_{L\downarrow}^\dagger|0\rangle$ are degenerate. When coupling the quantum dot to the Majorana bound state γ_L , this degeneracy is partially lifted and a two-fold degenerate ground state survives. For $t \ll \epsilon_M$, these two ground states correspond to $|0\rangle$ and $|\uparrow\rangle + |\downarrow\rangle$, while the state $|\uparrow\rangle - |\downarrow\rangle$ obtains a finite excitation energy t due to the coupling $H_{T,L}$ in Eq. (3.5.4b). In contrast, in the strong coupling limit $t \gg \epsilon_M$, the ground states correspond to $(|\uparrow\rangle + |\downarrow\rangle)/\sqrt{2} - f^\dagger|0\rangle$ and $|0\rangle - (|\uparrow\rangle + |\downarrow\rangle) \otimes f^\dagger|0\rangle/\sqrt{2}$, where again only the state with even spin superposition contributes. In both limits, the degeneracy is described by the Majorana operators γ_1 and γ_2 given by Eqs. (3.5.8) and (3.5.9). Thus, we conclude that by adjusting the energy levels of the quantum dot to the degeneracy point $\epsilon_d = 0$, a pair of exactly zero-energy Majorana states is produced similarly to the situation in section 3.3.

Similarly, for $\epsilon_{i\sigma} = -U$ the ground state of the quantum dot is degenerate with respect to being single or double occupied. Here, the empty state is blocked by the large negative quantum dot energy ϵ_d . In analogy to above, we find the ground-state wave functions

$$|\psi^o(\epsilon_d = -U)\rangle = \left[\frac{A_+}{\sqrt{2}}(d_{L\uparrow}^\dagger - d_{L\downarrow}^\dagger) - A_-d_{L\uparrow}^\dagger d_{L\downarrow}^\dagger f^\dagger \right] |0\rangle, \quad (3.5.10a)$$

$$|\psi^e(\epsilon_d = -U)\rangle = \left[-A_+d_{L\uparrow}^\dagger d_{L\downarrow}^\dagger + \frac{A_-}{\sqrt{2}}(d_{L\uparrow}^\dagger - d_{L\downarrow}^\dagger)f^\dagger \right] |0\rangle. \quad (3.5.10b)$$

As before, these two states span a two-dimensional ground-state space and the unitary operators γ_1 and γ_2 which describe rotations in this two-dimensional space of ground states are identical to the ones introduced above for $\epsilon_{i\sigma} = 0$ in Eqs. (3.5.8) and (3.5.9).

3.5.2. Two spinful quantum dots coupled to a pair of Majorana bound states

In this section, we consider the full system containing two interacting quantum dots and each dot is coupled to a Majorana bound state. Similarly, to the quantum dot–Majorana bound state system studied in the last section, we find a two-fold ground-state degeneracy for $\epsilon_{i\sigma} = 0$ and $\epsilon_{i\sigma} = -U_i$ for $i = L, R$.

In the following, we explicitly consider the special case $\epsilon_{i\sigma} = 0$, $t_{i\sigma} = t$, and $U_i = U$ for $i = L, R$ and $\sigma = \uparrow, \downarrow$. We find the lowest eigenenergies for even and odd parity,

$$E_{1,\pm}^{(e,o)} = \frac{1}{2} \left[\epsilon_M \pm \sqrt{\epsilon_M^2 + 32t^2} \right], \quad (3.5.11a)$$

$$E_{2,3,\pm,\pm}^{(e,o)} = \frac{1}{2} \left[\epsilon_M + U \pm \sqrt{\epsilon_M^2 + 16t^2 + U^2 \pm 2\sqrt{64t^4 + \epsilon_M^2 U^2 + 8t^2 U^2}} \right]. \quad (3.5.11b)$$

In analogy to the quantum dot–Majorana bound state system studied in the last section, the ground state does not contain contributions from doubly occupancy of the quantum dots due to the blocking by the Coulomb energy U . When solving the many-body Schrödinger equation analytically, we find the ground-state wave functions for odd and even parity,

$$|\psi^o(\epsilon_d = 0)\rangle = \left[A_+ (d_{L\uparrow}^\dagger + d_{L\downarrow}^\dagger - id_{R\uparrow}^\dagger - id_{R\downarrow}^\dagger) + \frac{A_-}{\sqrt{2}} (-2f^\dagger + i(d_{L\uparrow}^\dagger + d_{L\downarrow}^\dagger)f^\dagger(d_{R\uparrow}^\dagger + d_{R\downarrow}^\dagger)) \right] |0\rangle, \quad (3.5.12a)$$

$$|\psi^e(\epsilon_d = 0)\rangle = \left[\frac{A_+}{\sqrt{2}} (2 - i(d_{L\uparrow}^\dagger + d_{L\downarrow}^\dagger)(d_{R\uparrow}^\dagger + d_{R\downarrow}^\dagger)) - A_- ((d_{L\uparrow}^\dagger + d_{L\downarrow}^\dagger)f^\dagger - if^\dagger(d_{R\uparrow}^\dagger + d_{R\downarrow}^\dagger)) \right] |0\rangle. \quad (3.5.12b)$$

with $A_\pm = \sqrt{1 \pm \epsilon_M \sqrt{\epsilon_M^2 + 32t^2}} / \sqrt{8}$. The operators which describe the transformation between the two ground states are again given by a pair of Majorana operators

$$\gamma_1 = \frac{1}{\sqrt{2}} (d_{L\uparrow}^\dagger + d_{L\downarrow}^\dagger + d_{L\uparrow} + d_{L\downarrow}), \quad (3.5.13a)$$

$$\gamma_2 = \frac{i}{\sqrt{2}} (d_{R\uparrow}^\dagger + d_{R\downarrow}^\dagger - d_{R\uparrow} - d_{R\downarrow}). \quad (3.5.13b)$$

Here, the operator γ_1 (γ_2) is entirely located on the left (right) quantum dot in full analogy to section 3.4 where we modeled the quantum dots by single resonant levels. Thus, we conclude that for $\epsilon_{i\sigma} = 0$ the formation of the zero-energy Majorana states on the quantum

dots also appears in the case of interacting quantum dots. Numerically, we have also confirmed that these states exist for finite Zeeman energy splitting $\epsilon_{i\uparrow} - \epsilon_{i\downarrow}$. Therefore, we argue that the formation of the induced zero-energy Majorana states is a robust feature of quantum dots coupled to a pair of Majorana bound states and does not depend on the details of the system.

3.6. Summary

In this chapter, we have identified signatures in nonlocal charge transport which we believe are more specific of the Majorana nature than the zero-bias anomaly studied in recent tunneling experiments. The nonlocality of the pair of Majorana bound states can be probed by crossed Andreev reflection, i.e., the conversion of an incoming electron into a hole excitation in a separate lead electrode. We have shown that at sufficiently low voltages and small level broadening, crossed Andreev reflection by the pair of Majorana bound states is the dominating transport process and gives rise to positive current cross-correlations. In contrast, for large voltages the current is dominated by local Andreev reflection, and resonant tunneling of electrons and holes gives rise to negative current cross-correlations which exactly cancel the positive contributions. Because of the vanishing total cross-correlations for large voltages, we argue that coupling Majorana bound states directly to lead electrodes is not suitable to observe current cross-correlations.

Instead, we have suggested to connect the lead electrodes with the Majorana bound states via quantum dots in order to suppress local Andreev reflection and thus to provide a suitable tool to probe current cross-correlations even for large voltages. In our analysis, we have distinguished two parameter regimes. In the case of weak coupling between the quantum dots and the lead electrodes, we find a set of discrete transmission resonances in the differential conductance. However, we find that one type of resonances is special as it does not contribute to current correlations. When at least one of the quantum dot levels is tuned to the chemical potential of the superconductor, a zero-energy Majorana state forms in the respective quantum dot. Since the existence of zero-energy Majorana states implies a strongly reduced tunneling matrix element between the quantum dots, we find that these resonances yield only a small contribution to the current cross-correlations despite their large conductance. In the strong quantum dot-lead coupling regime, the current cross-correlations show a four-leaf clover pattern as function of quantum dot energies. This feature shows an approximate symmetry between symmetric and antisymmetric positions of the quantum dot levels due to the large level broadening of the quantum dots. The clover pattern can be clearly distinguished from the single ellipsoidal peak found without

split Majorana bound states.

In our numerical calculations, we have shown that the cloverlike pattern can be observed for realistic material parameters and can be clearly distinguished from the situation without split Majorana fermions. This pattern is robust against nonmagnetic disorder, a finite number of transverse subbands in the nanowire, and finite temperatures $k_B T \lesssim \epsilon_M$. In particular, we have shown that by varying the external magnetic field, the cross-correlation pattern oscillates between the cloverlike pattern for split Majorana bound states and a single ellipsoidal pattern originating from the superconducting proximity effect. We propose that the oscillation between the two different shot noise patterns is a robust signature of Majorana bound states in short topological superconductor nanowires.

4. Signatures of topological order in Coulomb blockade transport through semiconductor–superconductor nanowire rings

Identifying unambiguous experimental signatures and verifying their experimental realization is a key problem in the study of topological phases of matter. In chapter 3, we have investigated current and noise characteristics of Majorana bound states and compared the results with the characteristics for conventional superconductors. In particular, we have emphasized that tunneling experiments, which probe only one normal-state–superconductor junction, do not yield a definite proof of Majorana fermions since mundane physical effects such as nonmagnetic disorder [59], interface effects [61], and Kondo [62] yield similar tunneling characteristics under certain conditions. In contrast, normal-state–superconductor–normal-state systems are more suitable to probe the existence of Majorana fermions via current cross-correlations.

Recent experiments [55–57, 63] showed first evidence for Majorana end states in superconductors which were proposed to be topologically nontrivial. However, so far there are no experiments which directly investigate the topology of the superconducting state. In this chapter we propose an experiment which directly investigates the topological superconducting state rather than Majorana bound states. As pointed out in chapter 2.4, one characteristic property of topological phases is the dependence of the ground-state degeneracy on the topology of the manifold on which the system is defined. We consider a quasi one-dimensional ring-shaped superconductor in the limit where the gap Δ_{eff} is much larger than the single-particle level spacing d . In the Coulomb blockade regime, the total electron number and thus the parity of the superconductor nanowire are fixed by the charging energy $E_c > \Delta_{\text{eff}}$ and the degeneracy of grand canonical ground states is reflected in the excitation energies, which can be observed in nonlinear Coulomb blockade transport [74, 75]. In our numerical analysis, we concentrate on the semiconductor-superconductor heterostructure

which was introduced in chapter 2.5 and studied in a series of recent experiments. However, our main results are more general and can also be applied to other (quasi) one-dimensional topological superconducting systems.

This chapter is organized as follows: In section 4.1, we introduce the model system and the proposed experimental setup. We begin our analysis with a idealized one-dimensional ring-shaped nanowire in section 4.2. We then continue in section 4.3 with single-subband nanowires and study the robustness of the results from section 4.2 against details of the geometry, nonmagnetic disorder, and local variations of the superconducting pairing potential. In section 4.4, we make a departure from the case of strict one-dimensional nanowires and consider the experimentally realistic case of quasi one-dimensional nanowires with several partially occupied subbands. In section 4.5, we compare the current for the single-electron tunneling with the current due to cotunneling of Cooper pairs which turns out to be the transport channel which competes with sequential tunneling of single electrons. We make a connection to possible future experiments and discuss the expected differential conductance pattern in section 4.6. We conclude with a summary of the main results of this chapter in section 4.7.

4.1. Model system

4.1.1. Setup and Coulomb Hamiltonian

We consider a quasi one-dimensional semiconductor nanowire with strong spin-orbit coupling which is proximity coupled to an s -wave superconductor. The nanowire forms an annulus in the x - y plane with radius R and radial extension $L_{\perp} \ll R$. We assume a strong confinement in z direction, i.e., the extension perpendicular to the plane of the annulus $L_z \ll L_{\perp}$, such that only the lowest subband with momentum in z direction is occupied. This hybrid system is separated from a back-gate by a thin insulating layer and weakly tunnel-coupled to source and drain electrodes with symmetric electric potentials $\pm eV/2$. The proposed experimental setup is illustrated in figure 4.1.1

Assuming a strong capacitive coupling between the nanowire and the superconductor, the total number of electrons in this system is determined by the Coulomb Hamiltonian

$$H_C = E_c(N + N_{\text{SC}})^2 - eV_G(N + N_{\text{SC}}), \quad (4.1.1)$$

where E_c denotes the charging energy and N (N_{SC}) the number of excess electrons in the semiconductor (superconductor) attracted by the back-gate. Varying the gate potential eV_G allows to change the total electron number $N + N_{\text{SC}}$ in discrete units. A single-

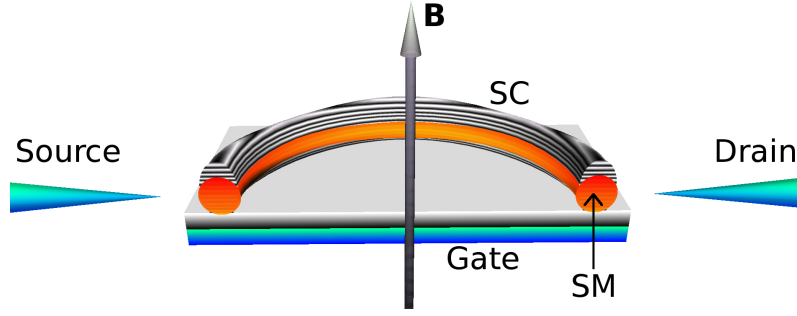


Figure 4.1.1.: Cross section of the experimental setup for a ring-shaped semiconductor-superconductor hybrid system. We consider a quasi one-dimensional semiconductor (SM) nanowire with strong spin-orbit coupling and a magnetic field B perpendicular to the plane of the semiconductor ring. The superconductor (SC) is sputtered on top of the semiconductor which itself is deposited on a gate electrode. The semiconductor is weakly tunnel coupled to source and drain electrodes.

electron current through this island involves changing the electron number from $N + N_{\text{SC}}$ to $N + N_{\text{SC}} \pm 1$ and creating or annihilating an odd number of quasiparticle excitations. Thus, resonances in the differential conductance appear when the condition

$$eV/2 = E_{N+N_{\text{SC}}\pm 1} - E_{N+N_{\text{SC}}}^{\text{gs}} \quad (4.1.2)$$

is satisfied, where $E_{N+N_{\text{SC}}}$ is the total energy of a state with $N + N_{\text{SC}}$ electrons and $E_{N+N_{\text{SC}}}^{\text{gs}}$ is the respective ground-state energy. The spacing between the resonance peaks for fixed V_G is independent of the charging energy E_c and displays the excitation spectrum for fixed electron number,

$$\delta E_{N+N_{\text{SC}}} = E_{N+N_{\text{SC}}} - E_{N+N_{\text{SC}}}^{\text{gs}}. \quad (4.1.3)$$

In figure 4.1.2(a), we illustrate a typical result for the nonlinear conductance pattern as function of gate and bias voltage. A finite single-electron conductance (yellow area) is only found for a set of bias and gate voltages (V, V_G) which satisfy the resonance condition Eq. (4.1.2). In the white areas, called *Coulomb diamonds* due to their shape, the current is fully suppressed by the Coulomb charging energy. The edges of the Coulomb diamonds are found from Eq. (4.1.2) if the state with $N+N_{\text{SC}}\pm 1$ electrons is a ground state. The distance between the diamonds as well as their height is mainly determined by E_c . For larger voltages (orange area) the transport is dominated by processes which change the electron number in the ring system by two or more. If we consider the nonlinear conductance for single-electron tunneling through an s -wave superconducting grain with quasiparticle gap E_G , we typically find a diamond pattern similar to the one in figure 4.1.2(b). Here, we find

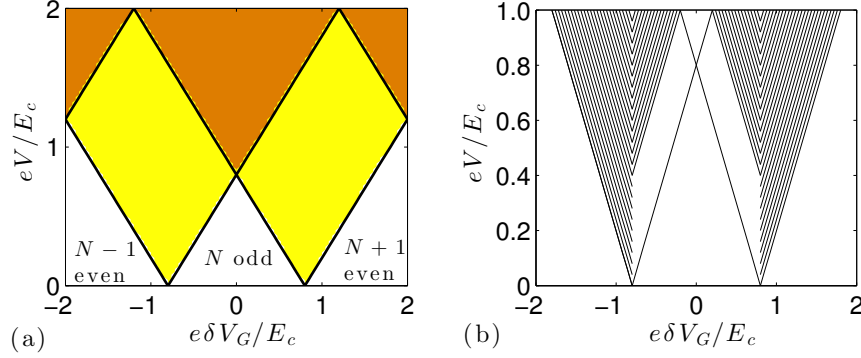


Figure 4.1.2.: Illustration of a stability diagram as function of gate potential $e\delta V_G = eV_G - NE_c$ and bias voltage V . (a) In the white area, transport is blocked by the Coulomb charging energy Eq. (4.1.1). In the yellow area, tunneling of single electrons is possible if the resonance condition Eq. (4.1.2) is satisfied. In the orange area, two-electron processes contribute to transport. (b) Idealized stability diagram for an s -wave superconducting grain (see e.g. reference [121]) with quasiparticle gap $E_G = E_c/5$ and single-particle level spacing $d = E_c/10$. The black lines denote resonances of the differential conductance. In the white areas of height $2E_G$ in the downward pointing diamonds centered around odd N , the current is suppressed by superconducting gap and hence there are no resonance lines. Note the different resonance pattern for tunneling from grains with odd to even parity with energy gap $2E_G$ and from even to odd parity without energy gap between the resonances.

a characteristic even-odd effect with an energy gap between the two lowest resonance lines for tunneling processes which change the parity from odd to even. In the opposite case, for tunneling processes from states with even to odd parity, this energy gap is absent and the separation between the resonance lines displays the single-particle level spacing. This even-odd effect was experimentally confirmed in ultrasmall superconducting aluminum grains by Black *et al.* [74]. In addition, we note that the location of the Coulomb diamonds is slightly shifted and the separation between two diamonds becomes $2E_c - 2E_G$ ($2E_c + 2E_G$) for the diamond centered around a ground state with odd (even) parity.

In our analysis, we assume that both the charging energy E_c and the quasiparticle gap Δ_s in the superconductor are larger than the effective gap Δ_{eff} in the semiconductor. Hence, for small voltages $eV \lesssim E_c, \Delta_s$ all electrons in the superconductor are paired and unpaired electrons as well as breaking of Cooper pairs can only show up in the semiconductor. As a consequence, the parity in the superconductor is always even and the parity in the semiconductor nanowire is determined by the total parity of the hybrid system. The Coulomb Hamiltonian Eq. (4.1.1) fixes the total electron number while the electron number in the semiconductor fluctuates because of the strong coupling between the semiconductor and

the superconductor. In the following, we assume that the average electron number in the semiconductor is fixed and whenever we refer to the electron number in the semiconductor, we refer to its average.

4.1.2. Hamiltonian for the semiconductor-superconductor hybrid system

We describe the low-energy physics of the semiconductor nanowire by the continuum Hamiltonian $H = H_{\text{SM}} + H_{\text{SC}}$ [32–36] with

$$H_{\text{SM}} = \int d^2r \sum_{\sigma} \psi_{\sigma}^{\dagger}(\mathbf{r}) \left\{ -\frac{\hbar^2}{2m^*} \frac{\partial^2}{\partial \mathbf{r}^2} - \mu + V(\mathbf{r}) + E_Z \hat{\sigma}_{\sigma\sigma}^z \right\} \psi_{\sigma}(\mathbf{r}) \\ + i\alpha\hbar \int d^2r \sum_{\sigma, \sigma'} \psi_{\sigma}^{\dagger}(\mathbf{r}) \left(\hat{\sigma}_{\sigma\bar{\sigma}}^y \frac{\partial}{\partial x} - \hat{\sigma}_{\sigma\bar{\sigma}}^x \frac{\partial}{\partial y} \right) \psi_{\sigma'}(\mathbf{r}), \quad (4.1.4)$$

where the operator $\psi_{\sigma}^{\dagger}(\mathbf{r})$ ($\psi_{\sigma}(\mathbf{r})$) creates (annihilates) an electron at position \mathbf{r} with spin σ and mass m^* . The first line in Eq. (4.1.4) describes the kinetic energy of a two-dimensional electron gas, the chemical potential μ , the nonmagnetic disorder potential $V(\mathbf{r})$, and the Zeeman energy splitting $E_Z = g\mu_B B/2$ due to the magnetic field in z direction. The second line in Eq. (4.1.4) represents the Rashba spin-orbit coupling with spin-orbit velocity α , and $\hat{\sigma}^s$ are the Pauli spin matrices with $s = x, y, z$. In our analysis, we incorporate the magnetic flux $\Phi(r)$, which is enclosed by the ring, by the azimuthal vector potential $\mathbf{A}(\mathbf{r}) = \Phi(r)\hat{e}_{\varphi}/2\pi r$ and the minimal coupling

$$-i\hbar \frac{\partial}{\partial \mathbf{r}} \rightarrow -i\hbar \frac{\partial}{\partial \mathbf{r}} + e\mathbf{A}(\mathbf{r}), \quad (4.1.5)$$

where $e > 0$ denotes the absolute value of the electron charge.

The proximity coupling between the s -wave superconductor and the nanowire is described by the effective s -wave pairing Hamiltonian

$$H_{\text{SC}} = \int d^2r \left(\Delta(\mathbf{r}) \psi_{\uparrow}^{\dagger}(\mathbf{r}) \psi_{\downarrow}^{\dagger}(\mathbf{r}) + \Delta^*(\mathbf{r}) \psi_{\downarrow}(\mathbf{r}) \psi_{\uparrow}(\mathbf{r}) \right) \quad (4.1.6)$$

with pairing potential $\Delta(\mathbf{r})$. We assume that the superconducting state of the s -wave superconductor is not affected by the semiconductor. Thus, we describe the s -wave superconductor within the Ginzburg-Landau formalism by the real space free energy density

$$f_{\text{GL}}[|\Delta_s|, \phi_s] = f_0(|\Delta_s|^2) + \frac{\hbar^2}{2m_s} \left| \left(-i \frac{\partial}{\partial \mathbf{r}} + 2 \frac{\Phi(r)\hat{e}_{\varphi}}{r\Phi_0} \right) \Delta_s \right|^2 + \frac{B^2}{2\mu_0}, \quad (4.1.7)$$

where f_0 is the free energy for zero magnetic flux, $\Delta_s = |\Delta_s|e^{i\phi_s}$ is the superconducting order parameter, Φ/Φ_0 is the magnetic flux in units of the flux quantum $\Phi_0 = h/e$, and m_s is the mass of the Cooper pairs [122]. Minimization of the Ginzburg-Landau free energy $F_{\text{GL}} = \int d^2r f_{\text{GL}}$ demands that $\delta F_{\text{GL}}/\delta |\Delta_s| = 0$ and that $\delta F_{\text{GL}}/\delta \phi_s = 0$. In the following, we neglect the small oscillations in $|\Delta_s|$ and focus on the effect of magnetic flux on the phase of the superconducting order parameter. The phase satisfies the periodic boundary condition $\phi_s(\varphi + 2\pi) = \phi_s(\varphi)$ such that the order parameter is a single-valued function. Since the length of the superconductor is much longer than its radial extension, we assume that $\partial \phi_s/\partial r = 0$ which simplifies the Ginzburg-Landau free energy density significantly,

$$f_{\text{GL}}[|\Delta_s|, \phi_s(\varphi)] = f_0(|\Delta_s|^2) + \frac{\hbar^2 |\Delta_s|^2}{2m_s r^2} \left(\frac{\partial \phi_s}{\partial \varphi} + 2 \frac{\Phi(r)}{\Phi_0} \right)^2 + \frac{B^2}{2\mu_0}. \quad (4.1.8)$$

Throughout this chapter, we assume that the s -wave superconductor fixes the phase of the proximity induced pairing potential

$$\Delta(\mathbf{r}) = |\Delta(\mathbf{r})|e^{i\phi_s(\varphi)}, \quad (4.1.9)$$

while the amplitude $|\Delta(\mathbf{r})|$ might fluctuate locally due to inhomogeneities in the interface transparency between the semiconductor and the superconductor. We note that in a microscopic model, in which the semiconductor and the superconductor are coupled via a single-particle tight-binding hopping Hamiltonian, the proximity induced gap is mainly given by $\Delta = \Delta_s \lambda / (\Delta_s + \lambda)$ with the interface transparency λ [123].

We diagonalize the full Hamiltonian H by defining the Bogoliubov quasiparticle operators

$$\alpha_l = \int d^2r \sum_{\sigma} \left[u_{\sigma l}(\mathbf{r}) \psi_{\sigma}(\mathbf{r}) + v_{\sigma l}(\mathbf{r}) \psi_{\sigma}^{\dagger}(\mathbf{r}) \right], \quad (4.1.10)$$

where $\{l\}$ is a complete set of quasiparticle quantum numbers. This yields

$$H = \sum_l E_l \alpha_l^{\dagger} \alpha_l + E_{\text{GC}} \quad (4.1.11)$$

with the quasiparticle energies $E_l > 0$ and the grand canonical ground-state energy

$$E_{\text{GC}} = -\frac{1}{2} \sum_l E_l + \frac{1}{2} \int d^2r \sum_{\sigma} \left\{ V(\mathbf{r}) - \mu + \frac{\hbar^2}{2m^*} \int d^2r' \left| \frac{\partial}{\partial \mathbf{r}} \delta(\mathbf{r} - \mathbf{r}') \right|^2 \right\}. \quad (4.1.12)$$

Here, the second term originates from the anti-commutation relation of the creation and annihilation operators in the normal-state Hamiltonian Eq. (4.1.4). We note that the

evaluation of Eq. (4.1.12) is nontrivial because the first term yields $-\infty$ due to the infinite number of quantum numbers l and the last integral term yields $+\infty$ due to the derivative of the delta function. To avoid the appearance of the diverging terms, we introduce an energy cutoff E_Λ and assume that all $E_l > E_\Lambda$ satisfy $E_l = \hbar^2 l^2 / 2m^*$ with the momentum l . This cutoff is justified since the kinetic energy term is the only second-derivative term and will dominate the energy spectrum for large momenta. This assumption introduces a characteristic lattice length scale $a = 2\pi/\Lambda = \hbar/\sqrt{2mE_\Lambda}$ which allows us to approximate the delta function by $\delta(\mathbf{r} - \mathbf{r}') = \delta_{n_x, n'_x} \delta_{n_y, n'_y} / a^2$ with $\mathbf{r} = (n_x a, n_y a)$ and $(n_x, n_y) \in \mathbb{N}^2$. Similarly, we rewrite the derivative as differential quotient and the integral as sum over lattice sites. With these approximations, we find the ground-state energy

$$E_{\text{GC}}^{\text{quasi1D}} = -\frac{1}{2} \sum_l^\Lambda E_l + \int d^2r \{V(\mathbf{r}) - \mu\} + 8 \frac{m^* R L_\perp}{\pi \hbar^2} E_\Lambda^2, \quad (4.1.13a)$$

$$E_{\text{GC}}^{\text{1D}} = -\frac{1}{2} \sum_l^\Lambda E_l + \int dx \{V(x) - \mu\} + 2 \frac{\sqrt{2m^*} R}{\pi \hbar} E_\Lambda^{3/2} \quad (4.1.13b)$$

for quasi one-dimensional and exactly one-dimensional semiconductor nanowires. We note that in solid state systems the cutoff Λ naturally appears as the size of the first Brillouin zone, i.e., as the inverse of the atomic lattice parameter.

The corresponding ground-state electron number is given by the expectation value of the particle number operator

$$\hat{N} = \int d^2r \sum_\sigma \psi_\sigma^\dagger(\mathbf{r}) \psi_\sigma(\mathbf{r}) \quad (4.1.14)$$

in the state where all quasiparticle levels are empty. Rewriting the particle number operator in terms of quasiparticle operators Eq. (4.1.10) and taking the expectation value with respect to the ground state $\langle \alpha_l^\dagger \alpha_{l'} \rangle = 0$, we find

$$N_{\text{GC}} = \int d^2r \sum_\sigma \sum_l |v_{\sigma l}(\mathbf{r})|^2. \quad (4.1.15)$$

The parity of the grand canonical ground state is determined by the pfaffian \mathbb{Z}_2 topological number

$$\mathcal{Q} = \frac{\text{Pf}(\mathcal{H} i \tau^x)}{\sqrt{|\det(\mathcal{H} i \tau^x)|}}, \quad (4.1.16)$$

where \mathcal{H} denotes the first quantized Bogoliubov-de Gennes Hamilton matrix in the basis $(\psi_\uparrow^\dagger(\mathbf{r}), \psi_\downarrow^\dagger(\mathbf{r}), \psi_\uparrow(\mathbf{r}), \psi_\downarrow(\mathbf{r}))$ and τ^x denotes the Pauli matrix acting on the particle-hole

space [76, 124]. Here, the topological number $\mathcal{Q} = +1(-1)$ corresponds to the even (odd) parity of the grand canonical ground state. From the grand canonical ground state with parity \mathcal{Q} we construct two classes of states with parity \mathcal{P} by creating N_{qp} quasiparticle excitations. The parity \mathcal{P} of these states is determined by

$$\mathcal{P} = (-1)^{N_{\text{qp}}} \mathcal{Q}, \quad (4.1.17)$$

i.e., depending on whether N_{qp} is even (odd), $\mathcal{P} = \mathcal{Q}$ ($\mathcal{P} = -\mathcal{Q}$).

The Coulomb Hamiltonian Eq. (4.1.1) fixes the parity in the nanowire since $\Delta_s \gg \Delta_{\text{eff}}$, and the total number of electrons in the hybrid system. Because of the strong tunnel coupling between the semiconductor and the superconductor, the individual electron number in each subsystem may fluctuate, however, we assume that the mean electron number in each subsystem is fixed by a relative charging energy $E_c^* \ll E_c$ which is discussed in the next section. Hence, we describe the semiconductor by the parity \mathcal{P} and the mean electron number N . Since the resonances in the differential conductance are determined by the total energy and not by the grand potential, we Legendre transform the class of states with parity \mathcal{P} into a pseudo-canonical ensemble with N_{qp} quasiparticles and mean electron number N . This ensemble contains states with energy

$$E[\{l_1, \dots, l_{N_{\text{qp}}}\}, N, \mathcal{P}] = E_{\text{GC}} + \sum_{j=1}^{N_{\text{qp}}} E_{l_j} + \mu N \quad (4.1.18)$$

and the chemical potential μ is determined by the constraint of fixed mean electron number,

$$N = N_{\text{GC}}(\mu) + \sum_{j=1}^{N_{\text{qp}}} \int d^2r \sum_{\sigma} \left\{ |u_{\sigma l_j}(\mathbf{r}, \mu)|^2 - |v_{\sigma l_j}(\mathbf{r}, \mu)|^2 \right\}. \quad (4.1.19)$$

4.1.3. Material parameters

Both InAs and InSb have been shown experimentally to be suitable semiconducting materials because of their strong spin-orbit coupling and their large g -factor $g \approx 20 \dots 50$ [55–57]. In the experimental situation, the confinement energy in transverse direction is the largest energy scale so that only a few subbands are partially occupied. It is useful to express the kinetic energy and the spin-orbit coupling in terms of a characteristic energy $\epsilon_{so} = m^* \alpha^2$ and a spin-orbit length $l_{so} = \hbar / m^* \alpha$. With these definitions, we rewrite the kinetic energy term $\hbar^2 / 2m^* = \epsilon_{so} l_{so}^2 / 2$ and the spin-orbit term $\hbar \alpha = \epsilon_{so} l_{so}$. Typical values for InAs, InSb, and related materials are $\epsilon_{so} = 0.1$ meV, $l_{so} = 100$ nm, and $g\mu_B / 2 = 1$ meV/T which corresponds to $g \approx 35$. Thus, we find with $R = 0.5$ μm , $E_Z = 1$ meV, and $\Delta = 0.5$ meV,

the single-particle level spacing at the Fermi energy of $d = 0.08$ meV and an effective quasiparticle excitation gap in the semiconductor of $\Delta_{\text{eff}} \approx 0.2$ meV. In the following, the magnetic field B is varied in discrete steps with the magnetic flux always being fixed modulo Φ_0 , such that the only effect is a change of the Zeeman energy E_Z .

To ensure single-electron tunneling through the semiconductor-superconductor hybrid system, we consider the case $\Delta_s, E_c \gg \Delta_{\text{eff}}$. In our model, we consider a strong capacitive coupling between semiconductor and superconductor in the sense that we only discuss the effect of a global charging energy for adding charge to the total systems with respect to particle exchange with an external reservoir. Additionally, there can be a relative charging energy E_c^* for the relative electron number in the semiconductor and the superconductor. Because of the strong capacitive coupling, we assume that $E_c \gg E_c^*$ and thus neglect E_c^* . Therefore, only the total electron number is a good quantum number while the individual electron numbers in the semiconductor and in the superconductor may fluctuate because of tunneling between them. A relative charging energy between the semiconductor and the superconductor of 1 meV together with a pairing gap $\Delta_s = 2$ meV in the superconductor would reduce Δ_{eff} by 20 % [125]. Thus, we conclude that a moderate relative charging E_c^* does not change our findings qualitatively and is hence neglected.

4.2. Idealized one-dimensional ring-shaped nanowire

We begin our analysis with a idealized one-dimensional nanowire of radial extension $L_\perp \rightarrow 0$ for spatially constant magnitude of the superconducting pairing $|\Delta(\mathbf{r})| = \Delta$ and vanishing disorder potential $V(\mathbf{r}) = 0$. To derive the Hamiltonian for a one-dimensional ring-shaped nanowire, we first rewrite the normal-state Hamiltonian Eq. (4.1.4) in polar coordinates,

$$H_{\text{SM}} = \sum_{\sigma\sigma'} \int d\varphi \int dr r \psi_{\sigma'}^\dagger(r, \varphi) \mathcal{H}_{\text{SM},\sigma\sigma'}(r, \varphi) \psi_{\sigma'}(r, \varphi) \quad (4.2.1)$$

with the first quantized 2×2 Hamilton matrix

$$\begin{aligned} \mathcal{H}_{\text{SM}}(r, \varphi) = & -\frac{\hbar^2}{2m^*} \left[\frac{\partial^2}{\partial r^2} + \frac{1}{r} \frac{\partial}{\partial r} + \frac{1}{r^2} \frac{\partial^2}{\partial \varphi^2} \right] - \mu + E_Z \sigma^z \\ & - \hbar \frac{\alpha}{r} \left(\cos(\varphi) \sigma^x + \sin(\varphi) \sigma^y \right) i \frac{\partial}{\partial \varphi} + i \hbar \alpha \left(\cos(\varphi) \sigma^y - \sin(\varphi) \sigma^x \right) \frac{\partial}{\partial r}. \end{aligned} \quad (4.2.2)$$

The naive derivation of the one-dimensional Hamiltonian could be obtained by replacing $r = R$ and neglecting the radial derivative terms. However, this yields an incorrect non-Hermitian operator. To derive the correct Hamiltonian, we first separate angular and radial

components of the electron wave function $\psi(r, \varphi) = \chi(r)\psi(\varphi)$. Then, the normalization of the wave function yields the equation $\int dr r \chi^2(r) = 1$. We assume that the electron wave function is confined to the ring by a radial confining potential and that only the lowest radial subband is occupied. Hence, we approximate $\int dr r \chi^2(r) \approx 1/R + \mathcal{O}(L_\perp/R^2)$. In the limit $L_\perp \rightarrow 0$, this approximation becomes exact and we find the integral

$$\int dr r \chi(r) \frac{\partial}{\partial r} \chi(r) = - \int dr \left(\frac{\partial}{\partial r} r \chi(r) \right) \chi(r) = -\frac{1}{2R}. \quad (4.2.3)$$

With this relation we obtain the Hamiltonian for the one-dimensional nanowire by integrating out the radial coordinate, $\mathcal{H}_{\text{SM},1D}(\varphi) = \int dr r \chi(r) \mathcal{H}_{\text{SM}}(r, \varphi) \chi(r)$, which yields (up to φ independent terms)

$$\begin{aligned} \mathcal{H}_{\text{SM},1D}(\varphi) = & -\frac{\hbar^2}{2m^*R^2} \frac{\partial^2}{\partial \varphi^2} - \mu + E_Z \sigma^z \\ & - \hbar \frac{\alpha}{R} (\cos(\varphi) \sigma^x + \sin(\varphi) \sigma^y) i \frac{\partial}{\partial \varphi} - \frac{i\hbar\alpha}{2R} (\cos(\varphi) \sigma^y - \sin(\varphi) \sigma^x). \end{aligned} \quad (4.2.4)$$

Here, the last term originates from the last term in Hamiltonian Eq. (4.2.2) which contained a first-order radial derivative and was therefore absent in the naive derivation of setting $r = R$. In the derivation of the correct Hamiltonian we did not specify the details of the confining potential and only assumed that the confining potential is rotation symmetric and that only the lowest transverse subband is occupied. Therefore, we argue that the result is the generic Hamiltonian for an idealized one-dimensional ring with spin-orbit coupling.

With the expression in Eq. (4.2.4) for the one-dimensional normal-state Hamiltonian, we write the full Hamiltonian for the semiconductor nanoring pierced by the magnetic flux Φ as

$$\begin{aligned} H_{\text{SM},1D} = \int_0^{2\pi} d\varphi \left\{ \sum_{\sigma} \psi_{\sigma}^{\dagger}(\varphi) \left[\frac{\hbar^2}{2m^*R^2} \left(-i \frac{\partial}{\partial \varphi} + \frac{\Phi}{\Phi_0} \right)^2 - \mu + E_Z \hat{\sigma}_{\sigma\sigma}^z \right] \psi_{\sigma}(\varphi) \right. \\ + \frac{\hbar\alpha}{R} e^{-i\varphi} \psi_{\uparrow}^{\dagger}(\varphi) \left(-i \frac{\partial}{\partial \varphi} + \frac{\Phi}{\Phi_0} - \frac{1}{2} \right) \psi_{\downarrow}(\varphi) \\ \left. + \frac{\hbar\alpha}{R} e^{i\varphi} \psi_{\downarrow}^{\dagger}(\varphi) \left(-i \frac{\partial}{\partial \varphi} + \frac{\Phi}{\Phi_0} + \frac{1}{2} \right) \psi_{\uparrow}(\varphi) \right\}. \end{aligned} \quad (4.2.5)$$

We rewrite this Hamiltonian by Fourier transforming the electron operators

$$\psi_{\sigma}(\varphi) = \frac{1}{\sqrt{2\pi}} \sum_{k \in \mathbb{Z}} e^{ik\varphi} \psi_{k\sigma}, \quad (4.2.6)$$

where the operator $\psi_{k\sigma}^\dagger$ ($\psi_{k\sigma}$) creates (annihilates) an electron with spin σ and angular momentum $\hbar k$. Hence, we find the Hamiltonian describing the lowest energy subband of the nanowire in momentum space [126]

$$H_{\text{SM},1D} = \sum_{k \in \mathbb{Z}} \left\{ \sum_{\sigma} \psi_{k\sigma}^\dagger \left[\frac{\hbar^2}{2m^* R^2} \left(k + \frac{\Phi}{\Phi_0} \right)^2 - \mu + \sigma E_Z \right] \psi_{k\sigma} + \frac{\hbar\alpha}{R} \left(k + \frac{1}{2} + \frac{\Phi}{\Phi_0} \right) \left(\psi_{k\uparrow}^\dagger \psi_{k+1\downarrow} + \psi_{k+1\downarrow}^\dagger \psi_{k\uparrow} \right) \right\}. \quad (4.2.7)$$

Here, the Rashba spin-orbit velocity, α , couples states $\{|k \uparrow\rangle, |k+1 \downarrow\rangle\}$ and creates two helical bands with the spin rotating within the x - y plane. The bands cross each other at $k = -1/2 - \Phi/\Phi_0$. The magnetic field, B , tilts the spin direction out of the x - y plane, removes the level crossing, and opens a spin gap $E_Z = g\mu_B B/2$. By diagonalizing the 2×2 normal-state Hamilton matrix

$$\mathcal{H}_{\text{SM},1D}(k) = \begin{pmatrix} \frac{\hbar^2}{2m^* R^2} \left(\tilde{k} - \frac{1}{2} \right)^2 - \mu + E_Z & \frac{\hbar\alpha}{R} \tilde{k} \\ \frac{\hbar\alpha}{R} \tilde{k} & \frac{\hbar^2}{2m^* R^2} \left(\tilde{k} + \frac{1}{2} \right)^2 - \mu - E_Z \end{pmatrix}, \quad (4.2.8)$$

we find the single-particle dispersion of the tilted helical bands,

$$\epsilon_{\pm, \tilde{k}} = \frac{\hbar^2 (\tilde{k}^2 + \frac{1}{4})}{2m^* R^2} - \mu \pm \sqrt{\left(E_Z - \frac{\hbar^2 \tilde{k}}{2m^* R^2} \right)^2 + \left(\frac{\alpha \hbar \tilde{k}}{R} \right)^2}, \quad (4.2.9)$$

where $\tilde{k} = k + \Phi/\Phi_0 + 1/2$. For $|\tilde{k}| \gg 1$, which is satisfied for the realistic parameters $R \gg l_{so}$ and $|\mu| \lesssim \epsilon_{so}$, we can approximate the single-particle energies by

$$\epsilon_{\pm, \tilde{k}} \approx \frac{\hbar^2 \tilde{k}^2}{2m^* R^2} - \mu \pm \sqrt{E_Z^2 + \left(\frac{\alpha \hbar \tilde{k}}{R} \right)^2}. \quad (4.2.10)$$

This expression is identical to the single-particle energy for a straight long nanowire, discussed in chapter 2.5, but with k replaced by $\tilde{k} = k + \Phi/\Phi_0 + 1/2$. Here, the appearance of the magnetic flux is a trivial shift of the angular momentum due to the perpendicular magnetic field which gives rise to a circular persistent current of the electrons.

The momentum shift of $1/2$ originates from the conservation of the total angular momentum of the electrons in the ring structure. More specifically, this conservation yields a spin-orbit coupling between states with equal total angular momentum $(\hbar k, \uparrow)$ and $(\hbar k + \hbar, \downarrow)$ and thus effectively shifts orbital angular momenta pR by $\pm \hbar/2$. This shift can be under-

stood by identifying it with a 2π spin rotation of an electron encircling the ring. Since electrons carry spin $1/2$ a rotation of 2π in spin space corresponds to a phase of $\frac{1}{2}(2\pi) \equiv \pi$ for a rotation in real space. This is equivalent to a Berry phase factor -1 , i.e., an effective shift of the magnetic flux by $-\Phi_0/2$. The Berry phase is exact up to corrections of order l_{so}/R for $|\mu| \lesssim \epsilon_{so}$. We use the parameters $l_{so}/R \ll \pi$ and $\mu \approx 0$ and therefore, the corrections are expected to be small.

For the strictly one-dimensional system, we write the Ginzburg-Landau free energy density Eq. (4.1.8) for the s -wave superconductor in momentum space as

$$f_{\text{GL}}[|\Delta_s|, q] = f_0(|\Delta_s|^2) + \frac{\hbar^2 |\Delta_s|^2}{2m_s R^2} \left(q + \frac{2\Phi}{\Phi_0} \right)^2 + \frac{B^2}{2\mu_0}, \quad (4.2.11)$$

where $\hbar q$ is the angular momentum of the condensate, i.e., $\phi_s = q\varphi$. Minimization of f_{GL} demands that \mathcal{Q} is the integer nearest to $-2\Phi/\Phi_0$ and that $\delta f_{\text{GL}}/\delta \Delta_s = 0$. In the following, we neglect the small oscillations in $|\Delta_s|$ and focus on the large effect of parity and magnetic flux on the excitation spectrum of the semiconductor ring. With the angular momentum of the Cooper-pair condensate, the proximity pairing term Eq. (4.1.6) becomes

$$\begin{aligned} H_{\text{SC}} &= \int_0^{2\pi} d\varphi \left\{ \Delta e^{-iq\varphi} \psi_{\uparrow}^{\dagger}(\varphi) \psi_{\downarrow}^{\dagger}(\varphi) + \Delta e^{iq\varphi} \psi_{\downarrow}(\varphi) \psi_{\uparrow}(\varphi) \right\} \\ &= \Delta \sum_{k \in \mathbb{Z}} \left\{ \psi_{k\uparrow}^{\dagger} \psi_{-k+q\downarrow}^{\dagger} + \psi_{-k+q\downarrow} \psi_{k\uparrow} \right\}, \end{aligned} \quad (4.2.12)$$

which couples states $|k \uparrow\rangle$ and $| -k + q \downarrow\rangle$. As a consequence, the total Hamiltonian $H = H_{\text{SM}} + H_{\text{SC}}$ is block diagonal, and within each block a quadruplet

$$\{|k \uparrow\rangle, |k + 1 \downarrow\rangle, | -k + q \downarrow\rangle, | -k - 1 + q \uparrow\rangle\} \quad (4.2.13)$$

is coupled. For odd \mathcal{Q} , the quadruplet for $k = (q - 1)/2$ reduces to a single doublet $\{|(q - 1)/2 \uparrow\rangle, |(q + 1)/2 \downarrow\rangle\}$. The pairing potential Δ , which is reduced in magnitude as compared to Δ_s , plays a crucial role since it sets two excitation energies. It both opens an effective pairing gap at the Fermi surface and it modifies the Zeeman gap at $\tilde{k} = 0$. For $\Delta^2 > E_Z^2 - \mu^2$ both helicities are occupied in the ground state and Δ pairs generalized time-reversed pairs at both sets of Fermi points. Hence, the nanowire is in a trivial state with superconductor gaps at both $\pm \tilde{k}_F$ and $\tilde{k} = 0$. For $\Delta^2 < E_Z^2 - \mu^2$ on the other hand, the band structure is different in an important way because now there is a spin gap at $\tilde{k} = 0$ and a superconducting gap only at $\pm \tilde{k}_F$. If $E_Z \gg \Delta, \mu$, it is justified to only consider the lower band and to project the proximity induced singlet pairing onto that band [34,36].

In this limit, the low-energy theory of the ring model with magnetic flux Φ can be mapped onto Kitaev's model [76] with periodic boundary condition and magnetic flux $\Phi + \Phi_0/2$. The projected model contains doublets $\{|p\rangle, |-p\rangle\}$ for $\Phi/\Phi_0 \in [n - 1/4, n + 1/4]$ with integer n and effective momentum $p = k - q/2 + 1/2$, whereas for $\Phi/\Phi_0 \in [n + 1/4, n + 3/4]$, the doublet for $p = 0$ reduces to the singlet $|p = 0\rangle$.

As discussed above, the Hamiltonian for the one-dimensional ring-shaped nanowire can be decomposed into a sum over quadruplets and depending on Φ into an additional doublet. Thus, the many-body wave function for this Hamiltonian can be written in an analytical form as the tensor product of the many-body wave function for the individual quadruplets. In the following, we define two classes of grand canonical ansatz wave functions with even and odd parity as generalized BCS wave functions [75]. Then, we determine the ground state by an unbiased minimization of the energy expectation value and the lowest excited states are given by pairwise creation of Bogoliubov quasiparticles. This method is fully equivalent to the method introduced above which only relied on the parity \mathcal{Q} of the many-body wave function and the quasiparticle excitations. In this section we prefer to use the wave-function based method because it is more intuitive than the pfaffian invariant and allows to clearly read off the ground as well as the excited states.

4.2.1. Wave functions: Spinless p -wave superconductor

Before investigating the full model, we discuss the system for $|\mu|, \Delta, \epsilon_{so} \ll E_Z$ where we can map the lower helical band onto the Kitaev model introduced in chapter 2.2 with the Hamiltonian

$$H_K = \sum_p \left\{ \epsilon_p c_p^\dagger c_p + \Delta_0 p c_p^\dagger c_{-p}^\dagger + \Delta_0^* p c_{-p} c_p \right\}, \quad (4.2.14)$$

where $\epsilon_p = \hbar^2 p^2 / 2m^* R^2 - E_Z$ and $\Delta_0 = \Delta \alpha \hbar / 2E_Z$ [see Eqs. (2.5.11) and (2.5.12)]. The angular momentum sum in (4.2.14) runs over $p + 1/2 \in \mathbb{Z}$ for $\Phi/\Phi_0 \in \mathbb{Z}$ and it runs over $p \in \mathbb{Z}$ for $\Phi/\Phi_0 + 1/2 \in \mathbb{Z}$. The operator c_p (c_p^\dagger) annihilates (creates) an electron with energy $\epsilon_{p,-}$ and momentum p in the lower helical band.

In analogy to the generalized variational approach in reference [75], we consider variational wave functions for the projected Hamiltonian. For each doublet, states with even and odd parity are generated by applying the operators

$$P_-(p) = s_p c_p^\dagger + t_p c_{-p}^\dagger, \quad (4.2.15a)$$

$$P_+(p) = u_p + v_p c_p^\dagger c_{-p}^\dagger \quad (4.2.15b)$$

to the vacuum state. General ansatz wave functions for even (odd) parity are

$$|\Psi_{e(o)}\{\tau_p\}\rangle = \prod_{p \geq 0} P_{\tau_p}(p)|0\rangle \text{ with } \prod_{p \geq 0} \tau_p = +1(-1), \quad (4.2.16)$$

where $|0\rangle$ is the vacuum for the c electrons.

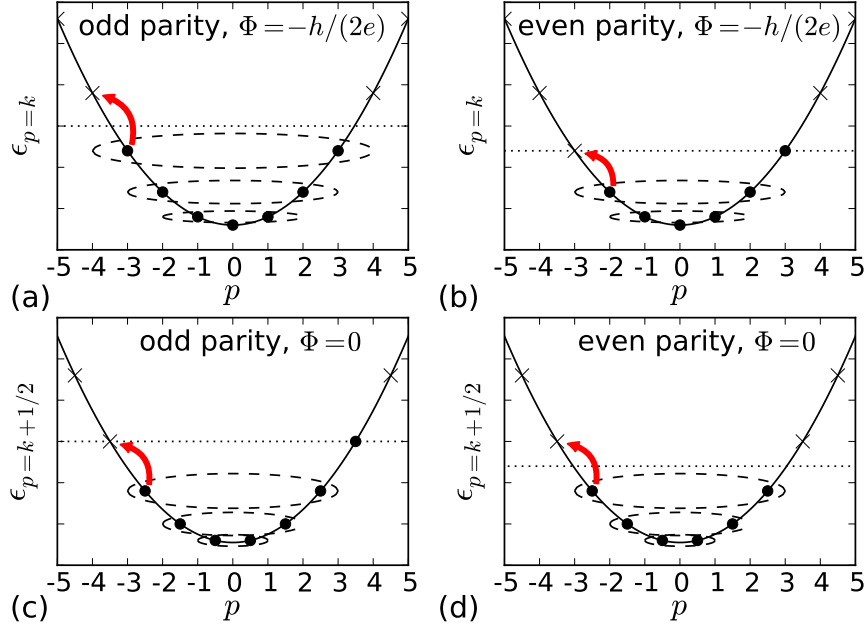


Figure 4.2.1.: Sketch of the dispersion and the effective pairing for the lower helical band $\epsilon_-(p)$. The \bullet markers (\times) denote the occupied (empty) single-particle levels for $\Delta \rightarrow 0$. The dashed ellipses illustrate the paired single-particle levels when switching on the proximity induced superconducting pairing potential. Arrows indicate the transport of a single quasiparticle to produce the lowest excited state.

To obtain the energy spectrum for arbitrary magnetic flux, we first minimize the Ginzburg-Landau free energy Eq. (4.2.11) to find the pair wave number \mathcal{Q} , which is then used to construct the grand canonical mean-field ansatz wave functions Eq. (4.2.16) via P_{\pm} . For each set of $\{\tau_p\}$, we determine the corresponding energy by unbiased minimization of $E(N, \{\tau_p\}) = \langle H_K \rangle + \mu_N N$ with respect to the variational parameters (s_p, t_p, u_p, v_p) . Here, μ_N is fixed by the mean electron number $N = \langle \sum_p c_p^\dagger c_p \rangle$ in the semiconductor nanowire. By rank-ordering the $E(N, \{\tau_p\})$, we find the ground states for both even and odd parity. To obtain the excited states, we then apply the Bogoliubov operators $a_{p,1}^\dagger = u_p c_p^\dagger - v_p c_{-p}$ and $a_{p,2}^\dagger = u_p c_{-p}^\dagger + v_p c_p$ with $p > 0$ to the ground-state wave function.

In figures 4.2.1(a) and (b) we sketch a bare parabolic dispersion and the single-particle excitation spectrum for $\Phi = -h/2e$. The ground-state wave function for odd parity is

given by

$$\left| \Psi_o^{\text{gs}} \left(\Phi = -\frac{h}{2e} \right) \right\rangle = P_-(0) \prod_{p>0} P_+(p) |0\rangle, \quad (4.2.17)$$

where all time-reversed partners are paired and the zero-momentum electron is unpaired. The lowest excited state has two unpaired electrons at the Fermi number p_F and at $p_F + 1$,

$$\left| \Psi_o^{ij} \left(\Phi = -\frac{h}{2e} \right) \right\rangle = a_{p_F, i}^\dagger a_{p_F+1, j}^\dagger \left| \Psi_o^{\text{gs}} \left(\Phi = -\frac{h}{2e} \right) \right\rangle, \quad (4.2.18)$$

which shows up in a spectroscopic gap of $2\Delta_{\text{eff}}$. On the other hand, the ground state for even parity is given by

$$\left| \Psi_e^{\text{gs}} \left(\Phi = -\frac{h}{2e} \right) \right\rangle = P_-(0) P_-(p_F) \prod_{p \neq 0, p_F} P_+(p) |0\rangle \quad (4.2.19)$$

with two unpaired electrons. In contrast to the odd parity case, we find the lowest excited state by breaking the pair at $p_F - 1$ and creating a new one at p_F ,

$$\left| \Psi_e^{ij} \left(\Phi = -\frac{h}{2e} \right) \right\rangle = a_{p_F, i} a_{p_F-1, j}^\dagger \left| \Psi_e^{\text{gs}} \left(\Phi = -\frac{h}{2e} \right) \right\rangle. \quad (4.2.20)$$

Therefore, the excitation energies for the even parity are determined by the single-particle level spacing. In figures 4.2.1(c) and (d) we illustrate the pairing for $\Phi = 0$. Here, we find that the behavior is reversed compared to the case $\Phi = -h/2e$; i.e., the ground state for the even parity contains only paired levels whereas the ground state for the odd parity has one unpaired electron at the Fermi surface.

4.2.2. Wave functions: Semiconductor-superconductor hybrid system

We now consider the full Hilbert space for the semiconductor Hamiltonian again. Since the Hamiltonian for the full model can be decomposed into a sum over quadruplets, we decompose the total wave function into a (tensor) product of the wave functions for the individual quadruplets. In analogy to what we explained above, we first define generalized operators $P_\pm(k)$ for each quadruplet of the full unprojected Hamiltonian and then construct the ansatz wave functions in analogy to Eq. (4.2.16). We define

$$P_-(k) = \sum_{\alpha} s_{\alpha} \alpha^\dagger + \sum_{\alpha < \beta < \gamma} t_{\alpha\beta\gamma} \alpha^\dagger \beta^\dagger \gamma^\dagger, \quad (4.2.21a)$$

$$P_+(k) = u_k + \sum_{\alpha < \beta} v_{\alpha\beta} \alpha^\dagger \beta^\dagger + w_k \psi_{-k-1+q, \uparrow}^\dagger \psi_{-k+q, \downarrow}^\dagger \psi_{k, \uparrow}^\dagger \psi_{k+1, \downarrow}^\dagger \quad (4.2.21b)$$

for $k \geq (q-1)/2$. Here, the greek summation indices correspond to the quadruplet fermion operators $\alpha, \beta, \gamma \in \{\psi_{-k-1+q,\uparrow}^\dagger, \psi_{-k+q,\downarrow}^\dagger, \psi_{k,\uparrow}^\dagger, \psi_{k+1,\downarrow}^\dagger\}$ and for notation reasons we defined an order of fermion operators $\psi_{-k-1+q,\uparrow}^\dagger < \psi_{-k+q,\downarrow}^\dagger < \psi_{k,\uparrow}^\dagger < \psi_{k+1,\downarrow}^\dagger$ with respect to the orbital angular momentum. Hence, the general ansatz wave functions for even (odd) parity are

$$|\Psi_{e(o)}\{\tau_k\}\rangle = \prod_{k \geq (q-1)/2} P_{\tau_k}(k)|0\rangle \text{ with } \prod_{k \geq (q-1)/2} \tau_k = +1(-1), \quad (4.2.22)$$

where $|0\rangle$ is now the vacuum for the ψ fermions.

We obtain the energy spectrum in full analogy to what we explained above for the Kitaev model. This leads to the following algorithm:

- (i) At first, we minimize the Ginzburg-Landau free energy Eq. (4.2.11) to find the Cooper pair wave number \mathcal{Q} .
- (ii) We use this information to construct the operators $P_\pm(k)$ and the grand canonical ansatz wave functions $|\Psi_{e(o)}\{\tau_k\}\rangle$ Eq. (4.2.22). Since $\tau_k = \pm 1$ for each k , we have in total 2^{n_Λ} ansatz wave functions, where n_Λ denotes the number of quadruplets with kinetic energy smaller than the cutoff E_Λ [see Eq. (4.1.13)]. In our numerical calculation, we choose $n_\Lambda = N$, i.e., the number of quadruplets is the number of electrons. In addition, each of the $2n_\Lambda$ operators P_\pm depend on eight variational parameters.
- (iii) For each set of $\{\tau_k\}$, we determine the corresponding eigenenergies by unbiased minimization of

$$E(N, \{\tau_k\}) = \langle \Psi\{\tau_k\} | H | \Psi\{\tau_k\} \rangle + \mu_N N \quad (4.2.23)$$

with respect to the variational parameters $(s_{k,i}, t_{k,i})$ for $i = 1, \dots, 4$ and $(u_k, v_{k,j}, w_k)$ for $j = 1, \dots, 6$. Here, the chemical potential μ_N is fixed by the mean electron number

$$N = \langle \Psi\{\tau_k\}(\mu_N) | \sum_{k\sigma} \psi_{k\sigma}^\dagger \psi_{k\sigma} | \Psi\{\tau_k\}(\mu_N) \rangle \quad (4.2.24)$$

in the semiconductor nanowire.

- (iv) By rank-ordering the set $\{E(N, \{\tau_k\})\}$, we find the ground states for both even and odd parity. We then obtain the excited states by choosing higher energy states in the rank-ordered set $\{E(N, \{\tau_k\})\}$.

4.2.3. Numerical results

In the following, the magnetic field is varied in discrete steps with the magnetic flux always being a (half-) integer multiple of Φ_0 , such that the only effect is a variation of the Zeeman energy. As discussed above, at $E_Z^2 = \Delta^2 + \mu^2$ the Zeeman energy drives the nanowire

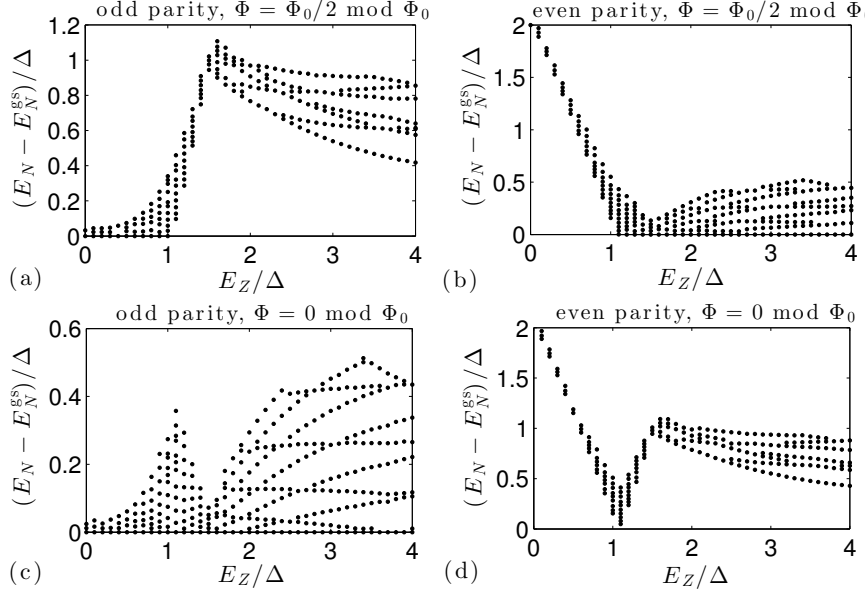


Figure 4.2.2.: Lowest excitation energies for fixed mean electron number as function of Zeeman energy for several combinations of magnetic flux and fermion parity. The magnetic field is varied in discrete steps with the magnetic flux always being a (half-) integer multiple of Φ_0 . The lowest excited states in the nontrivial phase ($E_Z \gtrsim \Delta$) are sketched in figure 4.2.1 for the projected model. Not all excited states are shown.

through a topological phase transition with the trivial phase for $E_Z < \sqrt{\Delta^2 + \mu^2}$ and the nontrivial phase for $E_Z > \sqrt{\Delta^2 + \mu^2}$ [162].

In figure 4.2.2, we plot the lowest excitation energy $\delta E_N = E_N - E_N^{\text{gs}}$ as function of Zeeman energy with N chosen such that $\mu \approx 0$. We see qualitative differences between the trivial phase of the nanowire for $E_Z \lesssim \Delta$ and the nontrivial phase for $E_Z \gtrsim \Delta$. For $E_Z \lesssim \Delta$, results are typical for s -wave superconductivity in ultrasmall metallic grains [74, 75]. For even parity, the excitation spectrum displays a large spectroscopic gap $2\Delta_{\text{eff}}$ independent of magnetic flux since all excited states contain two Bogoliubov quasiparticles. In contrast, the ground state for odd parity always has one Bogoliubov quasiparticle and therefore the spectrum is qualitatively independent of magnetic flux and determined by the single-particle level spacing as

$$\delta E = \zeta(n=1) - \zeta(n=0) \approx \frac{d^2}{2\Delta_{\text{eff}}} \quad (4.2.25)$$

for quasiparticle energies $\zeta(n) = \sqrt{n^2 d^2 + \Delta_{\text{eff}}^2}$ where n counts the energy levels relative to the Fermi energy. Similarly, a variation of magnetic flux by $\Phi_0/2$ changes $\zeta(n)$ on the order of d^2/Δ_{eff} .

For $E_Z \gtrsim \Delta$, we observe a strikingly different parity effect, and find that the excitation energies depend on both magnetic flux and electron parity. In figures 4.2.2(a) and (d) we find a spectroscopic gap $2\Delta_{\text{eff}}$ since the lowest excited states require two Bogoliubov quasiparticles and thus break a Cooper pair. In contrast, the excitation energies in figures 4.2.2(b) and (c) are determined by the single-particle level spacing as $d^2/2\Delta_{\text{eff}}$ since always one unpaired electron is located near the Fermi surface. As shown in figure 4.2.2(d), the characteristic signature of the topological phase transition is the closing and reopening of the excitation gap.

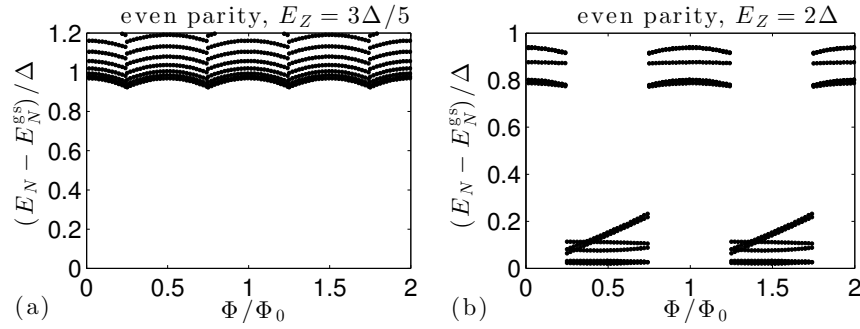


Figure 4.2.3.: Lowest excitation energies for fixed mean electron number as function of the magnetic flux, (a) for $E_Z = 0.6\Delta$, and (b) for $E_Z = 2\Delta$. Not all higher excitation energies are shown.

These different parity effects become even more impressive when fixing the Zeeman energy and varying the magnetic flux. In figure 4.2.3, excitation energies as a function of magnetic flux for both trivial ($E_Z = 0.6\Delta$) and nontrivial sectors ($E_Z = 2\Delta$) are shown for even parity. In the trivial phase, they are of order $2\Delta_{\text{eff}}$ with small $\Phi_0/2$ periodic oscillations of order d^2/Δ_{eff} as shown in figure 4.2.3(a). For the odd parity case (not shown), they are determined by the single-particle level spacing. In the nontrivial phase however, we find large oscillations with period Φ_0 and amplitude $2\Delta_{\text{eff}}$ as shown in figure 4.2.3(b). There, the excitation energies for $\Phi/\Phi_0 \in (1/4, 3/4)$ are determined by the single-particle level spacing, while they display the effective gap $2\Delta_{\text{eff}}$ for $\Phi/\Phi_0 \in (3/4, 5/4)$ due to the pairwise creation of Bogoliubov quasiparticles. For odd parity, we qualitatively find the same spectrum but shifted by $\Phi_0/2$, as follows from the earlier discussion. All these results back up the general arguments in the introduction, connecting ground state degeneracies on the torus to parity and magnetic flux periodicities of excitations.

In the last step, we relate the Φ_0 magnetic flux periodicity in the topologically nontrivial phase to the recently discovered 4π periodicity of the Josephson current between two topological superconductors [31, 76, 127]. To leading order in the tunnel coupling, the Josephson energy between two one-dimensional topological superconductors is given by

the Hamiltonian

$$H_J(\Delta\phi) = i\gamma_1\gamma_2\Gamma \cos\left(\frac{\Delta\phi}{2}\right), \quad (4.2.26)$$

where γ_1 and γ_2 are operators for the end Majorana states connected by the junction, Γ is the tunneling matrix element, and $\Delta\phi$ the phase difference between the two superconductors. The operator $i\gamma_1\gamma_2$ with eigenvalues ± 1 describes the parity of the neutral fermion state shared between the two Majoranas fermions. For a fixed parity, the Josephson energy is 4π periodic in the phase difference. We here consider the case that the 4π periodic Josephson junction is inserted into a ring structure. Then, the superconducting phase difference between the two ends is related to a magnetic flux through the ring via $\Delta\phi = (e/\hbar) \int_{S^1} d\mathbf{r} \cdot \mathbf{A}(\mathbf{r}) = 2\pi\Phi/\Phi_0$, and the 4π phase periodicity is equivalent to a Φ_0 flux periodicity. If the parity is not fixed, a change of $\Delta\phi$ by $2\pi \sim \Phi_0/2$ will change the occupancy $(i\gamma_1\gamma_2 + 1)/2$ of the neutral fermion and hence the ground state parity. This is in full agreement with our finding that in the nontrivial phase the parity of the ground state changes (if coupled to an electron reservoir) when changing the magnetic flux through the ring by $\Phi_0/2$. Since occupying the neutral fermion describes a change in the parity of the pairing wave function and not in the mean number of (charged) particles, the terminology “neutral fermion” is appropriate.

4.3. General single-band Hamiltonian

In this section we consider the full model and study the deviations from the ideal ring-shaped nanowire in order to make contact with possible experiments. For numerical purpose, we now consider a lattice model and replace the derivatives in Eq. (4.1.4) by a nearest-neighbor hopping. Thus, the low-energy physics of the nanowire is described by the lattice Hamiltonian $H = H_{\text{SM}} + H_{\text{SC}}$ with

$$H_{\text{SM}} = - \sum_{\mathbf{r}, \mathbf{r}', \sigma} t_{\mathbf{r}\mathbf{r}'} c_{\mathbf{r}\sigma}^\dagger c_{\mathbf{r}'\sigma} + \sum_{\mathbf{r}, \sigma} \left(E_Z \hat{\sigma}_{\sigma\sigma}^z - \mu + V_{\mathbf{r}} \right) c_{\mathbf{r}\sigma}^\dagger c_{\mathbf{r}\sigma} \\ + \frac{i\alpha}{2a} \sum_{\mathbf{r}, \sigma} \left(c_{\mathbf{r}\sigma}^\dagger \hat{\sigma}_{\sigma\bar{\sigma}}^y c_{\mathbf{r}+\boldsymbol{\delta}_x\bar{\sigma}} - c_{\mathbf{r}\sigma}^\dagger \hat{\sigma}_{\sigma\bar{\sigma}}^y c_{\mathbf{r}-\boldsymbol{\delta}_x\bar{\sigma}} - c_{\mathbf{r}\sigma}^\dagger \hat{\sigma}_{\sigma\bar{\sigma}}^x c_{\mathbf{r}+\boldsymbol{\delta}_y\bar{\sigma}} - c_{\mathbf{r}\sigma}^\dagger \hat{\sigma}_{\sigma\bar{\sigma}}^x c_{\mathbf{r}-\boldsymbol{\delta}_y\bar{\sigma}} \right), \quad (4.3.1)$$

where the operator $c_{\mathbf{r}\sigma}^\dagger$ ($c_{\mathbf{r}\sigma}$) creates (annihilates) an electron at site \mathbf{r} with spin σ and mass m^* . The first term describes hopping on a simple square lattice with lattice parameter a , $t_{\mathbf{r}, \mathbf{r}+\boldsymbol{\delta}_x} = t_{\mathbf{r}, \mathbf{r}+\boldsymbol{\delta}_y} \equiv t_0 = \hbar^2/2m^*a^2$ for the nearest-neighbor lattice vectors $\boldsymbol{\delta}_x = (a, 0)$, $\boldsymbol{\delta}_y = (0, a)$, and $t_{\mathbf{r}, \mathbf{r}} = -2t_0$. The proximity coupling between the s -wave superconductor

and the nanowire is described by the lattice s -wave pairing Hamiltonian

$$H_{\text{SC}} = \sum_{\mathbf{r}} \left(\Delta_{\mathbf{r}} c_{\mathbf{r}\uparrow}^\dagger c_{\mathbf{r}\downarrow}^\dagger + \Delta_{\mathbf{r}}^* c_{\mathbf{r}\downarrow} c_{\mathbf{r}\uparrow} \right). \quad (4.3.2)$$

To incorporate the magnetic flux Φ , we reformulate the minimal coupling Eq. (4.1.5) for the continuous system in terms of hopping matrix elements,

$$t_{\mathbf{r}, \mathbf{r}+\boldsymbol{\delta}} \rightarrow t_{\mathbf{r}, \mathbf{r}+\boldsymbol{\delta}} e^{-\frac{ie}{\hbar} \int_{\mathbf{r}}^{\mathbf{r}+\boldsymbol{\delta}} d\mathbf{r}' \cdot \mathbf{A}(\mathbf{r}')}, \quad (4.3.3a)$$

$$\alpha \rightarrow \alpha e^{-\frac{ie}{\hbar} \int_{\mathbf{r}}^{\mathbf{r}+\boldsymbol{\delta}} d\mathbf{r}' \cdot \mathbf{A}(\mathbf{r}')}, \quad (4.3.3b)$$

where $\int_{\mathbf{r}}^{\mathbf{r}+\boldsymbol{\delta}} d\mathbf{r}' \cdot \mathbf{A}(\mathbf{r}')$ is the line integral of the vector potential along the hopping path $\boldsymbol{\delta}$. This lattice version of the minimal coupling is called Peierls substitution. In analogy to the one-dimensional case Eq. (4.2.12), the superconducting order parameter is modulated by a complex phase

$$\Delta_{\mathbf{r}} \rightarrow \Delta_{\mathbf{r}} e^{i\mathbf{q} \cdot \mathbf{r}}, \quad (4.3.4)$$

where \mathbf{q} is the Cooper pair wavenumber which needs to be determined by minimizing the Ginzburg-Landau free energy Eq. (4.1.8).

For details about the numerical solution of the lattice Hamiltonian $H = H_{\text{SM}} + H_{\text{SC}}$, we refer to Appendix A.1.

4.3.1. Dependence on geometry details

In this section we study how details of the geometric realization of the ring topology affect the excitation spectrum. For this purpose, we compare the spectra for a ring, a square, and for a model with periodic boundary condition as sketched in figure 4.3.1(a). Above we have shown that the low-energy physics of the ring-shaped nanowire is equivalent to that of a strip of width L_{\perp} and length $L = 2\pi R \gg L_{\perp}$ with periodic boundary condition along the x direction and with vector potential $\mathbf{A} = (\Phi - \Phi_0/2)\hat{x}/L$ in the Landau gauge. Here, the first term in the bracket describes the magnetic flux penetrating the ring. The second term originates from the conservation of the total angular momentum of the electrons in the ring structure. More specifically, this conservation yields a spin-orbit coupling between states with equal total angular momentum (pR, \uparrow) and $(pR + \hbar, \downarrow)$ and thus effectively shifts orbital angular momenta pR by $\pm\hbar/2$ [126]. This shift was identified with a 2π spin rotation of an electron encircling the ring which is equivalent to a Berry phase factor -1 and an effective shift of the magnetic flux by $-\Phi_0/2$.

Experimentally, the fabrication of nanoring structures with radii of several hundred

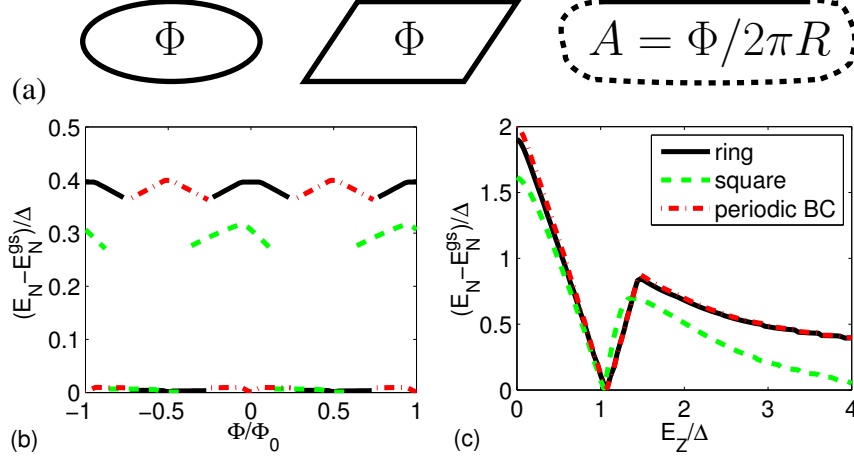


Figure 4.3.1.: (a) Sketch of three different geometric realizations of the S^1 topology of the circle: a ring, a square, and a straight nanowire with periodic boundary condition indicated by dots. (b) Lowest excitation energy for $E_Z = 2\Delta$ as function of magnetic flux, and (c) lowest excitation energy for $\Phi = 0 \pmod{\Phi_0}$ as function of Zeeman energy. The parameters used in the numerical calculation are: even parity, $N = 44$, $L = 2\pi R = 3 \mu\text{m}$, and $a = 2 \text{ nm}$. In (c), the magnetic flux for the system with periodic boundary condition is $\Phi = -\Phi_0/2 \pmod{2}$. The lines for panel (b) are defined in panel (c).

nanometers is challenging and the approximation of the ring by a triangle or a rectangle is likely. For this purpose, we consider a square-like structure made out of four nanowires, however, our results are qualitatively also valid for a triangular structure which consists of three nanowires.

In figure 4.3.1(b) and (c), we compare the fixed electron-number excitation spectrum for the three different geometric realizations of the lattice on which the Hamiltonian is defined; the ring of radius R , a quadratic approximation of the ring with edge lengths $\pi R/2$, and a straight nanowire of length $L = 2\pi R$ with periodic boundary condition. In our numerics, we model the ring-shaped nanowire by the one-dimensional tight-binding Hamiltonian Eq. (4.3.1) with spin-orbit coupling perpendicular to the nanowire, and thus rotating in the x - y plane. As function of the discretized azimuthal angle $\varphi_i = 2\pi i/n$ with $n = 2\pi R/a$ lattice sites, the spin-orbit direction is then given by

$$\sigma_{\text{SO,ring}}(i) = \sin(\varphi_i)\sigma^y + \cos(\varphi_i)\sigma^x. \quad (4.3.5)$$

Similarly, we model the square by abrupt changes in the spin-orbit direction at the position

of the corners,

$$\sigma_{\text{SO,square}}(i) = \begin{cases} \sigma^x, & \text{for } 0 < i \leq \frac{n}{4} \\ \sigma^y, & \text{for } \frac{n}{4} < i \leq \frac{n}{2} \\ -\sigma^x, & \text{for } \frac{n}{2} < i \leq \frac{3n}{4} \\ -\sigma^y, & \text{for } \frac{3n}{4} < i \leq n \end{cases} \quad (4.3.6)$$

and the straight nanowire with periodic boundary condition by a constant spin-orbit direction,

$$\sigma_{\text{SO,periodic}}(i) = \sigma^y. \quad (4.3.7)$$

The spectra for these three models are qualitatively very similar and show a Φ_0 flux period. As expected, we find that the model with periodic boundary condition yields the same spectrum as the ring model but with vector potential shifted by $-\Phi_0 \hat{x}/2L$ due to the Berry phase factor -1 which is exact up to corrections of the order of $d/\sqrt{E_Z^2 + (\alpha \hbar k)^2} \ll 1$. This phase shift originates from the 2π spin rotation, and therefore also exists for the square model where the spin rotation happens in discrete jumps rather than continuously. Without superconductivity $\Delta = 0$, the spectra for the ring and the square are identical since both Hamiltonians can be transformed into each other by a global gauge transformation with different gauge fields for spin up and spin down electrons. However, for $\Delta \neq 0$ this transformation is not possible since the spin singlet pairing Hamiltonian breaks the local gauge symmetry. As a consequence, the spectrum for the square geometry shows small deviations from that for the ring geometry because of the existence of corners where the spin-orbit direction jumps by $\pi/2$. In particular, we find that the excitation spectrum for the square is slightly shifted towards smaller values of the magnetic flux as compared to the ring geometry, with the shift being of the order of $\Delta_{\text{eff}}/\alpha \hbar k$. In addition to the nonuniversal phase shift, we find that quasiparticle states with reduced excitation energy exist, which are predominately localized near the corners of the square.

We see that our main results are robust against the details of the geometric realization and rely on the existence of a void such that the topology of the nanowire is homotopically equivalent to an annulus. All these results underline the general arguments in the introduction, connecting ground-state degeneracies on the torus to parity and magnetic flux periodicities of excitations.

4.3.2. Nonmagnetic disorder

On the one hand, disorder is known to often have drastic influence on the electronic properties of low-dimensional systems. On the other hand, superconducting pairing correlations in s -wave superconductors are protected against time-reversal invariant impurity scatter-

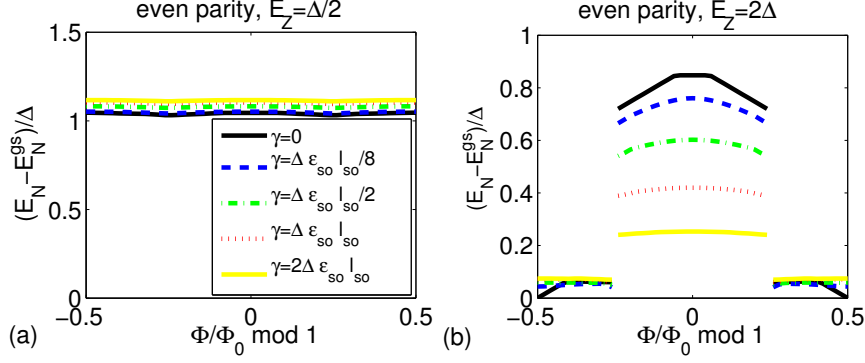


Figure 4.3.2.: Lowest excitation energy for a ring-shaped nanowire with $N = 44$, $L = 3 \mu\text{m}$, and $a = 5 \text{ nm}$ as function of magnetic flux and for several variances γ of the nonmagnetic disorder potential. The curves represent the average over 50 random disorder configurations. The lines are defined in panel (a).

ing by Anderson’s theorem [90]. This motivates us to address the question of how robust the ground-state degeneracies in the torus topology are against potential nonmagnetic disorder. In the following, we discuss the effect of disorder on the excitation energies in the regime where the effective gap is larger than the single-particle level spacing, i.e., for

$$\Delta_{\text{eff}} \equiv \frac{\Delta \epsilon_{so} l_{so} N}{4 R E_Z} > d. \quad (4.3.8)$$

Here, we used Eq. (2.5.12) with $\hbar \alpha = \epsilon_{so} l_{so}$ and $k_F = N/2R$. We model nonmagnetic disorder by a locally varying impurity potential $V_{\mathbf{r}}$ with vanishing mean value and Gaussian white noise correlator

$$\langle V_{\mathbf{r}} V_{\mathbf{r}'} \rangle = \gamma \frac{\delta_{\mathbf{r}, \mathbf{r}'}}{a}. \quad (4.3.9)$$

We here consider the regime of disorder strengths $\gamma \lesssim \gamma_m$ with $\gamma_m = \Delta \epsilon_{so} l_{so}$, since strong disorder $\gamma \gg \gamma_m$ breaks the nanowire into topological and nontopological domain walls and thereby destroys the excitation gap [128].

In figure 4.3.2 we display the excitation spectra for the topologically nontrivial and trivial phase as a function of magnetic flux, and in figure 4.3.3 we display the excitation spectrum as a function of Zeeman energy for several combinations of parity and magnetic flux. We find that the effect of nonmagnetic disorder is very different in the topologically trivial and the nontrivial phase. In the trivial phase, the quasiparticle excitation gap is remarkably robust against disorder which is characteristic for s -wave superconductivity [90]. In contrast, we find a significant reduction of the excitation gap due to disorder in the nontrivial phase. While the Φ_0 flux periodicity is not directly affected by disorder as shown in figure 4.3.2(b), there is a maximum level of nonmagnetic disorder $\gamma_m = \Delta \epsilon_{so} l_{so}$ such

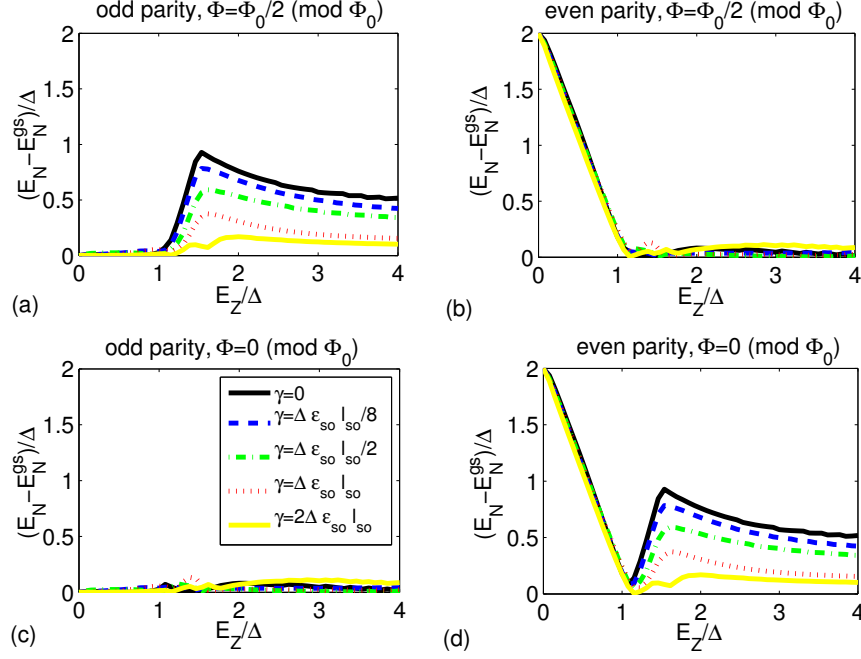


Figure 4.3.3.: Lowest excitation energy for a ring-shaped nanowire with $N = 44$, $L = 3 \mu\text{m}$, and $a = 5 \text{ nm}$ as function of Zeeman energy and for several variances γ of the nonmagnetic disorder potential. The curves represent the average over 50 random disorder configurations. The lines are defined in panel (c).

that only for $\gamma \lesssim \gamma_m$ the excitation gap $\approx 2\Delta_{\text{eff}}$ is larger than the single-particle level spacing d and the Φ_0 periodicity is observable. Since the topologically nontrivial phase for large Zeeman energies $E_Z \gg \Delta, \mu$ can be mapped onto a spinless p -wave superconductor [34], this reduction is in full agreement with the effect of disorder on the excitation gap in spinless p -wave superconductors [129,130]. Furthermore, we find that the reduction is very efficient near the topological phase transition since there already weak disorder breaks the nanowire into domains of different chemical potential and thereby shifts parts of the nanowire through the topological phase transition which reduces the excitation gap locally. Away from the topological phase transition, the reduction of the excitation gap is weaker because the existence of partially trivial domains due to disorder becomes unlikely. Furthermore, we find that disorder shifts the topological phase transition towards larger values of the Zeeman energy [130,131]. As before, we argue that this shift originates from local topological phase transitions at $E_Z^2 = \Delta^2 + (\mu + V_r)^2$ which are shifted towards larger Zeeman energies due to disorder.

Since the parity and magnetic flux dependence of excitation energies reflect the presence or absence of nontrivial topological order, our findings for the nonlinear Coulomb blockade transport are robust against nonmagnetic disorder and other perturbations as long

as the topological order is not destroyed by the formation of domain walls. In particular, we find a maximum variance γ_m of nonmagnetic disorder below which the condition $\Delta_{\text{eff}} > d$ is clearly satisfied, and the Φ_0 periodicity is observable. Before finishing this section, we discuss the physical interpretation of the maximum disorder strength γ_m . Using the definition of Δ_{eff} in Eq. (4.3.8), the Fermi momentum $k_F = N/2R$, and the Fermi velocity $v_F \approx 2E_Z/k_F$, we write $\gamma_m = \Delta_{\text{eff}}v_F$. The characteristic energy scale for a superconducting system is the quasiparticle gap Δ_{eff} and the characteristic length scale is the superconducting coherence length $\xi = v_F/\Delta_{\text{eff}}$. Thus, we find that the maximum disorder strength

$$\gamma_m = \Delta_{\text{eff}}^2 \xi \quad (4.3.10)$$

reflects the two characteristic scales of the topological superconductor in a natural way.

4.3.3. Non-superconducting segments

In this section we consider the situation that the proximity induced superconducting order parameter has a position dependence. Experimentally, this might appear due to the roughness of the nanowire/superconductor interface, or if the nanowire is not completely covered with the s -wave superconductor. As sketched in figure 4.3.4(a), we describe this spatial dependence of the superconducting pairing amplitude by a step function such that $\Delta_{\mathbf{r}} = 0$ for $0 < x < \lambda \ll L$ and $\Delta_{\mathbf{r}} = \Delta$ elsewhere. In figure 4.3.4(c), we display the excitation energies for several lengths λ of the non-superconducting segment. We find a significant reduction of the excitation gap in the trivial phase while the excitation energies in the nontrivial phase are only weakly reduced even for $\lambda \sim l_{so}$. We argue that the origin of the robustness of the excitation gap in the topological phase is the small effective gap $\Delta_{\text{eff}} < \Delta$ and the enhanced Fermi velocity $v_F(E_Z > \Delta) \sim 2v_F(E_Z = 0)$ due to the occupation of a single spinless band. Hence, the superconducting coherence length $\xi = v_F/\Delta_{\text{eff}}$ in the topologically nontrivial phase is significantly enhanced as compared to the trivial phase. Thus, in the nontrivial phase superconducting pairing correlations are more efficiently induced in the non-superconducting part of the nanowire which here shows up as the robustness of the superconducting gap against the existence of a quite long normal segment.

From the robustness of the excitation gap, we conclude that it is not necessary for our proposed setup that the nanowire is completely covered with the s -wave superconductor. In particular, we propose that it is sufficient to place superconducting grains on the nanowire in order to significantly increase the charging energy and to reduce Cooper pair cotunneling through the superconductor [see section 4.5]. We now assume that the nanowire contains

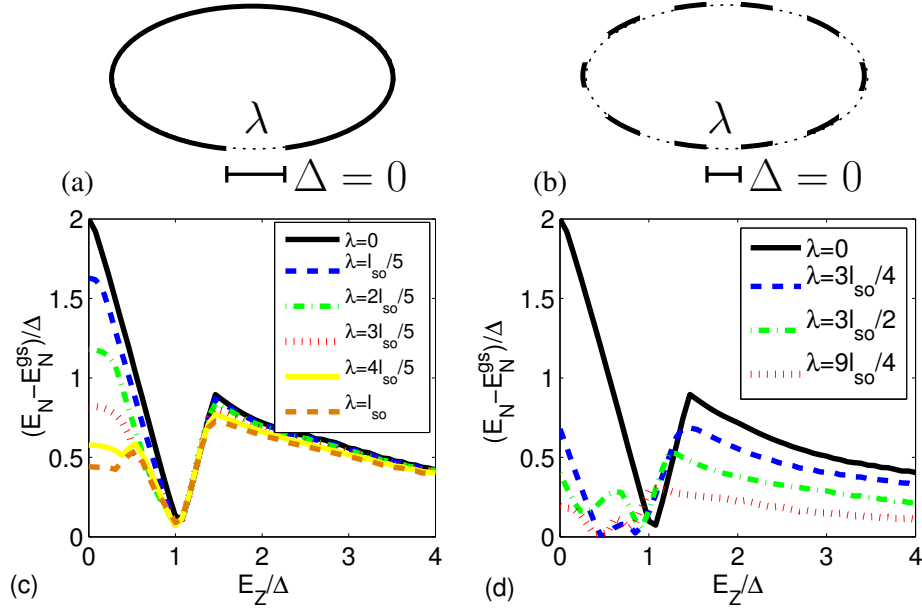


Figure 4.3.4.: Sketch of the nanowire with (a) one and (b) ten non-superconducting segments of length λ , i.e., segments which are not covered with superconducting material. (c), (d) Lowest excitation energy for a ring-shaped nanowire of length $L = 3 \mu\text{m}$ with even parity, $N = 44$, $\Phi = 0$, and $a = 5 \text{ nm}$ for the case with (c) one and (d) ten non-superconducting segments.

ten non-superconducting segments of length λ uniformly distributed over the nanowire as sketched in figure 4.3.4(b). In figure 4.3.4(d), we study the excitation spectrum for several characteristic lengths λ . While the excitation gap for $\lambda = 3l_{so}/2 \sim 150 \text{ nm}$ in the trivial phase is completely absent, we find that the excitation energies in the nontrivial phase are only reduced by 30% as compared to the situation where $\Delta \neq 0$ everywhere.

There is a renormalization of Δ_{eff} in the case of covering the semiconductor nanowire with superconducting grains. Such a situation was discussed by van Heck *et al.* in reference [127], and the mechanism for the renormalization of Δ_{eff} are phase fluctuations in the regions between two grains, which are enhanced by the existence of a relative charging energy between the superconducting grains. The dimensionless parameter controlling the strength of phase fluctuations is $\delta/\Delta_{\text{eff}}$, where δ denotes the energy for charging one grain relative to the other. For a covering with distance between the grains much smaller than the coherence length ξ , it is reasonable to assume that $\delta \ll E_c$ such that a regime with $\delta < \Delta_{\text{eff}}$ can be reached, where the renormalization of Δ_{eff} is unimportant.

4.4. Multi-band Hamiltonian

In this section we make a departure from the case of strict one-dimensional nanowires and consider the experimentally realistic situation of quasi one-dimensional nanowires of finite thickness with $a \ll L_\perp < \xi$. To ensure that the induced superconducting phase remains quasi one-dimensional and the nanowire exhibits a substantial gap, we demand that the width does not exceed the superconducting coherence length $\xi = v_F/\Delta_{\text{eff}}$ [131–136]. The spatial extension in y direction gives rise to the existence of additional transverse modes and thus subbands which might be partially occupied depending on the chemical potential. In figure 4.4.1(a), we plot the Bogoliubov quasiparticle spectrum for $\Phi = -\Phi_0/2$ as function of Zeeman energy and chemical potential. For

$$\mu \lesssim \frac{(2\pi\hbar)^2}{2m^*L_\perp^2} \quad (4.4.1)$$

only one subband is partially occupied and the excitation spectrum is equivalent to the one discussed in sections 4.2 and 4.3. With increasing chemical potential higher subbands are filled up consecutively and similarly to the single-band case, the higher subbands can be either topologically trivial or nontrivial depending on the chemical potential and the Zeeman energy.

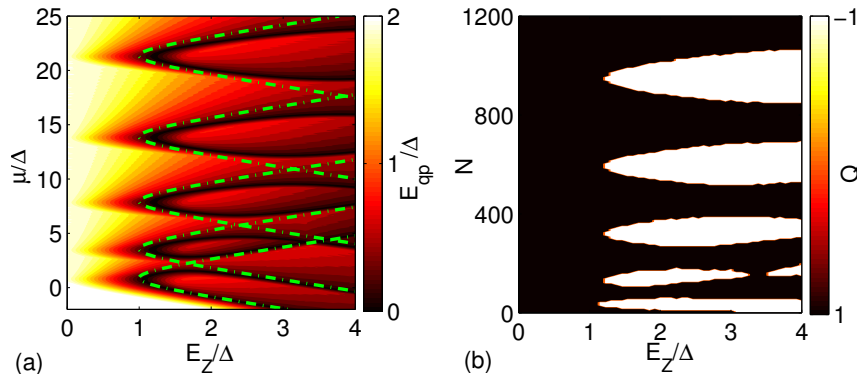


Figure 4.4.1.: (a) Lowest energy of the Bogoliubov quasiparticle spectrum as function of Zeeman energy and chemical potential and (b) phase diagram of the topological number Q as function of Zeeman energy and mean electron number. The green dashed lines in (a) represent the topological phase transition for the various subbands in the limit of uncoupled subbands $\alpha \rightarrow 0$. The parameters used in the numerical calculation are: $L_x = 3 \mu\text{m}$, $L_\perp = 100 \text{ nm}$, $a = 5 \text{ nm}$, and $\Phi = -\Phi_0/2$.

In figure 4.4.1(a), the topologically nontrivial phase shows up as islands which are enclosed by lines of vanishing excitation energies, i.e., by topological phase transitions. As-

suming that the subbands are uncoupled, we find a topological phase transition whenever the chemical potential lies well within one of the spin gaps at zero momentum and when the Zeeman energy satisfies the relation

$$E_Z^2 > \Delta^2 + (\mu - \epsilon_n)^2, \quad (4.4.2)$$

where $\epsilon_n = (\hbar n \pi)^2 / 2m^* L_\perp^2$ denotes the kinetic energy of subband n . However, the transverse spin-orbit term $\alpha c_{\mathbf{r},\sigma}^\dagger \sigma_{\sigma\sigma'}^x c_{\mathbf{r}+\delta_y,\sigma}$ couples the subbands and thereby modifies the lines where the topological phase transitions occur. These modifications are similar to avoided crossings with energy splitting $\delta\mu \approx 2\alpha k_{F,y}$ between the lines of topological phase transitions and thus reduce the size of the topologically nontrivial islands. With increasing chemical potential, the spin-orbit energy in transverse direction increases and thus the energy splitting due to the avoided crossing increases $\delta\mu \sim \alpha\sqrt{\epsilon_n}$.

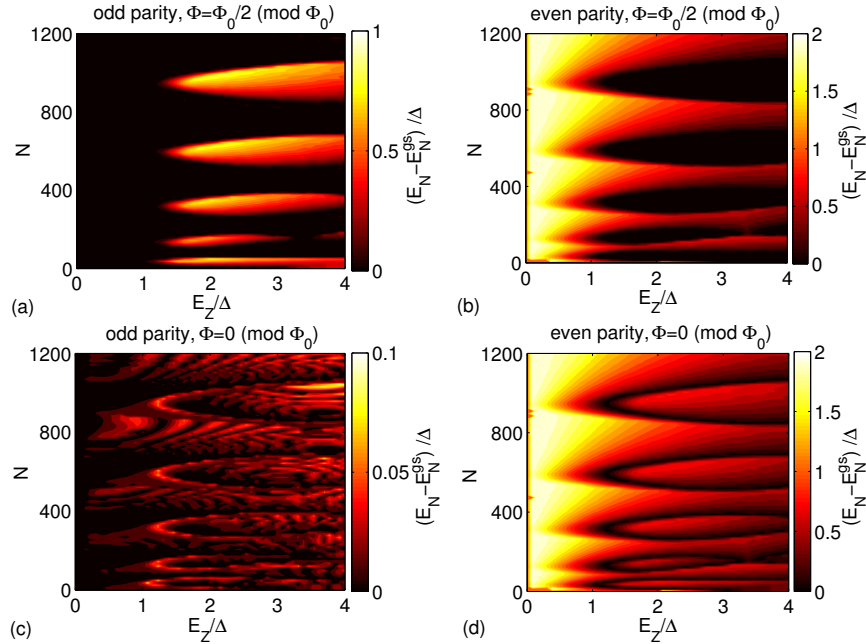


Figure 4.4.2.: Lowest excitation energy in the fermionic excitation spectrum with fixed mean electron number as function of magnetic field and mean electron number for several combinations of magnetic flux and electron parity; $L_x = 3 \mu\text{m}$, $L_\perp = 100 \text{ nm}$, and $a = 5 \text{ nm}$. Note the different color scale in (c) where all excitation energies are determined by the single-particle level spacing d .

In figure 4.4.1(b), we plot the topological number \mathcal{Q} as function of Zeeman energy and mean particle number N . As before, the topological number is $+1$ in the trivial and -1 in the nontrivial phase and thus we conclude that the parity of the grand canonical ground

states in both phases is different with even parity in the trivial and odd parity in the nontrivial phase. Similarly to figure 4.4.1(a), we find islands of topologically nontrivial phase which are enclosed by the trivial phase. We propose that the fixed electron-number excitation energies can be used as a tool to investigate the topological phase diagram.

In figure 4.4.2, we present the lowest excitation energy $\delta E_N = E_N - E_N^{\text{gs}}$ for the multi-band semiconductor hybrid system for several combinations of magnetic flux and parity as function of Zeeman energy and mean particle number. As before, our findings for the trivial phase (i.e., the dark region in figure 4.4.2(a)) are characteristic for *s*-wave superconductivity in ultrasmall metallic grains without excitation gap for odd parity [figures 4.4.2(a) and (c)] and with energy gap $2\Delta_{\text{eff}}$ for even parity [figures 4.4.2(b) and (d)]. These excitation energies do not change qualitatively when changing the magnetic flux and show small $\Phi_0/2$ periodic oscillations of order $d^2/\Delta_{\text{eff}} \ll \Delta_{\text{eff}}$.

In the topologically nontrivial phase (i.e., the bright region in figure 4.4.2(a)) the parity effect is very different. Here, the excitation energies depend on both magnetic flux and electron parity. In figures 4.4.2(a) and (d) we find a spectroscopic gap $2\Delta_{\text{eff}}$ since two Bogoliubov quasiparticle excitations are required and thus a Cooper pair needs to be broken. In contrast, the excitation energies in figures 4.4.2(b) and (c) are determined by the single-particle level spacing since always one unpaired electron is located near the Fermi surface. As shown in figure 4.4.2(d), the characteristic signature of the topological phase transition is the closing and reopening of the excitation gap. When studying the magnetic flux dependence of the excitation energies in the nontrivial phase, we find large oscillations with period Φ_0 and amplitude $2\Delta_{\text{eff}}$. For even parity, the excitation energies for $\Phi/\Phi_0 \in (-1/4, 1/4)$ are determined by the effective gap $2\Delta_{\text{eff}}$ while they are determined by the single-particle level spacing d^2/Δ_{eff} for $\Phi/\Phi_0 \in (1/4, 3/4)$. For odd parity, we qualitatively find the same spectrum but shifted by $\Phi_0/2$, as follows from the earlier discussion.

Thus, the excitation spectrum for fixed electron number directly reflects the topological phase diagram shown in figure 4.4.1(b). We conclude that the proposed nonlinear Coulomb blockade transport experiment can be used as a tool to clearly determine the topological order of the hybrid system by measuring the fermionic excitation spectrum.

Due to the finite width L_\perp of the nanowire, the area of the nanowire itself is penetrated by magnetic flux and thus the magnetic flux through the ring-shaped nanowire is not well-defined. However, the magnetic flux can be decomposed into a mean value for the central of the nanowire and deviations due to the finite thickness

$$\delta\Phi(y) = BL_x y \quad \text{for} \quad -\frac{L_\perp}{2} < y < \frac{L_\perp}{2}. \quad (4.4.3)$$

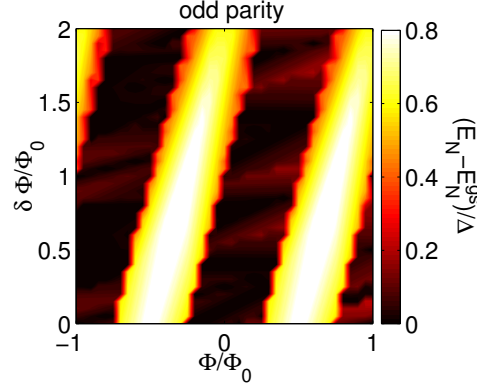


Figure 4.4.3.: Lowest excitation energy for fixed mean electron number as function of magnetic flux $\Phi \pmod{\Phi_0}$ which pierces the nanowire relative its central line and as function of additional magnetic flux $\delta\Phi = BL_x L_\perp/2$ due to the finite thickness of the nanowire. The parameters used in the numerical calculation are: odd parity, $N = 43$, $E_Z = 2\Delta$, $L_x = 2\pi R = 3 \mu\text{m}$, $L_\perp = 70 \text{ nm}$, and $a = 10 \text{ nm}$. For even parity, we find the same spectrum with Φ shifted by $\Phi_0/2$.

For nanowires with radius $R = L_x/2\pi \sim 0.5 \mu\text{m}$ and magnetic field strengths $B \lesssim 1 \text{ T}$, we find $\delta\Phi(L_\perp/2) > \Phi_0$. In figure 4.4.3, we plot the fixed electron-number excitation spectrum as function of mean magnetic flux $\Phi \pmod{\Phi_0}$ and additional flux $\delta\Phi(L_\perp/2)$. We find that the magnetic flux periodicity of the excitation spectrum is not changed, however, the excitation spectrum itself is shifted due to $\delta\Phi$. Thus, we conclude that additional magnetic flux due to the finite width of ring-shaped nanowires with large radii is unproblematic for the study of the magnetic flux periodicity of the excitation energies.

4.5. Cotunneling of Cooper pairs

In this section we estimate the magnitude of Cooper pair cotunneling and compare it with the current due to sequential tunneling of electrons. The tunneling between lead i and the superconductor is described by

$$H_{T,i} = \sum_{\mathbf{k}, \mathbf{q}, \sigma} \left\{ t_{\mathbf{k}, \mathbf{q}} a_{i\mathbf{k}\sigma}^\dagger (u_{\mathbf{q}\sigma} \gamma_{\mathbf{q}\sigma} + v_{\mathbf{q}\sigma} \gamma_{-\mathbf{q}-\sigma}^\dagger) + \text{H.c.} \right\}, \quad (4.5.1)$$

where $t_{\mathbf{k}, \mathbf{q}}$ are the tunnel matrix elements, $a_{i\mathbf{k}\sigma}$ are the fermion operators in lead i with energy $\epsilon_{i\mathbf{k}}$, and $\gamma_{\mathbf{q}\sigma}$ are quasiparticle operators for the superconductor with excitation

energy $E_{\mathbf{q}} = \sqrt{\xi_{\mathbf{q}}^2 + \Delta_s^2}$ [137]. The $u_{\mathbf{q}\sigma}$ and $v_{\mathbf{q}\sigma}$ are the BCS coherence factors

$$\begin{pmatrix} u_{\mathbf{q}\sigma} \\ v_{\mathbf{q}\sigma} \end{pmatrix} = \frac{1}{\sqrt{2}} \begin{pmatrix} \sqrt{1 - \frac{\xi_{\mathbf{q}}}{E_{\mathbf{q}}}} \\ \sigma \sqrt{1 + \frac{\xi_{\mathbf{q}}}{E_{\mathbf{q}}}} \end{pmatrix}. \quad (4.5.2)$$

Tunneling of Cooper pairs between lead i and the superconductor is described by an effective Hamiltonian which can be derived in second-order perturbation theory in $H_{T,i}$. In the first step, one electron with momentum \mathbf{k}_1 and spin σ is transferred from an initial state into an intermediate excited state with momentum \mathbf{q} of the superconducting island. In the second step, another electron with momentum \mathbf{k}_2 and spin $-\sigma$ tunnels into the partner state of the first electron $-\mathbf{q}$ such that both electrons form a Cooper pair. Hence, the final state contains an extra Cooper pair in the superconductor and two quasiparticle excitations in the lead. Similarly, we find the reverse process by splitting a Cooper pair followed by two consecutive electron tunneling events [138]. This yields the effective tunneling Hamiltonian

$$H_{\text{CP},i} = \langle \text{BCS} | H_{T,i} \frac{1}{i\eta - H_0} H_{T,i} | \text{BCS} \rangle, \quad (4.5.3)$$

where we traced out the quasiparticle operators via the BCS many-body ground state wave function $|\text{BCS}\rangle$ with $\gamma_{\mathbf{q}\sigma}|\text{BCS}\rangle = 0$. We find

$$H_{\text{CP},i} = \sum_{\mathbf{k}_1, \mathbf{k}_2} \left\{ A_{i\mathbf{k}_1, \mathbf{k}_2} a_{i\mathbf{k}_1\uparrow} a_{i\mathbf{k}_2\downarrow} + A_{i\mathbf{k}_1, \mathbf{k}_2}^* a_{i\mathbf{k}_2\downarrow}^\dagger a_{i\mathbf{k}_1\uparrow}^\dagger \right\} \quad (4.5.4)$$

with the effective tunneling matrix elements

$$A_{i\mathbf{k}_1, \mathbf{k}_2} = \sum_{\mathbf{q}} t_{\mathbf{k}_1, \mathbf{q}}^* t_{\mathbf{k}_2, -\mathbf{q}} u_{\mathbf{q}\uparrow} v_{-\mathbf{q}\uparrow} \left\{ \frac{1}{E_c + E_{\mathbf{q}} - \epsilon_{i\mathbf{k}_1} - \mu_i} + \frac{1}{E_c + E_{\mathbf{q}} - \epsilon_{i\mathbf{k}_2} - \mu_i} \right\}. \quad (4.5.5)$$

In the following, we consider the Andreev current through a normal-state–superconductor–normal-state structure with symmetric barriers and bias voltage $0 < V < \Delta_s/e$. Assuming that the voltage between the left (right) lead and the superconductor is $\pm V/2$, we calculate the rate for the Andreev reflection process using Fermi's golden rule

$$I = q \frac{2\pi}{\hbar} \sum_{i,f} |\langle f | T | i \rangle|^2 \delta(E_i - E_f), \quad (4.5.6)$$

where q is the transferred charge, T is the perturbation operator, $|i\rangle$ is the initial state, $|f\rangle$ is the final state, and the δ -function guarantees energy conservation. For Andreev

reflection, we have $q = 2e$ and $T = H_{\text{CP},i}$. The final state is given by the wave function

$$|f\rangle = a_{i\mathbf{k}_1\uparrow}a_{i\mathbf{k}_2\downarrow}|i\rangle \quad (4.5.7)$$

and the additional charge $2e$ on the superconducting island. Thus, we find the current for the scattering of two electrons from the left metallic lead into the superconductor reads

$$I_A(V) = 2e \frac{2\pi}{\hbar} \sum_{\mathbf{k}_1, \mathbf{k}_2} |A_{L\mathbf{k}_1, \mathbf{k}_2}|^2 f(\epsilon_{L\mathbf{k}_1}) f(\epsilon_{L\mathbf{k}_2}) \delta(\epsilon_{L\mathbf{k}_1} + \epsilon_{L\mathbf{k}_2} + \omega) \quad (4.5.8)$$

with $\omega = eV - 4E_c$ and Fermi distribution functions f . In reference [138] it was shown that the Andreev conductance $G_A = I_A/V$ for sequential Cooper pair tunneling can be written as

$$G_A(V) = \frac{e^2}{h} \frac{G^2(\omega)}{N_\perp}, \quad (4.5.9)$$

where G is the dimensionless normal-state conductance and N_\perp the number of transverse channels through the superconducting region in its normal state. Due to the charge $2e$ of Cooper pairs, sequential tunneling of Cooper pairs is not resonant for $eV/2 < E_c - \Delta_{\text{eff}}$ and can be neglected. In the expression for the current, this suppression shows up as shifted chemical potential $\omega = eV - 4E_c$.

We now calculate the current for Cooper pair cotunneling from the left lead to the right lead via the superconducting island by calculating the scattering rate in second-order perturbation theory in $H_{\text{CP},i}$ [139]. We find

$$I_{A,\text{cot}}(V) = 2e \frac{8\pi}{\hbar} \sum_{\mathbf{k}_1, \mathbf{k}_2, \mathbf{k}_3, \mathbf{k}_4} W_{\mathbf{k}_1\mathbf{k}_2\mathbf{k}_3\mathbf{k}_4} f(\epsilon_{L\mathbf{k}_1}) f(\epsilon_{L\mathbf{k}_2}) f(-\epsilon_{R\mathbf{k}_3}) f(-\epsilon_{R\mathbf{k}_4}) \quad (4.5.10)$$

with

$$W_{\mathbf{k}_1\mathbf{k}_2\mathbf{k}_3\mathbf{k}_4} = \frac{|A_{L\mathbf{k}_1, \mathbf{k}_2}|^2 |A_{R\mathbf{k}_3, \mathbf{k}_4}|^2}{(\epsilon_{L\mathbf{k}_1} + \epsilon_{L\mathbf{k}_2} + eV - 4E_c)^2} \delta(\epsilon_{L\mathbf{k}_1} + \epsilon_{L\mathbf{k}_2} - \epsilon_{R\mathbf{k}_3} - \epsilon_{R\mathbf{k}_4} + 2eV). \quad (4.5.11)$$

Building on the result for the sequential Cooper pair tunneling Eq. (4.5.9) and assuming $eV \lesssim E_c$, we rewrite the Andreev cotunneling current as

$$I_{A,\text{cot}}(V) \approx h \frac{G_A^2(eV) V^3}{E_c^2}. \quad (4.5.12)$$

In the expression for Eq. (4.5.12), the Andreev current $G_A(eV)$ is not suppressed by the Coulomb energy since the charge on the superconducting island after the tunneling events

is the same as the initial charge.

In contrast, we find for sequential electron tunneling a current

$$I_{\text{seq}} = \frac{e}{h} \Gamma, \quad (4.5.13)$$

where Γ is the tunneling rate between the lead and the semiconductor. For characteristic bias voltages smaller or equal to E_c/e , we compare the currents due to the sequential tunneling of electrons and the Andreev cotunneling of Cooper pairs. With Eq. (4.5.12) and the expression for the Andreev conductance, we find

$$\frac{I_{\text{seq}}}{I_{\text{A,cot}}} \approx \frac{N_{\perp}^2 \Gamma}{E_c G^4}. \quad (4.5.14)$$

We now make the conservative assumption $\Gamma \approx d/10$ and $d \approx E_c/10$, where d is the mean single-particle level spacing in the semiconductor, and demand that single-electron sequential tunneling be larger than Cooper pair cotunneling. In this way, we obtain the condition that $G < \sqrt{N_{\perp}}/3$, i.e., the dimensionless conductance of the junction between lead and the superconductor in its normal state has to be smaller than one third of the square root of the number of transverse channels. For a metal of diameter 10 nm and with Fermi wavelength 0.3 nm, the number of transverse channels is approximately (diameter/wavelength)² = 1000, and thus the dimensionless normal state conductance needs to satisfy $G < 10$, which is realistic for metallic quantum dots with current state technology.

One way to realize the condition $G < \sqrt{N_{\perp}}/3$ experimentally is to not cover the nanowire with superconducting material in the vicinity of the electrodes, and to significantly reduce the conductance between superconductor and electrodes in this way. One can even imagine that an extreme limit could be realized, in which all electrons entering the hybrid system have to do so via the semiconductor in the vicinity of the electrodes. One might argue that as a consequence of removing the superconductor near the electrodes, the proximity induced pairing amplitude in this region will be reduced as well. However, when the region not covered with superconducting material is considerably smaller than the coherence length in the semiconductor (of the order of 100 nm as shown in section 4.3.3), this effect will be small. In principle, one could go even further and only deposit superconducting nanograins on top of the nanowire instead of adding a fully connected superconductor, and in this way eliminate the influence of Andreev cotunneling almost completely.

In order to fully suppress cotunneling of Cooper pairs through the superconductor, we propose to use ferromagnetic leads with the polarization in magnetic field direction. While

ferromagnetic leads fully suppress Andreev processes and thus cotunneling of Cooper pairs in conventional s -wave superconductors, they do not significantly affect the current due to sequential tunneling of electrons.

4.6. Connection to possible experiments

Before concluding this section, we summarize our experimental prediction and discuss how our main findings show up in the nonlinear Coulomb blockade conductance pattern. In figure 4.6.1, we illustrate two typical Coulomb diamond patterns as function of gate and bias voltage. Both plots are identical but shifted relative to each other by the gate potential $e\delta V_G = 2E_c$ which corresponds to a shift in the electron number by one, i.e., by a change of the parity. We use the realistic material parameters $\Delta_{\text{eff}} = 0.2$ meV, $d = 0.1$ meV, and $E_c = 0.6$ meV which clearly satisfy our criterion $d < \Delta_{\text{eff}} < E_c$ for the single-electron transport. Hence, the experimentally relevant voltage window, in which single-electron tunneling through the hybrid system is the dominant transport channel, is bound by the threshold $e|V| \lesssim E_c - \Delta_{\text{eff}} = 0.4$ meV. Above this threshold, Andreev processes might become important and screen the resonance lines from single-electron tunneling.

As discussed in section 4.1.1, qualitatively figure 4.6.1(b) shows the typical diamond pattern for single-electron tunneling through an s -wave superconducting grain. Here, we find a characteristic even-odd effect with an energy gap between the two lowest resonance lines for tunneling processes which change the parity from odd to even. In the opposite case, for tunneling processes from even to odd parity states, this energy gap is absent. This reflects, that the lowest excited state above the ground state of a trivial superconductor with even parity involves two Bogoliubov quasiparticles and thus breaks a Cooper pair, incurring an excitation energy $\delta E \approx 2\Delta_{\text{eff}}$. In contrast, the ground state for odd parity always has one Bogoliubov quasiparticle, and hence the lowest excited state involves both annihilating and creating a Bogoliubov quasiparticle which costs the excitation energy $\delta E \approx d^2/\Delta_{\text{eff}} \ll 2\Delta_{\text{eff}}$. This even-odd effect was experimentally confirmed in ultrasmall aluminum grains by Black *et al.* [74]. In addition, we note that the location of the Coulomb diamonds is slightly shifted and the separation between two diamonds becomes $2E_c - 2\Delta_{\text{eff}}$ ($2E_c + 2\Delta_{\text{eff}}$) for the diamond around a ground state with odd (even) parity. In full analogy, the pattern in figure 4.6.1(b) also describes the nonlinear Coulomb blockade conductance pattern for the trivial superconducting phase of the semiconductor-superconductor nanoring. When changing the magnetic flux through the ring, this pattern shows small variations on the order $d^2/\Delta_{\text{eff}} \ll \Delta_{\text{eff}}$.

For topologically nontrivial superconductors the situation is very different. Here, ground

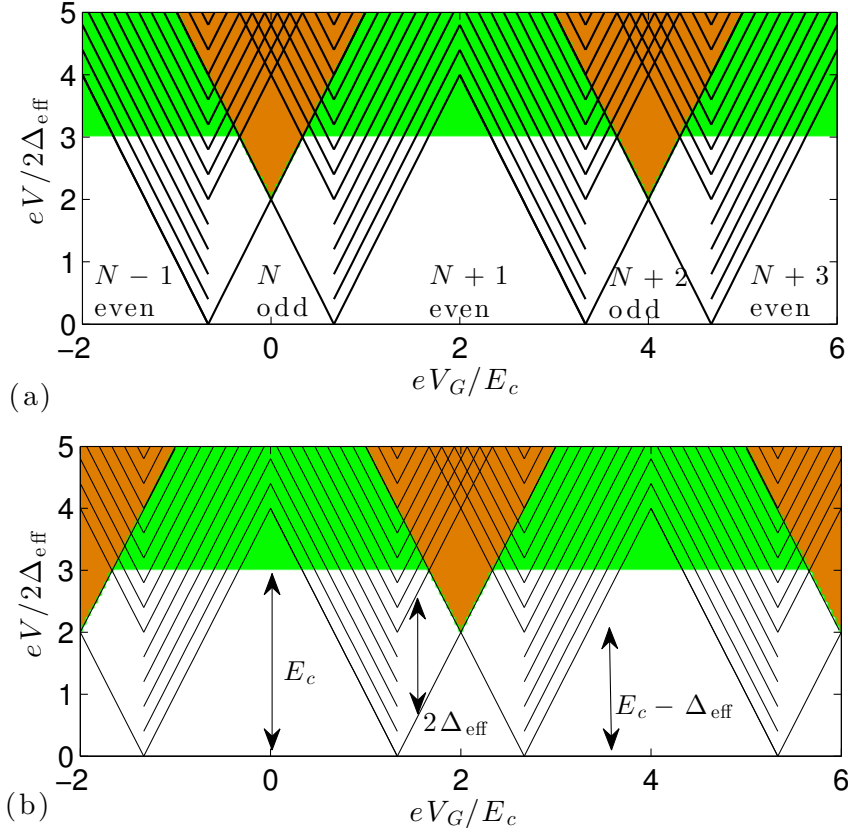


Figure 4.6.1.: Illustration of the stability diagram as function of gate voltage eV_G with effective gap $\Delta_{\text{eff}} = E_c/3$ and single-particle level spacing $d = E_c/6$. In the white upward pointing triangles, transport is blocked by the Coulomb charging energy Eq. (4.1.1). The black lines denote resonance lines of the differential conductance. In the hatched downward pointing white triangles, tunneling of single electrons is possible if the resonance condition Eq. (4.1.2) is satisfied. In the orange area, two-electron processes are allowed by the charging energy. As a consequence, Andreev processes dominate the orange area and single-electron tunneling is suppressed. The green area for $eV > E_c$ marks the regime where co-tunneling of Cooper pairs via the s -wave superconductor might become important and might screen the single-electron processes. (a) Stability diagram for the nontrivial semiconductor-superconductor nanoring with $\Phi = -h/2e$. In the white areas of height $2\Delta_{\text{eff}}$ in the downward pointing diamonds centered around odd N , the current is suppressed by superconducting gap $2\Delta_{\text{eff}}$ and hence there are no resonance lines. (b) Stability diagram for an s -wave superconducting grain or equivalently the semiconductor-superconductor nanoring with $\Phi = 0$. Note the different resonance pattern for tunneling from grains with odd to even parity with energy gap $2\Delta_{\text{eff}}$ and from even to odd parity without energy gap between the resonance lines. Note the symmetry between figures (a) and (b) under parity exchange.

states without unpaired electrons at the Fermi energy have odd parity for periodic boundary condition, and even parity for anti-periodic boundary condition. Therefore, the excitation energy δE oscillates between d^2/Δ_{eff} and $2\Delta_{\text{eff}}$ as function of magnetic flux with period h/e . Hence, we find that the differential conductance pattern oscillates as function of magnetic flux between the figures 4.6.1(a) and (b). In particular, this implies the opening and closing of the excitation gap $2\Delta_{\text{eff}}$ for single-electron tunneling processes from even to odd ground states and the closing and opening of the excitation gap $2\Delta_{\text{eff}}$ for single-electron tunneling processes from odd to even ground states. In addition, we find a periodic oscillation of the gate voltage regimes, in which the ground state has even or odd parity, i.e., the upward pointing white triangles in figure 4.6.1. This yields an oscillation of the diamond tips with magnitude $eV_G = 2\Delta_{\text{eff}}$.

4.7. Summary

In conclusion, we have proposed a nonlinear Coulomb blockade transport experiment to investigate the topological order of semiconductor-superconductor hybrid nanorings, and have shown that peculiar parity and magnetic flux periodicity effects in the excitation spectrum mirror the distinct ground-state degeneracies of trivial and nontrivial superconducting phases on manifolds with nonzero genus. In particular, the excitation spectrum for fixed mean electron number provides clear signatures of the topological phase transition and the h/e flux period in the nontrivial phase which is intricately related to the 4π periodicity of the Josephson current between two topological superconductors. All these findings are robust against geometry details of the realization of the ring structure and rely on the existence of a hole such that the system is homotopic equivalent to a circle.

We have shown that the spectroscopic gap in the topologically nontrivial phase is robust against moderate nonmagnetic disorder. Furthermore, the nontrivial phase is characterized by a large superconducting coherence length which allows to deposit superconducting nanograins on top of the nanowire instead of adding a fully connected superconductor, and in this way eliminate the Andreev cotunneling and enhance the charging energy. Finally, we have studied quasi one-dimensional multi-subband nanowires and we have shown that nonlinear Coulomb blockade transport can be used as a tool to map out the topological phase diagram.

5. Spin response in three-dimensional topological superconductors

In this chapter we make a departure from low-dimensional systems, where the topologically nontrivial state was engineered in semiconductor-superconductor heterostructure, and focus our attention on three-dimensional systems with an intrinsic topologically nontrivial electronic structure. Topological insulators are time-reversal-invariant systems with gapped bulk and protected massless Dirac modes at the surface [11, 12]. Semiconductors like the bismuth chalcogenides with strong spin-orbit coupling and a Fermi surface centered at the time-reversal-invariant momentum, are of particular interest because of their single helical Dirac cone at the surface [9]. Copper-doped Bi_2Se_3 is an unconventional superconductor [43, 44, 77, 78] with nontrivial surface states and a band structure similar to that of Bi_2Se_3 but with shifted chemical potential, reduced Fermi velocity, and enlarged surface dispersion [78].

By now, the surface states in $\text{Cu}_x\text{Bi}_2\text{Se}_3$ have been probed by photoemission [78] and point contact spectroscopy [79–83]. Currently, the experimental situation for the superconducting state of $\text{Cu}_x\text{Bi}_2\text{Se}_3$ is rather controversial [84]. Recent point contact spectroscopy experiments [79–81] showed signatures of subgap surface states and hence topological superconductivity from a zero-bias anomaly in the differential conductance. In contrast, no such signatures were found in the scanning tunneling experiment [82] and in nanoscale tunneling experiment [83]. As a consequence, at the moment the superconducting pairing symmetry of $\text{Cu}_x\text{Bi}_2\text{Se}_3$ cannot be unambiguously determined from tunneling spectroscopy, and data obtained by complementary experimental techniques are desirable.

Nuclear magnetic resonance (NMR) and quadrupole resonance, as well as the electron and muon spin resonance are another class of powerful techniques to investigate the electronic properties locally. The Knight shift for example is determined by the static spin susceptibility $K \sim \chi_s(\mathbf{q} = \mathbf{0}, \omega = 0)$, which is directly connected to the spin structure of the superconducting pairing. In conventional s -wave superconductors with spin-singlet pairing, the Knight shift is significantly reduced and vanishes for zero temperature because spins pair up and longitudinal spin excitations cost the pair-breaking energy 2Δ . However,

in superconductors with strong spin-orbit coupling the spin susceptibility is suppressed as compared to the normal state but does not vanish for zero temperature due to coupling between up and down spins [140]. In this chapter we study characteristic features in the spin response of odd-parity pairing in doped topological insulators and predict clear signatures for the above resonance techniques.

In reference [45], Fu and Berg showed that strong spin-orbit-coupled bands indeed favor an odd-parity interorbital unequal-spin pairing [85, 86]. To gain insight into its topologically nontrivial nature, we map this pairing Hamiltonian onto the conduction band, which yields an effective time-reversal invariant $p \pm ip$ pairing in three dimensions. Because of this topology, there is a pair of Majorana zero-energy modes located at each surface and protected by time-reversal symmetry. Additionally, there are unconventional surface Andreev bound states originating from the band inversion as shown in reference [87] for a linear $k \cdot p$ model. In addition to terms linear in momentum, we here consider quadratic momentum terms, which determine the energy range of coexistence between Dirac modes and unconventional surface Andreev bound states, and which may give rise to another species of zero-energy surface Andreev bound state. The main motivation for introducing the quadratic terms is the possibility to investigate the competition between the different surface states and the bulk. The coexistence of the Majorana zero-energy modes and the surface Andreev bound states originating from the band inversion [87] gives rise to two characteristic length scales. The Dirac modes decay on the nanometer scale ξ_0 [141–143] whereas the decay length ξ_1 for the Majorana zero-energy modes is hundreds of nanometer [87]. Hence, the local spin susceptibility shows different characteristic behavior in the bulk, at the surface, and within ξ_1 into the bulk.

Conventional bulk NMR can distinguish between competing pairing symmetries by the characteristic temperature dependence of the Knight shift and the spin-lattice relaxation rate. We propose that NMR in thin films of thickness $L \sim 500$ nm or depth controlled probes [88, 89] allow to clearly determine the pairing symmetry and investigate the Majorana zero-energy modes. Our work is motivated by $\text{Cu}_x\text{Bi}_2\text{Se}_3$, however, our results are more generally relevant for other inversion symmetric materials such as the ternary chalcogenides [144] and the PbTe class [145, 146]. Furthermore, our findings for doped topological insulators are complementary to the superfluid $^3\text{He-B}$ phase [147, 148] where spin relaxation reflects the gapless Majorana nature.

This chapter is organized as follows. In section 5.1, we introduce the model system for the topological insulator and competing superconducting pairing symmetries. We continue in section 5.2 with the study of the spin response where we concentrate on the real part of the longitudinal spin susceptibility, which yields the Knight shift, and the imaginary part

of the transverse spin susceptibility, which determines the spin lattice relaxation rate. In section 5.3, we compare the spin response for the various pairing symmetries and predict magnetic resonance experiments to observe the unconventional surface Andreev bound state in topological superconductors. We summarize our results in section 5.4.

5.1. Model system

5.1.1. Hamiltonian for the doped topological insulator

In this chapter we consider doped three-dimensional topological insulators described by the low-energy $k \cdot p$ Hamiltonian [9, 45]

$$H_{\text{TI}} = \sum_{\mathbf{k}} C_{\mathbf{k}}^{\dagger} \mathcal{H}_{\text{TI}}(\mathbf{k}) C_{\mathbf{k}} \quad (5.1.1)$$

with the 4×4 Hamilton matrix

$$\mathcal{H}_{\text{TI}}(\mathbf{k}) = m_0(\mathbf{k})\sigma_x + v_z k_z \sigma_y + v(k_x s_y - k_y s_x)\sigma_z - \mu, \quad (5.1.2)$$

where $m_0(\mathbf{k}) = m + B_1 k_z^2 + B_2(k_x^2 + k_y^2)$, $C_{\mathbf{k}} = (c_{i,\mathbf{k},s})_{i,s}$, $B_1, v_z > 0$, and $m < 0$. Here, the s_{λ} (σ_{λ}) denote the Pauli matrices for the spin (orbital) degree of freedom, and the operators $c_{i,\mathbf{k},s}$ annihilate an electron in orbital i , with momentum \mathbf{k} , and spin s . In our notation, we neglect the identity matrices for the spin/orbital space and implicitly identify the absence of a Pauli matrix with the identity matrix. As illustrated in figure 5.1.1(a), we consider a two-orbital model, where the two orbital Wannier functions are primarily p orbitals originating from the hybridization of the Se and Bi p_z atomic orbitals [9]. The doped charge density determines the chemical potential μ , and the Fermi surface $\{\mathbf{k}_F\}$ is given by the implicit equation

$$\mu^2 = m_0^2(\mathbf{k}_F) + v_z^2 k_{F,z}^2 + v^2(k_{F,x}^2 + k_{F,y}^2). \quad (5.1.3)$$

The crystal structure of topological insulators and thus the Hamiltonian is invariant under three discrete symmetry transformations [9]. (i) Time-reversal symmetry \mathcal{T} : The time-reversal operator is given by $\mathcal{T} = i s_y \mathcal{K}$ which transforms the electron operators $\mathcal{T} c_{i,\mathbf{k},s} \mathcal{T}^{-1} = s c_{i,-\mathbf{k},\bar{s}}$. Here, \mathcal{K} denotes the complex conjugation operator and we use the notation $\bar{s} = \uparrow$ (\downarrow) for $s = \downarrow$ (\uparrow). (ii) Inversion symmetry (parity) \mathcal{P} : The inversion operator transforms $\mathbf{r} \xrightarrow{\mathcal{P}} -\mathbf{r}$. In the two-orbital model, we explicitly find $\mathcal{P} = \sigma_z$ because of the alternating structure of the orbitals in z direction [figure 5.1.1(a)]. This yields

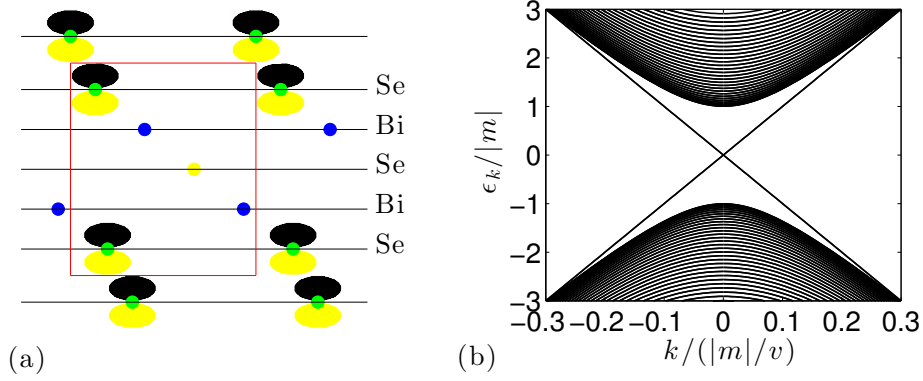


Figure 5.1.1.: (a) Side view of the layered crystal structure of the bismuth chalcogenide Bi_2Se_3 . The red square contains a cut through the unit cell with two outer Se layers, a central Se layer, and two intervening Bi layers. The low-energy physics is primarily determined by two p_z orbitals, which are hybridizations of the Bi and the outer Se atomic orbitals. (b) Bulk and surface band structure of the low-energy model for the Hamiltonian Eq. (5.1.2) confined to $-L < z < 0$ and with $\mu = 0$. For details about the numerical calculation, we refer to Appendix C.1.

$\mathcal{P}c_{i,\mathbf{k},s}\mathcal{P}^{-1} = c_{\bar{i},-\mathbf{k},s}$ with $\bar{i} = 1(2)$ for $i = 2(1)$. (iii) Three-fold rotational symmetry $\mathcal{R}_{2\pi/3}$ around the z axis: The rotation operator is given by $\mathcal{R}_{2\pi/3} = \exp(is_z/3)$. In the low-energy continuum model Eq. (5.1.1) the Hamiltonian is even rotational symmetry around the z axis with arbitrary angle ϕ . This continuous symmetry is described by the operator $\mathcal{R}_\phi = \exp(i\phi s_z/2)$. In particular, we note that \mathcal{R}_ϕ , where ϕ is the azimuthal angle corresponding to the vector (k_x, k_y) , transforms the Hamilton matrix $\mathcal{H}_{\text{TI}}(k_x, k_y, k_z)$ onto $\mathcal{H}_{\text{TI}}(\sqrt{k_x^2 + k_y^2}, 0, k_z)$. As a consequence, we only solve the Hamiltonian for $k_y = 0$, $k_x \in [0, \infty)$, and then, we create all other eigenvectors by applying the operator \mathcal{R}_ϕ .

By diagonalizing the 4×4 Hamilton matrix \mathcal{H}_{TI} , we find the Kramers degenerate eigenenergies

$$E_{\mathbf{k},\pm} = \pm \sqrt{m_0^2(\mathbf{k}) + v_z k_z^2 + v^2 k^2} - \mu, \quad (5.1.4)$$

where the “−” sign describes the valence band and the “+” sign the conduction band of the topological insulator. In figure 5.1.1(b), we show the bulk energy spectrum with valence and conduction bands separated by the band gap

$$E_{0,+} - E_{0,-} = 2|m|. \quad (5.1.5)$$

In the limit, where the linear momentum terms dominate over the quadratic momenta, we

find the electronic density of states for the bulk topological insulator

$$\begin{aligned}
 \mathcal{N}_N(\epsilon) &= 2 \int \frac{d^3k}{(2\pi)^3} \delta \left(|\epsilon| - \sqrt{m_0^2(\mathbf{k}_F) + v_z k_z^2 + v^2 k^2} \right) \\
 &= \frac{1}{\pi v_z v^2} \int d\lambda \lambda^2 \delta \left(|\epsilon| - \sqrt{m_0^2(\mathbf{k}_F) + \lambda^2} \right) \\
 &= \frac{1}{\pi v_z v^2} \int d\lambda \lambda^2 \delta(\lambda - \lambda_\epsilon) \left| \frac{\epsilon}{\lambda_\epsilon} \right|_{\lambda_\epsilon = \sqrt{\epsilon^2 - m_0^2(\mathbf{k}_F)} \Theta(|\epsilon| - |m_0(\mathbf{k}_F)|)} \\
 &= \frac{1}{\pi v_z v^2} \epsilon \sqrt{\epsilon^2 - m_0^2(\mathbf{k}_F)} \Theta(|\epsilon| - |m|).
 \end{aligned} \tag{5.1.6}$$

In our analysis, we are interested in electron doped topological insulators and therefore only consider the conduction band of the bulk electronic band structure. The conduction band of the doped topological insulator is described by the fermion operators $\alpha_{\mathbf{k},\tau} = \sum_{s,\sigma} \psi_\tau^{s,\sigma}(\mathbf{k}) c_{\sigma,\mathbf{k},s}$ with the four-component electronic wave function

$$\psi_\tau(\mathbf{k}) = \frac{1}{2\sqrt{E}} \begin{pmatrix} \sqrt{E + vk\tau} e^{i\chi/2} \\ \sqrt{E - vk\tau} e^{-i\chi/2} \end{pmatrix}_\sigma \otimes \begin{pmatrix} e^{i(\phi/2 + \tau\pi/4)} \\ e^{-i(\phi/2 + \tau\pi/4)} \end{pmatrix}_s, \tag{5.1.7}$$

which can be calculated by solving the eigenvalue equation $\mathcal{H}_{\text{TI}}(\mathbf{k}) \psi_\tau^*(\mathbf{k}) = E_{\mathbf{k},+} \psi_\tau^*(\mathbf{k})$. Here, k describes the in-plane momentum, ϕ denotes the azimuthal angle (k_x, k_y) ,

$$e^{i\phi} = \frac{k_x + ik_y}{k}, \tag{5.1.8}$$

$e^{i\chi}$ describes the complex phase of the off-diagonal orbital matrix elements in Eq. (5.1.2),

$$e^{i\chi} = \frac{m_0(\mathbf{k}) + iv_z k_z}{\sqrt{m_0^2(\mathbf{k}) + v_z^2 k_z^2}}, \tag{5.1.9}$$

and E denotes the energy of state $\psi_\tau(\mathbf{k})$,

$$E = \sqrt{m_0^2(\mathbf{k}) + v_z k_z^2 + v^2 k^2}. \tag{5.1.10}$$

The operators $\alpha_{\mathbf{k},\tau}$ annihilate an electron of energy $E > 0$, with momentum \mathbf{k} , and with pseudospin τ in the conduction band. The pseudospin operator is given by

$$\mathcal{S} = \frac{k_x s_y - k_y s_x}{k} \equiv \begin{pmatrix} 0 & -ie^{-i\phi} \\ ie^{i\phi} & 0 \end{pmatrix} \tag{5.1.11}$$

and with the eigenvalue equation $\mathcal{S} \psi_\tau^*(\mathbf{k}) = \tau \psi_\tau^*(\mathbf{k})$. Thus, the pseudospin is a measure for

the clockwise or counter-clockwise rotation of the spin when encircling the Fermi surface in the k_x - k_y plane and therefore directly related to the helicity. We note that the operators satisfy the condition

$$\alpha(k, \phi + 2\pi, k_z), \tau = -\alpha(k, \phi, k_z), \tau, \quad (5.1.12)$$

i.e., the operators are 4π periodic under rotation in momentum space. This is a direct consequence of the helical electronic structure which originates from the linear in-plane momentum term in Hamiltonian Eq. (5.1.2) and describes the rotation of a spin in the k_x - k_y plane.

In the following, we study the behavior of the operators $\alpha_{\mathbf{k}, \tau}$ under time-reversal and parity transformation. We find

$$\begin{aligned} \mathcal{T} \alpha_{\mathbf{k}, \tau} \mathcal{T}^{-1} &= \mathcal{T} \sum_{s, \sigma} \psi_{\tau}^{s, \sigma}(\mathbf{k}) c_{\sigma, \mathbf{k}, s} \mathcal{T}^{-1} = \sum_{s, \sigma} \left[\psi_{\tau}^{s, \sigma}(\mathbf{k}) \right]^* c_{\sigma, -\mathbf{k}, \bar{s}} \\ &\stackrel{\text{Eq. (5.1.7)}}{=} \sum_{s, \sigma} \psi_{\tau}^{\bar{s}, \sigma}(-\mathbf{k}) c_{\sigma, -\mathbf{k}, \bar{s}} = \sum_{s', \sigma} \psi_{\tau}^{s', \sigma}(-\mathbf{k}) c_{\sigma, -\mathbf{k}, s'} = \alpha_{-\mathbf{k}, \tau}, \end{aligned} \quad (5.1.13a)$$

$$\begin{aligned} \mathcal{P} \alpha_{\mathbf{k}, \tau} \mathcal{P}^{-1} &= \mathcal{P} \sum_{s, \sigma} \psi_{\tau}^{s, \sigma}(\mathbf{k}) c_{\sigma, \mathbf{k}, s} \mathcal{P}^{-1} = \sum_{s, \sigma} \psi_{\tau}^{s, \sigma}(\mathbf{k}) c_{\bar{\sigma}, -\mathbf{k}, s} \\ &\stackrel{\text{Eq. (5.1.7)}}{=} \sum_{s, \sigma} \tau \psi_{\tau}^{s, \bar{\sigma}}(-\mathbf{k}) c_{\bar{\sigma}, -\mathbf{k}, s} = \sum_{s, \sigma'} \tau \psi_{\tau}^{s, \sigma'}(-\mathbf{k}) c_{\sigma', -\mathbf{k}, s} = \tau \alpha_{-\mathbf{k}, \bar{\tau}}. \end{aligned} \quad (5.1.13b)$$

In particular, we note that the time-reversal operator inverts the momentum but leaves the pseudospin τ invariant. In contrast, the parity operator inverts both the momentum and the pseudospin. This is again a direct consequence of the helical spin structure which rotates the spin direction by π for $\phi \rightarrow \phi + \pi$ in analogy to the pseudospin operator.

5.1.2. Superconducting pairing Hamiltonians

Possible pairing terms depend on the specific mechanism and the lattice symmetry. For pairing induced by onsite density-density interactions, Fu and Berg [45] showed that for realistic material parameters the spin-orbit coupled bands favor odd-parity interorbital unequal-spin pairing,

$$H_{\text{SC}} = \Delta \sum_{\mathbf{k}} \left(c_{1, \mathbf{k}, \uparrow} c_{2, -\mathbf{k}, \downarrow} + c_{1, \mathbf{k}, \downarrow} c_{2, -\mathbf{k}, \uparrow} \right) + \text{H.c.}, \quad (5.1.14)$$

where odd-parity pairing denotes $\mathcal{P} H_{\text{SC}} \mathcal{P}^{-1} = -H_{\text{SC}}$ under parity transformation. However, if the pairing is induced by long-range interactions, such as the electron-phonon interaction, other unequal-spin pairing channels are also possible [85]. Additionally, we

consider (i) even-parity, intraorbital pairing

$$H_1 = \Delta_1 \sum_{\mathbf{k}} \left(c_{1,\mathbf{k},\uparrow} c_{1,-\mathbf{k},\downarrow} + c_{2,\mathbf{k},\uparrow} c_{2,-\mathbf{k},\downarrow} \right) + \text{H.c.}, \quad (5.1.15)$$

(ii) odd-parity, intraorbital pairing

$$H_2 = \Delta_2 \sum_{\mathbf{k}} \left(c_{1,\mathbf{k},\uparrow} c_{1,-\mathbf{k},\downarrow} - c_{2,\mathbf{k},\uparrow} c_{2,-\mathbf{k},\downarrow} \right) + \text{H.c.}, \quad (5.1.16)$$

and (iii) even-parity, interorbital pairing

$$H_3 = \Delta_3 \sum_{\mathbf{k}} \left(c_{1,\mathbf{k},\uparrow} c_{2,-\mathbf{k},\downarrow} - c_{1,\mathbf{k},\downarrow} c_{2,-\mathbf{k},\uparrow} \right) + \text{H.c.} \quad (5.1.17)$$

Before investigating the pairing Hamiltonians in detail, we briefly discuss the condition under which Hamiltonian Eq. (5.1.14) is the favored pairing symmetry and sketch its derivation. We here only sketch the main steps of how to determine unambiguously the superconducting phase diagram, however, we do not explicitly carry out the calculation. For a detailed analysis of the superconducting phase diagram, we refer to reference [45]. In reference [45], Fu and Berg considered Hamiltonian Eq. (5.1.1) with a phenomenological short-range density-density interaction

$$H_I = \int d^3r \left[U (n_1^2 + n_2^2) + 2V n_1 n_2 \right], \quad (5.1.18)$$

where $n_i(\mathbf{r}) = \sum_s c_{i,\mathbf{r},s}^\dagger c_{i,\mathbf{r},s}$ is the electron density in orbital i . The parameters U and $V > 0$ are onsite intraorbital and interorbital interactions. To investigate the electronic instabilities (Cooper instabilities), it is appropriate to consider the random phase approximation (RPA) for the normal-state susceptibilities

$$\chi_{ijkl}^C(\mathbf{q}, \tau) = \sum_{\mathbf{k}} \left\langle T_\tau c_{i,\mathbf{k}+\mathbf{q},\uparrow}(\tau) c_{j,-\mathbf{k}-\mathbf{q},\downarrow}(\tau) c_{k,\mathbf{k},\uparrow}^\dagger c_{l,-\mathbf{k},\downarrow}^\dagger \right\rangle. \quad (5.1.19)$$

With RPA we here mean the infinite sum over all ladder diagrams in a diagrammatic perturbation theory [115]. From Eq. (5.1.19), one obtains the static susceptibility by the analytic continuation $i\omega_n \rightarrow \omega + i0^+$ in Matsubara frequency space and subsequently taking the limit $\omega \rightarrow 0$. The static normal-state susceptibilities $\chi_{ijkl}^C(\mathbf{q}, \omega = 0)$ contain all necessary information about the electronic instabilities of the normal state. In particular, it diverges as one approaches the critical temperature T_c and the orbital symmetry of the superconducting order is directly related to the orbital character of $\chi_{ijkl}^C(\mathbf{q}, \omega = 0)$. One

then finds the leading electronic instability from the divergence of the static susceptibilities with the highest critical temperature T_c . One can identify the pairing potentials with the susceptibilities via $\chi_{1111}^C + \chi_{2211}^C \rightarrow \Delta_1$, $\chi_{1111}^C - \chi_{2211}^C \rightarrow \Delta_2$, $\chi_{1212}^C - \chi_{2112}^C \rightarrow \Delta_3$, and $\chi_{1212}^C + \chi_{2112}^C \rightarrow \Delta$. Fu and Berg found that for low temperatures, the system shows two different superconducting phases depending on the relative magnitude of U and V . Superconductivity is characterized by Δ_1 pairing for $U/V > 1 - 2m(k_F)^2/\mu^2$ and by Δ pairing for

$$U/V < 1 - 2\frac{m(k_F)^2}{\mu^2}. \quad (5.1.20)$$

Hence, in the limit where the interorbital interaction is the dominant attractive interaction, the Δ pairing is indeed the favored pairing symmetry.

For a detailed analysis of the different pairing symmetries, we refer to reference [45] where Fu and Berg investigated the electronic instabilities using a linearized gap equation approach. We believe that, if we had carried out the RPA explicitly, we would find exactly the same results as Fu and Berg. However, we argue that the gap equation approach is biased in the sense that one has to preselect possible order parameters, solve their gap equations, and compare their critical temperatures. Therefore, the validity of the results always depends on the selection of the order parameters. In contrast, the RPA is an unbiased approach since no preselection is required and the divergencies of the susceptibility directly reflect the leading order parameter.

5.1.3. Doped topological insulator with odd-parity interorbital pairing

In this section we investigate the doped topological insulator with odd-parity interorbital pairing Eq. (5.1.14). To study the effect of spin-orbit coupling on the pairing symmetry, we project Eq. (5.1.14) onto the basis $(\alpha_{\mathbf{k},\tau})$ spanned by the conduction band of the bulk topological insulator Eq. (5.1.2). For $\mu > |m| \gg \Delta$, this yields the effective pairing Hamiltonian

$$H_{\text{SC}} \approx i\Delta \sum_{\mathbf{k}} \frac{v_z k_z + i v k \frac{m_0(\mathbf{k})}{\mu}}{E_0(\mathbf{k})} \alpha_{\mathbf{k},+} \alpha_{-\mathbf{k},-} + \text{H.c.}, \quad (5.1.21)$$

where $E_0^2(\mathbf{k}) = v_z^2 k_z^2 + v^2 k^2$ and $k^2 = k_x^2 + k_y^2$. For a detailed derivation of this expression, we refer to Appendix C.2.

The effective pairing Hamiltonian is exact to first order in Δ/μ and yields a gapped bulk excitation spectrum with quasiparticle gap $2\Delta E_0(\mathbf{k})/\mu$. The corresponding Bogoliubov-de Gennes equations are in the same universality class as the ones for two copies of spinless superconductors with opposite chirality, which is known to be a time-reversal-invariant topological superconductor with Majorana zero-energy modes if the chemical potential

lies within the conduction band [14, 19]. From this analogy, we expect to find a Kramers pair of Majorana zero-energy modes for $k = 0$ and additionally a pair of zero-energy surface Andreev bound states whenever $m_0(\mathbf{k}_F) = 0$. In contrast, the bulk single-particle excitation spectrum is always fully gapped with weakly momentum dependent quasiparticle gap

$$E_G(\mathbf{k}) = \Delta \sqrt{1 - \frac{m_0^2(\mathbf{k})}{\mu^2}} > 0. \quad (5.1.22)$$

In the following, we investigate the existence and properties of surface states of the normal-state and the superconducting Hamiltonian. The normal-state Hamiltonian in Eq. (5.1.2) confined in z direction has a two-dimensional helical massless Dirac cone at the surface [9]. However, we also know that the effective pairing Hamiltonian Eq. (5.1.21) yields a pair of helical Majorana zero-energy modes at the time-reversal-invariant momentum $k = 0$ [14]. Hence, we obtain two species of surface states originating from the band inversion and the $p \pm ip$ pairing, respectively. We find these states by replacing $k_z \rightarrow -i\partial_z$ and solving the corresponding Schrödinger equation with boundary condition

$$\sigma_z \psi(z = 0) = \psi(z = 0), \quad (5.1.23)$$

which describes the vanishing of the wave function for orbital 2 at the surface. This boundary condition is justified by the layered atomic structure of the topological insulator where orbital 2 is underneath the orbital 1 surface layer.

For the normal-state Hamiltonian Eq. (5.1.2), we solve the 4×4 system of second-order differential equation

$$\left[(m - B_1 \partial_z^2 + B_2 k^2) \sigma_x - i v_z \partial_z \sigma_y + v k \tau \sigma_z \right] \psi_\tau = E \psi_\tau \quad (5.1.24a)$$

$$\frac{k_x s_y - k_y s_x}{k} \psi_\tau = \tau \psi_\tau \quad (5.1.24b)$$

and search for states localized at the surface. We obtain the surface dispersion $E_{D,\tau}(k) = vk$ and the surface wave functions

$$\psi_{D,\tau}(z, k, \phi) = \sqrt{\frac{\nu}{v_z}} \begin{pmatrix} e^{\nu z/v_z} \\ 0 \end{pmatrix}_\sigma \otimes \begin{pmatrix} 1 \\ i\tau e^{i\phi} \end{pmatrix}_s \quad (5.1.25)$$

with the exponent

$$\nu = \frac{1}{2B_1} \left(1 - \sqrt{1 + \frac{4B_1(m + B_2 k^2)}{v_z^2}} \right). \quad (5.1.26)$$

From this expression, we find the decay length

$$\xi_0 = \frac{v_Z}{\text{Re}(\nu)} = \begin{cases} \frac{2B_1}{v_z}, & \text{for } B_2 k^2 < (-m - \frac{v_z^2}{4B_1}) \\ \frac{2B_1}{v_z} \frac{1}{1 - \sqrt{1 + 4B_1(m + B_2 k^2)/v_z^2}}, & \text{for } (-m - \frac{v_z^2}{4B_1}) < B_2 k^2 < -m. \end{cases} \quad (5.1.27)$$

For $k^2 \rightarrow -m/B_2$, the decay length diverges and the surface states become bulk states as shown in figure 5.1.2(a).

Similarly as for the Dirac modes, we find the zero-momentum Majorana zero-energy modes by solving the Schrödinger equation. In our analytical calculations, we linearize the normal-state dispersion Eq. (5.1.10) by $v_F(-i\partial_z - k_{F,z})$ in the vicinity of the Fermi surface and we set $k_z^2 \rightarrow k_{F,z}^2$ in H_{SC} Eq. (5.1.21) with the normal-state Fermi momentum $k_{F,z}$ in z direction. Thus, we obtain the 2×2 system of ordinary differential equations

$$\begin{pmatrix} v_F(-i\partial_z - k_{F,z}) & \Delta \frac{v_z \partial_z - v k_{F,z} \frac{m_0(k, k_{F,z})}{\mu}}{\mu} \\ \Delta \frac{-v_z \partial_z - v k_{F,z} \frac{m_0(k, k_{F,z})}{\mu}}{\mu} & v_F(i\partial_z + k_{F,z}) \end{pmatrix} \psi = E\psi \quad (5.1.28)$$

with open boundary conditions and the ansatz $\psi \sim e^{\lambda z}$. In our analytical calculation, we approximate the wave function for the surface Andreev states by $\lambda = 1/\xi_1 - ik_{F,z}$ with $\xi_1, k_{F,z} \in \mathbb{R}$ which is exact to first order in $\Delta/v_{F,z}$. This yields the Majorana dispersion

$$E_M(k) \approx vk \frac{\Delta(m + B_1 k_{F,z}^2 + B_2 k^2)}{\mu^2} \quad (5.1.29)$$

near $k = 0$. The surface Andreev states decay on a characteristic length ξ_1 as shown in figure 5.1.2(b) where we plot ξ_1 as function of the chemical potential. We find

$$\xi_1(\mu) = \frac{v_{F,z}}{\Delta} \quad (5.1.30)$$

with the Fermi velocity in the z direction $v_{F,z} = \mu/k_{F,z}$. Typical values for ξ_1 are by a factor of $E_0/\Delta \sim 10^2$ larger than ξ_0 . In contrast to the Dirac modes, the zero-momentum Majorana zero-energy modes exist for all values of the chemical potential and enter the bulk for $\mu \rightarrow \infty$ only. For both species of surface states, the quadratic terms B_1 and B_2 significantly determine the behavior of the decay lengths. For $B_1 = B_2 = 0$, we obtain $\xi_0 = v_z/|m|$ and $\xi_1 = v_z/\Delta$ whereas the decay lengths for $B_1, B_2 > 0$ strongly depend on the Fermi velocity and thus on μ .

We find that the Majorana zero-energy modes are immune against band bending effects due to near-surface electrostatic potential variations [149] since the characteristic length

for band bending effects is nanometer and thus much smaller than the decay length ξ_1 . Furthermore, the Majorana zero-energy modes are robust against moderate nonmagnetic impurity scattering since pair-breaking effects are suppressed by an approximate chiral symmetry in the spin-orbital locked band structure [150].

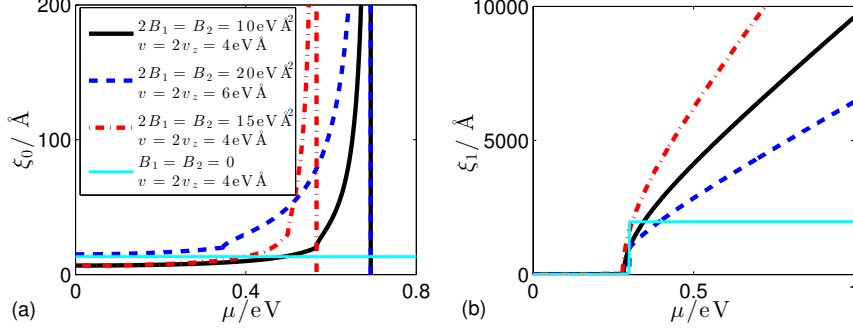


Figure 5.1.2.: Decay lengths of (a) the Dirac mode of the topological insulator and (b) the zero-momentum Majorana zero-energy mode of the odd-parity interorbital superconductor obtained from the analytical expressions for the wave functions for the semi-infinite topological insulator with $\Delta = 1 \text{ meV}$ and $m = -0.3 \text{ eV}$. The lines are defined in panel (a).

Depending on the doped charge density, the superconducting state could occur with the chemical potential either in the region where the Dirac modes are separated from the bulk conduction band [78] [see figures 5.1.3(a) and (b)] or where only the bulk states remain [see figures 5.1.3(c) and (d)]. Since the numerator of the effective pairing Hamiltonian Eq. (5.1.21) vanishes for the Dirac modes with $k_z \rightarrow -i\nu/v_z$ and $\mu = vk$, they are not gapped by H_{SC} and yield a ring structure of zero-energy surface Andreev bound states. Higher order terms which couple valence and conduction band, do not change the character of the surface modes qualitatively. The authors of reference [87] showed that a branch of surface Andreev bound states connects the Majorana zero-energy mode and the Dirac modes due to the mirror helicity of the Hamiltonian, which here shows up as the sign of the mass $m_0(\mathbf{k}_F)$ in Eq. (5.1.21). This mass is negative near the bottom of the conduction band and changes sign for $\mu^2 = -mv_z^2/B_1$. However, in contrast to the zero-momentum mode, the finite-momentum modes are not Majorana zero-energy modes in the sense that they are equal superpositions of electron and hole creation operators such that $\gamma = \gamma^\dagger$. Instead, the Bogoliubov operators for these finite-momentum modes satisfy $\gamma_{\mathbf{k}} = \gamma_{-\mathbf{k}}^\dagger$ with a finite electron-hole imbalance.

In figure 5.1.4(a) we plot the energy of the surface states as function of momentum and chemical potential where we see a Kramers pair of zero-momentum Majorana zero-energy modes for all μ and depending on the chemical potential, we find three regimes, which can be distinguished by the number of additional finite-momentum zero-energy modes.

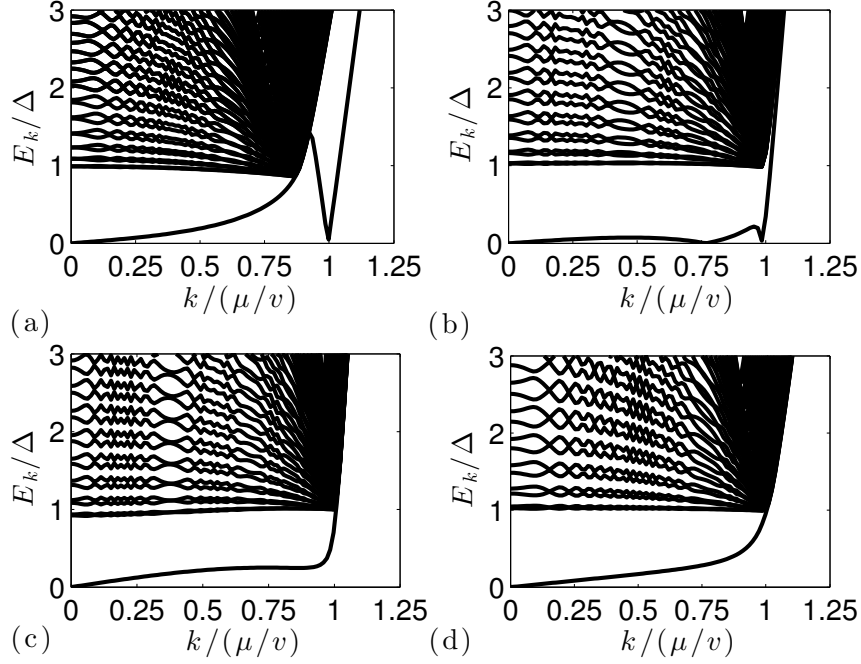


Figure 5.1.3.: Bulk and surface quasiparticle excitation energies for the doped topological insulator with odd-parity interorbital pairing symmetry. The system has a thickness of $L = 160$ nm. The oscillations in the k dependence of the energy levels originates from the finite thickness of the film. (a) $\mu = 0.5$ eV and $m = -0.3$ eV. (b) $\mu = 0.8$ eV and $m = -0.3$ eV. (c) $\mu = 1.1$ eV and $m = -0.3$ eV. (d) $\mu = 0.5$ eV and $m = 0$. For details about the numerical calculation we refer to Appendix C.1.

For small chemical potentials, $\mu^2 < -mv_z^2/B_1, -mv^2/B_2$, the mass term is negative, and hence, both the Majorana zero-energy mode and the branch of zero-energy surface Andreev bound state originating from the Dirac mode exist. On the other hand, for large chemical potentials, $-mv_z^2/B_1, -mv^2/B_2 < \mu^2$, the mass term $m_0(\mathbf{k}_F)$ is positive and only the zero-momentum Majorana zero-energy mode exists. In the regime of intermediate μ , we distinguish two cases $-mv_z^2/B_1 \gtrless -mv^2/B_2$. For $-mv_z^2/B_1 \leq \mu^2 < -mv^2/B_2$, there is a momentum \mathbf{k}_F such that the mass term $m_0(\mathbf{k}_F)$ vanishes. As shown in figure 5.1.4(a) this yields another species of zero-energy surface Andreev bound state emerging at $k = 0$, which now carries the negative velocity from the band inversion as expected from Eq. (5.1.21) and moves towards the Dirac mode with increasing μ and is located at the in-plane momentum

$$k \approx \sqrt{\frac{B_1\mu^2 - |m|v_z^2}{B_1v^2 - B_2v_z^2}}. \quad (5.1.31)$$

For $\mu = vk$, both finite-momentum surface Andreev bound state meet and gap out for $\mu^2 \rightarrow -mv^2/B_2$. In contrast, for $-mv^2/B_2 < \mu^2 < -mv_z^2/B_1$, the Dirac modes disap-

peared in the bulk and is replaced by the unconventional surface Andreev bound state discussed by Hsieh and Fu [87] while $m + B_1 k_{F,z}^2$ is negative. Moreover, with increasing chemical potential, this finite-momentum zero-energy surface Andreev bound state moves towards $k = 0$ and disappears for $\mu^2 \rightarrow -mv_z^2/B_1$. Thus, we conclude that the number of species of zero-energy surface Andreev bound state is even for $m^2 < \mu^2 < -mv_z^2/B_1$ and odd for $\mu^2 > -mv_z^2/B_1$. Hsieh and Fu [87] do not find the competition between these different sectors since the parameters B_1 and B_2 in their lattice model are small and thus they only consider the small chemical potential regime with the zero-momentum Majorana zero-energy mode and one species of finite-momentum modes.

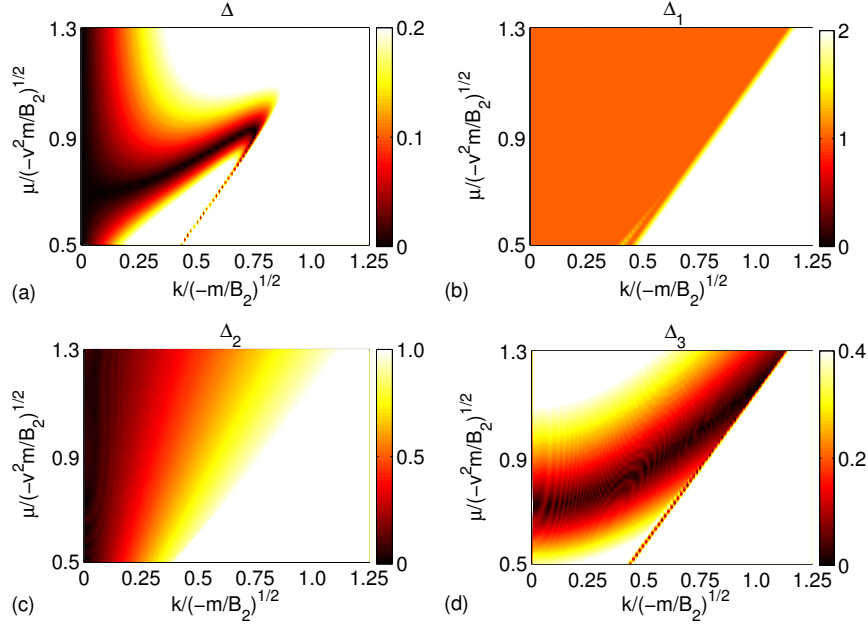


Figure 5.1.4.: Lowest quasiparticle energy in units of Δ_i for a thin film of thickness $L = 240$ nm confined in the z direction and with (a) Δ , (b) Δ_1 , (c) Δ_2 , and (d) Δ_3 pairing as function of in-plane momentum k and chemical potential μ . Note the different color scales.

In the following, we study the spin structure of the Majorana zero-energy mode. For that purpose, we consider the Hamiltonian in Eq. (5.1.1) with superconducting pairing Eq. (5.1.14) confined to the lower half space $z < 0$ and with $k = 0$. The Bogoliubov-de Gennes Hamiltonian for this system is given

$$H = \int dz \begin{pmatrix} C_{\mathbf{0}_\perp}^\dagger(z) & C_{-\mathbf{0}_\perp}(z) \end{pmatrix} [(m_0(k_{F,z})\sigma_x - iv_z\partial_z\sigma_y - \mu)\zeta_z - \Delta s_x\sigma_y\zeta_y] \begin{pmatrix} C_{\mathbf{0}_\perp}(z) \\ C_{-\mathbf{0}_\perp}^\dagger(z) \end{pmatrix}, \quad (5.1.32)$$

which yields for $E = 0$ the Bogoliubov-de Gennes equation

$$[(m_0(k_{F,z})\sigma_x - iv_z\partial_z\sigma_y - \mu)\zeta_z - \Delta s_x\sigma_y\zeta_y]\psi(z) = 0. \quad (5.1.33)$$

Here, the ζ_i for $i = x, y, z$ denote the Pauli matrices for the particle-hole space and $\psi = (\psi_{i,s,\zeta})$ is an eight-component wave function with $i \in \{1, 2\}$, $s \in \{\uparrow, \downarrow\}$, and $\zeta \in \{e, h\}$. It is evident that $s_x\psi(z) = s\psi(z)$ with $s = \pm 1$. For $\psi(z) \sim e^{\lambda z}$, we further simplify Eq. (5.1.33) by multiplying it by ζ_z ,

$$[m_0(k_{F,z})\sigma_x - iv_z\lambda\sigma_y - \mu - \Delta s\sigma_y(-i\zeta_x)]\psi(z) = 0. \quad (5.1.34)$$

It is evident that $\zeta_x\psi(z) = t\psi(z)$ with $t = \pm 1$. When separating this expression into real and imaginary parts and comparing both with the normal-state Hamiltonian in Eq. (5.1.2), we conclude that $\text{Re}(\lambda) = st\Delta/v_z \equiv st/\xi_1$ and $\text{Im}(\lambda) = \pm k_{F,z}$. In order to have an exponentially decaying wave function, we demand $st = +1$. This yields the two independent solutions

$$\xi_{\pm}(z) = \begin{pmatrix} 1 \\ e^{\pm i\theta} \end{pmatrix}_{\sigma} \otimes \begin{pmatrix} 1 \\ s \end{pmatrix}_s \otimes \begin{pmatrix} 1 \\ s \end{pmatrix}_{\zeta} e^{(\pm ik_{F,z} + \Delta/v_z)z}, \quad (5.1.35)$$

where $e^{i\theta} = (\mu + i\sqrt{\mu^2 - m_0(k_{F,z})^2})/\mu$ [87]. In order to satisfy the boundary condition Eq. (5.1.23), we choose a suitable linear superposition of ξ_{\pm} . This yields the final result

$$\psi_{s=\pm}(z) = \begin{pmatrix} \sin(k_{F,z}z - \theta) \\ \sin(k_{F,z}z) \end{pmatrix}_{\sigma} \otimes \begin{pmatrix} 1 \\ s \end{pmatrix}_s \otimes \begin{pmatrix} 1 \\ s \end{pmatrix}_{\zeta} e^{z/\xi_1}. \quad (5.1.36)$$

From these wave functions, we obtain a pair of zero-energy Majorana operators

$$\gamma_+ = \int_{-\infty}^0 dz \psi_+^{\dagger}(z) \cdot C(z), \quad (5.1.37a)$$

$$\gamma_- = i \int_{-\infty}^0 dz \psi_-^{\dagger}(z) \cdot C(z). \quad (5.1.37b)$$

In the following, we argue that the zero-energy Majorana modes described by the wave functions Eq. (5.1.36) can be identified with spinful Bogoliubov quasiparticles. Because of time-reversal symmetry, on each surface two modes reside at zero energy and span a two-dimensional vector space. One special basis of this vector space is determined by quasiparticle operators Eq. (5.1.37), which satisfy the Majorana criterion, $\gamma_{\pm} = \gamma_{\pm}^{\dagger}$. These basis vectors are invariant under time-reversal symmetry and thus the Majorana operators themselves are “spinless”. Similarly, we choose another basis for the quasiparticle operators

as superpositions of the Majorana operators, $\gamma_\sigma = \gamma_+ + \sigma i \gamma_-$. In contrast to the Majorana basis discussed above, these operators are fermion operators with $\gamma_\uparrow^\dagger = \gamma_\downarrow$ and thus non-Hermitian. Furthermore, these operators transform into each other under time-reversal symmetry, and in particular, they are fully spin polarized with spin σ in the z direction.

We conclude that without loss of generality the zero-energy surface Andreev bound state can be understood as a spinful quasiparticle. From this perspective, it becomes clear, that the Majorana zero-energy modes contribute to the magnetic properties of the topological superconductor. In particular, from the spin polarization one can easily see that for a Zeeman field in z direction, the spinful basis is an eigenbasis of the Zeeman coupling and the Majorana zero-energy modes acquire a finite energy proportional to the magnetic field. In contrast, in a spin-polarized p -wave topological superconductor, the combination of a spin \uparrow particle component and a spin \uparrow hole component indeed has zero net spin and would not contribute to the spin response [14].

5.1.4. Competing pairing symmetries

In analogy to the study of the odd-parity interorbital pairing, we here investigate the effect of spin-orbit coupling on the competing pairing symmetries. Hence, we project Eqs. (5.1.15)–(5.1.17) onto the basis $(\alpha_{\mathbf{k},\tau})$ spanned by the conduction band of the bulk topological insulator Eq. (5.1.2), which yields

$$H_1 \approx -i\Delta_1 \sum_{\mathbf{k},\tau}' \alpha_{\mathbf{k},\tau} \alpha_{-\mathbf{k},\tau} + \text{H.c.}, \quad (5.1.38a)$$

$$H_2 \approx -i\Delta_2 \sum_{\mathbf{k},\tau}' \frac{\tau v k}{\mu} \alpha_{\mathbf{k},\tau} \alpha_{-\mathbf{k},\tau} + \text{H.c.}, \quad (5.1.38b)$$

$$H_3 \approx \Delta_3 \sum_{\mathbf{k},\tau}' \frac{m_0(\mathbf{k})}{\mu} \alpha_{\mathbf{k},\tau} \alpha_{-\mathbf{k},\tau} + \text{H.c.}. \quad (5.1.38c)$$

For a detailed derivation of these expressions, we refer to Appendix C.2. The primed sum denotes the sum over all momenta without doubly counting \mathbf{k} and $-\mathbf{k}$. These equal pseudospin pairing terms do not vanish because of the 4π periodicity of the operators $\alpha_{\mathbf{k},\tau}$ under rotation in the k_x - k_y plane. Even if these effective pairing symmetries are very similar, we observe differences in the effect on the Dirac modes and characteristic bulk behavior when the mass term $m_0(\mathbf{k})$ changes sign. In figure 5.1.4, we plot the energy of the lowest quasiparticle level for the superconductor confined in the z direction as function of in-plane momentum k and chemical potential μ .

For Δ_1 -pairing Eq. (5.1.38a), the orbitals pair into singlets with the same sign for both

orbitals. In the projected Hamiltonian Eq. (5.1.38a), states with the same pseudospin are coupled because of the helical sin structure of the topological insulator. Hence, we find conventional s -wave behavior for a metal with spin-orbit coupling. As shown in figure 5.1.4(b), the single-particle excitation spectra in the bulk and at the surface are both fully gapped with gap $2\Delta_1$. The gap at the surface originates from the fact that the helical Dirac modes have only contributions from one orbital and the pairing is intraorbital. We find that even if the Dirac modes are gapped, they do not hybridize with the bulk states because there is no particle-hole mixing between the bulk and the surface and the gap at the surface arises from the pairing between the helical Dirac modes only.

For Δ_2 -pairing [figure 5.1.4(c)], the orbitals pair into singlets with a relative minus sign. Because of this relative minus sign, the effective pairing term Eq. (5.1.38b) is linear in k and vanishes for $k_x = k_y = 0$, which gives rise to point nodes in the bulk single-particle excitation spectrum and a linear dispersion for $\epsilon \ll \Delta_2$. However, for the Dirac modes with $\mu = vk$, we find as for the even parity case a gap $2\Delta_2$.

The effective pairing Hamiltonian for Δ_3 is shown in Eq. (5.1.38c) with a fully gapped bulk single-particle excitation spectrum for $m_0(\mathbf{k}_F) \neq 0$ and a momentum dependent gap $2\Delta_3|m_0(k)|/\mu$. Since $m_0(k)$ changes sign when k increases because of the band inversion at $k = 0$, we find a gap closing and reopening as function of μ , which is intricately related to the transition from the topological insulator phase into the band insulator phase. Furthermore, Δ_3 does not gap the Dirac modes for which $m_0(k, -i\nu/v_z) = \nu$ and the contributions from ν and $-\nu$ cancel. However, from the quasiparticle energies we see that the bulk spectrum has nodes whenever $m_0(k)$ changes sign as shown in figure 5.1.4(d). Similarly to the Δ case, we here find three qualitatively distinct sectors with transitions at $\mu^2 = -mv_z^2/B_1$ and $\mu^2 = -mv^2/B_2$. The origin of the nodes and distinct sectors is again the band inversion near $k = 0$, which changes into the trivial band order along the gapless line in figure 5.1.4(d). However, in contrast to the odd-parity interorbital case, here, the gapless modes are bulk modes. In our numerics, we only consider the case $\mu^2 < -mv_z^2/B_1 < -mv^2/B_2$, where the bulk is fully gapped and the Dirac modes are ungapped.

5.2. Density of states and linear magnetic response

In the following, we investigate signatures of the surface states in the local quasiparticle density of states and the local spin response of the doped topological insulator confined in the z direction. For the numerics we discretize the z direction of Hamiltonian Eq. (5.1.2)

with surfaces at $z = 0$ and $z = L$ by replacing

$$k_z \psi \rightarrow -i \frac{\psi_{n+1} - \psi_{n-1}}{2a} \quad (5.2.1a)$$

$$k_z^2 \psi \rightarrow -\frac{\psi_{n+1} + \psi_{n-1} - 2\psi_n}{a^2}, \quad (5.2.1b)$$

where $z = na$ and $n = 1, \dots, L/a$. In our numerical calculations, we consider a film of thickness $L = 240$ nm and with lattice constant $a = 6$ Å. Motivated by the Bi chalcogenides [12], we use the parameters $m = -0.3$ eV, $v = 2v_z = 4$ eVÅ, $B_2 = 2B_1 = 10$ eVÅ², $\mu = 0.5$ eV, and $\Delta = 3$ meV. The chemical potential is chosen such that the doped charge density corresponds to the experimentally observed value of 10^{20} cm⁻³. Here, B_2 is reduced as compared to Bi₂Se₃ to guarantee the existence of the Dirac modes and its separation from the conduction band as found for Cu_xBi₂Se₃ in angular resolved photoemission spectroscopy [12, 78]. From the above analysis, we know that the zero-momentum Majorana zero-energy modes and one finite momentum zero-energy surface Andreev bound state co-exist in this regime. For abbreviation, we neglect the quadratic momentum terms in our analytical results where they mainly renormalize the Fermi velocity. For details about the numerical calculation of the electronic bands, we refer to Appendix C.1.

The dynamical spin susceptibility is defined by

$$\chi_{ij}(\mathbf{q}, i\omega_n) = \int_0^\beta \langle T_\tau S_i(\mathbf{q}; \tau) S_j(-\mathbf{q}; 0) \rangle e^{i\omega_n \tau} d\tau, \quad (5.2.2)$$

where $S_{\mathbf{q}}^j$ is the spin operator,

$$S_j(\mathbf{q}) = \frac{1}{\mathcal{V}} \sum_{a,b=1,2} \sum_{\mathbf{k}} \sum_{s,s'} c_{a\mathbf{k}+\mathbf{q}s}^\dagger \frac{S_j^{ss'}}{2} c_{b\mathbf{k}s'}. \quad (5.2.3)$$

In our numerics, we use the analytical continuation $i\omega_n \rightarrow \omega + i\delta$ with the broadening $\delta = \Delta/10$. For a detailed derivation of the expressions for the spin susceptibilities, we refer to Appendix C.3.

5.2.1. Odd parity, interorbital unequal-spin pairing

Local density of states

In figure 5.2.1(a) we plot the local density of states which shows two qualitatively distinct regions. In the bulk we obtain

$$\begin{aligned}\mathcal{N}_B(\epsilon) &= \mathcal{N}_N(\mu) \int \frac{d\Omega}{4\pi} \int d\xi \delta \left(\epsilon - \sqrt{\xi^2 + \Delta^2 \frac{E_0^2(k_F)}{\mu}} \right) \\ &= \mathcal{N}_N(\mu) \frac{\epsilon}{\sqrt{\epsilon^2 + \Delta^2 \frac{E_0^2(k_F)}{\mu}}} \Theta \left(\epsilon - \frac{\Delta E_0(k_F)}{\mu} \right)\end{aligned}\quad (5.2.4)$$

with the normal-state density of states $\mathcal{N}_N(\mu)$ Eq. (5.1.6). Here, $\int d\Omega$ denotes the solid-angle integral and ξ the energy relative to the normal-state Fermi surface. The density of states is characterized by the quasiparticle gap $2\Delta E_0(k_F)/\mu$ and a sharp coherence peak, while there is a finite midgap local density of states at the surface. Depending on whether the Dirac modes already crossed the bulk band, we distinguish between $\mu^2 > v^2|m|/B_2$ where only the Majorana zero-energy modes appear with surface local density of states

$$\begin{aligned}\mathcal{N}_S(\epsilon, z \geq 0) &= \frac{2}{(2\pi)^2} \int d^2k |\psi_M(k, \phi, z)|^2 \delta(\epsilon - E_{M,\mathbf{k}}) \\ &\approx \frac{1}{\pi \xi_1} e^{-2z/\xi_1} \int_0^{vk|m|/\mu} dk k \delta(\epsilon - vk\Delta|m|/\mu^2) \\ &= \epsilon \frac{\mu^4}{\pi \xi_1 v^2 m^2 \Delta^2} \sin^2 \left(\frac{zE_0}{v_z} \right) e^{-2z/\xi_1}\end{aligned}\quad (5.2.5)$$

and $\mu^2 < v^2|m|/B_2$ where both the Majorana zero-energy mode and Dirac mode exist with

$$\mathcal{N}_S(\epsilon, z \geq 0) \approx \frac{\mu}{\pi \xi_0 v^2} e^{-2z/\xi_0} + \frac{\epsilon \mu^4}{\pi \xi_1 v^2 m^2 \Delta^2} \sin^2 \left(\frac{zE_0}{v_z} \right) e^{-2z/\xi_1} \quad (5.2.6)$$

for $\epsilon \ll \Delta$ as shown in figure 5.2.1(a). The different surface states can be clearly distinguished by their decay lengths $\xi_0 \ll \xi_1$ and their energy dependencies. While the local density of states of the Dirac modes is almost constant as function of energy, the local density of states of the Majorana surface Andreev bound state strongly depends on energy with a linear increase for $\epsilon \ll \Delta$ and a peak for $\epsilon \lesssim \Delta/2$ [87]. The origin for this very different energy behavior relies on the different energy scales. While the Dirac modes disperse on the scale of the band mass m , the Majorana surface Andreev bound states disperse on the scale $\Delta \ll |m|$. Hence, on the energy scale Δ the Dirac modes show a constant local

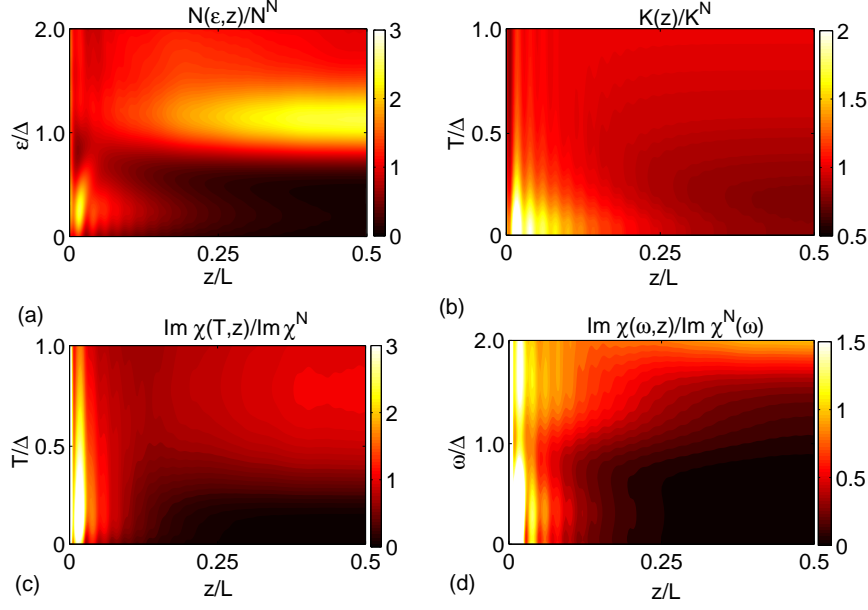


Figure 5.2.1.: Spin response for a topological insulator film of thickness $L = 240$ nm with odd-parity interorbital Δ pairing. (a) Local density of states, (b) Knight shift, and imaginary part of the transverse spin susceptibility as function of (c) temperature and (d) excitation energy with $T = 0$. All quantities are normalized to the normal-conducting bulk at $T = 0$.

density of states as function of energy. Furthermore, the Majorana zero-energy modes oscillate with a period $\lambda = v_z/E_0$, which is on the nanometer scale. For details about the numerical calculation of the local density of states, we refer to Appendix C.3.1.

Local longitudinal spin susceptibility

In figure 5.2.1(b), we plot the real part of the integrated local spin susceptibility which is proportional to the local Knight shift

$$K(z) \sim \text{Re} \int dz' \chi_{zz}(z, z'; \mathbf{q}_{\parallel} = \mathbf{0}; \omega = 0). \quad (5.2.7)$$

For a detailed discussion of the Knight shift and the derivation of Eq. (5.2.7), we refer to Appendix C.4. Here, the distinction between the bulk and the surface is even clearer than for the local density of states. Because of the unequal-spin pairing, we find a significantly reduced contribution in the bulk for $T < \Delta$. However, $K(T \rightarrow 0)$ does not vanish because of the strong spin-orbit coupling [140]. In contrast, we find a large shift for $T \ll \Delta$ near the surface, which is even larger than the bulk shift in the normal state because of the large midgap local density of states Eq. (5.2.6). The temperature dependence of the Knight shift is shown in figure 5.2.2(a) where the light feature is determined by the bulk and the weaker

lines at larger K by the surface states. The Knight shift from the surface states is spread over a wide range due to the exponential decrease in the local density of states and shows peak-like subfeatures determined by the local density of states oscillations. The lines with largest shift originate from the surface where Dirac mode and Majorana zero-energy modes sum up, which gives rise to a very large local density of states and therefore a large spin response.

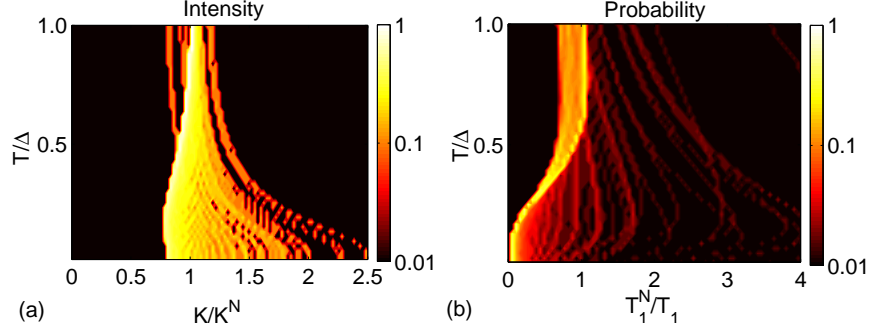


Figure 5.2.2.: Distribution of (a) Knight shift and (b) spin-lattice relaxation rate for a topological insulator film of thickness $L = 240$ nm with odd-parity interorbital Δ pairing as function of temperature. The bright features are determined by the bulk, while the broad subfeatures are the surface-state response. All quantities are normalized to the normal-state bulk at $T = 0$.

Local transverse spin susceptibility

The imaginary part of the transverse spin susceptibility, which is shown in figure 5.2.1(c), is proportional to the spin-lattice relaxation rate [151]

$$\frac{1}{T_1(z)T} \sim \text{Im} \sum_{\mathbf{q}_{||}} \lim_{\omega \rightarrow 0} \frac{\chi_{-+}(z, z; \mathbf{q}_{||}; \omega)}{\omega}. \quad (5.2.8)$$

For a detailed discussion of the spin-lattice relaxation and the derivation of Eq. (5.2.8) we refer to Appendix C.4. Similarly to the Knight shift, we clearly distinguish between the bulk and the surface. The bulk states give rise to an activation law for $T \ll \Delta$ and the Hebel-Slichter coherence peak for $T \rightarrow \Delta$. In contrast, we find a finite $T = 0$ value for $1/(T_1 T)$ near the surface where the contributions from the Dirac modes and the Majorana surface Andreev bound states can be distinguished by their temperature behavior due to the almost constant local density of states of the Dirac modes as function of energy. This temperature dependence is shown in figure 5.2.2(b) where the surface contribution is again spread with peak-like subfeatures. However, the rate directly from the surface ($z \lesssim \xi_0$)

is much larger than the rate from the Majorana zero-energy mode only ($z \gg \xi_0$), which allows us to clearly distinguish the Majorana zero-energy mode from the Dirac modes.

In figure 5.2.1(d), we show the imaginary part of the dynamical transverse spin susceptibility as function of excitation energy. The spin excitation spectrum shows a very different behavior at the surface and in the bulk. For $\omega > 2\Delta E_0(k_F)/\mu$, there is a continuum of bulk spin excitations, which is sharply bounded from below. In contrast, we find surface-surface spin excitations for $\omega < 2\Delta E_0(k_F)/\mu$ at the surface and bulk-surface spin excitations for $\omega > \Delta E_0(k_F)/\mu$. However, the intensity of the surface-surface spin excitations is significantly reduced as compared to the bulk-surface spin excitations.

5.2.2. Competing pairing symmetries

Even-parity intraorbital pairing Δ_1

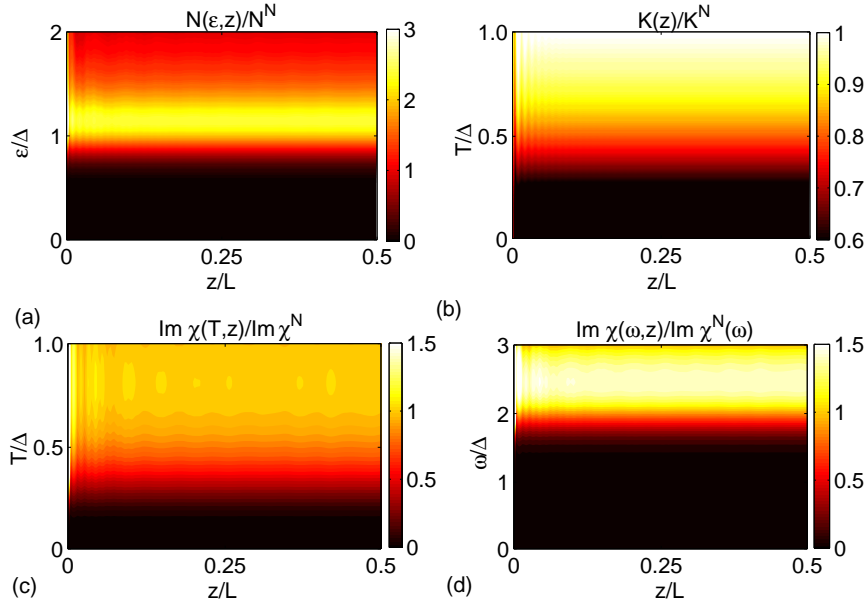


Figure 5.2.3.: Spin response for a topological insulator film of thickness $L = 240$ nm and Δ_1 pairing: (a) Local density of states, (b) Knight shift, and imaginary part of the transverse spin susceptibility as function of (c) temperature and (d) excitation energy. All plots are normalized to the normal-state bulk at $T = 0$.

The local density of states for Δ_1 pairing is shown in figure 5.2.3(a) with an ordinary s -wave

$$\mathcal{N}_B(\epsilon) = \mathcal{N}_N(\mu) \frac{\epsilon}{\sqrt{\epsilon^2 - \Delta_1^2}} \Theta(\epsilon - \Delta_1) \quad (5.2.9)$$

in the bulk. The derivation of this result is analogous to the one in Eq. (5.2.4) with the

replacement $\Delta E_0/\mu \rightarrow \Delta_1$. Depending on whether the Dirac modes of the topological insulator already crossed the bulk states, we distinguish between $\mu^2 > v^2|m|/B_2$ with bulk contributions only and $\mu^2 < v^2|m|/B_2$, where

$$\mathcal{N}_S(\epsilon, z > 0) \approx \frac{\mu}{\pi \xi_0 v^2} \frac{\epsilon}{\sqrt{\epsilon^2 - \Delta_1^2}} e^{-2z/\xi_0} \Theta(\epsilon - \Delta_1). \quad (5.2.10)$$

In our numerical calculations, we only consider the case $\mu^2 > v^2|m|/B_2$ with Dirac modes.

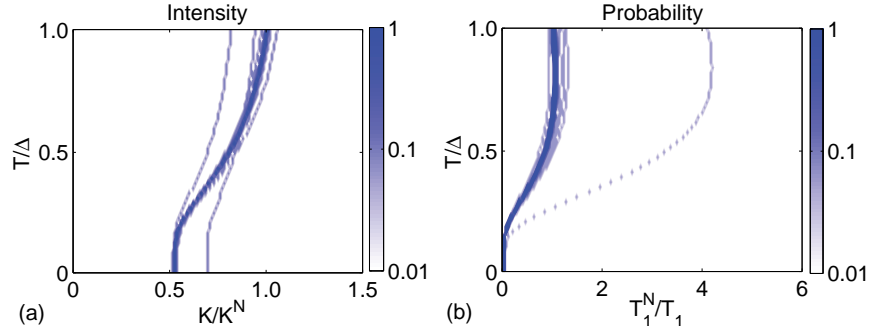


Figure 5.2.4.: Δ_1 pairing: Distribution of the temperature-dependent (a) Knight shift and (b) spin-lattice relaxation for a topological insulator film of thickness $L = 240$. All plots are normalized to the normal-state bulk at $T = 0$. The dark features are determined by the bulk, while the sub-features show the response from the Dirac surface modes.

As shown in figure 5.2.3(b), the Knight shift is significantly reduced in the bulk for $T < \Delta_1$ due to the superconducting gap and has a finite $T = 0$ value determined by the strong spin-orbit coupling. The temperature dependence of the Knight shift distribution is plotted in figure 5.2.4(a) where the dark feature is the signal from the bulk with a characteristic decrease for $T \rightarrow 0$. The line with larger shift originates from the Dirac modes and shows qualitatively the same temperature dependence as the bulk shift as expected from the gapped local density of states.

Similarly to the Knight shift, we find conventional s -wave behavior for $1/(T_1 T)$ in the bulk and at the surface with an activation law for $T \ll \Delta_1$ and the Hebel-Slichter coherence peak for $T \rightarrow \Delta_1$ as shown in figures 5.2.3(c) and 5.2.4(b). Again, the surface shows qualitatively the same behavior as the bulk but with a much larger rate due to the large surface local density of states. The transition between the characteristic surface and bulk behaviors occurs in a depth ξ_0 .

In figure 5.2.3(d) we plot the imaginary part of the transverse spin susceptibility as function of excitation energy. For $\omega > 2\Delta_1$, there is a featureless continuum of bulk spin excitations, which is sharply bounded from below at $\omega = 2\Delta_1$ because of the quasiparticle gap. Again we find a larger spin susceptibility at the surface as compared to the bulk as

a consequence of the large local density of states from the Dirac modes.

Odd-parity intraorbital pairing Δ_2

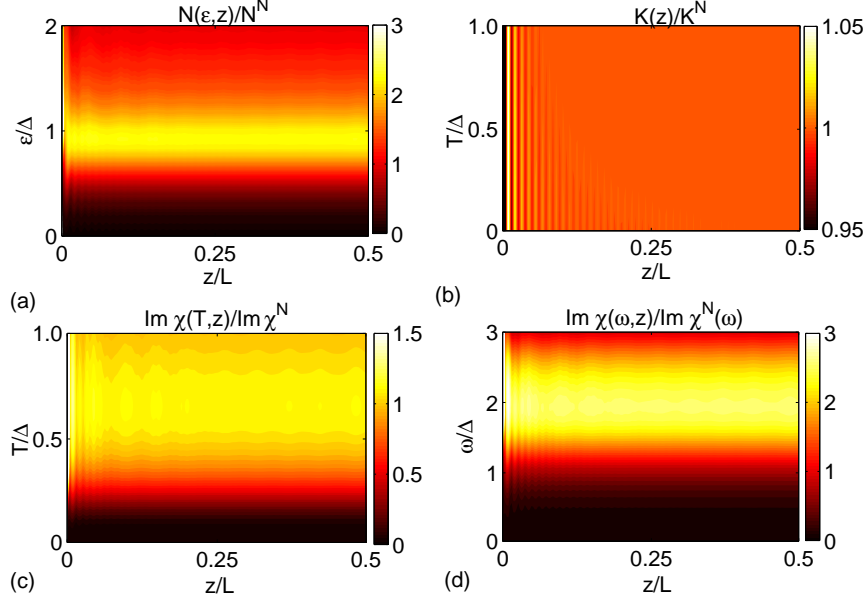


Figure 5.2.5.: Spin response for a topological insulator film of thickness $L = 240$ nm and Δ_2 pairing: (a) Local density of states, (b) Knight shift, and imaginary part of the transverse spin susceptibility as function of (c) temperature and (d) excitation energy. All plots are normalized to the normal-state bulk at $T = 0$.

In figure 5.2.5(a) we plot the local density of states for Δ_2 pairing, which is finite for all $\epsilon > 0$ due to the linear dispersion and shows a cusp at $\epsilon = \Delta_2$. In the bulk, we find for the local density of states the conventional result for superconductors with point nodes,

$$\begin{aligned}
 \mathcal{N}_B(\epsilon) &= \mathcal{N}_N(\mu) \int \frac{d\Omega}{4\pi} \int d\xi \delta\left(\epsilon - \sqrt{\xi^2 + \Delta_2^2 \sin^2(\theta)}\right) \\
 &= \mathcal{N}_N(\mu) \frac{1}{2} \int_{-1}^1 dx \frac{\epsilon}{\sqrt{\epsilon^2 + \Delta_2^2(1-x^2)}} \\
 &= \mathcal{N}_N(\mu) \frac{\epsilon}{2\Delta_2} \log \left| \frac{\epsilon + \Delta_2}{\epsilon - \Delta_2} \right|.
 \end{aligned} \tag{5.2.11}$$

As before, we distinguish between $\mu^2 > v^2|m|/B_2$ with bulk contributions only and $\mu^2 < v^2|m|/B_2$ with

$$\mathcal{N}_S(\epsilon, z > 0) \approx \frac{\mu}{\pi \xi_0 v^2} \frac{\epsilon}{\sqrt{\epsilon^2 - \Delta_2^2}} e^{-2z/\xi_0}. \tag{5.2.12}$$

The different energy dependence of the bulk and the surface dispersion yields strong evi-

dence for different characteristic temperature behavior in the bulk and at the surface.

As shown in figures 5.2.5(b) and 5.2.6(a), the Knight shift is essentially independent of temperature even for $T < \Delta_2$. Here, the weak subfeatures at smaller shift originate from the Dirac modes and show an s -wave behavior with reduced Knight shift below T_c in contrast to the constant bulk value.

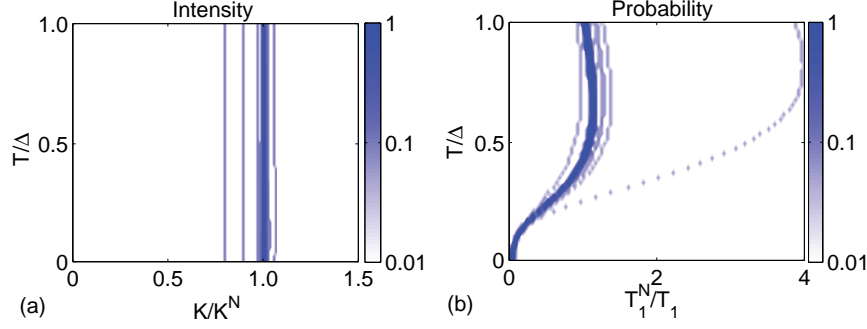


Figure 5.2.6.: Δ_2 pairing: Distribution of the temperature-dependent (a) Knight shift and (b) spin-lattice relaxation for a topological insulator film of thickness $L = 240$ nm. All plots are normalized to the normal-state bulk at $T = 0$. The dark feature is determined by the bulk, while the subfeatures show the response from the Dirac surface modes.

In figure 5.2.5(c) we plot the spin-lattice relaxation, which is much larger at the surface than in the bulk. The temperature dependence of the rate is shown in figure 5.2.6(b) where we can clearly distinguish between bulk and surface contributions. In stark contrast to the constant Knight shift, we find for $T \rightarrow 0$ a power law T^5 in the bulk, which is characteristic for point nodes and an activation law $\exp(-\Delta_2/T)$ from the surface contribution. For $T \rightarrow \Delta_2$ we obtain a Hebel-Slichter peak at the surface whereas the bulk yields just a small coherence peak due to the broadened local density of states Eq. (5.2.11).

The imaginary part of the dynamical transverse spin susceptibility is shown in figure 5.2.5(d) as function of the excitation energy. For all ϵ there is a continuum of single-particle spin excitations with an amplitude that behaves as function of energy like $\mathcal{N}_B^2(\omega/2, z)$ in the bulk and like $[\mathcal{N}_B(\omega/2, z) + \mathcal{N}_S(\omega/2, z)]^2$ at the surface. For $\omega \approx 2\Delta_2$, there is a peak in the spin spectrum resulting from the cusp in the local density of states.

Even-parity interorbital pairing Δ_3

As shown in figure 5.2.7(a), the local density of states in the bulk is

$$\mathcal{N}_B(\epsilon) = \frac{2\mu E_0(k_F)\epsilon}{\pi v^2 v_z \sqrt{\epsilon^2 - \frac{\Delta_3^2 m_0^2(k_F)}{\mu^2}}} \Theta\left(\epsilon - \frac{\Delta_3 |m_0(k_F)|}{\mu}\right) \quad (5.2.13)$$

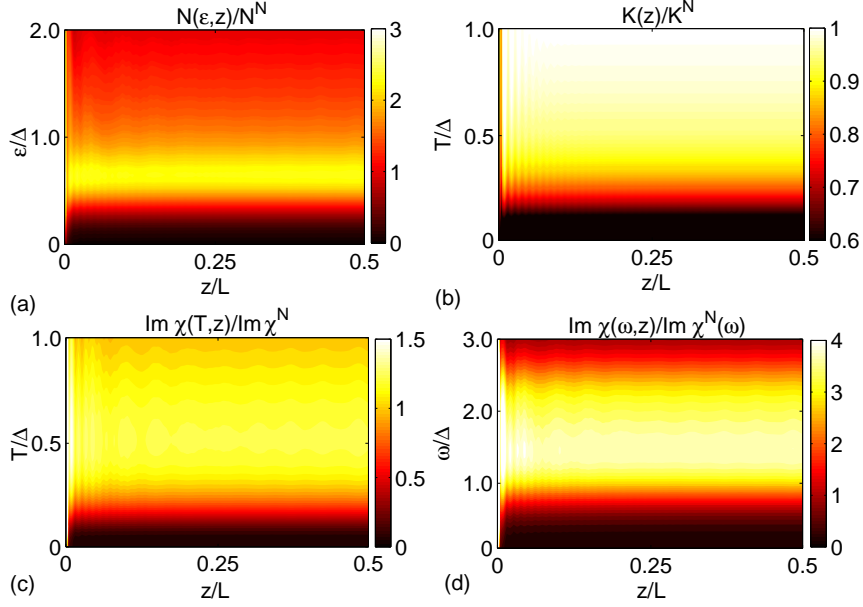


Figure 5.2.7.: Spin response for a topological insulator film of thickness $L = 240$ nm and Δ_3 pairing: (a) Local density of states, (b) Knight shift, and imaginary part of the transverse spin susceptibility as function of (c) temperature and (d) excitation energy. All plots are normalized to the normal-state bulk at $T = 0$.

with a quasiparticle gap $2\Delta_3|m_0(k_F)|/\mu$. The derivation of this expression is analogous to the one in Eq. (5.2.4) with the replacement $\Delta E_0 \rightarrow \Delta_3|m_0|$. From this expression, we see that the gap closes when $m_0(k)$ vanishes and decreases with increasing μ . As before, we distinguish between $\mu^2 > v^2|m|/B_2$ where only the bulk contributes and $\mu^2 < v^2|m|/B_2$ with a gapless surface local density of states

$$\mathcal{N}_S(\epsilon, z > 0) \approx \frac{\mu e^{-2z/\xi_0}}{\pi \xi_0 v^2}. \quad (5.2.14)$$

In figure 5.2.7(b) we plot the Knight shift $K(z)$ with qualitatively very different behavior in the bulk and at the surface. In the bulk we find a reduced shift for $T < \Delta_3$ with a finite $K(T \rightarrow 0)$ due to the strong spin-orbit coupling. In contrast, at the surface we find a larger shift for $T \ll \Delta_3$ because of the strongly spin-orbit coupled massless surface states. The temperature dependence of the Knight shift is shown in figure 5.2.8(a) where the strong feature is determined by the bulk and the second line by the Dirac modes.

In figure 5.2.7(c) we find similarly to the Knight shift a qualitatively different behavior for the spin-lattice relaxation in the bulk and at the surface. The gapped bulk gives rise to an activation law for $T \ll \Delta_3$ and a Hebel-Slichter coherence peak for $T \rightarrow \Delta_3$. In contrast, we find a finite $T = 0$ -value for $1/(T_1 T)$ at the surface which is characteristic for

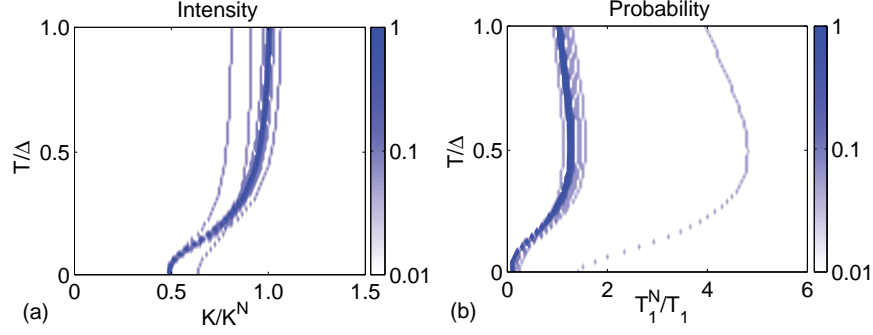


Figure 5.2.8.: Δ_3 pairing: Distribution of the temperature-dependent (a) Knight shift and (b) spin-lattice relaxation for a topological insulator film of thickness $L = 240$ nm. All plots are normalized to the normal-state bulk at $T = 0$. The dark features are determined by the bulk, while the subfeatures show the response from the Dirac surface modes.

metallic states. The temperature dependence is also plotted in figure 5.2.8(b), where the rate from the Dirac modes is much larger than the rate from the bulk because of the large gapless local density of states.

In figure 5.2.7(d), the imaginary part of the dynamical transverse spin susceptibility is displayed as function of excitation energy. The spin excitation spectrum in the bulk is very different from that at the surface. For $\omega > 2\Delta_3|m_0(k_F)|/\mu$, there is a continuum of excitations in the bulk which is sharply bounded at $\omega = 2\Delta_3|m_0(k_F)|/\mu$. In addition, we find low-energy spin excitations at the surface and bulk-surface excitations for $\omega > \Delta_3|m_0(k_F)|/\mu$ within a length ξ_0 into the sample.

5.3. Experimental detection scheme

Finally, we discuss experimental measurement schemes of the spin susceptibility. In references [152, 153] it has been shown that ^{77}Se and ^{209}Bi NMR are suitable methods to investigate the bulk of Bi_2Se_3 where the dipole hyperfine coupling dominates due to the p -orbital character of the Fermi surface. Similarly, ^{125}Te NMR has been successfully applied to study the metallic surface states of bismuth telluride nanoparticles [154]. We conclude that for low temperatures, NMR can also study the superconducting phase to determine the pairing symmetry. As shown in figures 5.3.1(a) and (b), we find significant differences in the bulk spin response for the competing pairing symmetries.

For the Knight shift, figure 5.3.1(a), we find three different behaviors below T_c . All pairing terms yield a finite value for the zero-temperature spin susceptibility because of the strong spin-orbit coupling. However, for Δ , Δ_1 , and Δ_3 we find a decrease of the Knight shift below T_c with a similar functional behavior for Δ_1 and Δ , which differ by

$K_N/4$ for $T = 0$. For Δ_3 we observe a qualitatively similar temperature dependence but the functional form is very different as for Δ and Δ_1 because of the strongly momentum dependent quasiparticle gap. In stark contrast to these reduced Knight shifts, we find no change of the Knight shift for Δ_2 below T_c . This also shows that a constant Knight shift for $T < T_c$ is not a clear signature for triplet pairing symmetry and can also appear for singlet pairing symmetries.

In the spin-lattice relaxation, figure 5.3.1(b), the differences between the pairing symmetries are not as strong as for the Knight shift. For Δ and Δ_1 , we find conventional s -wave type behavior with an activation law for $T \rightarrow 0$ and a sharp Hebel-Slichter coherence peak for $T \rightarrow T_c$. However, we can again clearly distinguish Δ_2 and Δ_3 from Δ and Δ_1 by their functional dependence. As shown above, we find a power-law T^5 behavior for Δ_2 due to the point nodes and for Δ_3 , the curve is compressed towards $T = 0$ due to the momentum-dependent gap and shows no sharp coherence peak.

Hence, bulk NMR can clearly distinguish Δ_2 and Δ_3 from Δ , while Δ and Δ_1 are qualitatively similar. Here, the main difference is that the response for Δ_1 is isotropic, whereas the Δ case yields an anisotropic Knight shift [159]. As shown in figure 5.2.2, a more direct way to distinguish Δ and Δ_1 are the surface Andreev bound states for Δ , which can be observed in powder samples and thin films as additional signals. The integrated intensity of the surface signal is reduced by a factor of ξ_1/L compared to the bulk signal where L is the thickness of the flakes. However, the surface signal shows a characteristic temperature behavior with decreasing spin susceptibility for $T \rightarrow \Delta$.

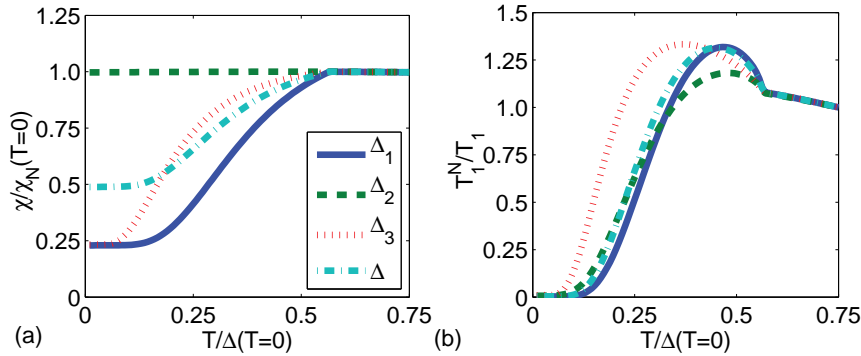


Figure 5.3.1.: Temperature dependence of (a) the Knight shift and (b) the spin-lattice relaxation rate in the bulk for the different pairing symmetries with $\Delta_i = 1$ meV. The lines are defined in (a).

As shown in figure 5.2.1(c), the surface Andreev bound states yield a spatially dependent relaxation rate up to $v_z/\Delta \sim 200$ nm into the sample, which is a characteristic signature for the topologically nontrivial nature of the superconducting state. To investigate this local magnetism, depth-resolved techniques such as muon spin resonance [88] and β -NMR [89,

155] are suitable. In particular, they could differentiate the regimes with one, two, or three zero-energy surface Andreev bound states, which occur depending on the relative strength of the linear and quadratic terms in the Hamiltonian as discussed above. For Bi_2Se_3 , it has been shown that the implanted muons most probably stop in the van der Waals gap between quintuple layers [156]. Despite our concentration on NMR and muon spin resonance, our results are more general and can also be applied to electron spin resonance and surface sensitive spin-flip Raman scattering [157, 158].

Doped topological insulators usually have superconducting shielding fractions of 50% while the rest is normal-state [79]. Here, bulk NMR could detect the mechanisms, which determine this fraction. Depending on μ in the normal part of the sample, there might be additional signals, which can be clearly distinguished from the superconducting ones by the very different temperature behavior. This key information about the distribution of dopants is an important step towards the understanding of unconventional superconductivity in topological insulators. In our analysis, we did not take vortices into account, which can be distinguished from the surface Andreev bound state by their temperature behavior and the different length scales.

5.4. Summary

In this chapter we have studied doped three-dimensional topological insulators with several types of unequal-spin superconducting pairing symmetries. We have investigated the existence of surface states and have shown that the odd-parity interorbital pairing is particularly interesting because of the existence of gapless surface Majorana modes and additional unconventional surface Andreev states. We have shown that these surface states have two characteristic length scales originating from the band inversion and the odd-parity pairing, and typically differ by two orders of magnitude. The quadratic momentum terms significantly determine the character of the different species of surface Andreev states. Depending on the material parameters, we find three regimes, which can be distinguished by the number of zero-energy modes. For small chemical potentials, both the Majorana zero-energy mode and the unconventional surface Andreev state, which originates from the Dirac mode, exist. On the other hand, for large chemical potentials only the zero-momentum Majorana zero-energy mode exists. In the regime of intermediate chemical potentials, there is a third type of zero-energy state emerging at zero momentum and moving towards the Dirac mode with increasing chemical potential.

We have proposed a nuclear magnetic resonance experiment to determine the pairing symmetry of electron doped three-dimensional topological insulators and to observe the

Majorana zero-energy modes in the odd-parity interorbital unequal-spin pairing channel. The surface Andreev states contribute to a local spin susceptibility, which can be clearly distinguished from the bulk by their characteristic temperature behavior and the large local density of states. Moreover, we have emphasized the usefulness of depth-controlled local probes, which directly show the existence of unconventional surface Andreev bound states. From our numerical analysis, we conclude that nuclear magnetic resonance experiments can distinguish between competing superconducting pairing symmetries and therefore suggest to use nuclear magnetic resonance in order to unambiguously determine the superconducting pairing symmetry in $\text{Cu}_x\text{Bi}_2\text{Se}_3$. Our work is motivated by $\text{Cu}_x\text{Bi}_2\text{Se}_3$, however, our results are more generally relevant for other inversion symmetric materials such as the ternary chalcogenides and the SnTe/PbTe class which also shows unconventional superconducting behavior.

6. Summary and conclusions

In this thesis we have theoretically identified signatures of topological superconductors and proposed realistic experiments to observe these signatures. Topological superconductors are a type of topologically nontrivial states of quantum matter. They are particularly interesting because their low-energy quasiparticle excitations are associated with Majorana fermions. Recently, Majorana fermions have attracted intense research efforts because of their exotic exchange statistics and possible applications in topological quantum computation. In the following, we summarize our main results, their physical interpretation, and possible experimental realizations.

In chapter 3, we have studied charge transport through a topological superconductor with a pair of Majorana end states coupled to normal-conducting lead electrodes. Due to the finite length of the topological superconductor nanowire, the Majorana end states are coupled to each other and have a finite energy splitting which gives rise to a nonzero tunneling matrix element between the ends of the nanowire. The nonlocality of the Majorana end states opens the possibility of crossed Andreev reflection with nonlocal shot noise. Crossed Andreev reflection denotes the nonlocal conversion of an incoming electron into a hole excitation in a separate lead electrode, in contrast to local Andreev reflection where the incoming electron and the hole excitation reside in the same lead electrode. In our analysis, we have concentrated on a device where the lead electrodes are coupled to the Majorana end states via resonant quantum dots in order to suppress local Andreev reflection and thus to provide a suitable tool to probe current cross-correlations. In the space of energies of the two resonant quantum dot levels, we have found a four-peaked cloverlike pattern for the strength of current cross-correlations due to crossed Andreev reflection, distinct from the single ellipsoidal peak found in the absence of split Majorana end states. If the energy of at least one of the quantum dots is aligned with the chemical potential of the superconductor, we have found that the current cross-correlations are significantly suppressed. This suppression originates from the formation of a zero-energy Majorana state on the quantum dot which is tuned to the chemical potential of the superconductor. Since crossed Andreev reflection relies on the existence of a nonzero tunneling matrix element between the ends of the nanowire, the zero-energy Majorana state contributes only weakly

to current cross-correlations and thus gives rise to the cloverlike pattern.

We have shown numerically that the cloverlike pattern can be observed for realistic material parameters in semiconductor-superconductor hybrid systems and can be clearly distinguished from the situation without split Majorana end states. This pattern is robust against nonmagnetic disorder, a finite number of transverse subbands, and finite temperatures smaller or equal the Majorana energy splitting. In particular, we have shown that by varying an external magnetic field the current cross-correlation pattern oscillates between the cloverlike pattern indicating split Majorana end states and a single ellipsoidal pattern originating from the superconducting proximity effect. This oscillation originates from a sinusoidal modulation of the Majorana energy splitting as function of magnetic field. We propose that the oscillation between these two current cross-correlation patterns is a clear and robust signature of Majorana fermions in semiconductor-superconductor hybrid systems.

In chapter 4, we have studied signatures of topological order in nonlinear charge transport through semiconductor-superconductor hybrid nanorings. Here, we associate topological order with the existence of ground-state degeneracies which depend on the manifold on which the system is defined. This hybrid system shows two topologically distinct phases and an external magnetic field allows to tune between them. Because of the ring topology, the nanowire has no ends and as a consequence, there are no Majorana end states in the topologically nontrivial phase. However, despite the absence of Majorana end states, this system shows an unconventional superconducting state. While trivial superconductors always have an even electron number parity due to the formation of Cooper pairs, we here have found that the parity of the ground-state wave function in the nontrivial phase depends on the magnetic flux which penetrates the nanoring. Due to the external magnetic field, the nontrivial phase is characterized by a single electronic band, and as a consequence, there is one unpaired electron at zero momentum for integer magnetic flux which is absent for half-integer magnetic flux in units of the flux quantum h/e . This unpaired electron gives rise to an unconventional superconducting ground state with odd parity.

To observe this unconventional parity effect, we have proposed a nonlinear Coulomb blockade transport experiment where the Coulomb energy fixes the parity of the electron wave functions. We have shown that peculiar parity and magnetic flux periodicity effects in the excitation spectrum mirror the distinct ground-state properties of topologically trivial and nontrivial superconducting phases. In particular, the excitation spectrum for fixed mean electron number provides clear signatures of the h/e flux period in the nontrivial phase which is doubled as compared to trivial superconductors. This h/e periodicity is intricately related to the recently discovered 4π periodicity of the Josephson current

between two topological superconductors. In addition, we have found that the closing and reopening of a quasiparticle excitation gap as function of magnetic field reflects the topological phase transition. All these findings are robust against geometry details of the realization of the ring structure and rely on the existence of a void such that the system is homotopic equivalent to a circle. Moreover, we have shown numerically that our results are robust against moderate nonmagnetic disorder, additional transverse subbands, and weak fluctuations in the superconducting order parameter. We conclude that nonlinear Coulomb blockade transport directly reflects the topological order of the semiconductor-superconductor nanoring and is therefore a suitable tool to map out the topological phase diagram.

In chapter 5, we have studied special examples of three-dimensional topological superconductors. We have considered an electron doped three-dimensional topological insulator equipped with several types of unequal-spin superconducting pairing symmetries. Topological insulators are materials with a bulk band gap like an ordinary insulator but with metallic surface states. We have investigated the low-energy properties of the superconducting pairing and have shown that the odd-parity interorbital pairing is particularly interesting. For this pairing, we have found two different types of unconventional surface states originating from the band inversion of the topological insulator and the odd-parity pairing, and the characteristic length scales of these two surface states typically differ by two orders of magnitude.

We have proposed a nuclear magnetic resonance experiment to determine the superconducting pairing symmetry of electron doped three-dimensional topological insulators and to observe the Majorana zero-energy modes in the odd-parity interorbital unequal-spin pairing channel. The surface Andreev states contribute to a local spin susceptibility, which can be clearly distinguished from the bulk by their characteristic temperature behavior and the large local density of states. Moreover, we emphasize the usefulness of depth-controlled local probes, which directly show the existence of unconventional surface Andreev bound states. From our numerical analysis, we conclude that nuclear magnetic resonance experiments can distinguish between competing superconducting pairing symmetries and therefore suggest to use nuclear magnetic resonance in order to unambiguously determine the superconducting pairing symmetry in $\text{Cu}_x\text{Bi}_2\text{Se}_3$, however, our results are more generally relevant for other materials such as the ternary chalcogenides and the SnTe/PbTe class.

A. Lattice model for the semiconductor-superconductor hybrid system

A.1. Lattice model for the semiconductor-superconductor hybrid system

In chapters 3 and 4, we have investigated a (quasi) one-dimensional semiconductor-superconductor hybrid system using a low-energy continuum model. There, we have complemented our analytical findings with numerical calculations for a tight-binding lattice model. In this appendix we derive the Bogoliubov-de Gennes Hamilton matrix which needs to be diagonalized numerically. We consider the lattice Hamiltonian

$$H = H_{\text{SM}} + H_{\text{SC}} \quad (\text{A.1.1})$$

with the normal-state tight-binding Hamiltonian

$$H_{\text{SM}} = - \sum_{\mathbf{r}, \mathbf{r}', \sigma} t_{\mathbf{r}\mathbf{r}'} c_{\mathbf{r}\sigma}^\dagger c_{\mathbf{r}'\sigma} + \sum_{\mathbf{r}, \sigma} \left(E_Z \hat{\sigma}_{\sigma\sigma}^z - \mu + V_{\mathbf{r}} \right) c_{\mathbf{r}\sigma}^\dagger c_{\mathbf{r}\sigma} + \frac{i\hbar\alpha}{2a} \sum_{\mathbf{r}, \sigma} \left(c_{\mathbf{r}\sigma}^\dagger \hat{\sigma}_{\sigma\bar{\sigma}}^y c_{\mathbf{r}+\delta_x\bar{\sigma}} - c_{\mathbf{r}\sigma}^\dagger \hat{\sigma}_{\sigma\bar{\sigma}}^y c_{\mathbf{r}-\delta_x\bar{\sigma}} - c_{\mathbf{r}\sigma}^\dagger \hat{\sigma}_{\sigma\bar{\sigma}}^x c_{\mathbf{r}+\delta_y\bar{\sigma}} + c_{\mathbf{r}\sigma}^\dagger \hat{\sigma}_{\sigma\bar{\sigma}}^x c_{\mathbf{r}-\delta_y\bar{\sigma}} \right) \quad (\text{A.1.2})$$

and the on-site superconducting pairing Hamiltonian

$$H_{\text{SC}} = \Delta_{\text{SC}} \sum_{\mathbf{r}} \left(c_{\mathbf{r}\uparrow}^\dagger c_{\mathbf{r}\downarrow}^\dagger + c_{\mathbf{r}\downarrow} c_{\mathbf{r}\uparrow} \right). \quad (\text{A.1.3})$$

Here, the operator $c_{\mathbf{r}\sigma}$ ($c_{\mathbf{r}\sigma}^\dagger$) annihilates (creates) an electron with spin σ at site \mathbf{r} . The only nonzero hopping matrix elements are $t_{\mathbf{r}, \mathbf{r} \pm \delta_x} = t_{\mathbf{r}, \mathbf{r} \pm \delta_y} = t_0$ and $t_{\mathbf{r}, \mathbf{r}} = -2t_0$.

In this appendix we derive the Bogoliubov-de Gennes Hamilton matrix for Eq. (A.1.1).

For clarity and compactness, we only consider a one-dimensional chain of N sites, we replace all vector indices by scalars, and neglect the hopping matrix elements in y direction. The generalization to two-dimensional or three-dimensional systems is analogous. We follow the procedure introduced in chapter 2.1 and combine the electron creation and annihilation operators into a single $4N$ -component vector

$$\Psi^\dagger = \left(c_{1\uparrow}^\dagger \ c_{1\downarrow}^\dagger \ \dots \ c_{N\uparrow}^\dagger \ c_{N\downarrow}^\dagger \ c_{1\uparrow} \ c_{1\downarrow} \ \dots \ c_{N\uparrow} \ c_{N\downarrow} \right). \quad (\text{A.1.4})$$

Then, in the next step we rewrite the individual terms of H using this new vector of electron operators. In this compact notation, we find the Hamiltonian

$$\begin{aligned} H &= \frac{1}{2} \Psi^\dagger \mathcal{H}_{\text{BdG}} \Psi + \frac{1}{2} \sum_{\sigma} \sum_x \left(E_Z \sigma_{\sigma\sigma}^z - \tilde{\mu} + V_x \right) \\ &= \frac{1}{2} \Psi^\dagger \mathcal{H}_{\text{BdG}} \Psi + \sum_x \left(-\tilde{\mu} + V_x \right) \end{aligned} \quad (\text{A.1.5})$$

with $\tilde{\mu} = \mu - 2t_0$ and with the Hermitian $4N \times 4N$ Bogoliubov-de Gennes matrix

$$\mathcal{H}_{\text{BdG}} = \begin{pmatrix} T & \hat{\Delta} \\ -\hat{\Delta}^* & -T^* \end{pmatrix}. \quad (\text{A.1.6})$$

Here, T is the Hermitian $2N \times 2N$ matrix, which describes the normal-state Hamiltonian H_{SM} , and $\hat{\Delta}$ is the skew-symmetric $2N \times 2N$ matrix, which describes the superconducting pairing H_{SC} . For the normal-state matrix T , we find

$$T = \left(\begin{array}{cc|cc|cc|cc} -\tilde{\mu} + E_Z & 0 & -t_0 & \frac{\hbar\alpha}{2a} & 0 & 0 & & \\ 0 & -\tilde{\mu} - E_Z & -\frac{\hbar\alpha}{2a} & -t_0 & 0 & 0 & & \\ \hline -t_0 & -\frac{\hbar\alpha}{2a} & -\tilde{\mu} + E_Z & 0 & -t_0 & \frac{\hbar\alpha}{2a} & 0 & 0 \\ \frac{\hbar\alpha}{2a} & -t_0 & 0 & -\tilde{\mu} - E_Z & -\frac{\hbar\alpha}{2a} & -t_0 & 0 & 0 \\ \hline 0 & 0 & -t_0 & -\frac{\hbar\alpha}{2a} & -\tilde{\mu} + E_Z & 0 & -t_0 & \frac{\hbar\alpha}{2a} \\ 0 & 0 & \frac{\hbar\alpha}{2a} & -t_0 & 0 & -\tilde{\mu} - E_Z & -\frac{\hbar\alpha}{2a} & -t_0 \\ \hline & & 0 & 0 & -t_0 & -\frac{\hbar\alpha}{2a} & \dots & \\ & & 0 & 0 & \frac{\hbar\alpha}{2a} & -t_0 & & \dots \end{array} \right), \quad (\text{A.1.7})$$

and for the superconducting pairing matrix $\hat{\Delta}$, we find

$$\hat{\Delta} = \left(\begin{array}{cc|cc|cc|c} 0 & \Delta_{\text{SC}} & 0 & 0 & 0 & 0 & \\ -\Delta_{\text{SC}} & 0 & 0 & 0 & 0 & 0 & \\ \hline 0 & 0 & 0 & \Delta_{\text{SC}} & 0 & 0 & \\ 0 & 0 & -\Delta_{\text{SC}} & 0 & 0 & 0 & \\ \hline 0 & 0 & 0 & 0 & 0 & \Delta_{\text{SC}} & \\ 0 & 0 & 0 & 0 & -\Delta_{\text{SC}} & 0 & \\ \hline & & & & & & \dots \\ & & & & & & \dots \end{array} \right). \quad (\text{A.1.8})$$

In chapters 3 and 4, we have obtained the quasiparticle energy spectrum by numerically solving the $4N \times 4N$ eigenvalue equation

$$\mathcal{H}_{\text{BdG}} \begin{pmatrix} U & V \\ V^* & U^* \end{pmatrix} = \begin{pmatrix} U & V \\ V^* & U^* \end{pmatrix} \begin{pmatrix} D & 0 \\ 0 & -D \end{pmatrix} \quad (\text{A.1.9})$$

with the nonnegative quasiparticle energies $D = \text{diag}(E_1, \dots, E_{2N})$ and

$$\Psi = \begin{pmatrix} U & V \\ V^* & U^* \end{pmatrix} \begin{pmatrix} A \\ A^{\dagger T} \end{pmatrix}, \quad (\text{A.1.10})$$

where $A^T = (a_1, \dots, a_{2N})$ is the vector of operators a_i which annihilate a quasiparticle with energy E_i .

A.2. Lattice model for the quantum dot–topological superconductor nanowire–quantum dot system

In chapter 3, we have studied transport signatures of a three-terminal quantum dot–topological superconductor nanowire–quantum dot system. In our numerical analysis, we have considered a semiconductor-superconductor nanowire which was recently studied experimentally in references [55–58]. We assume that the quantum dot is fully spin polarized by an external magnetic field and that the \uparrow spin determines the low-energy physics. The Hamiltonian for that system is given by

$$H_{\text{DND}} = H_{\text{SM}} + H_{\text{SC}} + \sum_{i=L,R} \epsilon_i d_i^\dagger d_i + t_L (d_L^\dagger c_{1\uparrow} + c_{1\uparrow}^\dagger d_L) + t_R (d_R^\dagger c_{N\uparrow} + c_{N\uparrow}^\dagger d_R) \quad (\text{A.2.1})$$

with H_{SM} and H_{SC} defined in the last section. The derivation of the corresponding $(4N + 4) \times (4N + 4)$ Bogoliubov-de Gennes Hamilton matrix is analogous to the derivation in the last section. Henceforth, we here only present the results. We find the $(4N + 4)$ -component vector of electron operators,

$$\Psi^\dagger = \left(d_L^\dagger \quad c_{1\uparrow}^\dagger \quad \dots \quad c_{N\downarrow}^\dagger \quad d_R^\dagger \quad d_L \quad c_{1\uparrow} \quad \dots \quad c_{N\downarrow} \quad d_R \right). \quad (\text{A.2.2})$$

and the Bogoliubov-de Gennes Hamilton matrix

$$\mathcal{H}_{\text{BdG}} = \begin{pmatrix} T_{DND} & \hat{\Delta}_{DND} \\ -\hat{\Delta}_{DND}^* & -T_{DND}^* \end{pmatrix} \quad (\text{A.2.3})$$

with the $(2N + 2) \times (2N + 2)$ matrices T_{DND} and $\hat{\Delta}_{DND}$. We find the normal-state matrix

$$T_{DND} = \left(\begin{array}{c|cccc|c} \epsilon_L & t_L & 0 & 0 & \dots & \\ \hline t_L & & & & & \\ 0 & & & & & \\ \dots & & & T & & \dots \\ \hline & & & & & t_R \\ & & & & & 0 \\ \hline & & & \dots & t_R & 0 & \epsilon_R \end{array} \right) \quad (\text{A.2.4})$$

and the superconducting pairing matrix

$$\hat{\Delta}_{DND} = \left(\begin{array}{c|ccc|c} & & \dots & 0 & 0 \\ \hline & & & & 0 \\ \dots & & \hat{\Delta} & & \dots \\ 0 & & & & \\ \hline 0 & 0 & \dots & & \end{array} \right) \quad (\text{A.2.5})$$

with the matrices T and $\hat{\Delta}$ which were defined in Eqs. (A.1.7) and (A.1.8). We obtain the energy spectrum by diagonalizing \mathcal{H}_{BdG} as discussed above in appendix A.1.

B. Majorana bound states coupled to quantum dots

B.1. Bogoliubov-de Gennes Hamiltonian for the coupled quantum dot–Majorana bound state system

In chapter 3.1 we have considered a pair of quantum dots coupled to a pair of Majorana bound states with the Hamiltonians

$$H_M = \frac{\epsilon_M}{2} i\gamma_L \gamma_R, \quad (\text{B.1.1a})$$

$$H_D = \sum_{i=L,R} \left\{ \epsilon_i d_i^\dagger d_i + t_i^* d_i^\dagger \gamma_i + t_i \gamma_i d_i \right\}. \quad (\text{B.1.1b})$$

There, we have obtained the energy spectrum for the total Hamiltonian $H = H_M + H_D$ by introducing Bogoliubov quasiparticle operators which contain both Majorana and ordinary fermion operators. As a consequence, the corresponding Bogoliubov-de Gennes Hamilton matrix was written in the unconventional basis $\{\gamma_L, \gamma_R, d_L^\dagger, d_R^\dagger, d_L, d_R\}$, and the Bogoliubov-de Gennes equation obtains the unconventional form Eq. (3.1.3) which could not be written in the usual form of an eigenvalue equation.

In this appendix we bring the Bogoliubov-de Gennes equation in the usual form by combining the Majorana fermions into a single fermion state described by the fermion operators

$$f^\dagger = \frac{1}{2} (\gamma_L + i\gamma_R), \quad f = \frac{1}{2} (\gamma_L - i\gamma_R). \quad (\text{B.1.2})$$

Rewriting the Hamiltonian in terms of the f operators and including the fermion operators into a single 6-component vector

$$\Psi^\dagger = \begin{pmatrix} f^\dagger & d_L^\dagger & d_R^\dagger & f & d_L & d_R \end{pmatrix}, \quad (\text{B.1.3})$$

we find up to a constant term

$$H = \frac{1}{2} \Psi^\dagger h_{\text{BdG}} \Psi \quad (\text{B.1.4})$$

with the 6×6 Bogoliubov-de Gennes Hamilton matrix

$$h_{\text{BdG}} = \left(\begin{array}{ccc|ccc} \epsilon_M & t_L & -it_R & 0 & -t_L^* & it_R^* \\ t_L^* & \epsilon_L & 0 & t_L^* & 0 & 0 \\ it_R^* & 0 & \epsilon_R & -it_R^* & 0 & 0 \\ \hline 0 & t_L & it_R & -\epsilon_M & -t_L^* & -it_R^* \\ -t_L & 0 & 0 & -t_L & -\epsilon_L & 0 \\ -it_R & 0 & 0 & it_R & 0 & -\epsilon_R \end{array} \right). \quad (\text{B.1.5})$$

With this Hamilton matrix and with Eq. (2.1.10), we find the Bogoliubov-de Gennes equation in the usual form,

$$h_{\text{BdG}} \psi = \epsilon \psi. \quad (\text{B.1.6})$$

We note that the energy spectrum obtained by diagonalizing h_{BdG} is identical to the result obtained in chapter 3.1 by solving the more complicated matrix equation (3.1.3).

B.2. Majorana energy splitting

In this appendix we derive the Majorana energy splitting ϵ_M for a one-dimensional spinless p -wave superconductor nanowire of length L which was introduced Eq. (2.3.5) in chapter 2.3. We write the Hamiltonian in matrix form as

$$H = \frac{1}{2} \int_0^L dx \begin{pmatrix} \psi^\dagger(x) & \psi(x) \end{pmatrix} \begin{pmatrix} -\frac{\hbar^2}{2m} \partial_x^2 - \mu & 2\Delta \partial_x \\ -2\Delta \partial_x & \frac{\hbar^2}{2m} \partial_x^2 + \mu \end{pmatrix} \begin{pmatrix} \psi(x) \\ \psi^\dagger(x) \end{pmatrix}. \quad (\text{B.2.1})$$

This Hamiltonian is characterized by two characteristic length scales $k_F = \sqrt{2m\mu}/\hbar$ and $\xi = \Delta k_F / v_F = \Delta 2m / \hbar^2$. Thus, we rewrite the Hamiltonian as

$$H = \frac{\Delta}{2} \int_0^L dx \begin{pmatrix} \psi^\dagger(x) & \psi(x) \end{pmatrix} \begin{pmatrix} -\xi \partial_x^2 - k_F^2 \xi & 2\partial_x \\ -2\partial_x & \xi \partial_x^2 + k_F^2 \xi \end{pmatrix} \begin{pmatrix} \psi(x) \\ \psi^\dagger(x) \end{pmatrix}. \quad (\text{B.2.2})$$

We obtain the Bogoliubov-de Gennes equations for this Hamiltonian by the Bogoliubov transformation

$$\psi(x) = \sum_l \left(u_l(x) \alpha_l + v_l(x) \alpha_l^\dagger \right) \quad (\text{B.2.3})$$

with $H = \sum_l E_l \alpha_l^\dagger \alpha_l$. The condition $[H, \alpha] = -E\alpha$ yields the Bogoliubov-de Gennes equations

$$\Delta \begin{pmatrix} -\xi \partial_x^2 - k_F^2 \xi & 2\partial_x \\ -2\partial_x & \xi \partial_x^2 + k_F^2 \xi \end{pmatrix} \begin{pmatrix} u(x) \\ v(x) \end{pmatrix} = E \begin{pmatrix} u(x) \\ v(x) \end{pmatrix} \quad (\text{B.2.4})$$

with hard-wall boundary conditions $u(0) = v(0) = u(L) = v(L) = 0$. We assume $L > \xi$ and $k_F \xi \gg 1$. To obtain the Majorana energy splitting ϵ_M , we first solve the ordinary differential equation for a zero-energy Majorana bound state in the limit $L \rightarrow \infty$ and then consider the case of finite L by computing the energy splitting in first order perturbation theory. The Majorana criterion $\alpha = \alpha^\dagger$ yields $E = 0$ and $u = v^*$. In the following, we assume that $u_0 = v_0 \in \mathbb{R}$ for the zero-energy solution in the interval $[0, L/2]$ and $iu_L = -iv_L \in \mathbb{R}$ for the zero-energy solution in the interval $[L/2, L]$.

Solving the second-order ordinary differential equation Eq. (B.2.4) in the vicinity of the two boundaries, we find the wave functions for the zero-energy Majorana bound states

$$u_0(x) = e^{-x/\xi} \frac{\sin\left(\sqrt{k_F^2 - \frac{1}{\xi^2}} x\right)}{\sqrt{\xi - \frac{1}{k_F^2 \xi}}}, \quad (\text{B.2.5a})$$

$$u_L(x) = ie^{-(L-x)/\xi} \frac{\sin\left(\sqrt{k_F^2 - \frac{1}{\xi^2}} (L-x)\right)}{\sqrt{\xi - \frac{1}{k_F^2 \xi}}}. \quad (\text{B.2.5b})$$

Then, the Majorana energy splitting for $L > \xi$ is given by first order-perturbation theory,

$$\begin{aligned} \epsilon_M &\approx i \frac{\Delta}{2} \int_0^L dx \begin{pmatrix} u_0(x) & v_0(x) \end{pmatrix} \begin{pmatrix} -\xi \partial_x^2 - k_F^2 \xi & 2\partial_x \\ -2\partial_x & \xi \partial_x^2 + k_F^2 \xi \end{pmatrix} \begin{pmatrix} u_L(x) \\ v_L(x) \end{pmatrix} \\ &= \frac{i\Delta}{2} \int_0^{L/2} dx \begin{pmatrix} u_0(x) & v_0(x) \end{pmatrix} \begin{pmatrix} -\xi \partial_x^2 - k_F^2 \xi & 2\partial_x \\ -2\partial_x & \xi \partial_x^2 + k_F^2 \xi \end{pmatrix} \begin{pmatrix} u_L(x) \\ v_L(x) \end{pmatrix} \\ &\quad + \frac{i\Delta}{2} \int_{L/2}^L dx \begin{pmatrix} u_0(x) & v_0(x) \end{pmatrix} \underbrace{\begin{pmatrix} -\xi \partial_x^2 - k_F^2 \xi & 2\partial_x \\ -2\partial_x & \xi \partial_x^2 + k_F^2 \xi \end{pmatrix} \begin{pmatrix} u_L(x) \\ v_L(x) \end{pmatrix}}_{=0} \\ &= \frac{i\Delta}{2} \int_0^{L/2} dx u_0(x) \begin{pmatrix} 1 & 1 \end{pmatrix} \begin{pmatrix} 1 \\ 1 \end{pmatrix} [-\xi \partial_x^2 - k_F^2 \xi - 2\partial_x] u_L(x) \\ &= i\Delta \int_0^{L/2} dx u_0(x) [-\xi \partial_x^2 - k_F^2 \xi - 2\partial_x] u_L(x). \end{aligned} \quad (\text{B.2.6})$$

Naively, one might argue that this expression vanishes since u_0 and u_L are both zero-energy solutions. However, the expression is nonzero as there are contributions originating from

the upper boundary of the integrals. With the relations

$$\int_a^b dx u_0(x) \partial_x u_L(x) = u_0(x) u_L(x) \Big|_a^b - \int_a^b dx (\partial_x u_0(x)) u_L(x), \quad (\text{B.2.7a})$$

$$\int_a^b dx u_0(x) \partial_x^2 u_L(x) = (u_0(x) \partial_x u_L(x) - (\partial_x u_0(x)) u_L(x)) \Big|_a^b + \int_a^b dx (\partial_x^2 u_0(x)) u_L(x), \quad (\text{B.2.7b})$$

we rewrite

$$\begin{aligned} \epsilon_M &= i\Delta \int_0^{L/2} dx u_L(x) \underbrace{[-\xi \partial_x^2 - k_F^2 \xi - 2\partial_x] u_0(x)}_{=0} \\ &\quad - i\xi \Delta (u_0(x) \partial_x u_L(x) - (\partial_x u_0(x)) u_L(x)) \Big|_0^{L/2} - 2i\Delta u_0(x) u_L(x) \Big|_0^{L/2} \\ &= -\xi i\Delta (u_0(L/2) \partial_x u_L(L/2) - (\partial_x u_0(L/2)) u_L(L/2)) - 2i\Delta u_0(L/2) u_L(L/2) \\ &= \Delta k_F^2 \xi e^{-L/\xi} \frac{2 \cos(L\sqrt{k_F^2 - 1/\xi^2}) + \sqrt{k_F^2 - 1/\xi^2} \xi \sin(L\sqrt{k_F^2 - 1/\xi^2})}{-1 + k_F^2 \xi^2}. \end{aligned} \quad (\text{B.2.8})$$

In the experimentally relevant limit $k_F \xi \gg 1$, we expand this expression and find the final result

$$\epsilon_M \approx \underbrace{\Delta k_F}_{=E_G} e^{-L/\xi} \sin(k_F L). \quad (\text{B.2.9})$$

B.3. Proximity induced superconducting pairing between two quantum dots

In chapter 3.4.5, we have studied the current cross-correlations mediated by the superconducting proximity effect. Here, we derive the effective pairing Hamiltonian between two quantum dots with opposite spin polarization. We consider the Hamiltonian

$$H_0 = \sum_{k,\sigma} E_k \gamma_{k\sigma}^\dagger \gamma_{k\sigma}, \quad (\text{B.3.1})$$

which describes the superconductor with energy gap Δ , and the tunnel-coupling Hamiltonian

$$H_T = \sum_k \left\{ t_{L,k} d_L^\dagger (u_{k\uparrow} \gamma_{k\uparrow} + v_{k\uparrow} \gamma_{-k\downarrow}^\dagger) + t_{R,k} d_R^\dagger (u_{k\downarrow} \gamma_{k\downarrow} + v_{k\downarrow} \gamma_{-k\uparrow}^\dagger) + \text{H.c.} \right\}, \quad (\text{B.3.2})$$

where $\gamma_{k\sigma}$ denotes the superconductor quasiparticle annihilation operator with excitation energy $E_k = \sqrt{\xi_k^2 + \Delta_{\text{SC}}^2}$, d_i denotes the spin-polarized quantum dot operator, and $t_{i,k}$ the quantum dot-superconductor coupling strength. The $u_{k\sigma}$ and $v_{k\sigma}$ are the BCS coherence factors [137]

$$\begin{pmatrix} u_{k\sigma} \\ v_{k\sigma} \end{pmatrix} = \frac{1}{\sqrt{2}} \begin{pmatrix} \sqrt{1 - \frac{\xi_k}{E_k}} \\ \sigma \sqrt{1 + \frac{\xi_k}{E_k}} \end{pmatrix}. \quad (\text{B.3.3})$$

Without loss of generality, we assume that $t_{L,k} = t_L$ and $t_{R,k} = t_R e^{ikL}$, where L denotes the length of the nanowire.

We derive the effective dot-dot pairing Hamiltonian H_{DD} in second-order perturbation theory similar to the calculations in section 4.5,

$$H_{DD} = \langle | H_T \frac{1}{i\eta - H_0} H_T | \rangle, \quad (\text{B.3.4})$$

where $| \rangle$ denotes the BCS many-body ground-state wave function [137] of the superconductor with $\gamma_{k\sigma} | \rangle = 0$. The convergence generating factor η is assumed to be infinitesimally small. In our analysis, we only consider contributions which are nonlocal in the quantum dot operators and neglect all local terms since they renormalize the bare quantum dot energy levels. This yields the effective Hamiltonian

$$\begin{aligned} H_{DD} &= \sum_k \langle | \left\{ t_{L,k} d_L^\dagger u_{k\uparrow} \gamma_{k\uparrow} + t_{L,-k}^* v_{-k\uparrow} \gamma_{k\downarrow} d_L \right\} \frac{1}{i\eta - H} \left\{ t_{R,-k} d_R^\dagger v_{-k\downarrow} \gamma_{k\uparrow}^\dagger + t_{R,k}^* u_{k\downarrow} \gamma_{k\downarrow}^\dagger d_R \right\} | \rangle \\ &\quad + \sum_k \langle | \left\{ t_{R,k} d_R^\dagger u_{k\downarrow} \gamma_{k\downarrow} + t_{R,-k}^* v_{-k\downarrow} \gamma_{k\uparrow} d_R \right\} \frac{1}{i\eta - H} \left\{ t_{L,-k} d_L^\dagger v_{-k\uparrow} \gamma_{k\downarrow}^\dagger + t_{L,k}^* u_{k\uparrow} \gamma_{k\uparrow}^\dagger d_L \right\} | \rangle \\ &= d_L^\dagger d_R^\dagger \sum_k \left\{ t_{L,k} t_{R,-k} \frac{u_{k\uparrow} v_{-k\downarrow}}{i\eta - \epsilon_R - E_k} - t_{L,-k} t_{R,k} \frac{u_{k\downarrow} v_{-k\uparrow}}{i\eta - \epsilon_L - E_k} \right\} + \text{H.c.} \\ &= d_L^\dagger d_R^\dagger t_L t_R \underbrace{\sum_k \left\{ -e^{-ikL} \frac{u_{k\uparrow} v_{-k\uparrow}}{i\eta - \epsilon_R - E_k} - e^{ikL} \frac{u_{k\uparrow} v_{-k\uparrow}}{i\eta - \epsilon_L - E_k} \right\}}_{\equiv \Delta} + \text{H.c.} \end{aligned} \quad (\text{B.3.5})$$

In the following, we solve the momentum integral for a one-dimensional superconductor. The results for higher dimensional systems can be obtained analogously. We assume that the quantum dot energy levels are close to the resonance $|\epsilon_i| \ll \Delta_{\text{SC}} \leq E_k$. With the BCS coherence factors $u_{k\uparrow} v_{-k\uparrow} = \Delta_{\text{SC}}/2E_k$, we rewrite

$$\Delta_{1D} = t_L t_R \sum_k 2 \cos(kL) \frac{\Delta_{\text{SC}}}{2E_k^2} = t_L t_R N_0 \text{Re} \int_{\mathbb{R}} d\xi e^{i(k_F + \xi/v_F)L} \frac{\Delta_{\text{SC}}}{\xi^2 + \Delta_{\text{SC}}^2}, \quad (\text{B.3.6})$$

where we have linearized the energy dispersion of the normal-state system in the vicinity

of the Fermi energy with constant density of states \mathcal{N}_0 and Fermi velocity v_F .

The energy integral can be solved using the residue theorem. For that purpose, we first close the integration path in the upper half of the complex plane to the closed contour \mathcal{C} . Then, in the next step we look for the singularities and apply the residue theorem. This yields

$$\begin{aligned}
 \Delta_{1D} &= t_L t_R \mathcal{N}_0 \operatorname{Re} e^{ik_F L} \int_{\mathbb{R}} d\xi e^{iL\xi/v_F} \frac{\Delta_{\text{SC}}}{(\xi + i\Delta_{\text{SC}})(\xi - i\Delta_{\text{SC}})} \\
 &= t_L t_R e^{-L\Delta_{\text{SC}}/v_F} \mathcal{N}_0 \operatorname{Re} e^{ik_F L} \int_{\mathbb{R}} d\xi e^{iL(\xi - i\Delta_{\text{SC}})/v_F} \frac{\Delta_{\text{SC}}}{(\xi + i\Delta_{\text{SC}})(\xi - i\Delta_{\text{SC}})} \\
 &= t_L t_R e^{-L\Delta_{\text{SC}}/v_F} \mathcal{N}_0 \operatorname{Re} e^{ik_F L} 2\pi i \frac{\Delta_{\text{SC}}}{2i\Delta_{\text{SC}}} \\
 &= \pi t_L t_R e^{-L\Delta_{\text{SC}}/v_F} \mathcal{N}_0 \cos(k_F L).
 \end{aligned} \tag{B.3.7}$$

Similarly, we obtain the result for a three-dimensional superconductor. There, we replace $\cos(kL) \rightarrow \cos(kL \cos(\theta))$ with the angle θ in Eq. (B.3.6). As a consequence, we find a similar result as the one in Eq. (B.3.7) but with $\cos(k_F L) \rightarrow \int_{-1}^1 d(\cos(\theta)) \cos(k_F L \cos(\theta))/2$. Solving this integral, we find

$$\Delta_{3D} = \frac{\pi}{2} t_L t_R e^{-L\Delta_{\text{SC}}/v_F} \mathcal{N}_0 \frac{\sin(k_F L)}{k_F L}. \tag{B.3.8}$$

B.4. Zero-voltage conductance for the quantum dot–Majorana bound state–quantum dot device

In this appendix we present the details of the scattering matrix formalism applied to the quantum dot–Majorana bound state–quantum dot device for $\epsilon = eV = 0$. In this limit, we find the scattering matrix using Eq. (3.1.11),

$$S(\epsilon = 0) = \frac{1}{X^2 + |Y|^2 |Z|^2} \left(\begin{array}{cc|cc} -Y^2 |Z|^2 & -XYZ & X^2 & -XYZ^* \\ XYZ & -|Y|^2 Z^2 & XY^* Z & X^2 \\ \hline X^2 & -XY^* Z & -Y^{*2} |Z|^2 & -XY^* Z^* \\ XYZ^* & X^2 & XY^* Z^* & -|Y|^2 Z^{*2} \end{array} \right) \tag{B.4.1}$$

with $X = 8t_L t_R \sqrt{\Gamma_L \Gamma_R}$, $Y = \sqrt{\epsilon_M}(\Gamma_L - 2i\epsilon_L)$, and $Z = \sqrt{\epsilon_M}(\Gamma_R - 2i\epsilon_R)$. Using the zero-temperature average current and shot noise formulas Eqs. (3.1.15) and (3.1.16), we

find the zero-bias differential conductance and the zero-bias current correlators

$$G_{\text{tot}} = \frac{4e^2}{h} T_A, \quad (\text{B.4.2a})$$

$$P_{ij} = \frac{4e^2}{h} T_A (1 - T_A), \quad (\text{B.4.2b})$$

with

$$T_A = \frac{1}{1 + \epsilon_M^2 \frac{(\Gamma_L^2 + 4\epsilon_L^2)(\Gamma_R^2 + 4\epsilon_R^2)}{64t_L^2 t_R^2 \Gamma_L \Gamma_R}}. \quad (\text{B.4.3})$$

In particular, we note that both the differential conductance and the current correlator are independent of the signs of the quantum dot energies. Moreover, for $\epsilon_L = \epsilon_R = 0$ in the weak-coupling limit $\Gamma_L, \Gamma_R \ll t_L, t_R, \epsilon_M$ we find $T_A \rightarrow 1$ which yields a quantized zero-bias conductance $G_{\text{tot}} = 4e^2/h$ and $P_{ij} = 0$.

B.5. Transport properties of a double-quantum dot system coupled via the superconducting proximity effect

In chapter 3.4.4, we have studied the current and the current cross-correlations mediated by the superconducting proximity effect. The Hamiltonian for that system has been defined in Eq. (3.1.1) and is given by

$$H = \epsilon_L d_L^\dagger d_L + \epsilon_R d_R^\dagger d_R + \Delta(d_L^\dagger d_R^\dagger + d_R d_L). \quad (\text{B.5.1})$$

We obtain the quasiparticle energy spectrum by diagonalizing the 4×4 Bogoliubov-de Gennes Hamilton matrix

$$h = \begin{pmatrix} \epsilon_L & 0 & 0 & \Delta \\ 0 & \epsilon_R & -\Delta & 0 \\ 0 & -\Delta & -\epsilon_L & 0 \\ \Delta & 0 & 0 & -\epsilon_R \end{pmatrix}. \quad (\text{B.5.2})$$

This yields the two quasiparticle energies

$$E_{\pm} = \left| \frac{\epsilon_L - \epsilon_R}{2} \pm \sqrt{\left(\frac{\epsilon_L + \epsilon_R}{2} \right)^2 + \Delta^2} \right|. \quad (\text{B.5.3})$$

In the following, we analytically study the transport properties for $\epsilon_L = \epsilon_R = 0$. Numeri-

cally, we have found that the current and the cross-correlations are peaked for $\epsilon_L = \epsilon_R = 0$. With the coupling matrix W from Eq. (3.1.13) we here find the scattering matrix using Eq. (3.1.11),

$$S(\epsilon) = \frac{1}{Z} \begin{pmatrix} 4\Delta^2 - \Gamma^2 - 4\epsilon^2 & 0 & 0 & -4i\Delta\Gamma \\ 0 & 4\Delta^2 - \Gamma^2 - 4\epsilon^2 & 4i\Delta\Gamma & 0 \\ 0 & 4i\Delta\Gamma & 4\Delta^2 - \Gamma^2 - 4\epsilon^2 & 0 \\ -4i\Delta\Gamma & 0 & 0 & 4\Delta^2 - \Gamma^2 - 4\epsilon^2 \end{pmatrix} \quad (\text{B.5.4})$$

with $Z = 4\Delta^2 + (\Gamma - 2i\epsilon)^2$. Using the zero-temperature current and noise formulas Eqs. (3.1.15) and (3.1.16), we find the total differential conductance and the current cross-correlator

$$G(eV = \epsilon) = \frac{4e^2}{h} T_A, \quad (\text{B.5.5a})$$

$$P_{LR}(eV = \epsilon) = \frac{4e^2}{h} T_A (1 - T_A), \quad (\text{B.5.5b})$$

where

$$T_A = \frac{16\Delta^2\Gamma^2}{[4\Delta^2 - 4\epsilon^2 + \Gamma^2]^2 + 16\epsilon^2\Gamma^2} \quad (\text{B.5.6})$$

is the probability that an incoming electron with energy ϵ is Andreev reflected as a hole in the different lead. We are interested in the current and the cross-correlations in the limit of large voltages. For analytical calculations, it is appropriate to consider the limit $V \rightarrow \infty$. With Eqs. (B.5.5), we obtain the current $I = \int_0^\infty d\epsilon G(\epsilon)$ and the crossed noise $S_{LR} = \int_0^\infty d\epsilon P_{LR}(\epsilon)$,

$$I = \frac{e}{h} \frac{8\pi\Gamma\Delta^2}{4\Delta^2 + \Gamma^2} \xrightarrow{\Gamma \gg \Delta} \frac{e}{h} \frac{8\pi\Delta^2}{\Gamma}, \quad (\text{B.5.7a})$$

$$S_{LR} = \frac{2e^2}{h} \frac{4\pi\Gamma\Delta^2(8\Delta^4 - 2\Delta^2\Gamma^2 + \Gamma^4)}{(4\Delta^2 + \Gamma^2)^3} \xrightarrow{\Gamma \gg \Delta} \frac{2e^2}{h} \frac{4\pi\Delta^2}{\Gamma}. \quad (\text{B.5.7b})$$

This yields the crossed Fano factor

$$F_{LR} = \frac{S_{LR}}{2eI} = \frac{8\Delta^4 - 2\Delta^2\Gamma^2 + \Gamma^4}{2(4\Delta^2 + \Gamma^2)^2} \xrightarrow{\Gamma \gg \Delta} \frac{1}{2}. \quad (\text{B.5.8})$$

C. Three-dimensional topological superconductors and spin response

C.1. Lattice Hamiltonian for the three-dimensional topological superconductor

In chapter 5, we have studied a tight-binding model for a doped three-dimensional topological insulator with several types of superconducting pairing symmetries. In this appendix we discuss some details about the numerical calculation of the excitation spectrum. We begin our discussion with the normal-state topological insulator confined to a film $-L < z < 0$ and with translational symmetry in x and y direction. In chapter 5, we have defined the $\mathbf{k} \cdot \mathbf{p}$ continuum Hamiltonian

$$H_{\text{TI}} = \sum_{\mathbf{k}_{\perp}} \int_0^L dz C_{\mathbf{k}_{\perp}}^{\dagger}(z) \left[(m - B_1 \partial_z^2 + B_2 k_{\perp}^2) \sigma_x - i v_z \partial_z \sigma_y + v(k_x s_y - k_y s_x) \sigma_z - \mu \right] C_{\mathbf{k}_{\perp}}(z) \quad (\text{C.1.1})$$

with the Pauli matrices s_i (σ_i) for the spin (orbital) degree of freedom, and the operators $C_{\mathbf{k}_{\perp}}(z) = (c_{i\mathbf{k}_{\perp}s}(z))_{is}$, where $c_{i\mathbf{k}_{\perp}s}(z)$ annihilates an electron in orbital i , with in-plane momentum $\mathbf{k}_{\perp} = (k_x, k_y)$, and spin s . From this Hamiltonian, we obtain the corresponding tight-binding lattice Hamiltonian by replacing

$$\partial_z C \rightarrow \frac{C_{z+a} - C_{z-a}}{2a}, \quad (\text{C.1.2a})$$

$$\partial_z^2 C \rightarrow \frac{C_{z+a} + C_{z-a} - 2C_z}{a^2}, \quad (\text{C.1.2b})$$

where a denotes the lattice constant. Thus, we rewrite

$$\begin{aligned}
 H_{\text{TI}} = \sum_{\mathbf{k}_\perp} \sum_{z=a}^{Na} \Big\{ & C_{\mathbf{k}_\perp, z}^\dagger \left[\left(m + 2\frac{B_1}{a^2} + B_2 k_\perp^2 \right) \sigma_x + v(k_x s_y - k_y s_x) \sigma_z - \mu \right] C_{\mathbf{k}_\perp, z} \\
 & - \frac{B_1}{a^2} \left[C_{\mathbf{k}_\perp, z}^\dagger \sigma_x C_{\mathbf{k}_\perp, z+a} + C_{\mathbf{k}_\perp, z+a}^\dagger \sigma_x C_{\mathbf{k}_\perp, z} \right] \\
 & - \frac{iv_z}{2a} \left[C_{\mathbf{k}_\perp, z}^\dagger \sigma_y C_{\mathbf{k}_\perp, z+a} - C_{\mathbf{k}_\perp, z+a}^\dagger \sigma_y C_{\mathbf{k}_\perp, z} \right] \Big\}, \quad (\text{C.1.3})
 \end{aligned}$$

where $N = L/a$ denotes the number of lattice sites. To diagonalize this Hamiltonian numerically, we include the fermion operators into a single $4N$ -component vector $\Psi_{\mathbf{k}_\perp}^\dagger$ for electron creation operators and a single vector $\Psi_{\mathbf{k}_\perp}$ for electron annihilation operators with in-plane momentum \mathbf{k}_\perp . We define

$$\Psi_{\mathbf{k}_\perp} = \left(c_{(1\uparrow),1} \quad c_{(1\downarrow),1} \quad c_{(2\uparrow),1} \quad c_{(2\downarrow),1} \quad \dots \quad c_{(1\uparrow),N} \quad c_{(1\downarrow),N} \quad c_{(2\uparrow),N} \quad c_{(2\downarrow),N} \right)^T, \quad (\text{C.1.4})$$

where we neglected for brevity the momentum index \mathbf{k}_\perp of the c -operators. Thus, we write

$$H_{\text{TI}} = \sum_{\mathbf{k}_\perp} \Psi_{\mathbf{k}_\perp}^\dagger \mathcal{H}_{\mathbf{k}_\perp} \Psi_{\mathbf{k}_\perp} \quad (\text{C.1.5})$$

with the Hermitian $4N \times 4N$ Hamilton matrix

$$\mathcal{H}_{\mathbf{k}_\perp} = \left(\begin{array}{cccc|cccc|c}
 -\mu & -ivk_- & \tilde{m} & 0 & 0 & 0 & -B_- & 0 & \\
 ivk_+ & -\mu & 0 & \tilde{m} & 0 & 0 & 0 & -B_- & \\
 \tilde{m} & 0 & -\mu & ivk_- & -B_+ & 0 & 0 & 0 & \\
 0 & \tilde{m} & -ivk_+ & -\mu & 0 & -B_+ & 0 & 0 & \\
 \hline
 0 & 0 & -B_+ & 0 & -\mu & -ivk_- & \tilde{m} & 0 & \\
 0 & 0 & 0 & -B_+ & ivk_+ & -\mu & 0 & \tilde{m} & \\
 -B_- & 0 & 0 & 0 & \tilde{m} & 0 & -\mu & ivk_- & \\
 0 & -B_- & 0 & 0 & 0 & \tilde{m} & -ivk_+ & -\mu & \\
 \hline
 & & & & & & & & \dots \\
 & & & & & & & & \dots
 \end{array} \right). \quad (\text{C.1.6})$$

Here, we abbreviated $B_\pm = B_1/a^2 \pm v_z/2a$, $k_\pm = k_x \pm ik_y$, and $\tilde{m} = m + 2B_1/a^2 + B_2 k_\perp^2$.

Starting from the lattice Hamiltonian for the topological insulator, we now present the Hamilton matrix for the system with superconducting pairing. We have defined the possible pairing Hamiltonians in Eqs. (5.1.14)–(5.1.17). In all these Hamiltonians, pairing is

between states with opposite spins and between time-reversed momenta, i.e., (\mathbf{k}, \uparrow) and $(-\mathbf{k}, \downarrow)$. If we Fourier transform the z component of the electron operators, we find that the pairing is between states $(\mathbf{k}_\perp, z; \uparrow)$ and $(-\mathbf{k}_\perp, z; \downarrow)$. The only differences between the pairing Hamiltonians is the different structure in orbital space. We distinguish between intra- and interorbital pairing, and between odd and even parity under orbital exchange. Following the procedure discussed in chapter 2.1, we find the Bogoliubov-de Gennes Hamilton matrix

$$\mathcal{H}_{\text{BdG}} = \begin{pmatrix} \mathcal{H}_{\mathbf{k}_\perp} & \hat{\Delta} \\ -\hat{\Delta}^* & -\mathcal{H}_{-\mathbf{k}_\perp}^* \end{pmatrix}. \quad (\text{C.1.7})$$

Here, \mathcal{H}_{BdG} is a $8N \times 8N$ matrix where the pre factor of 8 originates from the particle-hole, the spin, and the orbital degrees of freedom. We summarize all four pairing symmetries into the skew-symmetric $4N \times 4N$ pairing matrix

$$\hat{\Delta} = \begin{pmatrix} 0 & -\Delta_1 - \Delta_2 & 0 & -\Delta - \Delta_3 & 0 & 0 & 0 & 0 \\ \Delta_1 + \Delta_2 & 0 & -\Delta + \Delta_3 & 0 & 0 & 0 & 0 & 0 \\ 0 & \Delta - \Delta_3 & 0 & -\Delta_1 + \Delta_2 & 0 & 0 & 0 & 0 \\ \Delta + \Delta_3 & 0 & \Delta_1 - \Delta_2 & 0 & 0 & 0 & 0 & 0 \\ \hline 0 & 0 & 0 & 0 & \dots & & & \\ 0 & 0 & 0 & 0 & & \dots & & \\ 0 & 0 & 0 & 0 & & & \dots & \\ 0 & 0 & 0 & 0 & & & & \dots \end{pmatrix}. \quad (\text{C.1.8})$$

C.2. Projection of the pairing Hamiltonians for the doped three-dimensional topological insulator

In this appendix we derive the projection of the pairing Hamiltonian onto the conduction band of the doped topological insulator. In this projection, we assume that the valence band is completely filled and does not contribute to the superconducting pairing. This assumption is satisfied for $\Delta \ll |m| < \mu$ and thus naturally satisfied for realistic material parameters. In chapter 5.1, we have defined the Hamiltonian for the doped topological insulator and calculated the conduction band operators

$$\alpha_{\mathbf{k},\tau} = \sum_{s,\sigma} \psi_\tau^{s,\sigma}(\mathbf{k}) c_{\sigma,\mathbf{k},s} \quad (\text{C.2.1})$$

with the electronic wave function

$$\psi_\tau(\mathbf{k}) = \frac{1}{2\sqrt{E}} \begin{pmatrix} \sqrt{E + vk_\perp} \tau e^{i\chi/2} \\ \sqrt{E - vk_\perp} \tau e^{-i\chi/2} \end{pmatrix}_\sigma \otimes \begin{pmatrix} e^{i(\phi/2 + \tau\pi/4)} \\ e^{-i(\phi/2 + \tau\pi/4)} \end{pmatrix}_s \quad (\text{C.2.2})$$

with the definitions

$$e^{i\phi} = \frac{k_x + ik_y}{k_\perp}, \quad (\text{C.2.3a})$$

$$e^{i\chi} = \frac{m_0(\mathbf{k}) + iv_z k_z}{\sqrt{m_0^2(\mathbf{k}) + v_z^2 k_z^2}}, \quad (\text{C.2.3b})$$

$$E = \sqrt{m_0^2(\mathbf{k}) + v_z k_z^2 + v^2 k_\perp^2}. \quad (\text{C.2.3c})$$

We find the relations $\phi_{-\mathbf{k}} = \phi_{\mathbf{k}} + \pi$ and $\chi_{-\mathbf{k}} = -\chi_{\mathbf{k}}$ from the wave functions for opposite momenta. The index τ denotes the pseudospin \pm of the degenerate conduction band. Using the orthonormality of the wave functions ψ , we invert the definition of the α operators and find

$$c_{\sigma, \mathbf{k}, s} = \sum_\tau [\psi_\tau^{s, \sigma}(\mathbf{k})]^* \alpha_{\mathbf{k}, \tau}. \quad (\text{C.2.4})$$

We now project the Hamiltonians Eqs. (5.1.14)-(5.1.17) onto the conduction band by rewriting the Hamiltonians in terms of the new α operators. For that purpose, we write

$$\begin{aligned} c_{1, \mathbf{k}, \uparrow} c_{1, -\mathbf{k}, \downarrow} &= \frac{1}{4E} \sum_{\tau, \tau'} [\sqrt{E + vk_\perp} \tau e^{-\frac{i}{2}(\chi_{\mathbf{k}} + \phi_{\mathbf{k}} + \tau\pi/2)} \alpha_{\mathbf{k}, \tau}] [\sqrt{E + vk_\perp} \tau' e^{-\frac{i}{2}(\chi_{-\mathbf{k}} - \phi_{-\mathbf{k}} - \tau'\pi/2)} \alpha_{-\mathbf{k}, \tau'}] \\ &= \frac{-i}{4E} \sum_{\tau, \tau'} \sqrt{E + vk_\perp} \tau e^{-i\tau\pi/4} \sqrt{E + vk_\perp} \tau' e^{i\tau'\pi/4} \alpha_{\mathbf{k}, \tau} \alpha_{-\mathbf{k}, \tau'} \\ &= \frac{-i}{4E} \sum_\tau (E + vk_\perp \tau) \alpha_{\mathbf{k}, \tau} \alpha_{-\mathbf{k}, \tau} + \frac{1}{4E} \sqrt{E^2 - v^2 k_\perp^2} [\alpha_{\mathbf{k}, +} \alpha_{-\mathbf{k}, -} - \alpha_{\mathbf{k}, -} \alpha_{-\mathbf{k}, +}], \end{aligned} \quad (\text{C.2.5})$$

$$\begin{aligned} c_{2, \mathbf{k}, \uparrow} c_{2, -\mathbf{k}, \downarrow} &= \frac{1}{4E} \sum_{\tau, \tau'} [\sqrt{E - vk_\perp} \tau e^{\frac{i}{2}(\chi_{\mathbf{k}} - \phi_{\mathbf{k}} - \tau\pi/2)} \alpha_{\mathbf{k}, \tau}] [\sqrt{E - vk_\perp} \tau' e^{\frac{i}{2}(\chi_{-\mathbf{k}} + \phi_{-\mathbf{k}} + \tau'\pi/2)} \alpha_{-\mathbf{k}, \tau'}] \\ &= \frac{-i}{4E} \sum_{\tau, \tau'} \sqrt{E - vk_\perp} \tau e^{-i\tau\pi/4} \sqrt{E - vk_\perp} \tau' e^{i\tau'\pi/4} \alpha_{\mathbf{k}, \tau} \alpha_{-\mathbf{k}, \tau'} \\ &= \frac{-i}{4E} \sum_\tau (E - vk_\perp \tau) \alpha_{\mathbf{k}, \tau} \alpha_{-\mathbf{k}, \tau} + \frac{1}{4E} \sqrt{E^2 - v^2 k_\perp^2} [\alpha_{\mathbf{k}, +} \alpha_{-\mathbf{k}, -} - \alpha_{\mathbf{k}, -} \alpha_{-\mathbf{k}, +}], \end{aligned} \quad (\text{C.2.6})$$

$$\begin{aligned}
 c_{1,\mathbf{k},\uparrow}c_{2,-\mathbf{k},\downarrow} &= \frac{1}{4E} \sum_{\tau,\tau'} [\sqrt{E + vk_{\perp}}\tau e^{-\frac{i}{2}(\chi_{\mathbf{k}} + \phi_{\mathbf{k}} + \tau\pi/2)}\alpha_{\mathbf{k},\tau}] [\sqrt{E - vk_{\perp}}\tau' e^{\frac{i}{2}(\chi_{-\mathbf{k}} + \phi_{-\mathbf{k}} + \tau'\pi/2)}\alpha_{-\mathbf{k},\tau'}] \\
 &= \frac{-i}{4E} \sum_{\tau,\tau'} \sqrt{E + vk_{\perp}}\tau e^{-i\tau\pi/4} \sqrt{E - vk_{\perp}}\tau' e^{i\tau'\pi/4} e^{-i\chi_{\mathbf{k}}} \alpha_{\mathbf{k},\tau} \alpha_{-\mathbf{k},\tau'} \\
 &= \frac{-i}{4E} \sum_{\tau} \sqrt{E^2 - v^2k_{\perp}^2} \alpha_{\mathbf{k},\tau} \alpha_{-\mathbf{k},\tau} \\
 &\quad - \frac{e^{-i\chi_{\mathbf{k}}}}{4E} [(E + vk_{\perp})\alpha_{\mathbf{k},+}\alpha_{-\mathbf{k},-} - (E - vk_{\perp})\alpha_{\mathbf{k},-}\alpha_{-\mathbf{k},+}], \tag{C.2.7}
 \end{aligned}$$

$$\begin{aligned}
 c_{1,\mathbf{k},\downarrow}c_{2,-\mathbf{k},\uparrow} &= \frac{1}{4E} \sum_{\tau,\tau'} [\sqrt{E + vk_{\perp}}\tau e^{-\frac{i}{2}(\chi_{\mathbf{k}} - \phi_{\mathbf{k}} - \tau\pi/2)}\alpha_{\mathbf{k},\tau}] [\sqrt{E - vk_{\perp}}\tau' e^{\frac{i}{2}(\chi_{-\mathbf{k}} - \phi_{-\mathbf{k}} - \tau'\pi/2)}\alpha_{-\mathbf{k},\tau'}] \\
 &= \frac{i}{4E} \sum_{\tau,\tau'} \sqrt{E + vk_{\perp}}\tau e^{i\tau\pi/4} \sqrt{E - vk_{\perp}}\tau' e^{-i\tau'\pi/4} e^{-i\chi_{\mathbf{k}}} \alpha_{\mathbf{k},\tau} \alpha_{-\mathbf{k},\tau'} \\
 &= \frac{i}{4E} \sum_{\tau} \sqrt{E^2 - v^2k_{\perp}^2} \alpha_{\mathbf{k},\tau} \alpha_{-\mathbf{k},\tau} \\
 &\quad - \frac{e^{-i\chi_{\mathbf{k}}}}{4E} [(E + vk_{\perp})\alpha_{\mathbf{k},+}\alpha_{-\mathbf{k},-} - (E - vk_{\perp})\alpha_{\mathbf{k},-}\alpha_{-\mathbf{k},+}]. \tag{C.2.8}
 \end{aligned}$$

If we sum over all momenta, we find the important simplifications

$$\begin{aligned}
 &\sum_{\mathbf{k}} \frac{1}{4E} \sqrt{E^2 - v^2k_{\perp}^2} [\alpha_{\mathbf{k},+}\alpha_{-\mathbf{k},-} - \alpha_{\mathbf{k},-}\alpha_{-\mathbf{k},+}] \\
 &= \sum_{\mathbf{k}} \frac{1}{4E} \sqrt{E^2 - v^2k_{\perp}^2} [\alpha_{(k,\phi,k_z),+}\alpha_{(k,\phi+\pi,-k_z),-} - \alpha_{(k,\phi,k_z),-}\alpha_{(k,\phi+\pi,-k_z),+}] \\
 &= \sum_{\mathbf{k}} \frac{1}{4E} \sqrt{E^2 - v^2k_{\perp}^2} [\alpha_{(k,\phi,k_z),+}\alpha_{(k,\phi+\pi,-k_z),-} + \alpha_{(k,\phi+\pi,-k_z),+}\alpha_{(k,\phi,k_z),-}] \\
 &= \sum_{\mathbf{k}} \frac{1}{4E} \sqrt{E^2 - v^2k_{\perp}^2} [\alpha_{(k,\phi,k_z),+}\alpha_{(k,\phi+\pi,-k_z),-} + \underbrace{\alpha_{(k,\phi+2\pi,k_z),+}}_{=-\alpha_{(k,\phi,k_z),+}}\alpha_{(k,\phi+\pi,-k_z),-}] = 0, \tag{C.2.9}
 \end{aligned}$$

where we used the 4π periodicity of the α operators under rotations in the k_x - k_y plane in

the last line, and we find

$$\begin{aligned}
& - \sum_{\mathbf{k}} \frac{1}{4E} e^{-i\chi_{\mathbf{k}}} [(E + vk_{\perp})\alpha_{\mathbf{k},+}\alpha_{-\mathbf{k},-} - (E - vk_{\perp})\alpha_{\mathbf{k},-}\alpha_{-\mathbf{k},+}] \\
&= \sum_{\mathbf{k}} \frac{1}{4E} [(E + vk_{\perp})e^{-i\chi_{\mathbf{k}}}\alpha_{-\mathbf{k},-}\alpha_{\mathbf{k},+} + (E - vk_{\perp})e^{-i\chi_{\mathbf{k}}}\alpha_{\mathbf{k},-}\alpha_{-\mathbf{k},+}] \\
&= \sum_{\mathbf{k}} \frac{1}{4E} [-(E + vk_{\perp})e^{i\chi_{\mathbf{k}}}\alpha_{\mathbf{k},-}\alpha_{-\mathbf{k},+} + (E - vk_{\perp})e^{-i\chi_{\mathbf{k}}}\alpha_{\mathbf{k},-}\alpha_{-\mathbf{k},+}] \\
&= \sum_{\mathbf{k}} \frac{1}{4E} \left[-(E + vk_{\perp}) \frac{m_0(\mathbf{k}) + iv_z k_z}{\sqrt{m_0^2(\mathbf{k}) + v_z^2 k_z^2}} + (E - vk_{\perp}) \frac{m_0(\mathbf{k}) - iv_z k_z}{\sqrt{m_0^2(\mathbf{k}) + v_z^2 k_z^2}} \right] \alpha_{\mathbf{k},-}\alpha_{-\mathbf{k},+} \\
&= - \sum_{\mathbf{k}} \frac{1}{2E} \frac{m_0 v k_{\perp} + iv_z k_z E}{\sqrt{m_0^2 + v_z^2 k_z^2}} \alpha_{\mathbf{k},-}\alpha_{-\mathbf{k},+}. \tag{C.2.10}
\end{aligned}$$

Thus, we find

$$\Delta_1 \sum_{\mathbf{k}} (c_{1,\mathbf{k},\uparrow} c_{1,-\mathbf{k},\downarrow} + c_{2,\mathbf{k},\uparrow} c_{2,-\mathbf{k},\downarrow}) = \frac{-i\Delta_1}{2} \sum_{\mathbf{k}} \sum_{\tau} \alpha_{\mathbf{k},\tau} \alpha_{-\mathbf{k},\tau}, \tag{C.2.11a}$$

$$\Delta_2 \sum_{\mathbf{k}} (c_{1,\mathbf{k},\uparrow} c_{1,-\mathbf{k},\downarrow} - c_{2,\mathbf{k},\uparrow} c_{2,-\mathbf{k},\downarrow}) = \frac{-i\Delta_2}{2} \sum_{\mathbf{k}} \sum_{\tau} \frac{vk_{\perp}\tau}{E} \alpha_{\mathbf{k},\tau} \alpha_{-\mathbf{k},\tau}, \tag{C.2.11b}$$

$$\Delta_3 \sum_{\mathbf{k}} (c_{1,\mathbf{k},\uparrow} c_{2,-\mathbf{k},\downarrow} - c_{1,\mathbf{k},\downarrow} c_{2,-\mathbf{k},\uparrow}) = \frac{-i\Delta_3}{2} \sum_{\mathbf{k}} \sum_{\tau} \frac{|m_0(\mathbf{k})|}{E} \alpha_{\mathbf{k},\tau} \alpha_{-\mathbf{k},\tau}, \tag{C.2.11c}$$

$$\Delta \sum_{\mathbf{k}} (c_{1,\mathbf{k},\uparrow} c_{2,-\mathbf{k},\downarrow} + c_{1,\mathbf{k},\downarrow} c_{2,-\mathbf{k},\uparrow}) = -\frac{\Delta}{2} \sum_{\mathbf{k}} \frac{vk_{\perp} \frac{m_0(\mathbf{k})}{E} + iv_z k_z}{\sqrt{m_0^2(\mathbf{k}) + v_z^2 k_z^2}} \alpha_{\mathbf{k},-}\alpha_{-\mathbf{k},+}. \tag{C.2.11d}$$

For $\Delta_i \ll \mu$ and $E \approx \mu$, we find the final results

$$H_1 \approx \frac{-i\Delta_1}{2} \sum_{\mathbf{k},\tau} \alpha_{\mathbf{k},\tau} \alpha_{-\mathbf{k},\tau} + \text{H.c.}, \tag{C.2.12a}$$

$$H_2 \approx \frac{-i\Delta_2}{2} \sum_{\mathbf{k},\tau} \frac{\tau v k_{\perp}}{\mu} \alpha_{\mathbf{k},\tau} \alpha_{-\mathbf{k},\tau} + \text{H.c.}, \tag{C.2.12b}$$

$$H_3 \approx \frac{i\Delta_3}{2} \sum_{\mathbf{k},\tau} \frac{m_0(\mathbf{k})}{\mu} \alpha_{\mathbf{k},\tau} \alpha_{-\mathbf{k},\tau} + \text{H.c.}, \tag{C.2.12c}$$

$$H_{\text{SC}} \approx \frac{i\Delta}{2} \sum_{\mathbf{k},\tau} \frac{v_z k_z + iv k_{\perp} \frac{m_0(\mathbf{k})}{\mu}}{\sqrt{m_0^2(\mathbf{k}) + v_z^2 k_z^2}} \alpha_{\mathbf{k},-}\alpha_{-\mathbf{k},+} + \text{H.c.} \tag{C.2.12d}$$

C.3. Density of states and spin susceptibilities for superconductors

In this appendix we derive the local density of states and the local spin susceptibilities which we have studied in chapter 5.2. We consider a general bilinear superconducting system with spin and orbital degrees of freedom. We write the Hamiltonian

$$H = \sum_{i,j} \sum_{m,n} \sum_{s,s'} \left(c_{ims}^\dagger t_{ij;mn}^{ss'} c_{jns'} + c_{ims}^\dagger \Delta_{ij;mn}^{ss'} c_{jns'}^\dagger + c_{jns'} \Delta_{ij;mn}^{ss'*} c_{ims} \right), \quad (\text{C.3.1})$$

where i denotes the lattice site (or momentum), m the orbital, and s the spin quantum numbers. The matrix t describes the normal-state properties of the system and the matrix Δ describes the superconducting pairing. As discussed in chapter 2.1, we diagonalize the Hamiltonian by the Bogoliubov transformation

$$c_{ims}^\dagger = \sum_{\lambda} \left(u_{[ims]\lambda} \alpha_{\lambda}^\dagger + v_{[ims]\lambda} \alpha_{\lambda} \right), \quad (\text{C.3.2})$$

where we introduced Bogoliubov quasiparticle operators α_{λ} . In the basis of the α_{λ} operators, the Hamiltonian Eq. (C.3.1) can be written as $H = \sum_{\lambda} E_{\lambda} \alpha_{\lambda}^\dagger \alpha_{\lambda}$ with $E_{\lambda} \geq 0$ where the cardinality of the set of quantum numbers λ equals the number of sites times the number of orbitals times the number of spin directions. In chapter 5, we have studied Hamiltonian Eq. (C.3.1) with the special choices $m \in \{1, 2\}$, $s \in \{\uparrow, \downarrow\}$, and $i \in \{(k_x, k_y, z) | k_x \in \mathbb{R}, k_y \in \mathbb{R}, z \in [0, L]\}$.

C.3.1. Density of states

In the following, we define the local quasiparticle density of states $\mathcal{N}(\epsilon, z)$ as the number of quasiparticles in the volume element $[z, z + dz]$ and with energy in the interval $[\epsilon, \epsilon + d\epsilon]$ for $d\epsilon \rightarrow 0$ and $dz \rightarrow 0$. We write the quasiparticle density of states

$$\mathcal{N}(\epsilon, z) = \sum_{\lambda} \delta(\epsilon - E_{\lambda}) \sum_{m,s,k_x,k_y} \left(|u_{[k_x,k_y,m,s]\lambda}(z)|^2 + |v_{[k_x,k_y,m,s]\lambda}(z)|^2 \right), \quad (\text{C.3.3})$$

where the last term is the density of quasiparticles with energy E_{λ} at position z . In our numerical calculations in chapter 5, we have approximated the δ function by a Gaussian

distribution with variance a . This approximation yields

$$\mathcal{N}_a(\epsilon, z) = \frac{1}{\sqrt{2\pi a}} \sum_{\lambda} e^{-\frac{(\epsilon - E_{\lambda})^2}{2a}} \sum_{m,s,k_x,k_y} \left(|u_{[k_x,k_y,m,s]\lambda}(z)|^2 + |v_{[k_x,k_y,m,s]\lambda}(z)|^2 \right) \quad (\text{C.3.4})$$

with the limit $\mathcal{N}_a \rightarrow \mathcal{N}$ for $a \rightarrow 0$.

C.3.2. Spin susceptibilities

The total electron spin operator is defined as

$$\begin{aligned} S_i(z, \mathbf{q}_{\perp}) &= \frac{1}{\mathcal{V}} \sum_{a,b=1,2} \sum_{k_x,k_y} \sum_{s,s'} c_{a(k_x+q_x,k_y+q_y,z)s}^{\dagger} \frac{\sigma_{ss'}^i}{2} c_{b(k_x,k_y,z)s'} \\ &= \frac{1}{\mathcal{V}} \sum_{a,b=1,2} S_i^{ab}(z, \mathbf{q}_{\perp}), \end{aligned} \quad (\text{C.3.5})$$

where $\mathbf{q}_{\perp} \in \mathbb{R}^2$ is the momentum of the electron spin operator in the x - y plane. In chapter 5, we have defined the dynamical spin susceptibility as the two-particle Matsubara Green function

$$\begin{aligned} \chi_{ij}(z, z', \mathbf{q}_{\perp}; i\omega_n) &= \frac{1}{\mathcal{V}} \int_0^{\beta} d\tau e^{i\omega_n \tau} \langle T_{\tau} S_i(z, \mathbf{q}_{\perp}, \tau) S_j(z', -\mathbf{q}_{\perp}, 0) \rangle \\ &= \sum_{a,b,c,d=1,2} \chi_{ij}^{abcd}(z, z', \mathbf{q}_{\perp}; i\omega_n). \end{aligned} \quad (\text{C.3.6})$$

From Eq. (C.3.6), we obtain the retarded Green function by the analytical continuations $i\omega_n \rightarrow \omega + i\eta$ with the small broadening η . In the following, we neglect the indices k_x and k_y for brevity, and assume that they are implicitly contained in the index λ for the quantum number of the quasiparticles. This assumption is justified since k_x and k_y are good quantum numbers for a translationally invariant system in x and y directions.

In the following, we explicitly explain how to calculate the transverse spin susceptibility

$$\begin{aligned} \chi_{-+}^{abcd}(z, z', \mathbf{q}; i\omega_n) &= \sum_{k_x,k_y} \sum_{k'_x,k'_y} \frac{1}{\mathcal{V}} \int_0^{\beta} d\tau e^{i\omega_n \tau} \times \\ &\quad \left\langle c_{a(k_x+q_x,k_y+q_y,z)\downarrow}^{\dagger}(\tau) c_{b(k_x,k_y,z)\uparrow}(\tau) c_{c(k'_x-q_x,k'_y-q_y,z')\uparrow}^{\dagger} c_{d(k'_x,k'_y,z')\downarrow} \right\rangle. \end{aligned} \quad (\text{C.3.7})$$

In the first step, we use the Bogoliubov transformation (C.3.2) to replace the c -fermion operators by the α -fermion operators. The resulting expression for the spin susceptibility contains sixteen two-particle Green functions of the form $\langle T_{\tau} \alpha_{\lambda_1}^{s_1}(\tau) \alpha_{\lambda_2}^{s_2}(\tau) \alpha_{\lambda_3}^{s_3} \alpha_{\lambda_4}^{s_4} \rangle$, where

the upper indices $s_i \in \{1, \uparrow\}$ for $i = 1, \dots, 4$. In the next step, we calculate these sixteen Green functions using the equation of motion technique. Equivalently, we could apply Wick's theorem to express the two-particle Green functions as convolution of single-particle Green functions and then carry out the Matsubara sum [115]. We here prefer the equation for motion technique because it is less technical than carrying out Matsubara contour integrals.

Since the Hamiltonian is diagonal in the α -operators, the only nonzero two-particle Green functions are the ones which contain two creation and two annihilation operators. Hence, only six out of the sixteen Green functions are finite and need to be calculated explicitly. As an example, we here explicitly present the calculation for the Green function $G_{\lambda_1, \lambda_2, \lambda_3 \lambda_4}^{+-- +} = \langle T_\tau \alpha_{\lambda_1}^\dagger(\tau) \alpha_{\lambda_2}(\tau) \alpha_{\lambda_3} \alpha_{\lambda_4}^\dagger \rangle$. We find the equation of motion

$$\begin{aligned} \frac{\partial}{\partial \tau} G_{\lambda_1, \lambda_2, \lambda_3 \lambda_4}^{+-- +}(\tau) &= \delta(\tau) \left\langle \left[\alpha_{\lambda_1}^\dagger \alpha_{\lambda_2}, \alpha_{\lambda_3} \alpha_{\lambda_4}^\dagger \right] \right\rangle + \left\langle T_\tau \left[\underbrace{\sum_\mu E_\mu \alpha_\mu^\dagger \alpha_\mu}_{=H}, \alpha_{\lambda_1}^\dagger \alpha_{\lambda_2} \right] (\tau) \alpha_{\lambda_3} \alpha_{\lambda_4}^\dagger \right\rangle \\ &= \delta(\tau) \delta_{\lambda_1, \lambda_3} \delta_{\lambda_2, \lambda_4} (f(E_{\lambda_2}) - f(E_{\lambda_1})) + (E_{\lambda_1} - E_{\lambda_2}) G_{\lambda_1, \lambda_2, \lambda_3 \lambda_4}^{+-- +}(\tau), \end{aligned} \quad (\text{C.3.8})$$

where f denotes the Fermi distribution. After the Fourier transformation from imaginary time τ to Matsubara frequencies $i\omega_n$,

$$i\omega_n G_{\lambda_1, \lambda_2, \lambda_3 \lambda_4}^{+-- +}(i\omega_n) = \delta(\tau) \delta_{\lambda_1, \lambda_3} \delta_{\lambda_2, \lambda_4} (f(E_{\lambda_2}) - f(E_{\lambda_1})) + (E_{\lambda_1} - E_{\lambda_2}) G_{\lambda_1, \lambda_2, \lambda_3 \lambda_4}^{+-- +}(\tau), \quad (\text{C.3.9})$$

and the analytical continuation $i\omega_n \rightarrow \omega + i\eta$, we find the retarded two-particle Green function

$$G_{\lambda_1, \lambda_2, \lambda_3 \lambda_4}^{+-- +}(\omega) = -\delta_{\lambda_1, \lambda_3} \delta_{\lambda_2, \lambda_4} \frac{f(E_{\lambda_1}) - f(E_{\lambda_2})}{\omega + i\eta - (E_{\lambda_1} - E_{\lambda_2})}. \quad (\text{C.3.10})$$

Similarly, we find the five other nonzero two-particle Green functions

$$G_{\lambda_1, \lambda_2, \lambda_3 \lambda_4}^{-++ +}(\omega) = -\delta_{\lambda_1, \lambda_4} \delta_{\lambda_2, \lambda_3} \frac{f(-E_{\lambda_1}) - f(-E_{\lambda_2})}{\omega + i\eta - (-E_{\lambda_1} + E_{\lambda_2})}, \quad (\text{C.3.11a})$$

$$G_{\lambda_1, \lambda_2, \lambda_3 \lambda_4}^{-++ -}(\omega) = \delta_{\lambda_1, \lambda_3} \delta_{\lambda_2, \lambda_4} \frac{f(-E_{\lambda_1}) - f(-E_{\lambda_2})}{\omega + i\eta - (-E_{\lambda_1} + E_{\lambda_2})}, \quad (\text{C.3.11b})$$

$$G_{\lambda_1, \lambda_2, \lambda_3 \lambda_4}^{+-+ -}(\omega) = \delta_{\lambda_1, \lambda_4} \delta_{\lambda_2, \lambda_3} \frac{f(E_{\lambda_1}) - f(E_{\lambda_2})}{\omega + i\eta - (E_{\lambda_1} - E_{\lambda_2})}, \quad (\text{C.3.11c})$$

$$G_{\lambda_1, \lambda_2, \lambda_3 \lambda_4}^{+-+ +}(\omega) = (\delta_{\lambda_1, \lambda_4} \delta_{\lambda_2, \lambda_3} - \delta_{\lambda_1, \lambda_3} \delta_{\lambda_2, \lambda_4}) \frac{f(E_{\lambda_1}) - f(-E_{\lambda_2})}{\omega + i\eta - (E_{\lambda_1} + E_{\lambda_2})}, \quad (\text{C.3.11d})$$

$$G_{\lambda_1, \lambda_2, \lambda_3, \lambda_4}^{- - + +}(\omega) = (\delta_{\lambda_1, \lambda_4} \delta_{\lambda_2, \lambda_3} - \delta_{\lambda_1, \lambda_3} \delta_{\lambda_2, \lambda_4}) \frac{f(-E_{\lambda_1}) - f(E_{\lambda_2})}{\omega + i\eta - (-E_{\lambda_1} - E_{\lambda_2})}. \quad (\text{C.3.11e})$$

With these expressions for the two-particle Green functions and with the matrix elements u and v from the Bogoliubov transformation Eq. (C.3.2), we find for the transverse spin susceptibility

$$\begin{aligned} \chi_{-+}^{abcd}(z, z', \mathbf{q}_\perp; \omega) = \sum_{\lambda\mu} & \left[u_{[az\downarrow]\lambda} v_{[bz\uparrow]\mu}^* \left(v_{[cz'\uparrow]\mu} u_{[dz'\downarrow]\lambda}^* - v_{[cz'\uparrow]\lambda} u_{[dz'\downarrow]\mu}^* \right) \frac{f(E_\lambda) - f(-E_\mu)}{\omega + i\eta - (E_\lambda + E_\mu)} + \right. \\ & v_{[az\downarrow]\lambda} u_{[bz\uparrow]\mu}^* \left(u_{[cz'\uparrow]\mu} v_{[dz'\downarrow]\lambda}^* - u_{[cz'\uparrow]\lambda} v_{[dz'\downarrow]\mu}^* \right) \frac{f(-E_\lambda) - f(E_\mu)}{\omega + i\eta - (-E_\lambda - E_\mu)} + \\ & u_{[az\downarrow]\lambda} u_{[bz\uparrow]\mu}^* \left(u_{[cz'\uparrow]\mu} u_{[dz'\downarrow]\lambda}^* - v_{[cz'\uparrow]\lambda} v_{[dz'\downarrow]\mu}^* \right) \frac{f(E_\lambda) - f(E_\mu)}{\omega + i\eta - (E_\lambda - E_\mu)} + \\ & \left. v_{[az\downarrow]\lambda} v_{[bz\uparrow]\mu}^* \left(v_{[cz'\uparrow]\mu} v_{[dz'\downarrow]\lambda}^* - u_{[cz'\uparrow]\lambda} u_{[dz'\downarrow]\mu}^* \right) \frac{f(-E_\lambda) - f(-E_\mu)}{\omega + i\eta - (-E_\lambda + E_\mu)} \right]. \end{aligned} \quad (\text{C.3.12})$$

Similarly, we also find the longitudinal spin susceptibility

$$\chi_{zz}(z, z', \mathbf{q}_\perp; i\omega_n) = \frac{1}{V} \int_0^\beta d\tau e^{i\omega_n \tau} \langle T_\tau S_z(z, \mathbf{q}_\perp, \tau) S_z(z, -\mathbf{q}_\perp, 0) \rangle. \quad (\text{C.3.13})$$

C.4. Nuclear magnetic resonance

Nuclear magnetic resonance is a powerful experimental tool in which a sample is placed in a strong magnetic field and the magnetic response of the nuclear spins is measured. In experiments, one measures the resonance frequency of the nuclear spins, which is mainly determined by the Zeeman coupling between the nuclear spins and the external magnetic field. However, in metals one typically observes that the resonance frequency of particular nuclear isotope species is shifted with respect to the same nucleus in a specific insulating reference substance with a similar atomic configuration. This shift is proportional to the applied magnetic field and originates from two effects: (i) the motion of the charged electrons gives rise to an induced magnetic field at the position of the nucleus in addition to the external magnetic field. The shift due to this orbital effect is called chemical shift. (ii) The external magnetic field polarizes the electrons in the conduction band which gives rise to a finite spin polarization. The electron spins S and the nuclear spins I are coupled

by the hyperfine coupling

$$H_{hf} = \int \frac{d^3q}{(2\pi)^3} A(\mathbf{q}) \left\{ I_z S_z(\mathbf{q}) + I_+ S_-(\mathbf{q}) + I_- S_+(\mathbf{q}) \right\}, \quad (\text{C.4.1})$$

where $A(\mathbf{q})$ is the hyperfine coupling strength. As a consequence, the spin polarized conduction electrons give rise to an effective Zeeman coupling and therefore to a shift in the resonance frequency which is called spin shift or Knight shift.

C.4.1. Knight shift

The Knight shift is measured in samples with a strong external magnetic field \mathbf{B} which polarizes the conduction electrons due to the Zeeman coupling

$$V = g \mathbf{B} \cdot \mathbf{S}(\mathbf{q} = \mathbf{0}), \quad (\text{C.4.2})$$

where g denotes the coupling constant. Without loss of generality, we assume $\mathbf{B} = B\hat{z}$. We now derive the effective magnetic field at the nuclei due to the conduction electrons, $H_{hf} \approx g_N B_{\text{eff}} I_z$, using Kubo's formula with the external magnetic field as perturbation [115]. In order to guarantee the applicability of Kubo's formula, we assume that the conduction electrons show no magnetic order in zero magnetic field. This yields

$$\begin{aligned} \frac{B_{\text{eff}}(t)}{B} &= \frac{1}{g_N} \int \frac{d^3q}{(2\pi)^3} A(\mathbf{q}) \frac{\langle S_z(\mathbf{q}, t) \rangle_V}{B} \\ &\stackrel{\text{Kubo}}{=} -i \frac{g}{g_N} \int \frac{d^3q}{(2\pi)^3} A(\mathbf{q}) \int_{-\infty}^t dt' \langle [S_z(\mathbf{q}, t), S_z(\mathbf{q}' = \mathbf{0}, t')] \rangle_0 \\ &= \frac{g}{g_N} \int \frac{d^3q}{(2\pi)^3} A(\mathbf{q}) \int_{\mathbb{R}} dt' \chi_{zz}^R(\mathbf{q}, \mathbf{0}, t - t'). \end{aligned} \quad (\text{C.4.3})$$

with the retarded spin susceptibility

$$\chi_{zz}^R(\mathbf{q}, \mathbf{0}, t - t') = -i\Theta(t - t') \langle [S(\mathbf{q}, t), S_z(\mathbf{0}, t')] \rangle_0. \quad (\text{C.4.4})$$

In the limit $t \rightarrow \infty$, we find

$$\begin{aligned} K := \frac{B_{\text{eff}}}{B} &= \frac{g}{g_N} \int \frac{d^3q}{(2\pi)^3} A(\mathbf{q}) \underbrace{\chi_{zz}^R(\mathbf{q}, \mathbf{0}, \omega = 0)}_{\sim \delta(\mathbf{q} - \mathbf{0})} \\ &= \frac{g}{g_N} A(\mathbf{0}) \chi_{zz}^R(\mathbf{0}, \omega = 0), \end{aligned} \quad (\text{C.4.5})$$

where

$$\chi_{zz}^R(\mathbf{0}, \omega = 0) = \int_{\mathbb{R}} dt'' \chi_{zz}^R(\mathbf{0}, t''). \quad (\text{C.4.6})$$

Thus, we conclude that for nonmagnetic systems the Knight shift is determined by the static uniform spin susceptibility. We note that the order of the limits in energy space and momentum space is crucial.

If we apply this formalism to a simple noninteracting electron gas description of a metal, we find for the spin susceptibility

$$\chi_{zz}^R(\mathbf{q}, \omega) = \sum_{\mathbf{k}} \frac{f(\epsilon_{\mathbf{k}+\mathbf{q}}) - f(\epsilon_{\mathbf{k}})}{\omega + i\eta - (\epsilon_{\mathbf{k}+\mathbf{q}} - \epsilon_{\mathbf{k}})} \xrightarrow{\omega=0, \mathbf{q} \rightarrow \mathbf{0}} - \sum_{\mathbf{k}} \left. \frac{\partial f(\epsilon)}{\partial \epsilon} \right|_{\epsilon=\epsilon_{\mathbf{k}}} \approx \mathcal{N}(\mu), \quad (\text{C.4.7})$$

where η is a positive infinitesimal number and $\mathcal{N}(\mu)$ is the density of states at the Fermi energy. For interacting systems, η is the quasiparticle lifetime and given by the imaginary part of the self energy.

C.4.2. Spin-lattice relaxation rate

Another important quantity is the spin-lattice relaxation time T_1 which is the time for the recovery of the z component of the nuclear spin towards its equilibrium value. The spin-lattice relaxation time yields valuable information on the dynamics of the low-energy spin excitations. In metallic systems, the relaxation is determined by the coupling between the nuclear spin and the spin magnetic moments of the conduction electrons. The lifetime of the nuclear $|\uparrow\rangle$ spin state can be calculated in perturbation theory using Fermi's golden rule

$$\frac{1}{T_1} = \sum_{f,i} |\langle f, \downarrow | H_{hf} | i, \uparrow \rangle|^2 e^{-\beta E_i} \delta(\omega_0 + E_f - E_i). \quad (\text{C.4.8})$$

To evaluate this expression, we write

$$\begin{aligned} |\langle \downarrow, f | H_{hf} | i, \uparrow \rangle|^2 &= \int \frac{d^3 q}{(2\pi)^3} A(\mathbf{q}) \int \frac{d^3 q'}{(2\pi)^3} A(\mathbf{q}') \langle \uparrow, i | S_-(\mathbf{q}') I_+ | f, \downarrow \rangle \langle \downarrow, f | S_+(\mathbf{q}) I_- | i, \uparrow \rangle \\ &= \int \frac{d^3 q}{(2\pi)^3} A(\mathbf{q}) \int \frac{d^3 q'}{(2\pi)^3} A(\mathbf{q}') \langle i | S_-(\mathbf{q}') | f \rangle \langle f | S_+(\mathbf{q}) | i \rangle \end{aligned} \quad (\text{C.4.9})$$

and

$$\delta(\omega_0 + E_f - E_i) = \int \frac{dt}{2\pi} e^{-i(\omega_0 + E_f - E_i)t}. \quad (\text{C.4.10})$$

This yields

$$\begin{aligned} \frac{1}{T_1} &= \int \frac{dt}{2\pi} e^{-i\omega_0 t} \int \frac{d^3 q}{(2\pi)^3} A(\mathbf{q}) \int \frac{d^3 q'}{(2\pi)^3} A(\mathbf{q}') \sum_{f,i} \underbrace{\langle i | e^{iE_i t} S_-(\mathbf{q}') e^{-iE_f t} | f \rangle}_{S_-(\mathbf{q}', t)} \langle f | S_+(\mathbf{q}) | i \rangle e^{-\beta E_i} \\ &= \int \frac{dt}{2\pi} e^{-i\omega_0 t} \int \frac{d^3 q}{(2\pi)^3} A(\mathbf{q}) \int \frac{d^3 q'}{(2\pi)^3} A(\mathbf{q}') \text{Tr}_{el} \{ S_-(\mathbf{q}', t) S_+(\mathbf{q}) e^{-\beta H_{el}} \}. \end{aligned} \quad (\text{C.4.11})$$

Here, Tr_{el} denotes the trace over the eigenstates of the electronic Hamiltonian H_{el} and the frequency ω_0 is a small excitation energy due to the external magnetic field. The last term in Eq. (C.4.11) contains the spin-spin correlation function. Using the fluctuation-dissipation theorem [117], we rewrite the spin-spin correlation function in terms of the imaginary part of the spin susceptibility and we find for the spin-lattice relaxation rate

$$\frac{1}{T_1} = \int \frac{d^3 q}{(2\pi)^3} A(\mathbf{q}) A(-\mathbf{q}) \frac{\text{Im} \chi_{-+}(\mathbf{q}, \omega_0)}{1 - e^{-\beta \omega_0}}, \quad (\text{C.4.12})$$

where χ_{-+} denotes the transverse spin susceptibility and where we used that the susceptibility is diagonal in the momentum of the spin operator. The energy ω_0 is usually small compared to the natural frequency scales of electrons. For analytical calculations, it is appropriate to consider the limit $\omega_0 \rightarrow 0$ and to expand the denominator to first order in $\beta \omega_0$,

$$\frac{1}{T_1 T} = \int \frac{d^3 q}{(2\pi)^3} A(\mathbf{q}) A(-\mathbf{q}) \frac{\text{Im} \chi_{-+}(\mathbf{q}, \omega_0)}{\omega_0}. \quad (\text{C.4.13})$$

In chapter 5, we consider an inhomogeneous system with spatially dependent relaxation times. Applying the above introduced calculation to this situation and assuming $A(q_x, q_y, z) = \text{const.}$, we find

$$\frac{1}{T_1(z) T} \sim \int \frac{dq_x}{(2\pi)} \int \frac{dq_y}{(2\pi)} \int dz \frac{\text{Im} \chi_{-+}(q_x, q_y, z, \omega_0)}{\omega_0}. \quad (\text{C.4.14})$$

Bibliography

- [1] P. W. Anderson, *Science* **177**, 393 (1972).
- [2] X.-G. Wen, *Quantum Field Theory of Many Body Systems*, Oxford University Press, London, 2004.
- [3] L. D. Landau, *Zh. Eksp. Teor. Fiz.* **30**, 1058 (1956).
- [4] V. L. Ginzburg and L. D. Landau, *Zh. Eksp. Teor. Fiz.* **20**, 1064 (1950).
- [5] K. v. Klitzing, G. Dorda, and M. Pepper, *Phys. Rev. Lett.* **45**, 494 (1980).
- [6] D. J. Thouless, M. Kohmoto, M. P. Nightingale, and M. den Nijs, *Phys. Rev. Lett.* **49**, 405 (1982).
- [7] B. A. Bernevig, T. L. Hughes, and S. C. Zhang, *Science* **314**, 1757 (2006).
- [8] M. König, S. Wiedmann, C. Brüne, A. Roth, H. Buhmann, L. W. Molenkamp, X.-L. Qi, and S.-C. Zhang, *Science* **318**, 766 (2007).
- [9] H. Zhang, C.-X. Liu, X.-L. Qi, X. Dai, Z. Fang, and S.-C. Zhang, *Nat. Phys.* **5**, 438 (2009).
- [10] D. Hsieh, D. Qian, L. Wray, Y. Xia, Y. S. Hor, R. J. Cava, and M. Z. Hasan, *Nature* **452**, 970 (2008).
- [11] M. Z. Hasan and C. L. Kane, *Rev. Mod. Phys.* **82**, 3045 (2010).
- [12] X. L. Qi and S. C. Zhang, *Rev. Mod. Phys.* **83**, 1057 (2011).
- [13] A. P. Schnyder, S. Ryu, A. Furusaki, and A. W. W. Ludwig, *Phys. Rev. B* **78**, 195125 (2008).
- [14] X. L. Qi, T. L. Hughes, S. Raghu, and S.-C. Zhang, *Phys. Rev. Lett.* **102**, 187001 (2009).
- [15] M. Sato, *Phys. Rev. B* **81**, 220504(R) (2010).

- [16] E. Majorana, *Nuovo Cimento* **14**, 171 (1937).
- [17] N. B. Kopnin and M. M. Salomaa, *Phys. Rev. B* **44**, 9667 (1991).
- [18] G. E. Volovik, *Zh. Eksp. Teor. Fiz.* **70**, 601 (1999).
- [19] N. Read and D. Green, *Phys. Rev. B* **61**, 10267 (2000).
- [20] G. Moore and N. Read, *Nucl. Phys. B* **360**, 362 (1991).
- [21] C. W. J. Beenakker, *Annu. Rev. Con. Mat. Phys.* **4**, 113 (2013).
- [22] J. Alicea, *Rep. Prog. Phys.* **75**, 076501 (2012).
- [23] M. Leijnse and K. Flensberg, *Semicond. Sci. Technol.* **27**, 124003 (2012).
- [24] J. M. Leinaas and J. Myrheim, *Nuovo Cimento* **37B**, 1 (1977).
- [25] F. Wilczek, *Phys. Rev. Lett.* **49**, 957 (1982).
- [26] R. B. Laughlin, *Phys. Rev. Lett.* **50**, 1395 (1983).
- [27] C. Nayak, S. H. Simon, A. Stern, M. Freedman, and S. Das Sarma, *Rev. Mod. Phys.* **80**, 1083 (2008).
- [28] M. Greiter, X. G. Wen, and F. Wilczek, *Nucl. Phys. B* **374**, 567 (1992).
- [29] S. Das Sarma, C. Nayak, and S. Tewari, *Phys. Rev. B* **73**, 220502(R) (2006).
- [30] M. Sato, Y. Takahashi, and S. Fujimoto, *Phys. Rev. Lett.* **103**, 020401 (2009).
- [31] L. Fu and C. L. Kane, *Rhys. Rev. Lett.* **100**, 096407 (2008); *Phys. Rev. B* **79**, 161408(R) (2009).
- [32] J. Alicea, *Phys. Rev. B* **81**, 125318 (2010).
- [33] J. D. Sau, R. M. Lutchyn, S. Tewari, and S. Das Sarma, *Phys. Rev. Lett.* **104**, 040502 (2010).
- [34] R. M. Lutchyn, J. D. Sau, and S. Das Sarma, *Phys. Rev. Lett.* **105**, 077001 (2010).
- [35] Y. Oreg, G. Refael, and F. von Oppen, *Phys. Rev. Lett.* **105**, 177002 (2010).
- [36] J. Alicea, Y. Oreg, G. Refael, F. von Oppen, and M. P. A. Fisher, *Nat. Phys.* **7**, 412 (2011).

- [37] T. D. Stanescu and S. Tewari, J. Phys.: Condes. Matter **25**, 233201 (2013).
- [38] J. Linder, Y. Tanaka, T. Yokoyama, A. Sudbø, and N. Nagaosa, Phys. Rev. Lett. **104**, 067001 (2010).
- [39] L. Jiang, T. Kitagawa, J. Alicea, A. R. Akhmerov, D. Pekker, G. Refael, J. I. Cirac, E. Demler, M. D. Lukin, and P. Zoller, Phys. Rev. Lett. **106**, 220402 (2011).
- [40] J. Klinovaja, S. Gangadharaiah, and D. Loss, Phys. Rev. Lett. **108**, 196804 (2012).
- [41] M. Leijnse and K. Flensberg, Phys. Rev. B. **86**, 134528 (2012).
- [42] A. Cook and M. Franz, Phys. Rev. B **84**, 201105(R) (2011).
- [43] Y. S. Hor, A. J. Williams, J. G. Checkelsky, P. Roushan, J. Seo, Q. Xu, H. W. Zandbergen, A. Yazdani, N. P. Ong, and R. J. Cava, Phys. Rev. Lett. **104**, 057001 (2010).
- [44] P. Das, Y. Suzuki, M. Tachiki, and K. Kadowaki, Phys. Rev. B **83**, 220513(R) (2011).
- [45] L. Fu and E. Berg, Phys. Rev. Lett. **105**, 097001 (2010).
- [46] A.Y. Kitaev, Ann. Phys. **303**, 2 (2003).
- [47] M. Wimmer, A. R. Akhmerov, J. P. Dahlhaus, and C. W. J. Beenakker, New J. Phys. **13**, 053016 (2011).
- [48] M. Leijnse and K. Flensberg, Phys. Rev. B **84**, 140501(R) (2011).
- [49] D. E. Liu and H. U. Baranger, Phys. Rev. B **84**, 201308(R) (2011).
- [50] A. R. Akhmerov, J. Nilsson, and C. W. J. Beenakker, Phys. Rev. Lett. **102**, 216404 (2009).
- [51] E. Grosfeld and A. Stern, Proc. Natl. Acad. Sci. U.S.A. **108**, 11810 (2011).
- [52] S. Tewari, J. D. Sau, V. W. Scarola, C. Zhang, and S. Das Sarma, Phys. Rev. B **85**, 155302 (2012).
- [53] A. R. Akhmerov, J. P. Dahlhaus, F. Hassler, M. Wimmer, and C. W. J. Beenakker, Phys. Rev. Lett. **106**, 057001 (2011).
- [54] C.-X. Liu and B. Trauzettel, Phys. Rev. B **83**, 220510(R) (2011).

- [55] V. Mourik, K. Zuo, S. M. Frolov, S. R. Plissard, E. P. A. M. Bakkers, and L. P. Kouwenhoven, *Science* **336**, 1003 (2012).
- [56] M. T. Deng, C. L. Yu, G. Y. Huang, M. Larsson, P. Caroff, and H. Q. Xu, *Nano Lett.* **12**, 6414 (2012).
- [57] A. Das, Y. Ronen, Y. Most, Y. Oreg, M. Heiblum, and H. Shtrikman, *Nat. Phys.* **8**, 887 (2012).
- [58] H. O. H. Churchill, V. Fatemi, K. Grove-Rasmussen, M. T. Deng, P. Caroff, H. Q. Xu, and C. M. Marcus, *Phys. Rev. B* **87**, 241401(R) (2013).
- [59] J. Liu, A. C. Potter, K. T. Law, and P. A. Lee, *Phys. Rev. Lett.* **109**, 267002 (2012).
- [60] G. Kells, D. Meidan, and P. W. Brouwer, *Phys. Rev. B* **86**, 100503(R) (2012).
- [61] D. I. Pikulin, J. P. Dahlhaus, M. Wimmer, H. Schomerus, and C. W. J. Beenakker, *New J. Phys.* **14**, 125011 (2012).
- [62] E. J. H. Lee, X. Jiang, R. Aguado, G. Katsaros, C. M. Lieber, and S. De Franceschi, *Phys. Rev. Lett.* **109**, 186802 (2012).
- [63] L. P. Rokhinson, X. Liu, and J. K. Furdyna, *Nat. Phys.* **8**, 795 (2012).
- [64] L. Jiang, D. Pekker, J. Alicea, G. Refael, Y. Oreg, and F. von Oppen, *Phys. Rev. Lett.* **107**, 236401 (2011).
- [65] J. D. Sau, E. Berg, and B. I. Halperin, *arXiv:1206.4596* (2012).
- [66] J. M. Byers and M. E. Flatté, *Phys. Rev. Lett.* **74**, 306 (1995).
- [67] S. G. den Hartog, C. M. A. Kapteyn, B. J. van Wees, T. M. Klapwijk, and G. Borghs, *Phys. Rev. Lett.* **77**, 4954 (1996).
- [68] Th. Martin, *Phys. Lett. A* **220**, 137 (1996).
- [69] C. J. Bolech and E. Demler, *Phys. Rev. Lett.* **98**, 237002 (2007).
- [70] J. Nilsson, A. R. Akhmerov, and C. W. J. Beenakker, *Phys. Rev. Lett.* **101**, 120403 (2008).
- [71] L. Hofstetter, S. Csonka, J. Nygård, and C. Schönenberger, *Nature* **461**, 960 (2009).

- [72] L. G. Herrmann, F. Portier, P. Roche, A. Levy Yeyati, T. Kontos, and C. Strunk, *Phys. Rev. Lett.* **104**, 026801 (2010).
- [73] A. Das, Y. Ronen, M. Heiblum, D. Mahalu, A. V. Kretinin, and H. Shtrikman, *Nat. Commun.* **3**, 1165 (2012).
- [74] C. T. Black, D. C. Ralph, and M. Tinkham, *Phys. Rev. Lett.* **76**, 688 (1996).
- [75] J. von Delft and D.C. Ralph, *Phys. Rep.* **345**, 61 (2001).
- [76] A. Kitaev, *Phys. Usp.* **44**, 131 (2001).
- [77] M. Kriener, K. Segawa, Z. Ren, S. Sasaki, and Y. Ando, *Phys. Rev. Lett.* **106**, 127004 (2011); M. Kriener, K. Segawa, Z. Ren, S. Sasaki, S. Wada, S. Kuwabata, and Y. Ando, *Phys. Rev. B* **84**, 054513 (2011).
- [78] L. A. Wray, S.-Y. Xu, Y. Xia, Y. S. Hor, D. Qian, A. V. Fedorov, H. Lin, A. Bansil, R. J. Cava, and M. Z. Hasan, *Nat. Phys.* **6**, 855 (2010); *Phys. Rev. B*, **83**, 224516 (2011).
- [79] S. Sasaki, M. Kriener, K. Segawa, K. Yada, Y. Tanaka, M. Sato, and Y. Ando, *Phys. Rev. Lett.* **107**, 217001 (2011).
- [80] T. Kirzhner, E. Lahoud, K. B. Chaska, Z. Salman, and A. Kanigel, *Phys. Rev. B* **86**, 064517 (2012).
- [81] X. Chen, C. Huan, Y. S. Hor, C. A. R. Sá de Melo, and Z. Jiang, *arXiv:1210.6054* (2012).
- [82] N. Levy, T. Zhang, J. Ha, F. Sharifi, A. A. Talin, Y. Kuk, and J. A. Stroscio, *Phys. Rev. Lett.* **110**, 117001 (2013).
- [83] H. Peng, D. De, B. Lv, F. Wei, and C.-W. Chu, *Phys. Rev. B* **88**, 024515 (2013).
- [84] Y. Ando, *arXiv:1304.5693* (2013).
- [85] L. Hao and T. K. Lee, *Phys. Rev. B* **83**, 134516 (2011).
- [86] A. Yamakage, K. Yada, M. Sato, and Y. Tanaka, *Phys. Rev. B* **85**, 180509(R) (2012).
- [87] T. H. Hsieh and L. Fu, *Phys. Rev. Lett.* **108**, 107005 (2012).
- [88] E. Morenzoni, F. Kottmann, D. Maden, B. Matthias, M. Meyberg, Th. Prokscha, Th. Wutzke, and U. Zimmermann, *Phys. Rev. Lett.* **72**, 2793 (1994).

- [89] G. D. Morris, W. A. MacFarlane, K. H. Chow, Z. Salman, D. J. Arseneau, S. Daviel, A. Hatakeyama, S. R. Kreitzman, C. D. P. Levy, R. Poutissou, R. H. Heffner, J. E. Elenewski, L. H. Greene, and R. H. Kiefl, *Phys. Rev. Lett.* **93**, 157601 (2004).
- [90] P. W. Anderson, *J. Phys. Chem. Solids* **11**, 26 (1959).
- [91] A. Y. Kitaev, *Ann. Phys.* **321**, 2 (2006).
- [92] A. Altland and M. R. Zirnbauer, *Phys. Rev. B* **55**, 1142 (1997).
- [93] X.-G. Wen, *Int. J. Mod. Phys. B* **4**, 239 (1990).
- [94] A. Kitaev and J. Preskill, *Phys. Rev. Lett.* **96**, 110404 (2006).
- [95] M. Levin and X.-G. Wen, *Phys. Rev. Lett.* **96**, 110405 (2006).
- [96] M. Oshikawa, Y. B. Kim, K. Shtengel, C. Nayak, and S. Tewari, *Ann. Phys.* **322**, 1477 (2007).
- [97] T. H. Hansson, V. Oganesyan, and S. L. Sondhi, *Ann. Phys.* **313**, 497 (2004).
- [98] Z. Wang, X.-L. Qi, and S.-C. Zhang, *Phys. Rev. Lett.* **105**, 256803 (2010).
- [99] V. Gurarie, *Phys. Rev. B* **83**, 085426 (2011).
- [100] M. Cheng, R. M. Lutchyn, V. Galitski, S. Das Sarma, *Phys. Rev. Lett.* **103**, 107001 (2009).
- [101] S. Das Sarma, J. D. Sau, and T. D. Stanescu, *Phys. Rev. B* **86**, 220506(R) (2012).
- [102] B. H. Wu and J. C. Cao, *Phys. Rev. B* **85**, 085415 (2012).
- [103] A. Golub and B. Horovitz, *Phys. Rev. B* **83**, 153415 (2011).
- [104] G. Strübi, W. Belzig, M.-S. Choi, and C. Bruder, *Phys. Rev. Lett.* **107**, 136403 (2011).
- [105] S. B. Chung, X.-L. Qi, J. Maciejko, and S.-C. Zhang, *Phys. Rev. B* **83**, 100512(R) (2011).
- [106] K. T. Law, P. A. Lee, and T. K. Ng, *Phys. Rev. Lett.* **103** 237001 (2009).
- [107] G. Lesovik, T. Martin, and G. Blatter, *Eur. Phys. J. B* **24**, 287 (2001).
- [108] P. Recher, E. V. Sukhorukov, and D. Loss, *Phys. Rev. B* **63**, 165314 (2001).

- [109] J. Rech, D. Chevallier, T. Jonckheere, and T. Martin, Phys. Rev. B **85**, 035419 (2012).
- [110] S. Takei, B. M. Fregoso, H.-Y. Hui, A. M. Lobos, and S. Das Sarma, Phys. Rev. Lett. **110**, 186803 (2013).
- [111] J. Schindele, A. Baumgartner, and C. Schönenberger, Phys. Rev. Lett. **109**, 157002 (2012).
- [112] L. Fu, Phys. Rev. Lett. **104**, 056402 (2010).
- [113] R. Landauer, IBM Journal of Research and Development **1**, 223 (1957).
- [114] M. Büttiker, Phys. Rev. B **46**, 12485 (1992).
- [115] H. Bruus and K. Flensberg, *Many-Body Quantum Theory in Condensed Matter Physics: An Introduction*, Oxford University Press, 2004.
- [116] M. P. Anantram and S. Datta, Phys. Rev. B **53**, 16390 (1996).
- [117] A. Altland and B. Simons, *Condensed Matter Field Theory*, Cambridge University Press, 2006.
- [118] Ya. M. Blanter and M. Buttiker, Phys. Rep. **336**, 1 (2000).
- [119] H.-F. Lü, H.-Z. Lu, and S.-Q. Shen, Phys. Rev. B **86**, 075318 (2012).
- [120] H. P. Breuer and F. Petruccione, *The Theory of Open Quantum Systems*, Oxford University Press, London, 2002.
- [121] D. C. Ralph, C. T. Black, and M. Tinkham, Phys. Rev. Lett. **78**, 4087 (1997).
- [122] M. Tinkham, *Introduction to Superconductivity*, McGraw-Hill, New York, 1996.
- [123] J. D. Sau, R. M. Lutchyn, S. Tewari, and S. Das Sarma, Phys. Rev. B **82**, 094522 (2010).
- [124] S. Tewari and J. D. Sau, Phys. Rev. Lett. **109**, 150408 (2012).
- [125] P. M. Ostrovsky, M. A. Skvortsov, and M. V. Feigel'man, Phys. Rev. Lett. **92**, 176805 (2004).
- [126] F. E. Meijer, A. F. Morpurgo, and T. M. Klapwijk, Phys. Rev. B **66**, 033107 (2002).

- [127] B. van Heck, F. Hassler, A. R. Akhmerov, and C. W. J. Beenakker, Phys. Rev. B **84**, 180502(R) (2011).
- [128] K. Flensberg, Phys. Rev. B **82**, 180516(R) (2010).
- [129] O. Motrunich, K. Damle, and D. A. Huse, Phys. Rev. B **63**, 224204 (2001).
- [130] P.W. Brouwer, M. Duckheim, A. Romito, and F. von Oppen, Phys. Rev. B **84**, 144526 (2011).
- [131] R. M. Lutchyn, T. D. Stanescu, and S. Das Sarma, Phys. Rev. Lett. **106**, 127001 (2011); T. D. Stanescu, R. M. Lutchyn, and S. Das Sarma, Phys. Rev. B **84**, 144522 (2011).
- [132] M. Wimmer, A. R. Akhmerov, M. V. Medvedyeva, J. Tworzydło, and C. W. J. Beenakker, Phys. Rev. Lett. **105**, 046803 (2010).
- [133] A. C. Potter and P. A. Lee, Phys. Rev. Lett. **105**, 227003 (2010).
- [134] B. Zhou and S.-Q. Shen, Phys. Rev. B **84**, 054532 (2011).
- [135] K. T. Law and P. A. Lee, Phys. Rev. B **84**, 081304 (2011).
- [136] R. M. Lutchyn and M. P. A. Fisher, Phys. Rev. B **84**, 214528 (2011).
- [137] J. R. Schrieffer, *Theory of Superconductivity*, Addison-Wesley, Redwood City, 1983.
- [138] F. W. J. Hekking, L. I. Glazman, K. A. Matveev, and R. I. Shekhter, Phys. Rev. Lett. **70**, 4138 (1993).
- [139] D. V. Averin and Yu. V. Nazarov, Phys. Rev. Lett. **65**, 2446 (1990).
- [140] P. W. Anderson, Phys. Rev. Lett. **3**, 325 (1959).
- [141] J. Linder, T. Yokoyama, and A. Sudbø, Phys. Rev. B **80**, 205401 (2009).
- [142] C.-X. Liu, HaiJun Zhang, B. Yan, X.-L. Qi, T. Frauenheim, X. Dai, Z. Fang, and S.-C. Zhang, Phys. Rev. B **81**, 041307 (2010).
- [143] H.-Z. Lu, W.-Y. Shan, W. Yao, Q. Niu, and S.-Q. Shen, Phys. Rev. B **81**, 115407 (2010).
- [144] H. Lin, R. S. Markiewicz, L. A. Wray, L. Fu, M. Z. Hasan, and A. Bansil, Phys. Rev. Lett. **105**, 036404 (2010).

- [145] T. H. Hsieh, H. Lin, J. Liu, W. Duan, A. Bansil, and L. Fu, *Nat. Commun.* **3**, 982 (2012).
- [146] S. Sasaki, Z. Ren, A. A. Taskin, K. Segawa, L. Fu, and Y. Ando, *Phys. Rev. Lett.* **109**, 217004 (2012).
- [147] S. B. Chung and S.-C. Zhang, *Phys. Rev. Lett.* **103**, 235301 (2009).
- [148] Y. Nagato, S. Higashitani, and K. Nagai, *J. Phys. Soc. Jpn.* **78**, 123603 (2009).
- [149] M. S. Bahramy, P. D. C. King, A. de la Torre, J. Chang, M. Shi, L. Patthey, G. Balakrishnan, Ph. Hofmann, R. Arita, N. Nagaosa, and F. Baumberger, *Nat. Commun.* **3**, 1159 (2012).
- [150] K. Michaeli and L. Fu, *Phys. Rev. Lett.* **109**, 187003 (2012).
- [151] L. C. Hebel and C. P. Slichter, *Phys. Rev.* **113**, 1504 (1959).
- [152] R. E. Taylor, B. Leung, M. P. Lake, and L.-S. Bouchard, *J. Phys. Chem. C* **116**, 17300 (2012).
- [153] B.-L. Young, Z.-Y. Lai, Z. Xu, A. Yang, G. D. Gu, Z.-H. Pan, T. Valla, G. J. Shu, R. Sankar, and F. C. Chou, *Phys. Rev. B* **86**, 075137 (2012).
- [154] D. Koumoulis, T. C. Chasapis, R. E. Taylor, M. P. Lake, D. King, N. N. Jarenwatananon, G. A. Fiete, M. G. Kanatzidis, and L.-S. Bouchard, *Phys. Rev. Lett.* **110**, 026602 (2013).
- [155] M. M. Vazifeh and M. Franz, *Phys. Rev. B* **86**, 045451 (2012).
- [156] Z. Salman, E. Pomjakushina, V. Pomjakushin, A. Kanigel, K. Chashka, K. Conder, E. Morenzoni, T. Prokscha, K. Sedlak, and A. Suter, arXiv:1203.4850.
- [157] F. Perez, C. Aku-leh, D. Richards, B. Jusserand, L. C. Smith, D. Wolverson, and G. Karczewski, *Phys. Rev. Lett.* **99**, 026403 (2007).
- [158] L. Hao, P. Thalmeier, and T. K. Lee, *Phys. Rev. B* **84**, 235303 (2011).
- [159] T. Hashimoto, K. Yada, A. Yamakage, M. Sato, and Y. Tanaka, *J. Phys. Soc. Jpn.* **82**, 044704 (2013).
- [160] M. Sato and S. Fujimoto, *Phys. Rev. B* **79**, 094504 (2009).
- [161] G. E. Volovik, *JETP Lett.* **90**, 398 (2009).

- [162] J. D. Sau, S. Tewari, R. Lutchyn, T. Stanescu, and S. Das Sarma, Phys. Rev. B **82**, 214509 (2010).

Original publications

The chapters of the present thesis are based on the following original publications:

1. Chapter 3

B. Zocher and B. Rosenow, *Modulation of Majorana-Induced Current Cross-Correlations by Quantum Dots*, Phys. Rev. Lett. **111**, 036802 (2013).

2. Chapter 4

B. Zocher, M. Horsdal, and B. Rosenow, *Proposed Detection of the Topological Phase in Ring-Shaped Semiconductor-Superconductor Nanowires Using Coulomb Blockade Transport*, Phys. Rev. Lett. **109**, 227001 (2012).

3. Chapter 4

B. Zocher, M. Horsdal, and B. Rosenow, *Robustness of Topological Order in Semiconductor-Superconductor Nanowires in the Coulomb Blockade Regime*, New J. Phys. **15**, 085003 (2013).

4. Chapter 5

B. Zocher and B. Rosenow, *Surface states and local spin susceptibility in doped three-dimensional topological insulators with odd-parity superconducting pairing symmetry*, Phys. Rev. B **87**, 155138 (2013).

Scientific talks and posters

Talks

- B. Zocher, *Coulomb blockade signatures of the topological phase transition in semiconductor-superconductor nanowires*, DPG Spring meeting, Berlin, 26.03.2012.
- B. Zocher, *Crossed Andreev reflection and noise through Majorana bound states*, Ringberg, Max Planck Institute for Solid State Research, Ringberg, 25.09.2012.
- B. Zocher, *Crossed Andreev reflection and noise through Majorana bound states*, Group seminar Condensed Matter Theory, TU Dresden, 26.10.2012.
- B. Zocher, *Local spin susceptibility and surface states in doped three-dimensional topological insulators with odd-parity superconducting pairing symmetry*, DPG Spring meeting, Regensburg, 15.03.2013.

Posters

- B. Zocher, *Proposed detection of a topological phase transition in semiconductor superconductor nanowires using Coulomb blockade transport*, Workshop, Max Planck Institute for Physics of Complex Systems, Dresden, June 2012.
- B. Zocher, *Proposed detection of a topological phase transition in semiconductor superconductor nanowires using Coulomb blockade transport*, Symposium Quantum Coherence in Nanostructures, Leipzig, 04.10.2012.
- B. Zocher, *Modulation of Majorana induced current cross-correlations by quantum dots*, DPG Spring meeting, Regensburg, 14.03.2013.

Academic Curriculum Vitae

Personal Details

Name	Björn Zocher
Date of birth	December 05, 1987
Place of birth	Borna
Nationality	German

Education

1994 – 1998	Grundschule Bad Lausick (Primary school)
1998 – 2006	Friedrich Schiller Gymnasium Bad Lausick (Secondary School)
07.07.2006	School leaving degree: Abitur
2006 – 2008	Basic studies Physics, Technische Universität Dresden
28.02.2008	Undergraduate degree: Vordiplom Physik
2008 – 2011	Main studies Physics, Technische Universität Dresden
29.11.2010	Diploma thesis: "Spin Density Waves in Multi Band Models" Institut für Theoretische Physik, Theorie der Kondensierten Materie Supervisor: Prof. Dr. Carsten Timm Degree: Dipl.-Phys.
2011 – 2013	Universität Leipzig, PhD student
2011 – 2013	Scholarship from the International Max Planck Research School Mathematics in the Sciences
Feb. – June 2013	PhD student, Max Planck Institute for Solid State Research, Stuttgart

Acknowledgement

First and foremost, I would like to thank my supervisor Prof. Dr. Bernd Rosenow for the advice and many interesting discussions. Bernd Rosenow has attracted my attention to a wide variety of different phenomena taking place in low-dimensional electronic systems. With many suggestions and instructive directions he gave important pulses to this work. I also thank him for giving me the opportunity to continue working in his research group. Among my colleagues in the Statistical Physics group, whose friendly and encouraging atmosphere I highly appreciate, it is difficult to single out particular persons for acknowledgment. I am grateful for many valuable discussions with Dr. Mats Horsdal, Dr. Timo Hyart, and Lukas Kimme. I thank Martin Treffkorn, Alexander Janot, and Dr. Daniel Scherer for interesting discussions about physics. Moreover, I thank Martin Treffkorn for his work as admin and for solving all my computer problems. I am happy to have shared office with Lukas Kimme and Christoph Lehmann, thank you both for the nice time and the computer support.

I thank Prof. Dr. J. Haase, Dr. D. Rybicki, and N. Georgieva for stimulating discussions about NMR and their data on NMR in topological insulators. I also thank Prof. Dr. C. Timm and Dr. P. M. R. Brydon for teaching me the basics of scientific research and scientific writing.

Moreover, I thank the International Max Planck Research School Mathematics in the Sciences for offering financial support and interesting lectures. I would like to express my gratitude to the Max Planck Institute for Mathematics in the Sciences for the opportunity to work in this wonderful research environment. Furthermore, I would like to thank the secretaries Lea Voigt, Gabriele Menge, Susan Hussack, and Elke Herrmann for always supporting me in the bureaucratic burdens.

I would like to thank my wife Teresa and my son Lukas for their patience, love, and encouragement. Thank you both for being beautiful rays of sunshine after a long day in the office. Finally, I would especially like to thank my parents and my sister for their permanent support and encouragement during the last years.

Erklärung

Mit meiner Unterschrift versichere ich, dass ich die vorliegende Arbeit ohne unzulässige Hilfe Dritter und ohne Benutzung anderer als der angegebenen Hilfsmittel angefertigt habe. Die aus fremden Quellen direkt oder indirekt übernommenen Gedanken sind als solche kenntlich gemacht.

Ich versichere, dass außer den in der Danksagung genannten, weitere Personen bei der geistigen Herstellung der vorliegenden Arbeit nicht beteiligt waren, insbesondere nicht die Hilfe eines Promotionsberaters in Anspruch genommen wurde und weitere Personen von mir oder in meinem Auftrag weder unmittelbar noch mittelbar geldwerte Leistungen für Arbeiten erhalten haben, die im Zusammenhang mit dem Inhalt der vorgelegten Dissertation stehen.

Ich versichere weiterhin, dass die vorgelegte Arbeit weder im Inland noch im Ausland in gleicher oder in ähnlicher Form einer anderen Prüfungsbehörde zum Zwecke einer Promotion oder eines anderen Prüfungsverfahrens vorgelegt und in ihrer Gesamtheit noch nicht veröffentlicht wurde.

Ich versichere außerdem, dass keine früheren erfolglosen Promotionsversuche stattgefunden haben.

Zocher, Björn

Leipzig, 05. September 2013

